Ph.D. Thesis

Amorphous Carbon (a-C:H): Atomic Bonding Structure, Electrical and Optical Properties

by

Said Hussien Sayed Moustafa
B.Sc. (1988), M.Sc. (1993)
(Helwan University)

supervisor

Dr. Margit Koós
Candidate of Physical Science

Research Institute for Solid State Physics and Optics
Budapest - Hungary

1998.

CONTENTS

1. INTRODUCTION

The last two decades have seen a continuous growth in our knowledge of amorphous materials and our understanding of their properties, together with a considerable increase of technological exploitation. The material at the focus of our investigation here is hydrogenated amorphous carbon (a-C:H), which exhibits a number of attractive technological properties similar to those of diamond. These include hardness, low coefficient of friction, transparency in the infra-red / visible region, chemical inertness and low dielectric constant. Another interesting property of a-C:H is that its optical properties can be varied over a wide range. In addition, as a coating material, it can be deposited on large surfaces held at low temperature with an ultra-smooth surface finish. Utilization of this coating material for various applications has promoted extensive research in this field in recent years.

The electron structure and the effect of disorder on the electronic processes of amorphous carbon are very different from other amorphous semiconductors such as amorphous silicon because of the existence of sp^2 sites. Carbon atoms in a-C:H enable hybridization of its orbitals sp^3, sp^2, and sp^1 in three different ways. In the sp^3 hybridized state the carbon atom is bonded tetrahedrally as in diamond; at a carbon sp^2 site, there are three strong σ bonds and one π bond lying normal to the σ bonding plane; in the sp^1 configuration two of four valence electrons form linearly directed σ bonds, and the other two electrons are sited in two π-bonds, orthogonal to each other in a plane perpendicular to the σ orientation. The considerable uncertainty concerning the microscopic origins of the interesting properties of a-C:H seems to originate from carbon's varied bonding forms. Hydrogen, incorporated in this structure, plays a crucial role in the stabilization of the tetrahedrally bonded carbon atoms, and produces a wide variety of materials with different properties.

Thin a-C:H layers are used quite extensively at present as a hard mechanical coating in devices ranging from cutting tools to magnetic hard disks (Winchesters), to infrared detectors/transmitters. What is surprising therefore is what little agreement there is regarding how the microstructure and bonding of these a-C:H films are related to their macroscopic properties. The detailed structure of the bonding network in a-C:H is still under investigation – through a number of theoretical models have been proposed. Angus and Jansen [72] have suggested a random covalent network model and found a link between hydrogen concentration and the ratio of sp^3 to sp^2 bondings. But the most popular of the various models is the two phase model of Robertson [22] which has turned out to be fruitful in interpreting several macroscopic properties. According to this model the amorphous carbon consists of sp^2 bonded planar carbon clusters (fused sixfold rings) embedded in a randomly oriented sp^3 bonding matrix. The matrix connectivity largely controls the mechanical properties, whereas the cluster structure of the sp^2 phase controls the electronic properties.

One of the most strongly disputed problems is the medium range ordering (MRO), or clustering of sp^2 carbon sites. Raman measurements have supplied evidence on the formation of graphite clusters, but the neutron diffraction data strongly suggest olefinic chains of different lengths as the dominant form of MRO. Further difficulties arise when we try to explain optical gap values of a-C:H samples obtained by interpreting Raman spectra based on the microcrystalline graphite picture. It would seem that the Raman results give only a limited picture about the intermediate range ordering of sp^2 sites in view of which they should be considerably revised. Therefore investigations were carried out on sample series with gradually increasing sp^2 content; this work has yielded experimental data which are essential in understanding the structural properties of a-C:H.

Those properties which are important in optical and electrical applications of a-C:H are influenced essentially by localized states in the gap and near band edges; these states can be tested by electrical transport measurements. In contrast, the optical properties near the absorption edge region supply important data on the quasilocalized states of valence – and conduction band tails as well as on extended states beyond the mobility edges. Our approach to the experimental work was as follows: i) study the bonding properties of a-C:H samples prepared using different deposition parameters in order to understand the influence of these parameters on hydrogen content, as well as to learn how the sp^2 and sp^3 carbon sites are distributed in the as prepared samples and the influence of annealing on these properties; ii) investigate direct current conduction near and above room temperature in an attempt to understand the role of localized and tail states in electrical transport in a-C:H samples of different structure; iii) investigate different optical properties, dielectric function, refractive index, optical gap, as a means of finding a relationship between optical characteristics and structural properties of a-C:H thin layers.

The research work presented here was motivated by the question how the electrical, transport and optical properties are linked with the bonding characteristics and nanostructure of a-C:H. For this reason a-C:H thin layers characterized by a variety of bonding properties and by different intermediate range ordering were prepared in a well controlled way and their bonding, electrical and optical properties were studied experimentally.

First we briefly introduce this work in chapter 1 and chapter 2 contains a review about the crystalline and amorphous forms of carbon. In chapter 3 we reviewed results obtained by different laboratories in the research of amorphous carbon – more exactly in the study of hydrogenated amorphous carbon (a-C:H). In this chapter we introduce our main results concerning the structure of a-C:H and several macroscopic properties; in addition, we discuss those difficulties, questions or contradictions which have a close bearing on our work. In chapter 4 we describe the deposition system used for sample preparation in our laboratory. Results obtained by different experimental methods for the structural of properties of a-C:H samples are presented in chapter 5. Chapter 6 discusses the results of dc electrical measurements and their comparison with different transport models. Optical data obtained by spectral ellipsometry and transmission measurements are introduced in chapter 7. The final chapter (chapter 8) summarizes our results.

2. DIFFERENT FORMS OF CRYSTALLINE AND AMORPHOUS CARBON

Carbon is considered an extremely important element in our life, it is the main constituent of organic compounds and has two crystalline forms, have been studied since ancient times, diamond and graphite. Carbon lies in the fourth group in the periodic table but it differs from its neighbours such as Ge or Si which in both amorphous and crystalline forms exists only in sp^3 bonding configuration. But the bonding possibilities of carbon atoms are sp^3, sp^2 and sp^1 configurations (will be discussed in chapter 3) what gives carbon a large possibility to constitute many different structural compositions. For example, in two crystalline forms of carbon, in diamond has only sp^3 configuration and in graphite it has only sp^2 configurations. Recently, new crystalline forms of carbon discovered such as fullerenes (C_{60}) [1], carbon nanotubes and their relation to fullerenes [2] and carbolities [3] demonstrate also the bonding variability of carbon atom.

The most important properties of carbon materials are low specific gravity, chemical inertness preserved up to 700 K, high antifrictional power, large neutron attenuation factor, sublimation temperature above 3900 K, their ability to retain their mechanical characteristics at temperatures approaching 3500 K and the capacity of varying widely their resistivity in response to heat treatment or intercalation with various substances. These all properties of carbon materials makes carbon as an interested material and inserted it in a modern technological applications.

In this chapter we will introduce some structural, optical, electrical, and other properties of the two crystalline carbon forms, diamond and graphite. Then, we write about polycrystalline and thin film forms of diamond, and discuss the diamond problem that is why the scientists started to produce the disordered and thin film forms of diamond. After then, we are dealing with some disordered carbon forms among those especially with the amorphous hydrogenated carbon thin films being this is the point of our interest.

Diamond

The one crystalline form of carbon is the diamond, its crystal structure with tetrahedral bonds of carbon atoms is shown in Fig. 2.1. The space lattice of diamond is face centred cubic. The nearest neighbour is four atoms and the second nearest neighbour is 12 atoms. In addition to the eight corner atoms and six face centre atoms (shaded), there are four atoms (hashed) spaced on one quarter of a cubic diagonal which are from the adjacent interpenetrating lattices (two of them connected by the dotted line). Hexagonal diamond structure was also observed at first in meteorites and other form of diamond is also supposed to be in very small particles.

Natural diamond classified as type I and type II. Type I is rich nitrogen; type Ia has a nitrogen sufficient to agglomerate and to presents no spin resonance, and type Ib has nitrogen dispersed atomically as in most artificial diamond and exhibits a spin resonance. Type II is free from nitrogen and it is classified type IIa, which is electrically insulator and type IIb, which P-type semiconductor looks like, where born concentration is greater than background nitrogen concentration. [5]

Table. 2.1 summarizes some structural data and physical properties of diamond and for comparison of graphite too. Carbon atom in diamond has purely covalent bonds, its bonding configuration is sp^3. These strong saturated bonds give its strength which makes diamond to be

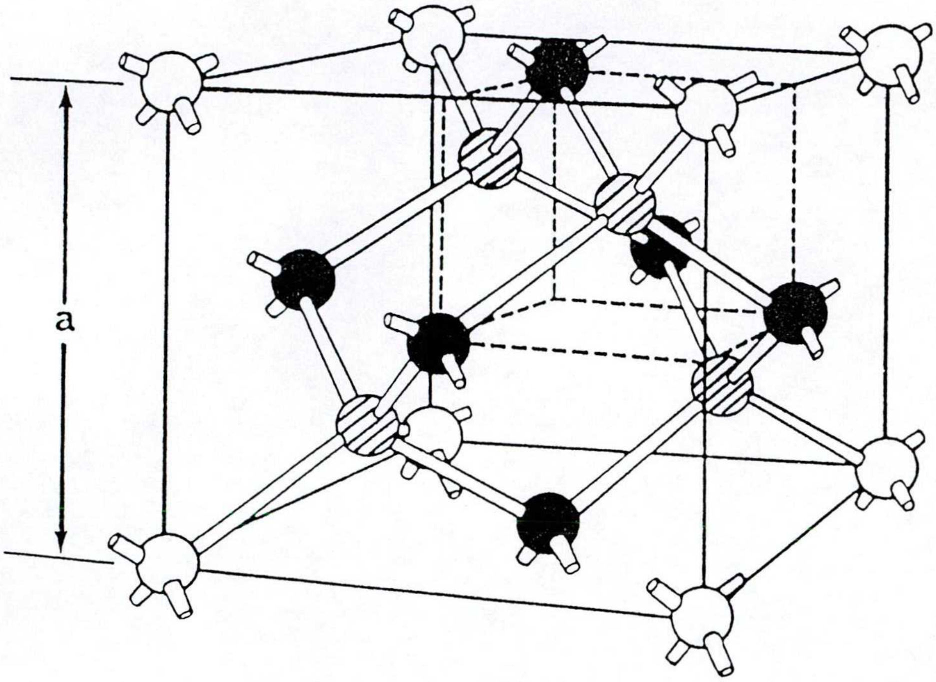

Fig. 2.1 Tetrahedral structure of diamond [4]

the hardest material in nature. Because the diamond covalent bonds are not simple to break, it has a high resistant to the chemical attack and all the reactions up to 700K. Unique thermal conductivity makes it promising material for heat dissipation. Exceptional mechanical and thermal properties of diamond is combined with favourable optical properties which are promising in possible application as optical coating material

Table. 2.1 Some structural and physical constants of crystalline diamond and graphite.

Parameter	**Diamond**	**Graphite**
Thermal conductivity (watts/cm-°C)	20	0.8 - 2.5
Thermal expansion coefficient	0.8 at 300 K	8.8 in-plane 27.3 along c axis
Hardness (Kg/mm^2)	10^4	-
Density (gm cm^{-3})	3.515	2.267
Refractive index	2.41 - 2.44 (656-486 nm.)	-
Band gap (eV)	5.5	-0.04
Conductivity (Ω^{-1} cm^{-1})	10^{-18}	2.5x10^4 ($\perp_C$)
Space group	Oh^7;Fd3m	$D_{6H}{}^4$
Unit cell constants	Cubic 0.457 nm.	a=0.246 nm. c=0.671 nm.
C-C nearest neighbour distance	0.154 nm.	0.142 nm.
Bonding	sp^3	sp^2
Young modulus (GPa)	1050	686

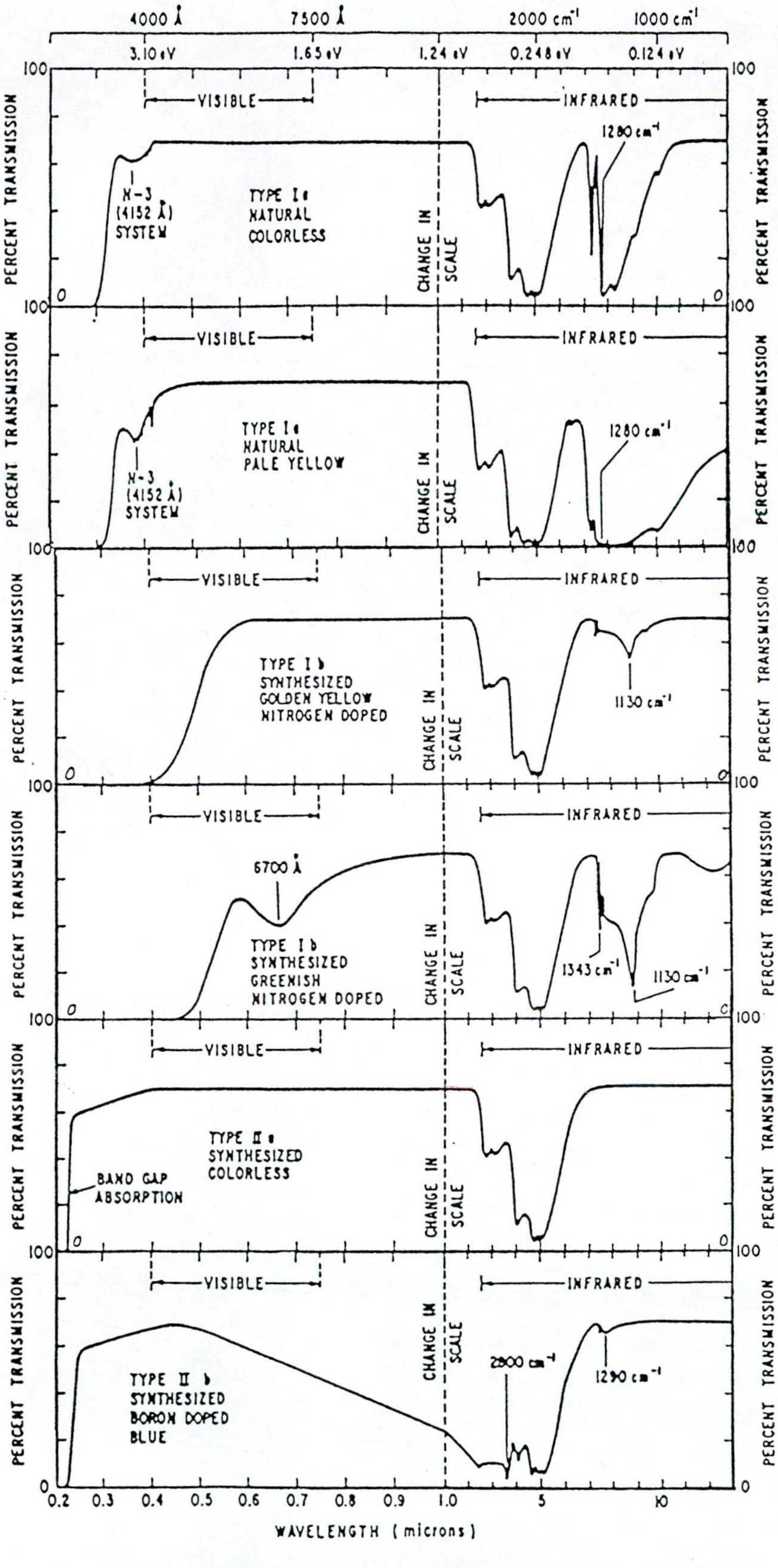

Fig. 2.2 Optical transparency of I and II type diamond in the UV, Visible and IR region [5].

Diamond transparent in a wide wavelength range from ultraviolet absorption edge through the visible spectrum and in the infrared region. Depending on the diamond type (impurities), the visibility of light through diamond changes. For example, type I diamond is transparent from 330 nm to 2.5 μm and over 10 μm whereas type II diamond is transparent from 220 nm to 2.5 μm and over 6 μm. Fig. 2.2 shows optical transparency of these two types of natural diamond.

The electronic band structure of diamond is shown in Fig. 2.3, where the graphite band structure is given too. The diamond bands around the gap are like those of Si. The gap of 5.5 eV is indirect. The electron states form sit degenerate valleys with surfaces in the form of prolate spheroids. The effective mass of the holes is about 0.7 m_o [6] and of electrons 0.48 m_o [7], where m_o is the free electron mass.

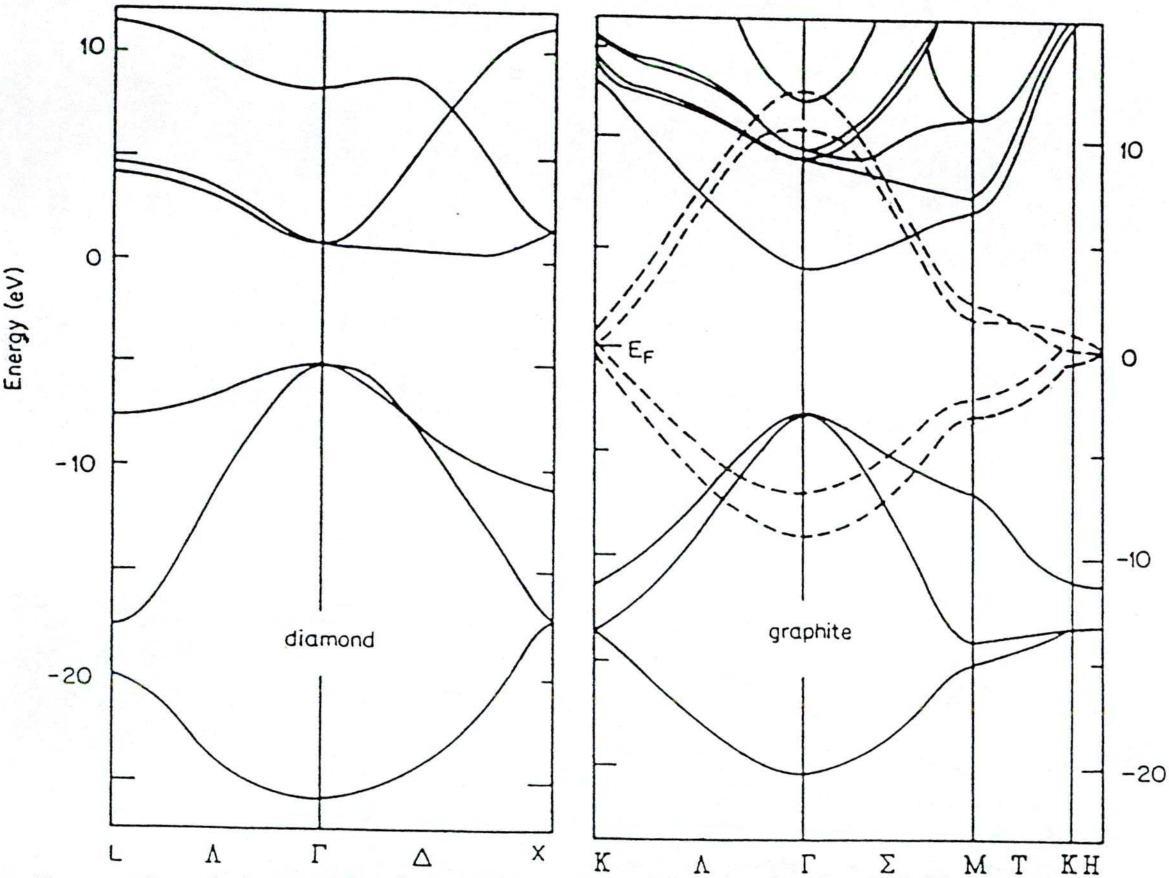

Fig. 2.3 Band structure of diamond [8](a) and graphite[9](b). Solid lines for σ bonds and dotted lines represents π bonds.

Diamond has two direct energy gaps at 7 eV and 12.5 eV which appeared as a two peaks in the reflectance curve [10] Fig. 2.4 where the photon energy at these peaks exhibits critical points in the density of states. That happens wherever valence and conduction band edges are parallel and allow direct transitions. But although diamond has two direct energy gaps, the absorption edge at 5.5 eV band gap is very pronounced. Diamond is characterised by a refractive index of 2.41 at 656 nm wavelength. This value is considerably smaller than that of most common semiconductors, but nearly twice of that of most common insulator. Therefore diamond window may be optically matched to air or vacuum by a coating having a refractive index of 1.55. In such an arrangement, the reflectivity of a normal incident wave would be nil.

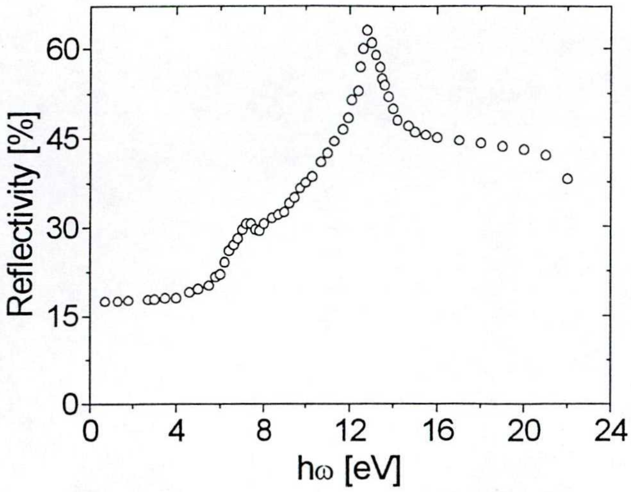

Fig. 2.4 Reflectance curve of diamond in a wide photon energy range [11].

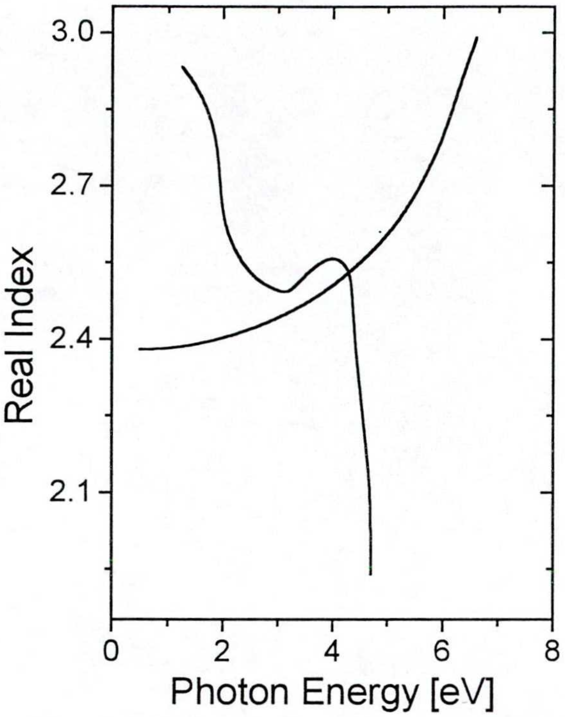

Fig. 2.5 Spectral dependence of refractive index of diamond and graphite [12].

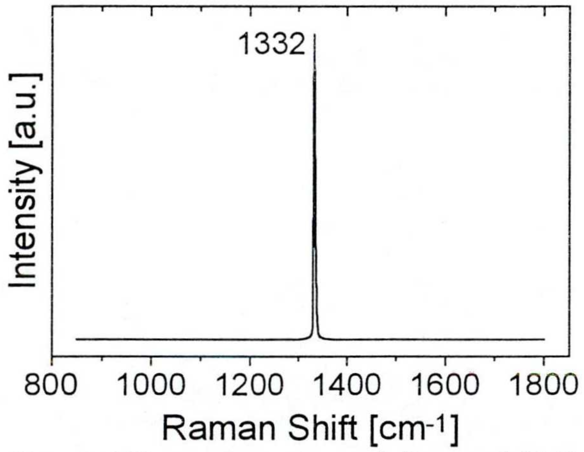

Fig. 2.6 Raman spectrum of diamond [15].

For example quartz is such a material. The spectral dispersion of refractive index fits empirical formula

$$n^2 - 1 = \frac{a\lambda^2}{\lambda^2 - \lambda_1^2} + \frac{b\lambda^2}{\lambda^2 - \lambda_2^2},$$

where a=0.3306, b=4.3356, λ_1=175.0 nm and λ_2=106.0 nm.

Fig. 2.5 shows spectral dependence of refractive index of diamond and, for a comparison, of graphite in a wide wavelength range.

Raman spectroscopy is known as a convenient nondestructive tool to characterise carbon materials. Raman scattering is very powerful method due to its ability to distinguish different bonding type and sensitivity for internal stresses and domain sizes. Raman spectra inform us about bonding configurations of carbon atom as well as about crystallographic arrangement. Diamond is characterised by the F_{2g} triply degenerate Raman active mode at 1332.5 cm^{-1} [13]. The band width at half intensity less than 1.8 cm^{-1}. Fig. 2.6 shows raman spectrum of diamond. For natural diamonds of different origin, the peak frequencies varies in the range of 1331-1336 cm^{-1} and half band width from 1.8 to 3 cm^{-1} depending on the distortion crystal structure [14].

Most electrical properties of diamond are extrinsic, i.e strongly dependent on the impurity content. Excepting for electron velocity, the electrical properties of diamond exceed those of virtually all other semiconductors. Room temperature resistivity is 10^{16} Ωcm and the breakdown field is as high as 10^7 V/cm. Its 1800 cm^2/Vs hole mobility is 3 times larger than that for silicon. Diamond is thought to exhibit a negative electron affinity on its (111) surface.

Exceptional physical and chemical properties of diamond reviewed so far offer large variety of its possible applications. Diamond can give a good protective coating on surfaces exposed to abrasive, aggressive, corrosive or chemically attacking environment. Strength and hardness together with the optical smooth surface the diamond may be applied as protective coatings on compact discs. Diamond is considered as excellent protective coating material for optical elements as well. Transparent windows in visible and other spectral ranges can be fabricated from diamond. Another offering field of diamond application is the electrically insulating heat dissipator for electrical devices such as diodes, transistors, integrated circuits and as an emitter cathode in field emission displays. Of coarse artificial diamond is used in cutting, drilling, grinding tools and surgical blades. A last we should not forget the biocompatibility of diamond what opens an important, promising possibility of diamond applications. Requirements of the diamond use for these purposes cannot be fulfilled with natural and artificial diamond stones what stimulates development of new diamond technologies discussed later in this section.

Graphite

Graphite is the other crystalline form of carbon which is more stable allotrope modification especially at high temperatures, that is why many disordered forms of carbon have structures based on graphite lattice. It is an anistropic material. Its structure consists of hexagonal layers of purely sp^2 hybridised carbon atoms weakly bonded together by van der Waals forces in ABAB stacking sequence along c axis as shown in Fig. 2.7 with an interplaner spacing of d=3.354 Å. Each layer is similar to a large molecule consisting from the flat benzene molecules. The different strength of bonds in the plane of aromatic rings and perpendicular to it is responsible for the strong anisotropy observed in many properties of graphite. This anisotropy means that the properties in the direction parallel to aromatic layers different from those in the direction perpendicular to this layers.

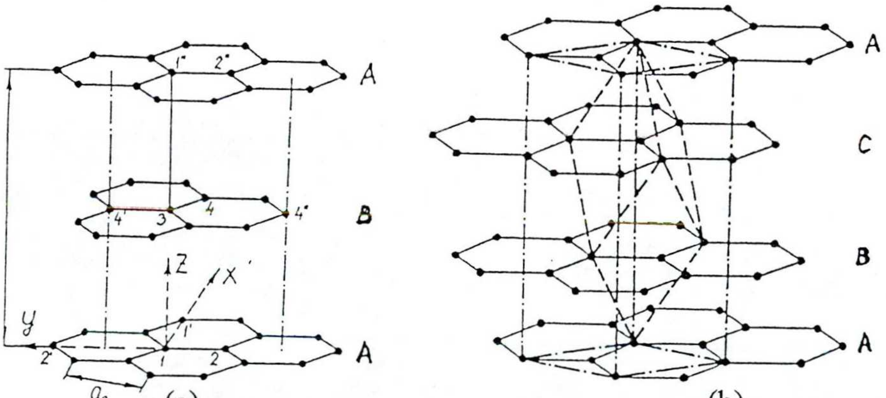

(a) (b)

Fig. 2.7 Crystal structure of graphite [16](a) Hexagonal, (b) rhombohedral (the hedron is formed by the dashed lines). The A, B, C denote non-equivalent graphite layers.

Graphite is a soft material; even though the hardness within the aromatic layers approaches the diamond hardness, due to the weak resistance of interlayer movement. Some structural and physical properties of graphite is summarised in Table. 2.1 and its band structure is shown on Fig. 2.3.b.

Graphite has a high absorption coefficient and a negative band gap. The upper most valence band and the lower most conduction band interfere with each other Fig. 2.3.b which makes graphite to have semimetal properties and negative band gap. The π electrons in the graphite layers weakens the C–C bonds. These π electrons has a high mobility which causes the high electrical conductivity in the plane of a graphite layer and makes graphite electrical conductivity to approach the metallic or semimetalic conduction properties. Fig. 2.4 shows the spectral dependence refractive index for graphite.

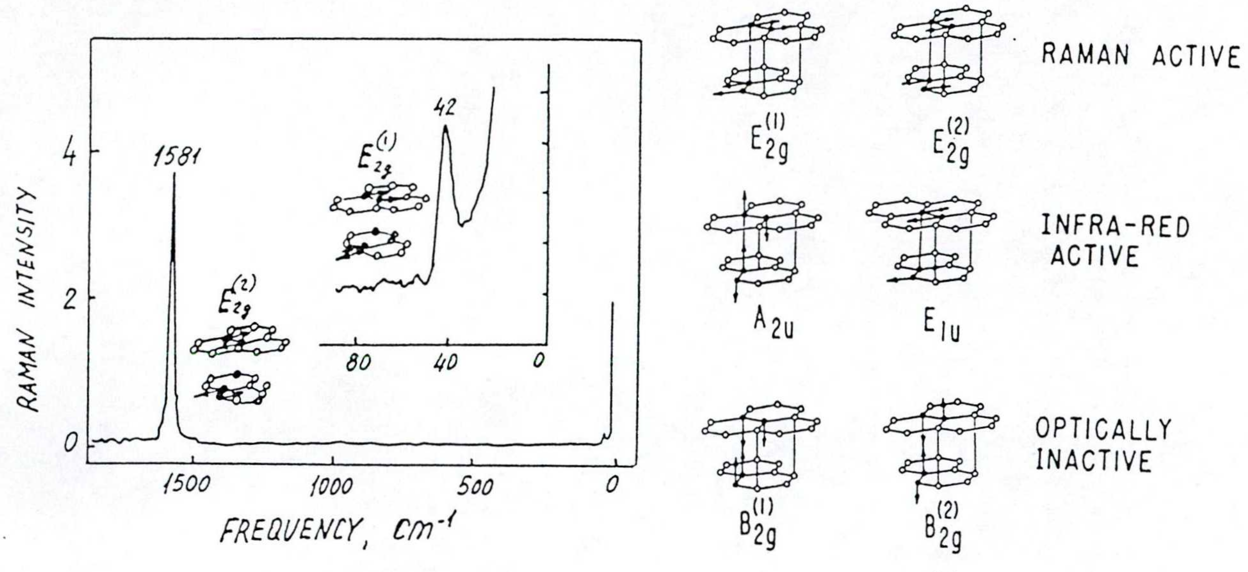

(a) (b)

Fig. 2.8 Raman spectrum of graphite(a)[17], and atomic displacement of the zone centre optic vibrations (b) [18]

Graphite structure has both Raman and infrared active optic modes; the atomic displacement of the zone centre optic vibrations is shown in Fig. 2.8.b. The $E_{2g}^{(2)}$ in plane layer mode is Raman active with a characteristic Raman shift of 1581 cm^{-1}. The Raman cross section of this $E_{2g}^{(2)}$ graphite mode being ~50 times larger than the F_{2g} diamond mode [19] makes the Raman spectroscopy to be a sensitive method in identification of sp^2 aromatic layers in any carbon structures. Fig. 2.8.a shows this Raman scattering due to this $E_{2g}^{(2)}$ normal mode of graphite. The other Raman active vibration is the $E_{2g}^{(1)}$ vibration which gives very small peak at 42 cm^{-1}. The “out-of-plane” A_{2u} symmetry mode and the “in-plane” E_{1u} symmetry mode are infrared active and their frequencies are 868 cm^{-1} and 1588 cm^{-1} respectively as it is shown in Fig. 2.9. The $B_{2g}^{(1)}$ and $B_{2g}^{(2)}$ modes are optically inactive.

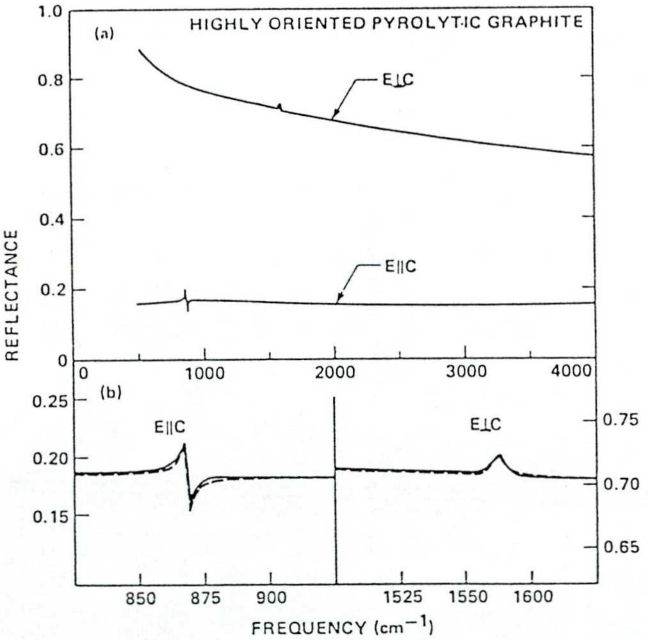

Fig. 2.9 The $E\parallel c$ and $E\perp c$ reflectance of graphite. The oscillator sits to the data in the region of the phonon features are shown as dashed (---) lines in (b), while the solid lines are the data [18].

Graphite can be produced by the pyrolysis of many organic materials. The end product of graphite preparation process depends on heat treatment and the starting material [20,21]. The three main stages of graphite preparation are the carbonisation, polymerisation and graphitisation [22].

The most ordered form of synthetic graphite is called highly oriented pyrolytic graphite (h.o.p.g.). It produced by heat and pressure treatments up to 3600 °C. Its d spacing is 3.354 - 3.359 Å and its crystalline sizes are of the order of 1μm [23].

A variety of graphite application is known for many years, however graphite related materials due to their unique properties offer a more wide varying possibility of application than graphite itself. Recently graphite intercalation compounds (GICs) which formed by the insertion of layers of guest species between the graphite layers promise the enhanced battery performance relative to lost graphite material [24,25]. The carbon nanotubes [2] are the most recently discovered carbon form which attracted attention to this field and opens further application possibilities.

Polycrystalline and thin film forms of carbon

Fig. 2.10 shows the phase diagram of carbon in which numbers of extreme and attractive properties of diamond from the view point of practical applications have stimulated research in diamond technology since a long time. the difficulty of diamond preparation is plausible from the carbon phase diagram shown in Fig. 2.10 [26]. The region of diamond appears at very high pressures and at very high temperatures, so that we need to have high technologies to produce diamond and its coast is also very high. Artificial diamond is prepared for a long time at high pressure and temperature.

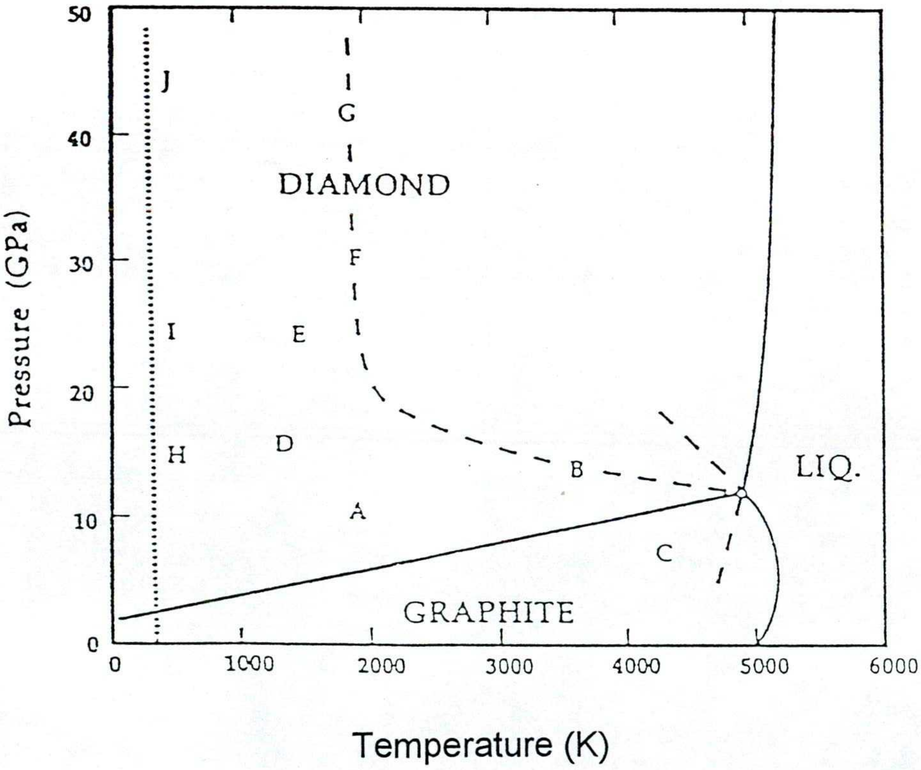

Fig. 2.10 Phase diagram of carbon [26]

After obtaining the diamond crystals there is another problem which is the sizes of these crystals is so small. That means, diamond is more limited to size and coast constraints [27]. Polycrystalline diamond (PCD) can be produced from diamond powder compacted with a binder phase. The maximum size which can be produced in the range 70-100 mm and the tools with complex shapes can be manufactured from electrically conducting PCD grades by spark erosion [28] but this is an expensive and time consuming process.

Potential implied in diamond properties can be realised after working out a low coast diamond technology which is able to produce diamond on large area and complex surfaces. Therefore researchers did many efforts to find diamond preparation process which is suitable for these requirements. The first successful deposition of diamond film at low pressure (a few tens torr) and moderate temperature (~1300 °C) [29] resulted in rapid development in the research field of diamond preparation. Diamond in the thin film form can be deposited by chemical vapour deposition (CVD) and physical vapour deposition (PVD) techniques as well. Diamond films are practically microcrystalline material characterised with diamond properties.

In order that diamond films to be used in a wide range of technological applications, a number of problems technical and economic ones as well will need to solve. Here we shortly review some technical problems:

1- Large area (>1 m^2) deposition per coating cycle. Good quality diamond films with uniform thickness and properties should be reliably produced on the single large components or on many small components in single deposition cycle.
2- Coating of complex shapes with reasonable rates (i.e.>1 μm/h) onto flat plates. It necessary to produce uniform coatings with reproducible properties on all important parts of component.
3- Diamond coatings onto a range of technological materials will need to be developed. This will involve the lowering of the deposition temperature to increase the range of substrate materials.
4- The adhesion of diamond coatings on all substrates will need to be improved if the coatings are to be used in any high stress trobological applications.
5- For the purpose to produce thin pinhole-free continuos diamond films on a range of substrate and on components with couple shapes, techniques will need to be developed to improve nucleation density of the coating.

Most of these problems can be avoided by using amorphous carbon films with diamond like properties as coating material what makes the investigation of these amorphous carbon films important from both basic research and application point of view.

Disordered forms of carbon

The study of disordered carbon system offers, even today, many opportunities for fundamental and systematic research in areas such as glassy carbons, carbon fibres, activated carbons, porous carbons, ion-implanted carbons and others. Investigation of the diamond like and other carbon films in a new and rapidly developing field of disordered carbon research. Here we review briefly some forms of disordered carbons and in chapter 3 will be discussed the hydrogenated amorphous carbon (a-C:H) and tetrahedrally bonded amorphous carbon (ta-C) in more details.

Glassy carbon

This type of carbon is a non-graphitic form of carbon, its basal plane correlation length is L_a and a c axis correlation length is L_c. Fig. 2.11.a shows the schematic illustration of the structure of glassy carbon. It consists of entangled ribbons of graphite polymeric molecules. L_c denotes the thickness of the ribbon and L_a the width. It is also perhaps locally flat over a length L_a. The difficulty of graphitization and its strength is attributed to the entanglement of ribbons. The ribbons having no ends, what may results in the chemical inertness. The entanglements also give glassy carbon its porosity and its low density (1.2-1.6) gm cm^{-3}.

Glassy carbon is essentially metallic and it contains approximately 100 % sp^2 sites. Jenkins and Kawamura 1976 [21] measured the glassy carbon structure parameters and they deduced that L_a =60 -120 Å and L_c = 40 Å . This indicates that, glassy carbon possesses too high degree of ordering to be classified as amorphous.

Carbon fibres

Carbon fibres exhibits great strength under tension, which is best achieved when carbon fibres are prepared from a polymeric precursor such as polyacrylonitrile (PAN), whereas fibres prepared from a mesophase pitch liquid crystal precursor are used for high modulus (stiffness) application. The tensile strength of carbon fibres is five times greater than steel, also the modulus of carbon fibres is four times greater than that of steel that is why carbon fibres is used for niche applications.

Carbon fibres are anisotropic and consists of an array of carbon fibril units of length at least 1000 Å with a preferential parallel alignment. The schematic illustration of the structure of carbon fibres is shown in Fig. 2.11.b. Their structure resembles that of glassy carbon i.e. they are non-graphitizing and their diffraction patterns show only the (hk0) and (002) peaks of the graphite lattice, from which it is deduced that L_a= 60-120 Å and L_c = 40 Å [21].

These fibres considered an excellent host material in studying the transport properties of graphite and its intercalation compounds. Its resistivity (55 μΩcm) slightly higher than the single-crystal graphite resistivity (40 μΩcm). Recent demonstrations [30] that both vapour-grown carbon fibres and multi-wall carbon nanotube originate from a single-wall carbon nanotube have stimulated interest in comparative studies between vapour-grown carbon fibres and carbon nanotubes in the hope of further carbon fibre synthesis techniques.

Carbon for battery, porous carbons and carbon aerogels

Large amount of Li may be accommodated into carbon structures and the LiC_x systems may be used as active anode materials in Li ion batteries with enhanced cell capacities. It has been recently shown that some disordered carbons can accommodate very large amounts of lithium with Li:C ratio close to 1:2 [31] which offers a good advantage for practical applications. It is an exceptional property of sp^2–bonded carbons their ability to form porous materials with very high surface area (1000-3000 m^2/g). Small pore sizes, large specific surfaces and fractal properties of both porous carbons and carbon aerogels offer a number of advantages for practical purposes.

Amorphous carbon thin layers (a-C, a-C:H, diamond-like a-C:H)

Amorphous carbon thin layers is a high disordered form of amorphous carbon and differs from glassy carbon in being truly amorphous and semiconducting. a-C exhibits $\sim 10^{-3}\ \Omega^{-1}cm^{-1}$ room temperature conductivity, (0.4-0.7 eV) optical gap and 2 g/cm^3 density.

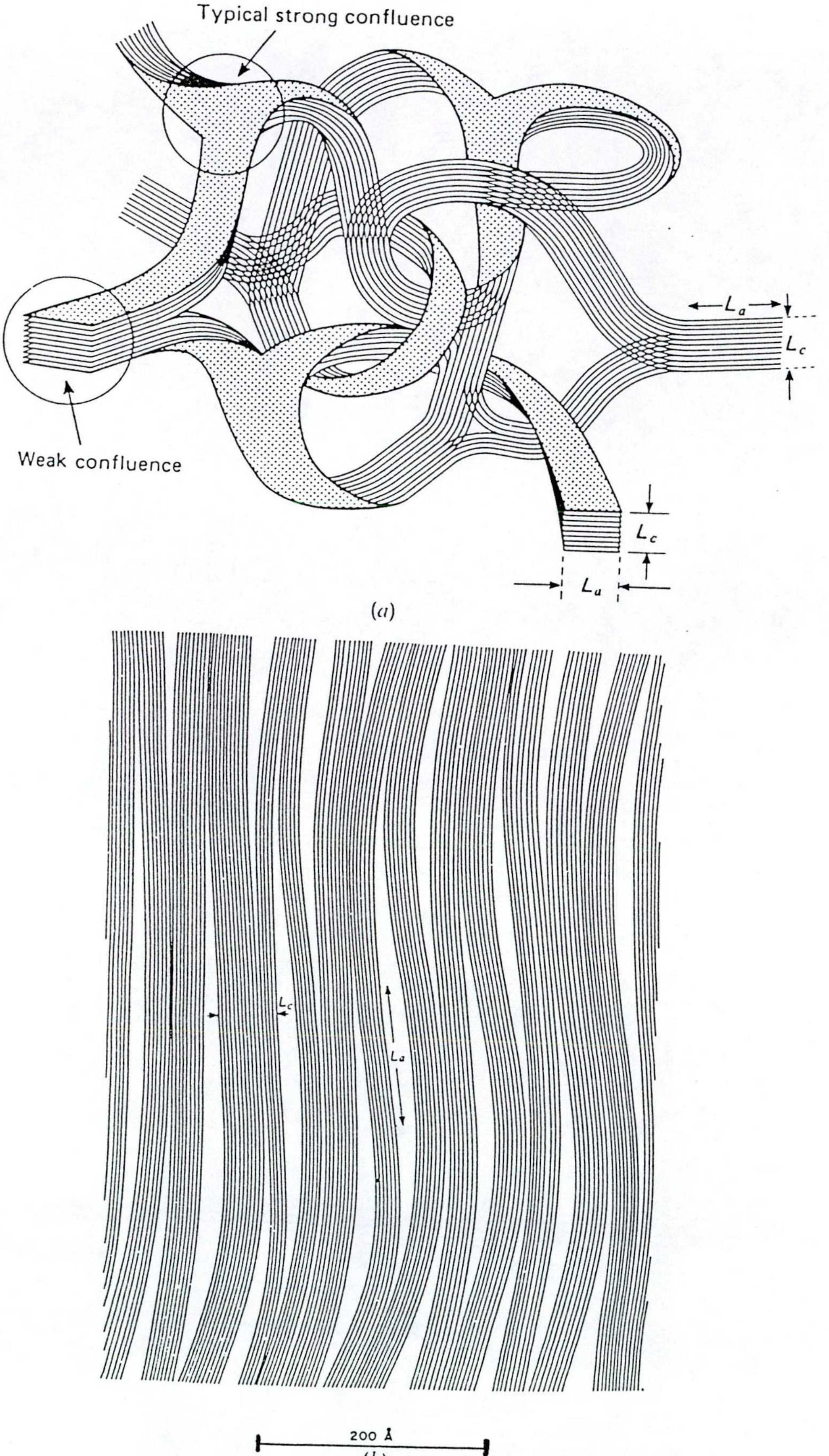

(a)

(b)

Fig. 2.11 Schematic illustration of the structure of glassy carbon (a) and carbon fibres (b), after Jenkins and Kawamura [21].

The presence of semiconducting band gap is a crucial difference and its structure is not so easily classified. It is generally believed that glassy carbon contains 100 % sp^2 sites, while evaporated a-C contains 1-10 % sp^3 sites, proportion of which can be raised by ion-beam deposition methods. In general evaporated a-C has much fewer potential for practical application than the plasma deposited a-C:H.

Hydrogenated amorphous carbon (a-C:H) has been prepared by plasma deposition method since ~20 years, but a-C:H has stated its carrier after realisation of that thin layers deposited at given parameters exhibits similar macroscopic properties to diamond films in many respect. These films are called diamond-like amorphous carbon (DLAC); due to hydrogen content of these amorphous layers the name of diamond-like hydrogenated carbon is used also frequently. There are amorphous carbon films without hydrogen which show similarly diamond-like properties and these are called tetrahederally bonded amorphous carbon (ta-C). In Table. 2.2 [32] we give comparisons of the properties of diamond with those of diamond-like carbons.

Table. 2.2 Properties of diamond and related materials.

Property	**Diamond**	**DLC**
Physical		
Hardness (kg mm^{-2})	700-10000	2000-5000
Coefficient of friction	0.1 (air)	0.02 (vac.)-0.7 (air)
Lattice constant (Å)	3.567	Amorphous
Density (gm cm^{-3})	3.51	2.0-3.0
Young's modulus (GPa)	1050	120-900
Chemical		
Bonding	Covalent sp^3	Mixed sp^2, sp^3 and C–H
Impurities	N, B	H
Reactivity	Inert in acids, solvents, salts, water	Generally inert
Thermal		
Conductivity (W m^{-1} K^{-1})	1100-2000	100
Electrical		
Resistivity (Ω cm)	$> 10^{16}$	10^{6}-10^{16}
Dielectric constant	5.5	5-9.5
Dopants	B, N, P, Li	P, B
Optical		
Band gap (eV)	5.45	0.8-2.0
Refractive index	2.42 (at 589.3 nm)	1.8-2.3
Optical transparency (μm)	0.225 to > 80	2.5 to > 50
Fabrication		
Deposition temperature (°C)	400-1100	60-800
Large area deposition (> 1 m^2)	No	Yes
Uniformity on complex components	Can be good	Good

Properties of a-C:H we discuss in more details in the next two chapters and some results for ta-C will be presented too. Commonly diamond-like properties of a-C:H and ta-C are emphasised although they offer another advantages for practical applications, e.g. due to low electron affinity and effective room temperature luminescence a-C:H would be promising material for cold cathode and luminescent display.

3. AMORPHOUS CARBON (A REVIEW OF LITERATURE

3.1. STRUCTURE OF AMORPHOUS CARBON AND NANO SCALE

3.1.1. Bonding properties of carbon atom

The rapidly increasing interest towards a-C:H and ta-C as well stimulates several research in this field. Several intriguing questions have been rised among those how the diamond-like properties relate to the structure of amorphous thin layers. How the different bonding possibility of carbon atom and nanoscale arrangement of differently hybridized of a-C:H. What is the role of hydrogen in the structural stabilization and how it is bonded to carbon atom. What is the structural origin of the properties changing from semimetallic through diamond-like to insulating ones. All of these problems how relate to deposition technique and parameters. Number of question similar to these listed before have motivated research amorphous carbon layers since realization of its potential in general application respects. In this chapter we review recent achievements in the research of a-C:H and the results. Problems and questions related closely to our investigations.

Carbon is a member of the fourth group in the periodic table. Its atomic number is 6 and its atomic weight is 12.011. The electronic configuration of these six electrons in the ground state of carbon is $1s^2\ 2s^2\ 2p^2$. The ionization potential of the carbon atom is 11.217 eV. Its well known the distribution of the s-electrons in carbon is spherically symmetric, whereas that of the p-electrons resembles a dumb-bell with an infinitely thin handle, its center being on the nucleus. The shape of these spatial distributions is altered when the wave functions for the respective states are hybridized. The hybridization of wave functions of these orbitals produce three different bonding configurations which are sp^3, sp^2 and sp^1.

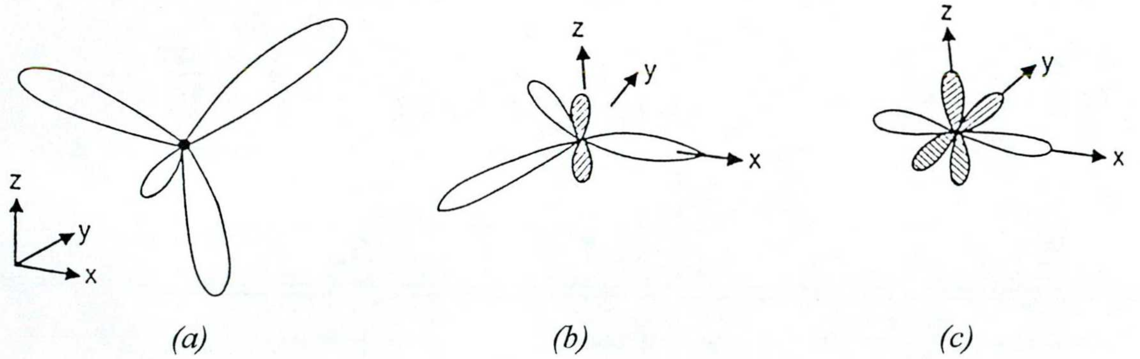

Fig. 1.1.1. Schematic representation of sp^3, sp^2 and sp^1 hybridized carbon atoms.

In sp^3 configuration, one of the 2s orbital electrons is promoted to 2p orbital to give four equivalent orbitals from the $2s^1\ 2p^3$ electronic configuration, each of those four valence electrons is assigned to a tetrahedrally directed sp^3 hybrid orbital which then form a strong sigma (σ) bond with an adjacent atom. The four equivalent bonds making the same angle with each other and directed towards the corners are shown in Fig. 1.1.1a.

In sp^2 configuration, one of the original p-orbitals is left unchanged and the sp^2 hybridization gives rise to three hybrid orbitals lying in the same plane at 120° to each other as shown in Fig. 1.1.1b. These hybrid orbitals form the σ–bonds between carbon-carbon atoms. The remaining p-orbital extends above and below the molecular plane in a direction perpendicular to it and, this p-orbital overlaps with the p-orbital of a neighboring carbon atom to produce a π–bond.

In sp^1 configuration the state of one s electron is mixed with that of one p electron, thereby giving rise to two hybrid electron clouds in the shape of two asymmetric dumbbells. The angle between two σ bonds is then equal to 180°, the bonds themselves being directed along one of the coordinate axes Fig. 1.1.1.c. the electron clouds formed by the remaining two p electrons are elongated in the direction of the other two rectangular axis, which are normal to the σ bond. The overlap between these electrons belonging to the neighboring atoms gives rise to two π bonds.

The degree of overlap of the π–bond is much less than that of σ–bond and this is reflected in the binding energy of the bonds. For example, 6.33 eV is required to break a single σ–bond and only 3.98 eV required to break a double σπ–bond into a single σ–bond.

A σ–bond between two sites is called a single bond and is represented by a single line and the systems which has this type of bonds called saturated systems, while a σ–π bond pair called a double bond and is represented by two lines and the systems which has this type of bonding called unsaturated systems, for example as in olifinic systems such as ethylene $H_2C{=}CH_2$ or as in aromatic systems such as six membered rings of benzene C_6H_6 and graphite.

When double and triple carbon-carbon bonds are formed, they grow shorter, stronger and their interaction energy will increase. The change in bond length may be caused by the varying extent of hybridization of the s- and p-electrons. The larger the contribution of the s-electrons, the shorter and stronger hybrid bond.

3.1.2. sp^3 and sp^2 coordinated carbons in the condensed matter.

Amorphous carbon may contain both sp^2 and sp^3 coordinated carbon atoms in a disordered network. If we would like to understand the physical basis for a given film properties, such as hardness, optical transparency, resistance to chemical attack etc., we must examine the basic atomic structure of the material involved. For carbon, it is evident, the starting point should be the determination of the ratio of carbon atoms in each coordination. Another important point is the determination of absolute hydrogen content which influences considerably the coordination of carbon atoms too.

The bonding configuration of carbon atoms is in close relation with deposition parameters used for preparation of a-C:H films and it depends on preparation techniques too. In a plasma discharge process the deposition self bias, the plasma pressure, source gas and substrate temperature are the important parameters while the ion energy is also frequently used as important parameter for characterization of deposition process. Infrared (IR) absorption, electron energy loss spectroscopy (EELS) as well as ^{13}C nuclear magnetic resonance (NMR) spectroscopy including proton decoupling provide convenient methods for measuring sp^2 to sp^3 of a-C:H. In this section we summarised recent results for the sp^2 and sp^3 coordinated carbon content gained by different experimental techniques.

Effect of deposition parameters and hydrogen incorporation

In the case of plasma discharge deposition of a-C:H, the gas pressure and the self bias are regulated in general under preparation process while other parameters are constant. Large number of samples prepared by decomposition of C_2H_2 was studied by IR spectroscopy and the sp^3/sp^2 ratio has been determined by the deconvolution of the 2900 cm^{-1} C–H stretch band [33]. Fig. 1.2.1 shows deconvolution of the C–H stretch region of the infrared spectrum of three a-C:H film. Deconvolution of the spectra is indicated with bands at wave numbers from sp^3–CH_2 at 2850 cm^{-1} and 2920 cm^{-1}, sp^3–CH at 2920 cm^{-1}, sp^2–(olifinic) CH at 3000 cm^{-1}, sp^2 (aromatic) CH at 3060 cm^{-1} and sp^1 – CH at 3300 cm^{-1} [34]. As the pressure at given self bias voltage increases the total absorption i.e. the hydrogen concentration and the percentage of sp^3 bonding increases as it is clear from Fig. 1.2.1.a-c. The sp^3/sp^2 ratio determined by IR spectroscopy is given on Fig. 1.2.2.a as a function of self bias and on Fig. 1.2.2.b as a function of pressure [33]. With increasing negative self

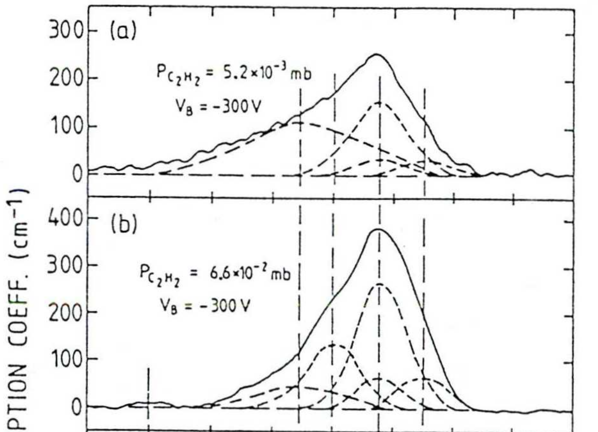

Fig. 1.2.1. Deconvolution of the C–H stretch region of the IR spectrum of three a-C:H samples with deposition parameters as indicated [33].

bias the bonding ratio decreases from 1.7 to 1.1. This reflects the transition of the film from diamond-like a-C:H with increasing ion energy (negative bias voltage). Similar results has been formed on films deposited by plasma decomposition of CH_4 [35]. Gas pressure effects also considerably the sp^3/sp^2 ratio shown in Fig. 1.2.2.a, by enhancing pressure at a given self bias, the sp^3/sp^2 ratio increases from 1.1 to 2.4.

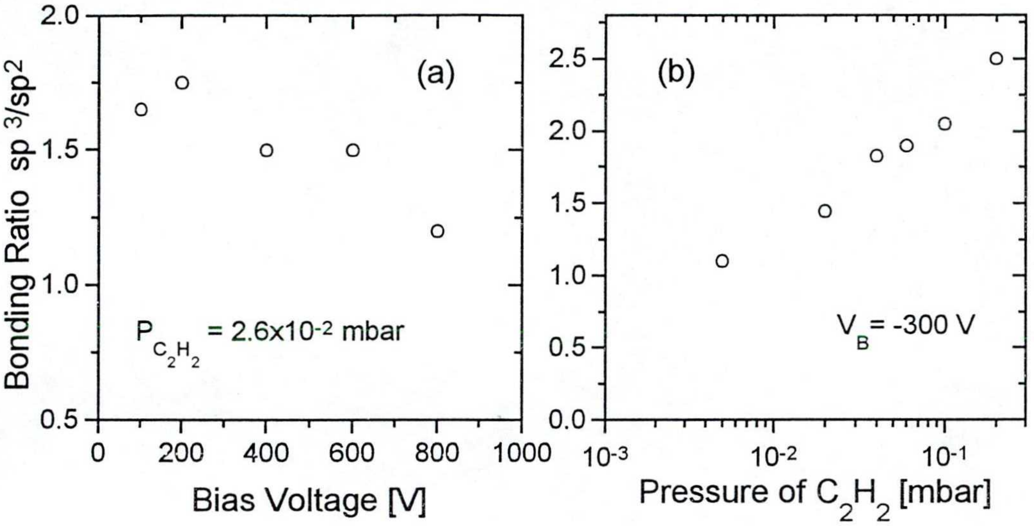

Fig. 1.2.2. Bonding ratio sp^3/sp^2 as a function of bias voltage (a) and as a function of pressure (b) [33].

Incorporation of the hydrogen into amorphous carbon layer plays important role in formation of sp^3 coordinated carbons in two possible way: I) by closing carbon dangling bonds or free chain ends and ii) by transfer the sp^2 coordinated carbon atoms into sp^3 ones. It is in good agreement with increasing C–H stretch band when gas pressure increases Fig. 1.2.1 and it gain further evidence from elastic recoil detection (ERD) measurements from which absolute hydrogen content of carbon films can be determined. Fig. 1.2.3 shows dependence of X_H atomic ratio (H/C+H) as a function of self bias and pressure.

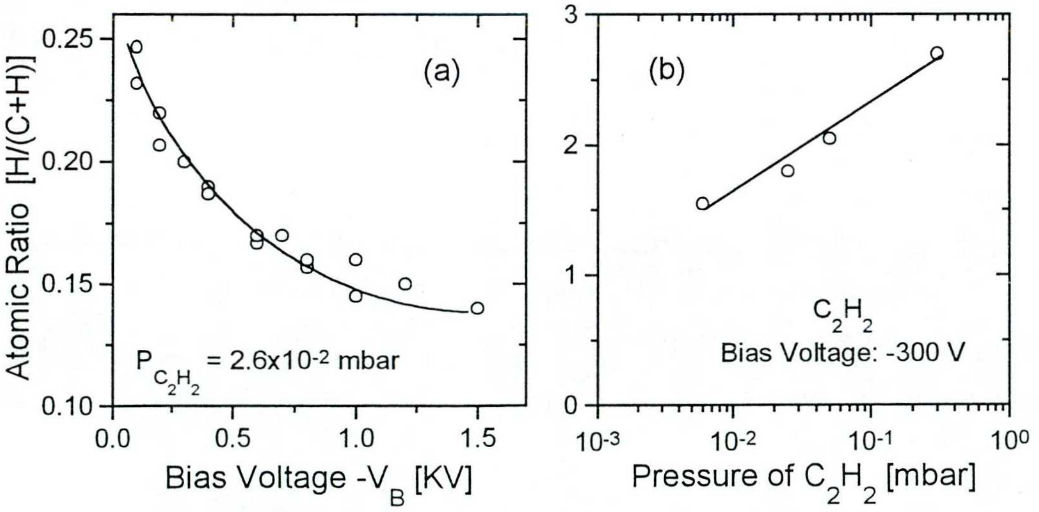

Fig. 1.2.3. Atomic ratio X_H as a function of bias voltage (a) and as a function of pressure (b)[33].

Numerous samples prepared by methane plasma discharge have been studied by ^{13}C NMR method and considerably different sp^3/sp^2 ratio was determined by Tamor and his coworkers [36] comparing to IR measurements performed on a-C:H prepared from C_2H_2. They have done careful measurements with appropriate choosing of decoupling parameters and four classes of carbon bonding environment were resolved: threefold with protonation f_3^H (covalent bonding to hydrogen) and without protonation f_3^C (graphitic carbon), and fourfold coordination with protonation f_4^H and without protonation f_4^C (quaternary carbon). The relative population of each of these carbon enviroments is shown in Fig. 1.2.4 as a function of substrate bias voltage (and hence ion kinetic energy) for a-C:H layers deposited from methane plasma [36]. Similar tendency with self bias to that measured by IR spectroscopy can be seen in this figure, however the ratios at given self biases are different. Mainly because NMR measures unhydrogenated carbon atoms too. It is interesting to see how the compressive stress and hardness changes with self bias; these are shown on Fig. 1.2.5 for samples prepared similarly to those measured by NMR method [36]. The stress is small for polymer-like films, increases rapidly to maximum near 50 V, then decreases monotonically. Hardness has a maximum for samples prepared at (~ -200 V) self bias. Correlation between hardness, compressive stress and the fraction of four coordinated carbon f_4^C in Fig. 1.2.4 is clear.

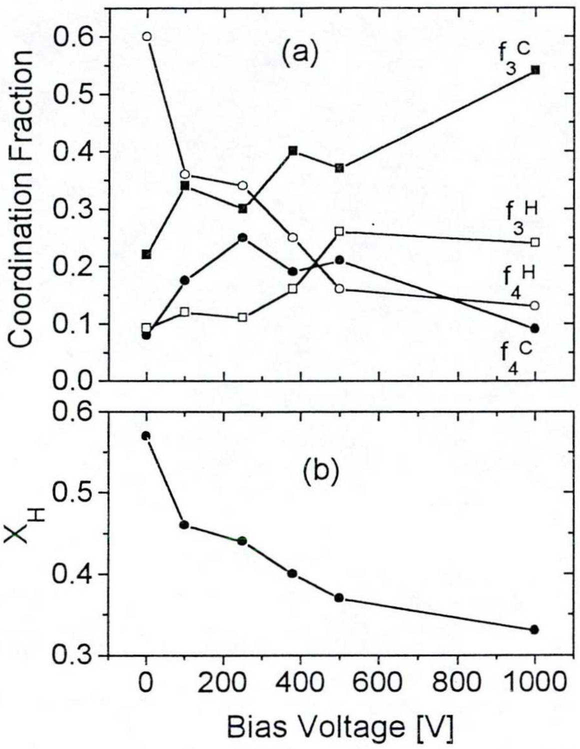

Fig. 1.2.4. Bias voltage dependence of the four carbon coordination fractions for a-C:H prepared by methane decomposition (a) and the atomic fraction of hydrogen (b)[36].

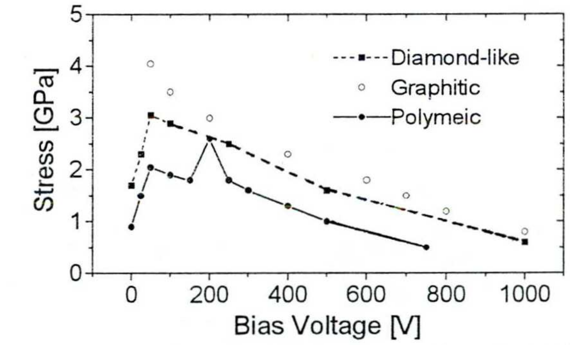

Fig. 1.2.5 Bias voltage dependence of the compressive stress in a-C:H films [36].

Dependence some film properties and sp^2 coordinated carbon fraction, measured by NMR method, as a function of mean ion energy are summarized in Table. 1.2.1 for a-C:H films prepared from C_2H_2 plasma [37]. Comparison of sp^2 fractions with results of Tamor et al. [36], these are also smaller, what indicates the effect of source gas. Low energy ions produce films with poor mechanical properties and high hydrogen content which favors the sp^3 hybridised carbon atoms in the a-C:H network. Ion energy higher than 145 eV lead to a close-packed network (ρ=1.8-2.0 g cm^{-3}) with an sp^2 fraction of ~60 at % and hardness value up to 40 GPa.

Table. 1.2.1. Dependence of film properties on deposition parameters

No.	Pressure (mbar)	Mean ion energy (eV)	NMR sp^2 fraction (at. %)	Density ρ (g cm^{-3})	H content (at. %)	Knoop hardness (GPa)	Interna l stress (GPa)
1	$8.2x10^{-3}$	~30	27	1.6	45	5	0.2
2	$8.2x10^{-3}$	90	39	1.6	40	7	1.2
3	$4.4x10^{-3}$	100	42	1.65	37	11	1.2
4	$2.1x10^{-3}$	125	43	1.7	34	12	2.1
5	$1.7x10^{-3}$	145	44	1.75	32	12	2.1
6	$1.4x10^{-3}$	170	60	1.8	32	20	2.1
7	$8.2x10^{-4}$	250	–	2	28	30-40 NI 40	4.4
8	$5.5x10^{-4}$	290	–	1.7	26	35	3.0

Effect of annealing

As we see before the sp^2 and sp^3 coordinated fraction of carbon in a-C:H samples is in close relation of hydrogen content incorporated into amorphous network. Self bias and gas pressure under deposition process influences dominantly the amount of hydrogen incorporated into the layer. Thermal annealing of as deposited films can also considerably influence the hydrogen content and indirectly the sp^2 and sp^3 coordinated fraction.

Fig. 1.2.6 shows the IR C–H stretch absorption spectra for a-C:H samples prepared by rf plasma decomposition of benzene vapour on germanium substrates, as well as the assignments of each C–H mode. The samples annealed for 4 hours in a sealed evacuated quartz tubes. In Fig. 1.2.6.a the original grown film showed. By increasing the annealing temperature up 300 °C the sp^1 C–H stretch mode disappeared and the optical gap not changed. As well as, the total C–H stretch signal increases by 30 % and the weakly bonded hydrogen converted to normally bonded hydrogen indicating removal of unsaturated sp^2 bonds by hydrogen attachment and cross-linking. Between 300 and 600 °C, the total hydrogen effuses and the optical gap reduced from 1.2 eV (grown film) to 0.17 eV indicating that the all carbon atoms at 600 °C have the aromatic sp^2 hybridization (Fig. 1.2.6.e).

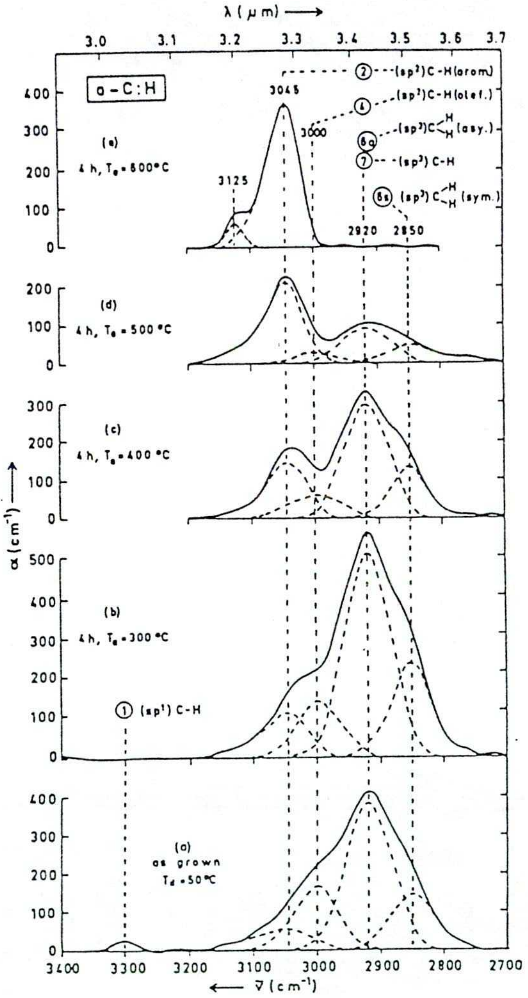

Fig. 1.2.6 Normalized C–H stretch absorption spectra for a-C:H. (a) as grown, (b)-(e) annealed as indicated. Deconvolution of overlapping bands are shown by broken lines [34].

Fig. 1.2.7 shows the dependence of sp^2 and sp^3 coordinated carbon fraction on the annealing temperature [38]. From room temperature until 300 °C the sp^3 and sp^2 ratios nearly has a constant values but above 300 °C the H_2 starts to evolve from the samples, not only the H_2 molecules but also the hydrocarbon molecules.

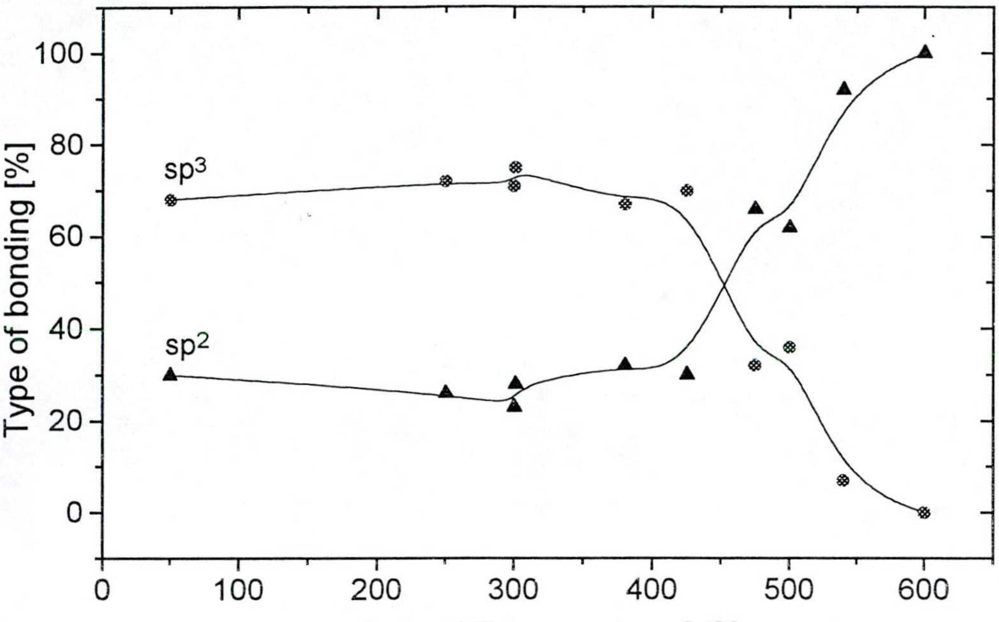

Fig. 1.2.7 The percentage of sp^3 and sp^2 as a function of annealing temperature [38].

As a result of losing hydrogen the bonds became more unsaturated and the sp^2 fraction start to increase in the expense of sp^3 at 400 °C as shown in the figure. As the annealing temperature increase the sp^2 carbon sites increase until 600 °C the sp^2 fraction will be 100 % and the gap closed. The sp^2 carbon sites is not graphitic groups at all but the main point, the all sp^2 exists in aromatic groups because the hydrogen still bounded to sp^2 sites what was proved by Y.Bounouh et al [39] from the analysis of low frequency part of the IR absorption spectrum. The remaining hydrogen atoms are certainly very strongly bonded to aromatic sp^2 carbon sites and it start to evolve as H_2 at quite high temperature more than 700 °C.

Finally, the sp^2 and sp^3 ratio can be detected by the Fink et al [40,41] EELS measurements. They prepared a-C:H samples onto negatively biased NaCl substrates in a rf plasma reactor from benzene vapour. They found that, in all grown films, about one third (1/3) of the carbon atoms is in the sp^2 configuration and two thirds (2/3) is in sp^3 configuration. They also annealed their samples and they found that the gap is closed near 600 °C and after hydrogen released above this temperature, the transformation of the amorphous carbon to graphitic structure is observed.

3.1.3. Determination of structure from different experiments.

In an amorphous material it is well known, that the lattice is lost and with it, the ability to describe the position of every atoms to achieve such a description of an amorphous material, we would need three coordinates, that is clearly impossible. As a results one asks simpler questions. In particular, one asks about the average coordination of each atomic species in the material. What is the average distance to the near neighbors. What are the type of near neighbors? How many neighbors are there. These some questions are asked about second neighbors, and the third neighbors, and so on. Thus, a type of statistical description of the atomic arrangement is sought. This is, in fact, the sort of information one gets from radial distribution functions (RDFs) obtained from X-ray, electron or neutron diffraction. But those parameters is not enough to describe appropriate way the structure of amorphous materials especially the amorphous carbon which has different bonding possibilities due to variability of carbon bonds and to the hydrogen incorporation. Therefore there are other parameters which need to describe give the structure of this type of materials.

The sp^3 and sp^2 content and their ratio are an important parameter which characterize the structure of different disordered carbon forms. The direct spectroscopic techniques which were used to probe the sp^3:sp^2 ratio are the Nuclear Magnetic Resonance (NMR), X-ray near edge structure (XANES), Electron Energy Loss Spectroscopy (EELS), and infrared (IR) spectroscopy. For example XANES and EELS techniques give apparent data about the existence of sp^2 and sp^3 sites while NMR and IR give a quantitative data about the sp^3 and sp^2 carbon sites concentration.

The hydrogen content considered an important parameter in determining the structure of a-C:H. It can be determined by using proton NMR, Nuclear Reaction Analysis (NRA) and by Electron Recoil Detection Analysis (ERDA). The hydrogen bonding can be detected by inelastic neutron diffraction analysis too.

In this section we have to show some of those techniques which mentioned above to determine the structure of amorphous carbons.

Nuclear Magnetic Resonance (NMR)

NMR method gives a direct quantities of sp^3 and sp^2 carbon fractions. The advantage of NMR is that, each different hybridization gives rise to chemically shifted peak whose area is directly proportional to its concentration. The limitation of the NMR technique are the sample sizes must be large and the long time needed to gotten the data.

The nuclear spins C^{13} nuclei or proton (H^1) can be interest from our point of view. The unlike spins and the chemical shift anisotropy will broaden the NMR peaks on an inhomogenous way, and to overcome this problem magic angle spinning (MAS) used to reduce this peak broadening. The strong dipolar field of the proton spins covers the whole C^{13} spectra, what can be resolved by "proton decoupling" which make the C^{13} peaks reasonable.

Because the predominant source of C^{13} line broadening is the H–C interaction, the H–C interactions can be used to distinguish between hydrogenated and unhydrogenated sites by turning off the proton decoupling signal which broadens the spectra of the hydrogenated sites into the baseline, at that moment, the remaining spectra peaks will correspond to the unhydrogenated sites. That appeared in Fig. 1.3.1 which shows the NMR spectra of carbon film, deposited at substrate temperature 250 °C by rf plasma decomposition of C_2H_2 at U_{SB} = -150 V, obtained by proton decoupling. The sp^2 and sp^3 appeared with ratio 1.6:1 [42] respectively. In (b) without proton decoupling the unhydrogenated sp^2 only appeared, and in (c) the difference between (a) and (b), where the percentage of hydrogenated $sp^2:sp^3 \sim 1:1$.

The position of peaks at 130 ppm (sp^2 resonance) and at 65 ppm (sp^3 resonance) consistent with many authors. The ratio of single:double bonds obtained by (Jäger et al 1994) [43] is 4:1. The $sp^2:sp^3$ ratio obtained 60% : 40% for a-C:H samples produced by saddle field fast atom source from C_2H_2. The NMR results obtained by different authors [44-46] are greatly affected by the samples deposition parameters.

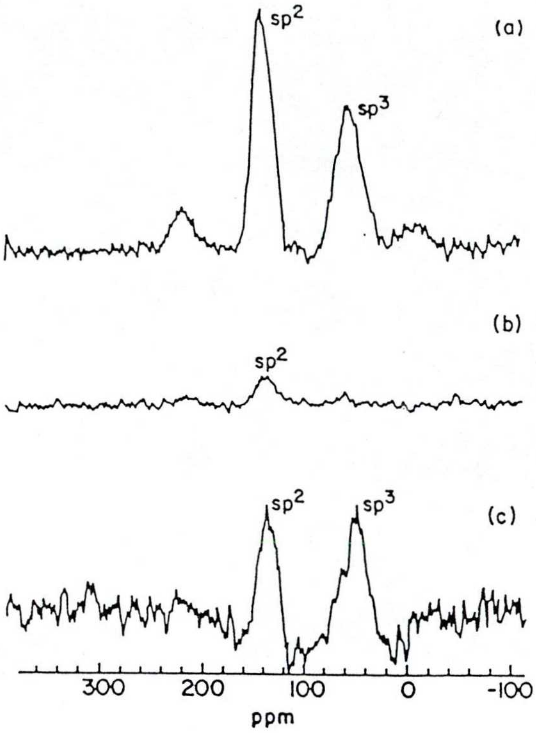

Fig. 1.3.1 NMR spectra for carbon film deposited at 250°C. (a) Obtained with proton decoupling. (b) Obtained without proton decoupling. (c) Difference spectrum between (a) and (b) [42].

Diffraction methods

It is a fundamental property of all waves that they diffract on meeting an obstacle, and this effect is most pronounced when the size of the obstacle is comparable to the wavelength of the wave. This is as true for electrons and neutrons as it is for, say, X-ray, and since all can have wavelengths comparable to atomic dimensions, it is expected that diffraction from atoms in the condensed state will occur. This, of course, is the basis of the technique of X-ray diffraction used in conventional single crystal studies of which, if constructive interference is to occur among the outgoing beams of X-rays of wavelength λ, elastically from regular planes of atoms, the Bragg condition

$$2d \sin\theta = n\lambda \tag{1.3.1}$$

is obeyed. Here d is the spacing of planes and n is an integer. Thus diffracted beams of, say, X-ray are observed only for scattering angles 2θ and wavelength λ for which is satisfied; this gives rise to a series of sharp spots being detected in a plane perpendicular to the monochromatic incident beam. We will not discuss further the subtleties of single crystal structure determination, which utilize the intensity variation as well as the position of the spots, since amorphous materials do not produce an X-ray or electron diffraction pattern similar to those of single crystals (nor even the pattern of concentric sharp circles of intensity produced by randomly oriented crystals) but instead characteristic diffuse haloes are observed.

The scattering from an electron whose charge is distributed in a certain volume dV as ρ dV, rather than being confined to a point; the scattering is then ρ dV times the amplitude of the classical scattering from a single electron. The path differences between the various scattered rays from different parts of the charge distribution at r from and arbitrary origin mist be considered, giving the following expression for the scattering intensity in e.u. as:

$$f_{eu} = f_e f_e^* \qquad (1.3.2)$$

where f_e is the scattering factor. For an atom containing several electrons, the atomic scattering factor of form factor is simply the sum of individual amplitudes:

$$f = \sum_n f_{en} = \sum_n \int_0^\infty 4\pi r^2 \ \rho_n(r) \frac{\sin \ kr}{kr} dr \qquad (1.3.3)$$

and the total scattered intensity is $I_{eu} = ff^*$. Clearly; the quantity $\sum_n \int_0^\infty 4\pi r^2 \ \rho_n(r)dr$ is simply the total number of electrons in the atom (i.e. the atomic number Z); since sin kr →1 for small kr, and f tends to the value Z as k (or $\sin \theta/\lambda$) tends to zero.

The structure factor is related to the radial distribution function (RDF), J(r) by Fourier transform as in the next equation:

$$S(k) = \int_0^\infty \{J(r)/r - 4\pi\rho_0 r\} \sin(kr)dr \qquad (1.3.4)$$

The RDF is known as the probability of finding another atom at a distance r from a given atom. It consists of a series of peaks which represented by a smooth parabolic curve J(r) at large distance r, where $J(r) = 4\pi r^2 \rho_0$ and ρ_0 is the microscopic density.

The RDF first peak as shown in Fig. 1.3.2 lies at the average nearest neighbor distance or bond length r_1 and its area equal to the coordination number n_1. The second peak lies at the second neighbor distance r_2 from which the bond angle θ is found, where θ is related, to the first and second neighbor distances r_1 and r_2 respectively, by

$$r_2 = 2r_1 \sin(\theta/2) \qquad (1.3.4)$$

Often, the RDF plotted in the reduced form G(r) as in equation (1.3.5) and when G(r)→0, the bond length r→∞. The natural width of the peak plus the resolution

$$G(r) = J(r)/r - 4\pi r \rho_0 \qquad (1.3.5)$$

of the experiment is equal to the peak widths of the RDF. Because Carbon has a short bond length r_1, the K_{max} limitation are significant, where K_{max} is the highest value of k used. To know the structure of other semiconductors, it is sufficient to determine carefully the four parameters r_1, n_1, θ and ρ_0.

Table. 1.3.1 (Robertson 1991 and the included references) [47] shows the inter-atomic distance (r), coordination number (n) and density of various carbon forms which deduced by

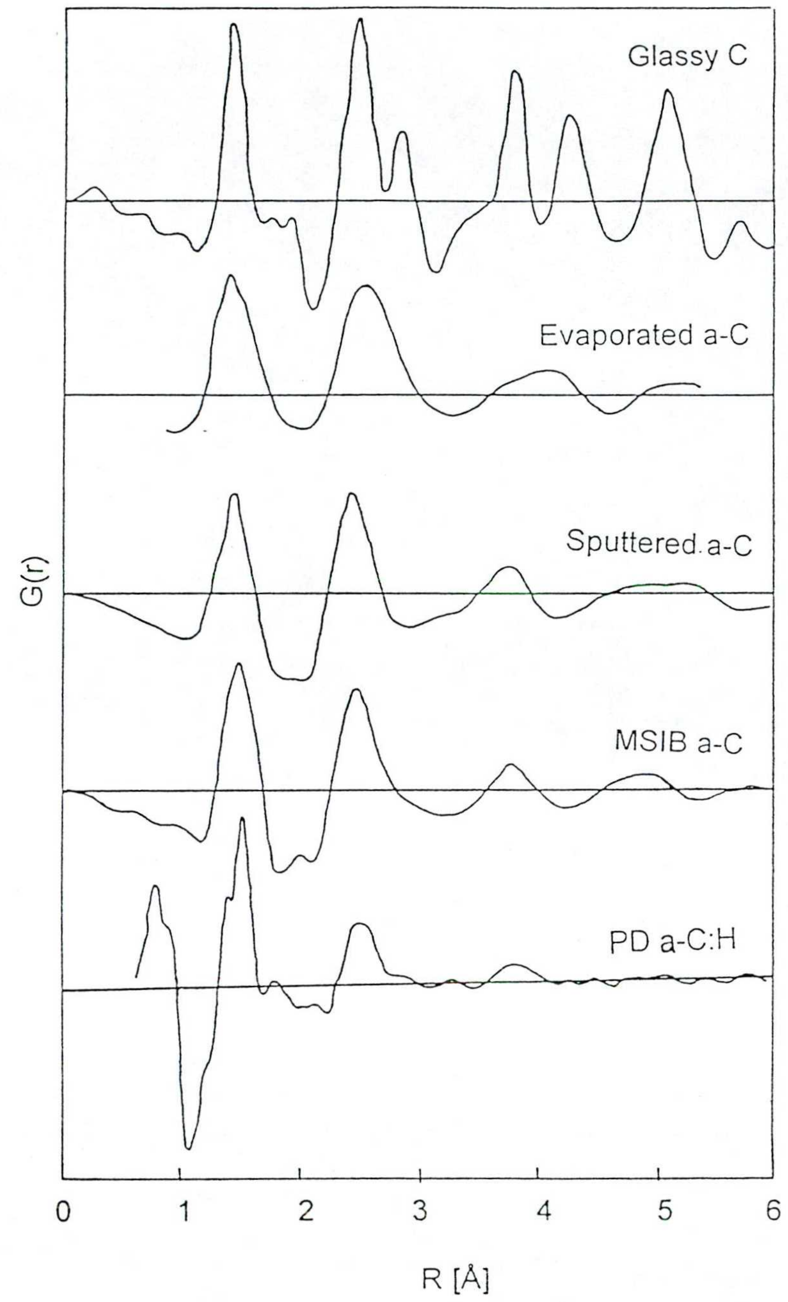

Fig. 1.3.2 The RDF for different disordered carbon forms [47]

Table. 1.3.1 The structure parameters determined by different methods for some different forms of carbon.

Carbon form	**r_1 (Å)**	**n_1**	**r_2 (Å)**	**n_2**	**Local density $gm.cm^{-3}$**
Graphite	1.42	3	2.45	6	2.45
Diamond	1.544	4	2.512	12	3.515
Glassy C	1.425	2.99	2.45	6.1	1.49
a-C (evap)	1.43	3.3	2.53	8.8	2.0
a-C (sput)	1.46	3.34	2.49	6.7	2.44
a-C:H	1.39,1.52	2.5	-	-	1.5-1.8

using different methods to determine the structure factors. The nearest neighbor distances for a-C:H are 1.39 Å, 1.52 Å which are near to 1.42 Å bond length of graphite and 1.554 Å bond length of diamond.

1- *X-ray Diffraction*

X-ray diffraction measurements was also performed on powder and thin film a-C:H produced by ion beam or fast atom beam source from acetylene and propane forms [48]. The diffraction data of powder samples was taken at 0.6 Å whereas the thin films was measured at 1 Å. The glancing incident with a critical angle of X-ray on samples makes the rays path through only the samples, not through the samples and substrates.

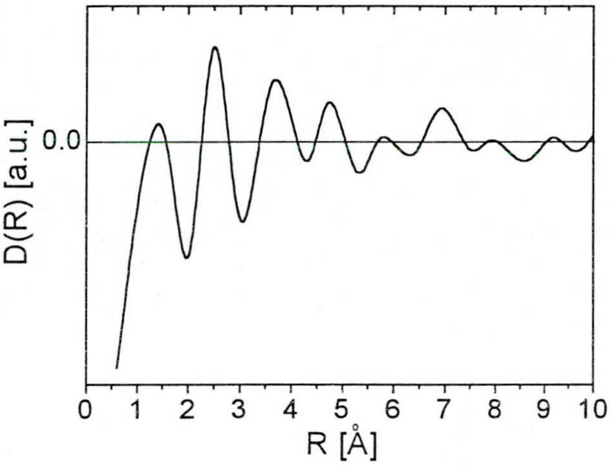

Fig. 1.3.3 Pair correlation function D(r) for thin film of a-C:H deposited by glancing angle X-ray diffraction (Incident angle = 0.1°) [48].

Fig. 1.3.3 shows the pair correlation function D(R) (which is related directly to the probability of finding an atom at a distance R from another atom at the origin) for a-C:H sample prepared from acetylene. Fourier transformation is used to produce D(R) from the structure factor of the glancing angle X-ray diffraction (incident angle=0.1°). The analysis of the structure factor appeared the dominant bonding is the C–C bonds beside C–H bonding, that means, the dominant bonding is the sp^3 with some evidence of sp^2 carbons. The disadvantage in using X-ray is the insensitivity in determining the coordination numbers especially the second shell coordination number and the difficulty to deduce quantitatively the coordination numbers by X-ray or electron diffractions.
X-ray and electron diffraction both deals with the electrons surrounding the nucleus, whereas the neutron diffraction deals with the nucleus itself. For these reasons other methods such as NMR and neutron diffraction methods are used to determine the structure parameters. Next, we will show the neutron diffraction and inelastic neutron scattering studies.

2- *Neutron diffraction*

Neutron diffraction is considered as one of the good diffraction methods which can give in details the bonding environments of carbons. Several authors have measured the structure factor of a-C:H samples prepared form different hydrocarbons. Huxley et al. [49] fitted with a series of gaussians the RDF of a-C:H samples deposited from acetylene plasma. The peak positions as shown in Fig. 1.3.4 indicate the mean bond lengths and the peak area indicate the average coordination numbers.

The values determined from Gaussain fitting of RDF summarized in Table. 1.3.2 and the assignments are also shown. The C–C saturated bond length is 1.52 Å which is less than the saturated C–C bond of diamond (1.554 Å). The C=C unsaturated bond length is 1.35 Å which differs from graphite bond length of 1.42 Å and the aromatic 1.39 Å, however this value is near to the olifinic bond length of 1.34 Å. The table show also the proportion of bond types derived from neutron diffraction. Moreover, those results [49] used to determine the proportion of bond

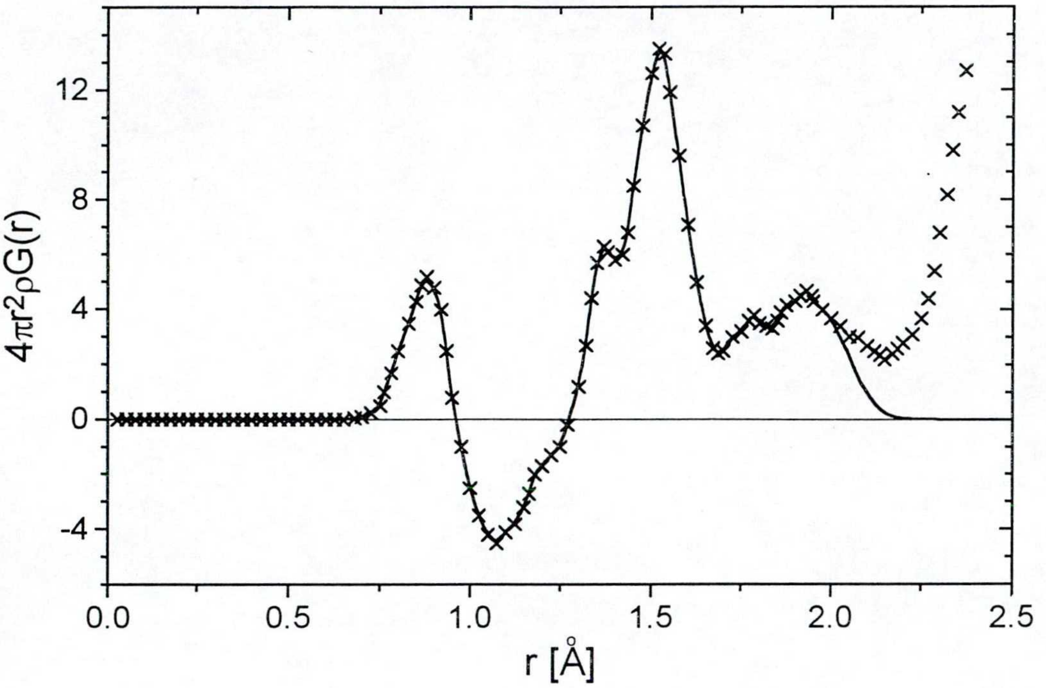

Fig. 1.3.4 The peak fits (solid line) to the experimentally derived radial distribution function $4\pi r^2 G(r)$ (crosses) [49].

types as sp^3 saturated = 0.26-0.27, sp^2 (unsaturated) =0.38-0.39 of which 0.32-0.35 is in olifinic groups with the small reminder being in aromatic or graphite groups.

Table 1.3.2 Bond lengths and Coordination numbers determined from fitting of experimental data shown in Fig. 1.3.4 [49].

Peak position (Å)	Peak area (atoms)	Assignment
0.9	1.1	H–H (molecular)
1.05	1.2	C–H + H–C
1.35	0.7	C=C (aromatic, double)
1.52	2.2	C–C (single bond)
1.8	1.5	H–C–H (tentative)

Similar results was determined for a-C:H samples prepared from propane and acetylene at 500 eV “mean ion energy” [50]. A peak at 2.5 Å assigned to the second shell C–C–C carbon bond was also observed. These results suggest the bonds in a-C:H are predominantly sp^2 hybridized, even in the case of intermediate hydrogen content samples. The single: double bond was found 2.5:1. Furthermore, the C=C bond length of 1.34 Å corresponds very closely to the olifinic bond distance rather than aromatic graphitic bond distances. The precise statement can not be made for 2.5 Å peak which contribute to the C–C–C correlations, because the valid angle checking produce an angle extended to 120° [51].

The problem in neutron diffraction measurements is the low resolution at Q<2 Å (unreliable values of r (r < ~1 Å)).

3- *Inelastic Neutron Scattering (INS)*

The INS is used to examine in details the hydrogen bonding enviroments in amorphous materials such as in a-C:H. There are many possible bonding environments in a-C:H system which give rise to vibrations over a range of frequencies. The hydrogen (H_2) vibrations are at higher frequencies than the network vibrations because the H_2 mass is lighter than the carbon mass. The univalence of H_2 makes its connection to the network by only one bond. The number of local bonding environments need to be considered to sp^3 CH, CH_2 and CH_3 groups, sp^2 olifinic and aromatic CH and olifinic CH_2 and sp^1 CH.

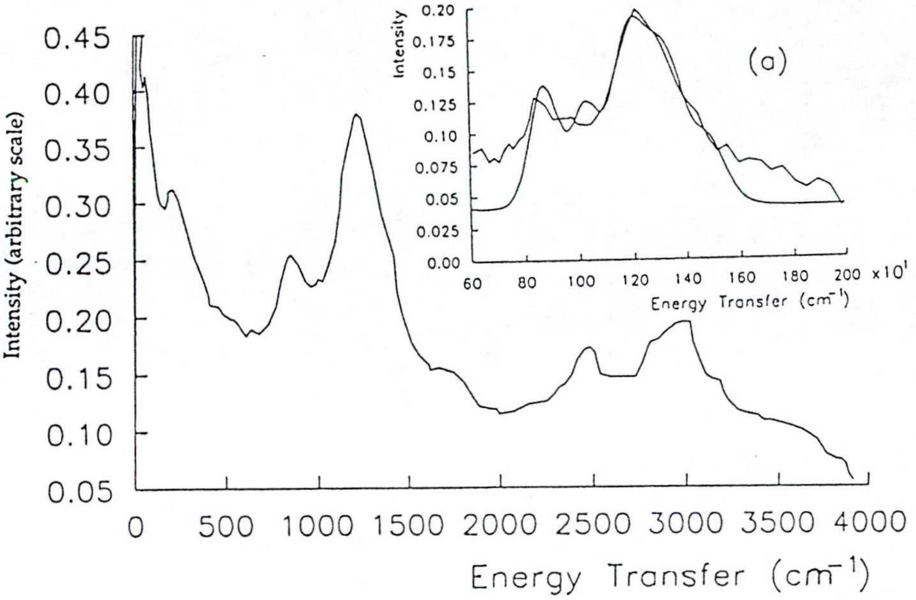

Fig. 1.3.5 INS spectra for a-C:H sample prepared from acetylene at energy 500 eV obtained on the TFXA spectrometer. Inset show the CLIMAX model fits to experimental data [51].

The INS spectra for a-C:H samples [51] which mentioned before shown in Fig. 1.3.5 consists of two regions. A low frequency region (< 500 cm^{-1}) which is dominated by scattering from residual quantities of the liquid nitrogen used to quench the samples and a high-frequency region (> 500 cm^{-1}) consisting of localized CH_n stretch and bend vibrations. The CH_n bending vibrations lie between 700 and 1500 cm^{-1} and the CH_n stretch band and overtone of the CH_n stretching vibrations occur at 2500 and 3000 cm^{-1}, respectively. The frequencies assignments used [51] are given in Table (1.3.3) with comparison to compared to the IR results of Dischler

Table 1.3.3 Frequency assignments used in modelling the INS spectra [51] and comparison with IR results of [52] and [53].

Vibration	Walters et al [51]	Dischler[52]	Dollish [53]
CC stretch	875 cm^{-1}	885 cm^{-1}	1132-885 cm^{-1}
CH_2 rock	1030 cm^{-1}	700 cm^{-1}	1060-719 cm^{-1}
CH bend	1190 cm^{-1}	1370 cm^{-1}	1160 cm^{-1}
CH_2 twist	1300 cm^{-1}	1170 cm^{-1}	1310-1175 cm^{-1}
CH_2 wag	1330 cm^{-1}	1030 cm^{-1}	1411-1174 cm^{-1}
CH_2 bend	1470 cm^{-1}	14440 cm^{-1}	1473-1446 cm^{-1}

[52] and Dollish et. al. [53] measurements.

Models based on these assignments (Table. 1.3.3) failed in fitting the observed INS spectrum, in particular, the theoretical intensity at 700 cm^{-1} is too large and only a poor fit could be obtained to the 1280 cm^{-1} peak. The problem in INS technique is that at higher frequencies, the measurements is similar to each other in the hydrogen distributions because the INS resolution in this region is low.

3.1.4. Vibrational properties

Vibrational spectroscopy is an indirect structural probe, as it requires a theory or model to relate spectral features to specific types of local bonding arrangements. It is complementary to other probes of local atomic structure, such as X-ray or neutron scattering which give direct information about bond-lengths and other aspects of atomic-scale geometry. Describing local atomic structure can be made on different scale. The short range order (SRO) describes those aspects of the local structure that are associated with the bonding at each specific type of atomic sites. The medium range order (MRO) includes those aspects of local structure that include more than three atoms and the following elements of atomic geometry: dihedral angle, third neighbor distances, small or larger rings of atoms, the local topology, whether it is fully three dimensional, layer-like and two-dimensional, or chain-like and one-dimensional.

Bonding heterogeneity and inhomogenous distribution of different bonded carbon atoms makes the vibrational studied especially important in determination of the structure of a-C:H. Due to amorphous structure the k selection rule breaks down and all vibration modes can be observed. In the previous section we have discussed the results gained by inelastic neutron scattering for vibration properties of a-C:H; here we deal with the results of Raman scattering and Infrared absorption studies and the effect of annealing on the vibrational properties.

Raman spectra

The Raman active modes of diamond and graphite discussed in chapter 2 help us to understand Raman scattering properties of amorphous carbon. Sharp peak at 1332 cm^{-1} is a characteristic feature of diamond Raman spectrum, while graphite has a very intensive band of E_{2g} symmetry at 1580 cm^{-1} and a weak rigid layer mode at 46 cm^{-1}.

The first order Raman spectra of two crystalline and some amorphous forms of carbon is shown in Fig. 1.4.1 [54,55,56]. Microcrystalline graphite and all non-crystalline form of carbon shows two peaks or a broad band which can be deconvoluted into two Gaussian bands. The peak located near 1560 cm^{-1} is called G peak and it is assigned to optic zone centre graphite mode of E_{2g} symmetry. The peak near 1350 cm^{-1} is called disordered (D) peak and it is supposed to arise from scattering by disorder activated optical zone edge phonons and it has no relation with Raman active diamond mode.

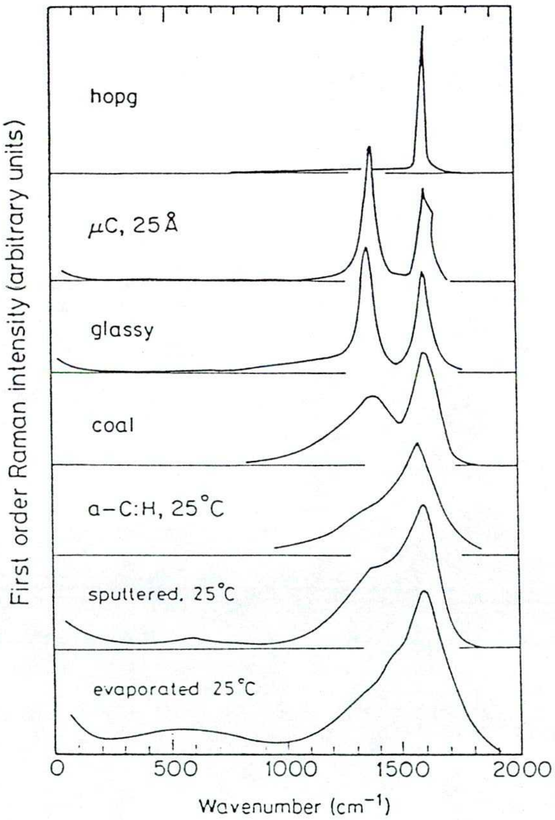

Fig. 1.4.1 First order Raman scattering for different carbon forms [54,55,56].

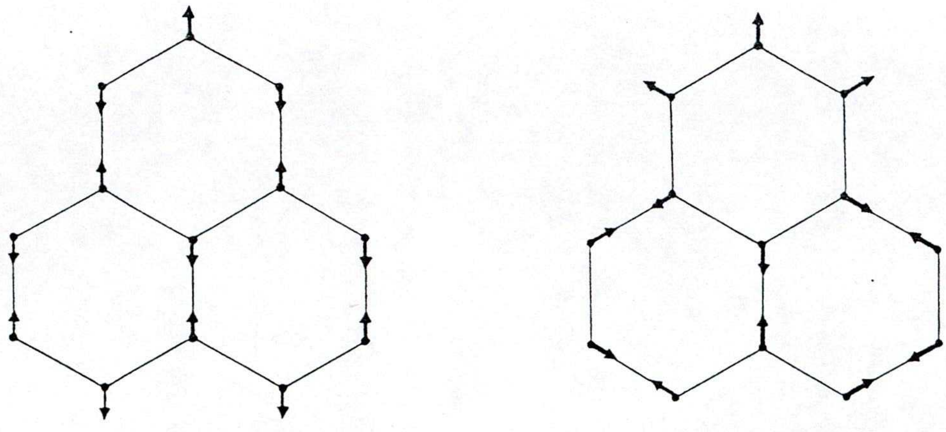

E_{2g} Raman mode at Γ

A_{1g} disorder mode

Fig. 1.4.2 Atomic eigenvectors of the Raman active modes.

Fig. 1.4.2 compare the eignvectors of the A_{1g} and E_{2g} mode for a single graphite layer. The A_{1g} mode is inactive for an infinite layer, but when k is not longer conserved the mode develops a strong Raman active [58]. Hence, the D mode can dominate the G mode in small crystallites as seen in Fig. 1.4.1. This D mode, which associated with disorder in graphite lattice, corresponds to a peak in the Raman density of states (PDOS) of graphite due to A_{1g} mode at K point of the Brilloiun zone. The glassy carbon curve is more sharper than the a-C curve, that attributed to a more ordering of glassy than a-C. The lattice dynamic calculations of Beeman et al. (1984) [59] confirmed the above interpretations. He calculated the phonon density of states (DOS) for diamond and graphite as shown in Fig. 1.4.3 using the equation of motion method [60] and a simple valence force field (VFF) approximation to the atomic interactions. Fig. 1.4.3 also shows a two peaks for graphite, a large peak at 1350-1550 cm^{-1} due to bond-stretching vibrations and another two lower peaks due to mixed bond stretching/bending modes at ~300 and ~600 cm^{-1}. In addition, the diamond spectra have a large peak at 1100-1280 cm^{-1} due to bond-stretching modes and a two lower peaks at 900 and 600 cm^{-1}.

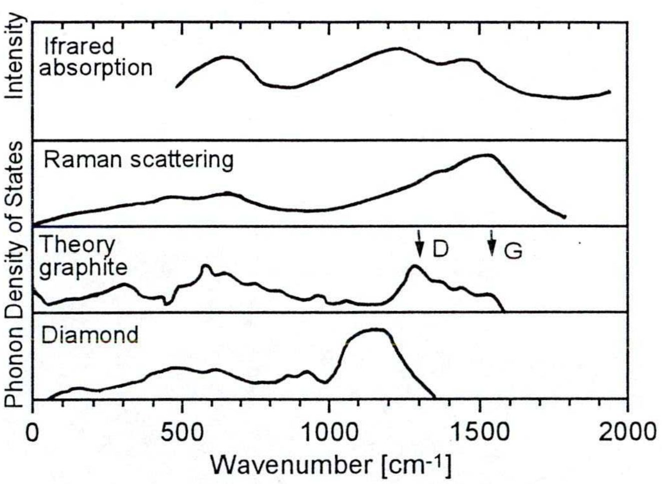

Fig. 1.4.3 Infrared and Raman spectra of evaporated a-C compared to the phonon DOS of graphite and diamond.

Deposition voltage dependence of Raman scattering studied by S.Xu et al. [65] in the range of 0-950 V and shown in Fig. 1.4.4 for a-C:H samples prepared from decomposition of methane (0.1 mbar pressure). Except for (deposition voltage) U_{SB} = 0 V all spectra look very similar: They show a peak at around 1500 cm^{-1} with a shoulder on the low energy side. Second order Raman scattering appears at around 3000 cm^{-1}. Those results fitted by a two Gaussian termed G-peak (~1540 cm^{-1}) and D-peak (~1300 cm^{-1}). The above results coincides with Tamor et al. results [66] except the dependence of G-peak position on deposition voltage. In addition, Tamor et al. (1994) confirmed their results and produced a relations between the deposition voltage and the a-C:H macroscopic properties [67]. They conclude that, the hardness and the material density increased by increasing U_{SB} while the optical gap and the hydrogen content decreased by increasing U_{SB}. They agreed the two phase model, since the sp^2 dominate most optical properties and sp^3 coordinated carbon atoms dominate the mechanical properties.

Excitation energy dependence of Raman spectra for a-C:H samples prepared by rf plasma deposition from hydrocarbon gases shown in Fig. 1.4.5 [68], since the drawn lines indicate the underlying luminescence background, the dashed line marks the peak frequency found for excitation at 4.82 eV. The figure also shows a shifting of G-peak position from around 1500 cm^{-1} to 1600 cm^{-1} by increasing the excitation energy from 2.18 eV to 4.82 eV and decreasing of the D-peak intensity by increasing the photon energy in the same energy range. This frequency shift is understood in terms of scattering from π-boded sp^2 carbon clusters which is reasonantly enhanced for incident photon energies close to π–π^* transition. This attribution is agreed with the Robertson model [22,69].

From structural modelling of Raman spectra it was concluded, that the sp^2 coordinated carbon atoms form graphitic clusters of different sizes embedded into sp^3 coordinated carbon atoms. This intermediate range ordering determine several macroscopic properties which related electronic density of states near band edges.

Effect of annealing on the Raman spectra of amorphous carbon gives further information about the real structural background of the Raman scattering. Fig. 1.4.6.a shows the change of Raman spectra for a-C:H sample under annealing in the range of 25°C - 800°C [22]. The D mode grows from a shoulder to a peak and the G peak shifts towards higher frequencies. That can be attributed to the decrease of sp^3 coordinated carbon proportion under the

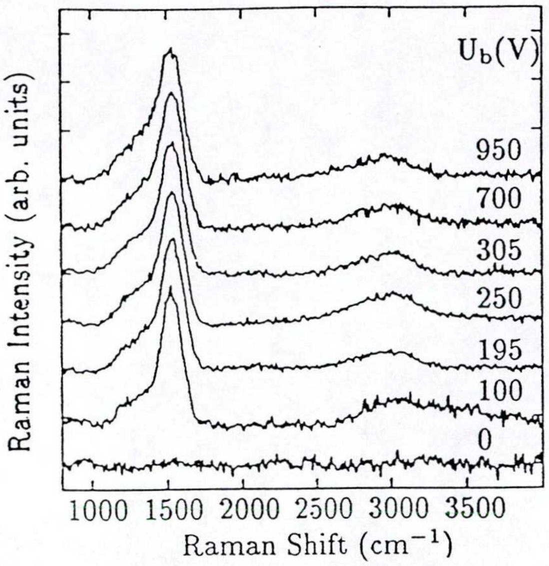

Fig. 1.4.4 Raman spectra for a-C:H samples prepared at different self biases [65].

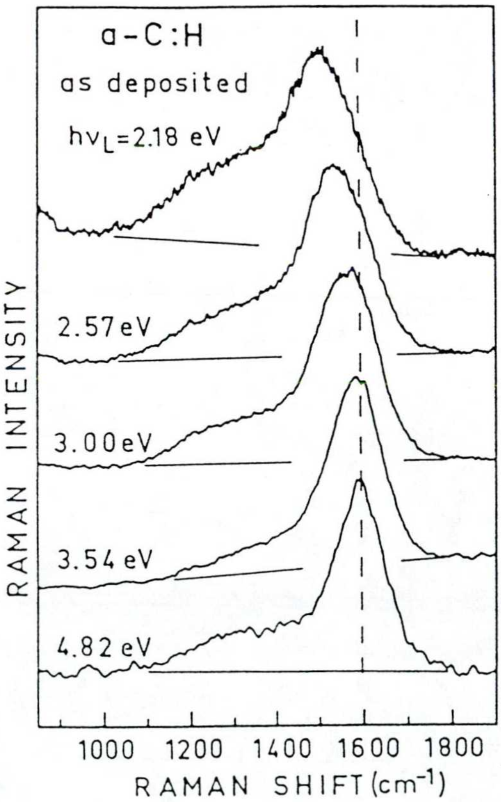

Fig. 1.4.5 Raman Spectra of plasma-deposited hard a-C:H excited at different photon energies given in the figure.

effect of graphitization. Fig 1.4.6.b [57] shows The effect of the same annealing temperature range for ion-beam sputtered a-C and the same Raman spectra dependence shown as for a-C:H samples. As the annealing temperature increased, the crystallites grow in size and/or number, and thus they began to contribute to the Raman spectrum, causing the I_D/I_G intensity ratio increase as shown in Fig. 1.4.6. The increase of crystallite sizes 16 and 38 Å for the films annealed at 800 and 900°C agree with the Wada et al. [70] results.

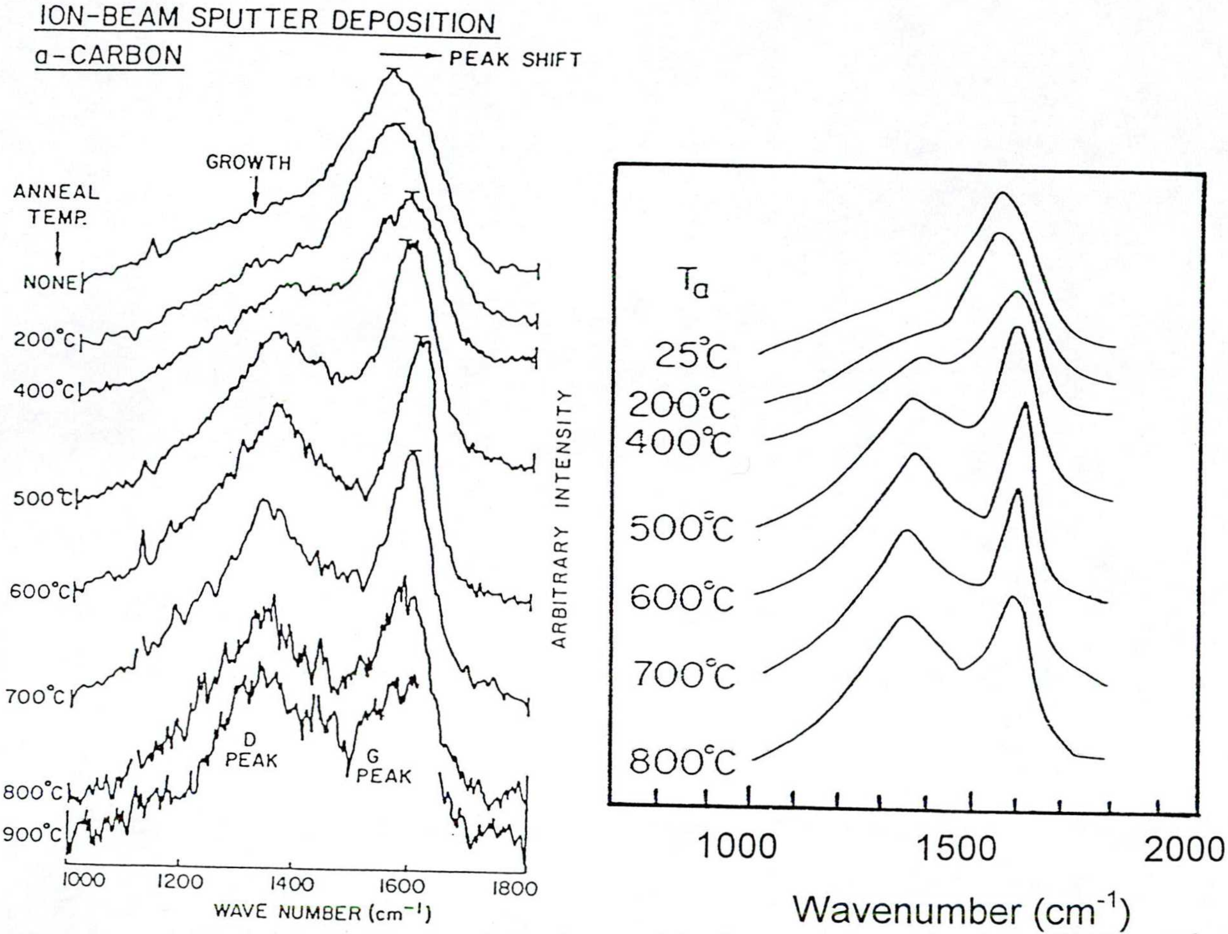

Fig. 1.4.6 Annealing temperature dependence of the Raman spectra for (a) a-C:H samples and (b) ion-beam sputtered a-C.

Infrared absorption (IR)

IR considered a very popular method to probe the vibrational properties because of its wide availability and ease of use. There is no IR active mode for diamond but for graphite there are two IR active modes, the main E_{1u} at 1585 cm^{-1} and the out-of-plane mode A_{2u} at 868 cm^{-1} [18]. The IR spectra for a-C and a-C:H were measured by many authors [61,62,71-76].

Fig. 1.4.7 shows the absorption coefficient versus the wave number for a-C:H prepared by plasma deposition from methane [61]. The IR spectra has characteristic features in the 700-1600 cm^{-1} and 2800-3000 cm^{-1} wavenumber range. Peak positions can be determined from second derivatives of absorption coefficients as it is shown in Fig. 1.4.7. Table. 1.4.1 summarizes the peak positions and their assignment. The C–H stretching and C–H deformation vibrations observed in a-C:H samples prove that the incorporated hydrogen is distributed between sp^2 and sp^3 coordinated carbon atoms. Fink et al. [63] found that the hydrogen bonds to sp^3 and olifinic sp^2 sites with similar probability. Monohydrogen is clearly dominate over dihydrogen [62] and the bonds are observed for monohydrogen bond to aromatic sp^2 carbon (at 3045 cm^{-1}) or olifinic sp^2 carbon (at 3000 cm^{-1}). Many authors [62,39,33,35,74-76] find the hydrogen bonds preferentially to sp^3 sites. The weak 3300 cm^{-1} line due to ≡CH groups is the only evidence of any sp^1 hybridized carbon in a-C:H or in a-C.

From IR spectra it is also clear that sp^2 and sp^3 coordinated carbon atoms form aromatic and olefinic type bonds as well, therefore the medium range ordering of sp^2 carbon sites can not be exclusively graphitic clusters but olefinic chains can also be formed. The concentration of each species can be determined by using the normalized intensities, however comparison

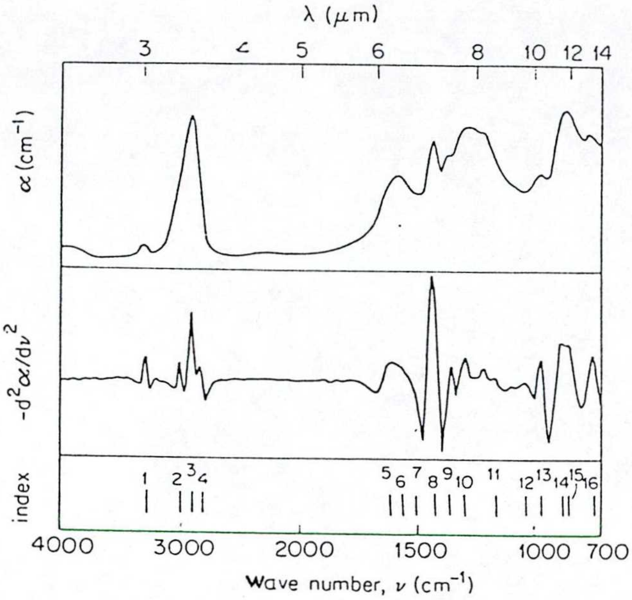

Fig. 1.4.7 Infrared absorption of a-C:H sample [61].

Table(1.4.1) Infrared absorption bands observed in a-C:H and their assignments according to Dischler et al. [61,62] and Meckenzie et al. [82].

Band	Observed frequency (cm^{-1})	Predicted frequency (cm^{-1})	Assignment	Type of vibrations
1	3300	3305	sp^1 CH	A stretch
2	3045	3050	sp^2 CH (aromatic)	A stretch
	--	3020	sp^2 CH_2 (olifinic)	B_1 antisymmetric stretch
3	3000	3000	sp^2 CH (olifinic)	A stretch
	--	2960	sp^3 CH_3	E symmetric deformation
	--	2950	sp^2 CH_2 (olifinic)	A_1 symmetric stretch
4	2920	2925	sp^3 CH_2	B_1 antisymmetric stretch
5	2920	2915	sp^3 CH	A_1 stretch
6	2850	2855	sp^3 CH_2	A_1 symmetric stretch
7	1620	1620	sp^2 C=C (olifinic)	stretch
8	1570	1575	sp^2 C–C (aromatic)	stretch
9	1509	--	--	--
10	1430	--	sp^2 C–C (aromatic)	stretch
11	1367	1355	Disorder mode	--
12	1300	1330	sp^3 C–C	stretch
13	880	--	sp^2 C–H (aromatic)	B bend “deformation”
14	780-820	--	sp^2 C–H (aromatic)	B bend “deformation”

of Fourier transform infrared (FTIR) absorption spectroscopy, high resolution ^{13}C nuclear magnetic resonance spectroscopy, and hydrogen evaluation by forward recoil elastic scattering (FRES) measurements shows that IR absorption can not be used to determine the carbon hybridization or total hydrogen content of a-C:H film [64].

The deposition voltage IR absorption dependence shown in Fig. 1.4.8 in the range of 0-1000 V for a-C:H samples prepared by capacitively coupled rf plasma decomposition of methane, as well as for ta-C:H [76]. The anodic film and samples deposited with less than 90 V self bias are obviously of polymeric character: C–H stretching modes are resolved and characteristic water bands are observed at 1700 cm^{-1} and around 3300 cm^{-1} which due to water diffused into open columnar structure of this material. The IR spectra indicate a significant structural change between 50 and 140 V self bias with the 90 V sample being of intermediate character: it is already so dense that it resists the diffusion of water, but still reveals a large hydrogen signal with rather narrow bands in the stretching mode regime. Above 200 V self bias further gradual changes occur as witnessed by a slight additional reduction of bending and stretching absorption band intensity. Between 200 and 1000 V films therefore as typical representatives of DLC (diamond-like carbon).

The thermal annealing effect on the hydrogen bonding properties was studied by different authors [62,71,39]. Dischler et al. [62] studied the influence of thermal annealing in the 320-880 K temperature range and it was found that annealing temperature range can be divided into two regions as was discussed in section (3.1.2).

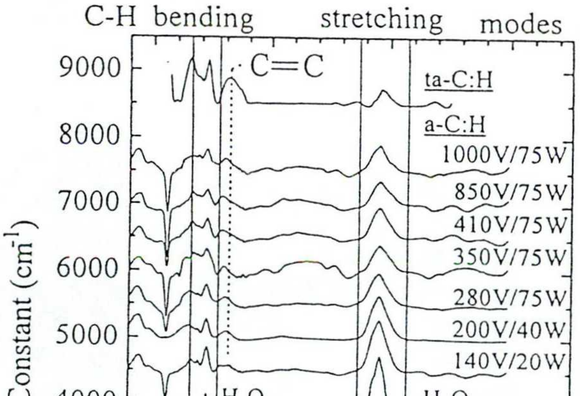

Fig. 1.4.8 IR absorption spectra of a-C:H and ta-C:H samples [27].

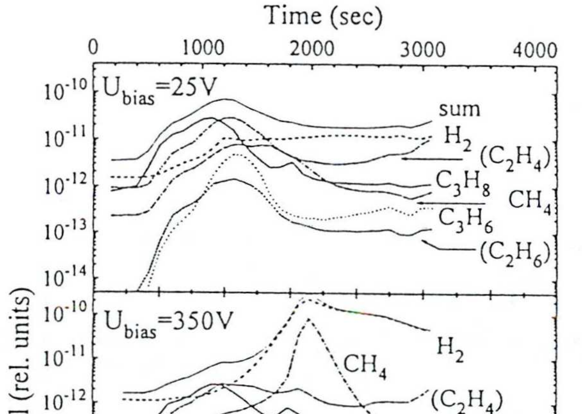

Fig. 1.4.9 Effusion of Transients of six selected masses from a polymeric, DLC and ta-C:H sample [27].

Hydrogen effusion experiment [76] give more precise information about changes under annealing from room temperature up to 1000 °C. Fig. 1.4.9 shows the effusion of six selected masses from a polymeric, DLC and ta-C:H sample. The polymeric samples release 70 % of their total hydrogen as C_3H_8, 17 % in the form of H_2 and approximately 7 % in the form of C_3H_6 and CH_4 each. The effusion starts with a rather weak threshold around 200 °C. While the emission of hydrocarbons is essentially terminated after 30 min. (600 °C) the hydrogen transient did not decrease even after 50 min. (at 1050 °C). In the DLC material H is detected predominantly as molecular hydrogen (75 %) with a separate, second threshold at around 550 °C. The first effusion threshold in DLC material tentatively is 200 °C, mainly C_3H_8 again and the second sharp threshold (H_2 and CH_4) to that of CH_2 and CH groups accompanied by the collapse of the amorphous network to as essentially graphitic (sp^2 aromatic) structure.

3.1.5. Structural modelling

In spite of great potential of amorphous carbon and experimental results gathered so far, the structure of these materials at the atomic level is not fully understood. This is of course mainly due to the large variability of potential, bonding environments which allows a complex mixing of atomic-scale correlations. The one important question is the precise nature of carbon bonding in amorphous matter because the sp^2 and sp^3 hybridized carbon bonding enviroments lead to vastly different physical characteristics. Ratio of sp^2 and sp^3 hybridized carbon atoms and their arrangement in the real space have the crucial role to play in determining bulk properties. In plasma deposited a-C:H, the incorporated hydrogen is a further factor which influences macroscopic properties.

Theoretical structural models of amorphous carbon were developed by using empirical pseudopotential [77], different type of molecular dynamic [78-80], energy relaxed, band-built random network [59] and quantum chemical calculations [69]. The simple model which gives a homogenous structure consists of a covalent random network of sp^2 and sp^3 hybridized carbon atoms and some hydrogen terminated bands [62]. Multiphase structure, including amorphous graphite, diamond-like and polymeric regions with a heterogeneous distribution of hydrogen over the different carbon fractions was suggested by Smith [81]. Recently, the most commonly used model is the so called "two phase" model [82,83], the first phase consists of π bonded (sp^2) clusters, which are embedded on the second phase, an sp^3 bonded phase, which in hard a-C:H is highly crosslinked, and in soft a-C:H is a polymeric hydrogenated phase. The sp^2 phase determines optical properties of the material, while the sp^3 phase determines its mechanical properties. This two phase model was subsequently used by Robertson [69] as a basis of his quantum chemical calculations.

The electronic density of states which determines several macroscopic properties was placed into the focus of Robertson model [69]. The key to understanding the electronic structure of all amorphous carbon is to realize that this is controlled by the π states of sp_2 sites [84,22] as these lie closest to the Fermi level E_F. This is plausible from comparison of diamond and graphite density of states (DOS); the sp^3 hybridization of carbon in diamond results in a large band gap between the valence band of occupied bonding (σ^*) states aid conduction band of empty antibonding (σ^*) states however, although in graphite the $\sigma$and σ^* states are situated near similar energetic portions but the π states form a band which lies across the $\sigma-\sigma^*$ gap with minimum in the DOS at E_F.

Recently the most discussed issue is the π states distribution and its structural background. Robertson [69] have approximated this problem on the ground of Huckel model. The standard approximation is to decouple the π and σ states and to treat them separately. This is possible because the orbitals lie perpendicular to each other for planar sp^2 sites and because their states tend to lie in different energy ranges, which minimizes their coupling. Another important difference between σ and π states is the following. The σ states are two centre bands, their bonding is very localized and bonding energy can be expressed as the sum of the energies of each bond on their energetic can also be expressed as a short range valence force field. this causes the σ electrons to control the Short-Range Order (SRO) of the network, i.e. its bond lengths and bond angles, but it leaves the longer range order undefined.

The π states are more complex, they can form both localized two centre bands as in ethylene and multicentre or resonant bands as in benzene or graphite. Their bonding energy is longer range and non-local and therefore it cannot in general be subdivided into the contribution from individual bands. In this way π electrons may introduce Medium Rang Order (MRO) into the structure [22]. By using tight-binding Hamiltonian [69] it has been found that π bonding strongly favors aromatic rings over olefinic chains and also favors clustering of separate rings into graphitic sheets. this means that, the aromatic ring clusters expected to be the dominant species of sp^2 sites. The σ biding energy is independent of the degree of clustering. Hence, for a given fraction of sp^2 and sp^3 sites, π bonding favors forming sizable graphitic clusters rather than being spread homogeneously through the sample. This atomic scale structure is able to explain electronic density of states measured experimentally, Raman scattering, optical and electrical properties [22] but difficulties arise in fitting diffraction data.

The radial distribution function obtained by neutron diffraction of amorphous carbon films is compared to three recent theoretical models [85] (Fig. 1.5.1). Although all theoretical model reproduce the main experimental features, they differ in details as it is clear from Table. 1.5.1 which summarizes important parameters. Here the comparison with different models will not be discussed but one important feature we should emphasize. The pair correlation function T(r) does not show any feature in that graphite across (2.84 Å). The peak corresponding to that of graphite at ~4.15 Å is missing in experimental T(r) curve. These results give significant evidence for the back of ordered hexagonal ring structure in a-C films and demonstrates that other models of a-C based on ordered graphite-like sixfold rings [69,70] with a high degree of intermediate range order are not correct. The observation of a broad peak at 3.8 Å corresponds to third-bonded chainlike configurations which is consistent with the theoretical models which exhibit bond-angle disorder the resonance of five-and seven atom rings, and rather distorted nonplanar character of threefold sites.

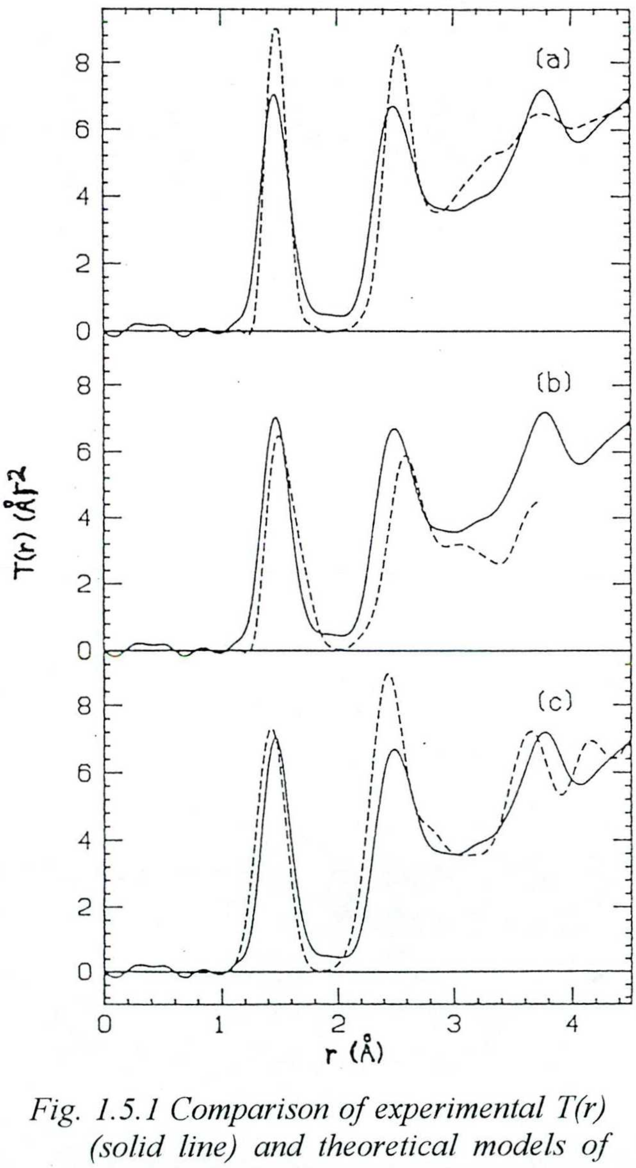

Fig. 1.5.1 Comparison of experimental T(r) (solid line) and theoretical models of a-C (dashed), (a) empirical pseudopotential [77]; (b) molecular dynamics [78]; (c) relaxed bans-built C340 [59]. This figure is taken from Ref. 85.

A complex experimental study of hydrogenated amorphous carbon using time of flight neutron diffraction, inelastic neutron scattering, NMR, and infrared spectroscopy, presents evidence for a new structural model for a-C:H which does not include graphitic clusters as intermediate

Table 1.5.1 Comparison of various parameters associated with peak position, most probable band angles, densities and integrated coordination numbers [85].

	a-C expt.	**Ref. 77**	**Ref. 78**	**Ref. 59**	**Graphite**
T(r):					
r_1 (Å)	1.46[a]	1.48	1.49	1.43	1.42
r_2 (Å)	2.49	2.53	2.59	2.44	2.46
θ (deg)	117	177.4	120.7	118.4	120
J(r):					
r0 (g/cm^3)	2.44	2.38	2.0	2.69	2.26
z (r_{min}) (atoms)	3.34[b]	3.07	3.2	3.28	3.00
$\frac{z(r_2)-z(r_{min})}{z(r_{min})}$	1.04	1.04	0.88	1.26	1.00

[a] A value of 1.45 Å is obtained for a cutoff, without a Lorch function

[b] This value corresponds to r_{min} = 1.90 Å. Other r_{min} will give slightly different results.

range ordering [51]. Fig. 1.5.2 shows the pair correlation functions for three different a-C:H samples and graphite powder, for comparison. The results of the gaussain hint are summarised in Table. 1.5.2.

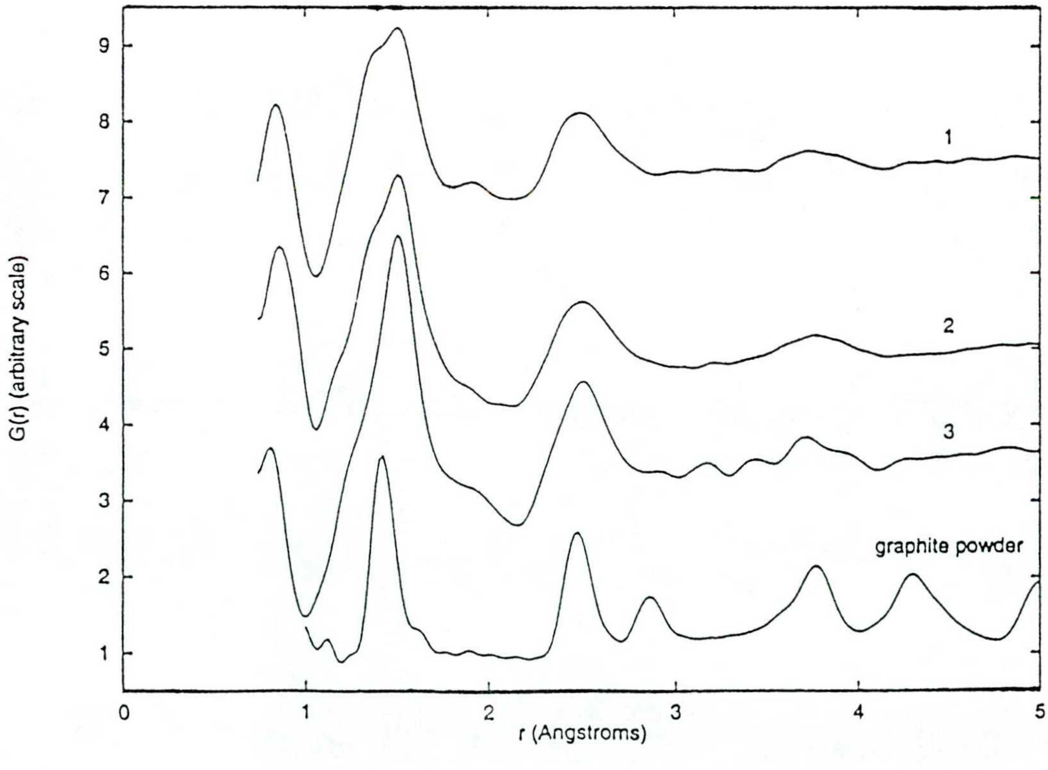

Fig. 1.5.2 Pair correlation function for three different a-C:H samples and graphite powder (offset) obtained from neutron diffraction experiments [51].

Table. 1.5.2 Bond lengths and coordination numbers derived from the neutron data; (a) for sample 1; (b) for sample 2; (c) for sample 2 [51].

(a)

Peak position (± 0.01 Å)	Peak area (± 0.3 atoms)	Assignment
0.88	0.84	H–H
1.03	0.18	C–H and H–C
1.34	0.84	C=C
1.52	2.17	C–C
1.7-2.2	--	H–C–H and C–C–H
~2.5	--	C–C–C

(b)

Peak position (± 0.01 Å)	Peak area (± 0.3 atoms)	Assignment
0.86	0.41	H–H
1.06	0.16	C–H and H–C
1.34	1.12	C=C
1.53	2.64	C–C
1.7-2.2	--	H–C–H and C–C–H
~2.5	--	C–C–C

(c)

Peak position (± 0.01 Å)	Peak area (± 0.3 atoms)	Assignment
0.85	0.18	H–H
1.04	0.78	C–H and H–C
1.18	0.31	C≡C
1.34	0.34	C=C
1.51	2.40	C–C
1.7-2.2	--	H–C–H and C–C–H
~2.5	--	C–C–C

All three hybridization of carbon atom are observed : sp^3 C–C at ~1.53 Å, sp^2 C=C at ~1.34 Å and sp^1 C≡C at 1.18 Å. Peaks at ~ 0.86 Å give clear evidence for the presence of molecular hydrogen. The unsaturated C=C band length of 1.34 Å in every samples corresponds exactly to olefinic sp^2 C=C bands, that indicates that most of the sp^2 carbon present is as the olefinic, not aromatic/graphitic form [50]. Experimental neutron diffraction data were compared with theoretically calculated curves for the molecular dynamics generated a-C:H models as it is shown in Fig. 1.5.3. The modes are mainly composed of two-fold and three-fold coordinated carbon atoms, with the fraction of four fold-coordinated sites not exceeding 30 %.

The models show a system of short chainlike segments with a marked by low tendency towards aromaticity. The sp^2 atoms are interconnected by homogeneously distributed sp^3 chainlike segments. Counting the different type of carbon bond gives a ratio between single and double bands which agrees very well with the experimental derived values. The models also confirm the existence of sp^3 H and sp^3 H_2 groups and can demonstrate the existence of H_2 molecules. It is found that differently hybridized carbon atoms tend to cluster. Although π bonding is the main source for such cluster effects, the five-, six, and seven-membered rings are strongly cross-liked by inclusion of at least one or two fourfold coordinated carbon atoms and are thus not aromatic. Separated aromatic like ring groups have not been formed under the constraint of a cross-linked rigid network; the sp^2 atoms are rather arranged in olefinic groups.

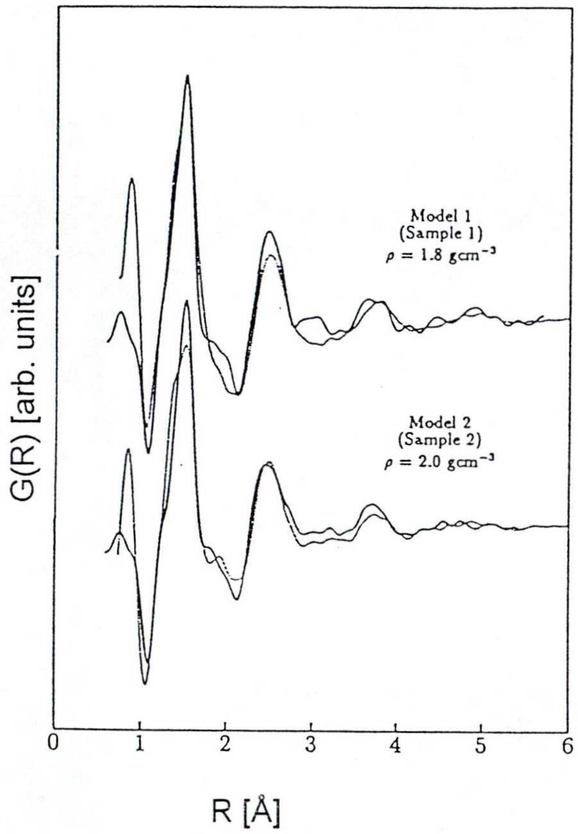

Fig. 1.5.3 Total pair correlation function G(r) for the molecular dynamics generated a-C:H models coupled with the neutron diffraction data [79].

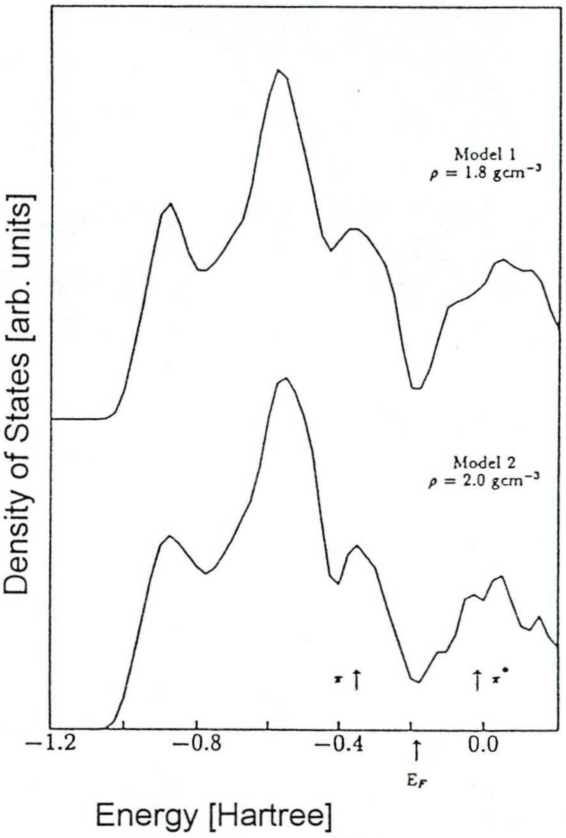

Fig. 1.5.4 Electronic density of states for the two a-C:H models for molecular dynamics simulation [79].

Fig. 1.5.4 shows the total density of electronic states (TDOS) derived from the simulation for the two a-C:H model. The relative small group width (~1-2 eV) are not caused by the formation of separated aromatic ring grouping of different sizes. It si rather, a consequence of the π–π^* splitting realized by embedding the local p electron systems of σ bonded atomic arrangements in the strained bonding environment of a rigid cross-linked network, in which "mixed" bands dominate [51].

At this point we can conclude, that medium range ordering the sp^2 coordinated carbon atoms is the central question of different structural models of amorphous carbon, however we need more diffraction data on different amorphous carbon forms to arrive a real model.

3.2. ELECTRONIC STRUCTURE

3.2.1. Electronic density of states

The electronic density of states N(E) is defined as the number of energy states per unit energy per unit volume. It is the valid concept of crystalline and non-crystalline materials. In this section we will deal with the valence and conduction band states. The conduction and valence band density of states can be determined experimentally by using the photoemission spectroscopy and electron energy loss spectroscopy (EELS). X-ray absorption near edge structure technique (XANES) can be also used to detect the conduction band states.

The theoretical calculations of the density of states for non-crystalline materials are still few and some of its given in (Mott and Davis 1979) [86]. In this section we have to show the electronic density of states, derivation and meaning, the factors that affect the density of states, and the experimental techniques which used to probe the conduction and valence band states which are mentioned above. Finally, we will show some UPS, XPS, XANES, and EELS results measured amorphous carbon samples.

For an electron in the system with a given spin direction and lie in the range between E and E+dE, the number of eigen states in unit volume is N(E) dE. Then at temperature T, the number of electrons for each spin direction is N(E) f(E) dE, where f(E) is the Fermi distribution function

$$f(E) = \frac{1}{\exp[(E - E_F)/KT] + 1}$$

and it is a function of T where E_F separates occupied from non-occupied states and its limitation attained when T tends to zero ($T \to 0$). The energy E for each electron from the free electron approximation is

$$E = \frac{\hbar^2 K^2}{2m}$$

where K is the wavevector and m is the effective mass. Hence, in this case the Fermi surface is spherical and

$$N(E) = E^{1/2} \,.\, \text{const}$$

this equation represent a parabolic function of K and represent also the electronic density of states in crystalline materials.

In non-crystalline materials, the disorder makes a deviation from this configurations of density of states and large deviations will occur if the scattering is strong. In amorphous semiconductors the effect of disorder and the random distribution of centers in space play a more effective role than do impurities in controlling the conductivity the density of states. The form of the density of states (DOS) near band edges frequently determine transport properties. The proportionality between N(E) and $E^{1/2}$ obtained for crystals is not to be expected. For some cases we shall assume that $N(E) \propto E^n$, where n can be determined empirically.

The main factors determining the density of states for a given material are the first coordination number and the interatomic distance. Thus if the former in unchanged, no major change in the density of states is likely except that due to changes in the specific volume. Coordination numbers higher than the first will of course influence the density of states to some extent. In Germanium, the third coordination number is different in the crystalline and amorphous forms; in crystalline tellurium higher coordinations strongly affect the magnitude of the smallest energy gap and this is very much changed in the amorphous form (Mott and Davis 1971) [87].

Photoemission spectroscopy

The electronic density of states can be determined by two photoemission techniques, which are the ultraviolet photoemission spectroscopy (UPS) and the X-ray photoemission spectroscopy (XPS). The photoemission techniques widely used to explore the electronic band structures of semiconductors, i.e. it can explore the valence and conduction band densities of states. It measures the energy distribution of photoemitted electrons as a function of incident photon energies. The used photon sources are the ultraviolet UV line spectra of rare gas discharge lamps for UPS or X-ray anodes for XPS. The corresponding photon energies are 10-50 eV for the UV and 1286.6 eV (Al) and 1253.6 eV (Mg) for the K_α X-ray lines.

The photo-emitted electrons can be analysed by a retarding grid analyser or by a dispersive electrostatic analyser. To minimize the surface contamination, the experiment processed under ultra-high vacuum. Since the escape depth of the photoelectrons is very small (~5 Å for UPS and ~50 Å for XPS), these experiments are relatively difficult and give results mainly from the surface layer..

For photons of energy $\hbar\omega$, the energy distribution function of emitted electrons is given by

$$N(E,\hbar\omega)dE = \left\{\frac{f(\hbar\omega)}{\alpha(\hbar\omega)}\right\} T(E)S(E,\hbar\omega)N_C(E)N_V(E-\hbar\omega)dE$$

where f is a scale factor which includes parameters to the experimental apparatus, α is the absorption coefficient, T is an escape function, and S is the fraction of excited electrons of energy E lost because of scattering.

Photoemission looks like the normal optical absorption measurements, it gives the joint density of states in the valence and conduction bands. But the optical absorption only measure the difference between the two absorption edges, the lower of conduction band and upper of valence band. Otherwise, the photoemission spectroscopy can determine the all energy states quantitatively. That means it can give the spectrum of the states in the conduction and valence bands as a function of energy, this is the advantage of the photoemission spectroscopy technique.

The 120 eV photoemission spectra UPS [40] and XANES [88] are shown in Fig. 3.2.1 for graphite, diamond, a-C and a-C:H. It should mentioned that a-C spectrum was taken an a-C:H sample after annealing at 773 K. UPS used to probe the VB and XANES used to probe the conduction band. That means Fig. 3.2.1 show the VB and conduction band spectra. The more intensive peak in the photoemission DOS at 0-12 eV is due to p states and the lower peak at

12-22 eV due to s states. The upper peak contains both σ and π bonding states. The π bonding states appear as a shoulder near 3 eV on the graphite spectrum and as a weak shoulder on the a-C spectrum but no shoulder is visible on the wide band of a-C:H spectrum, whereas the NMR measurements proved that the π states exist for the same sample type.

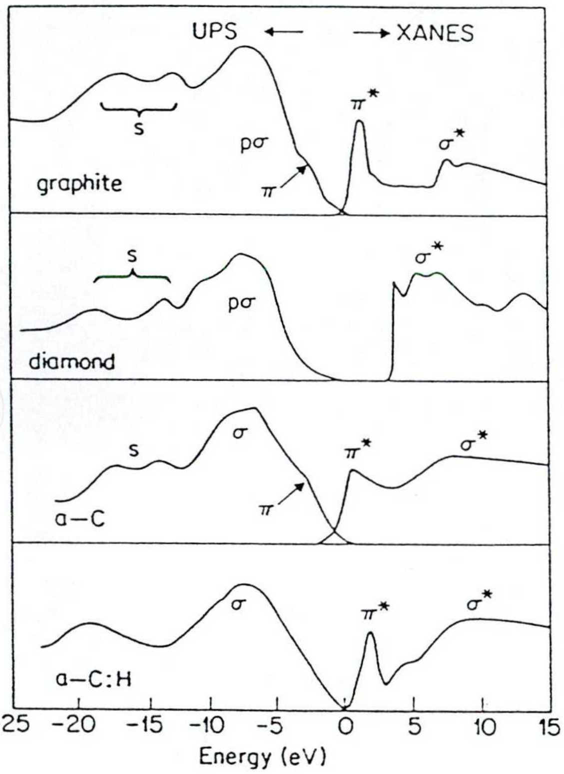

Fig. 3.2.1 UPS [40] and XANES [88] spectra for different carbon forms.

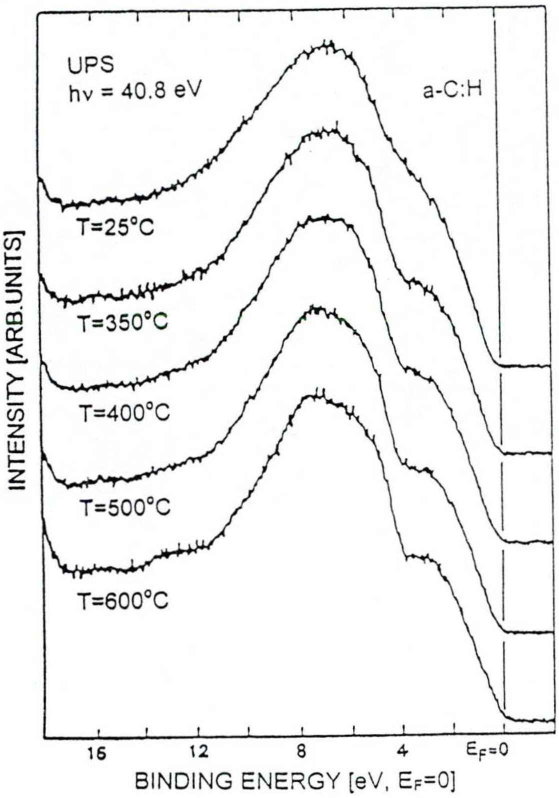

Fig. 3.2.2 Photoemission spectra of a-C:H as a function of annealing [89].

Another feature appeared in the UPS spectra of Fig. 3.2.1 is that the hydrogen existence are not seen in the UPS spectra because the photoemission matrix element for hydrogen is very low. Second, the s band in the case of graphite, diamond, and a-C split into two peaks while in the case of a-C:H has a one peak feature that attributed to the presence of odd membered rings in the random network.

On the conduction band states density of a-C:H shown by XANES spectrum in Fig. 3.2.1 the antibonding π states appears as a well resolved peak similarly to graphite spectra. It proves that conduction band states near to the band edge consist from π* states and this gives further evidence of forming sp^2 hybridized carbon atoms in a-C:H. The π states is more visible in the UPS spectra of a-C:H measured by Oelhafen et. al. [89] and shown in Fig. 3.2.2. The π states form as a shoulder near 4 eV in the as deposited sample and the increasing peak in the annealed samples. This spectrum confirms that the valence band edge of a-C:H is π–like.

The XPS spectrum of a-C:H sample prepared by rf plasma CVD system from CH_4 [90] at -200 V self bias shown in Fig. 3.2.3, as well as the density of states and the partial densities of states which calculated by using the molecular dynamics (MD) calculations for the quenching from the melt. The total and the C_{2S}, C_{2P}, H_{1S} partial densities of states which given by the calculations shown in the figure. The calculation tends to overestimate the binding energies of the s-bands of sp^2-bonded material. The analysis shows the true position of P_1 is thus more likely at a binding energy lower than 15.5 eV (Fig. 3.2.3.a) and it will therefore contribute to the broad shoulder around 13 eV as indicated in the VB (valence band) spectrum of Fig. 3.2.3.b. In addition, the P_2 in a-C:H shifts in the simulation as well as in the experiment to higher binding energies i.e. to 12.4 eV and merges with P_1 at 13 eV in the VB spectrum. Finally they [90] conclude that, due to the anisotropy of the P-orbitals, P_2 will be of predominantly C_{2P} character and thus more sensitive to disorder.

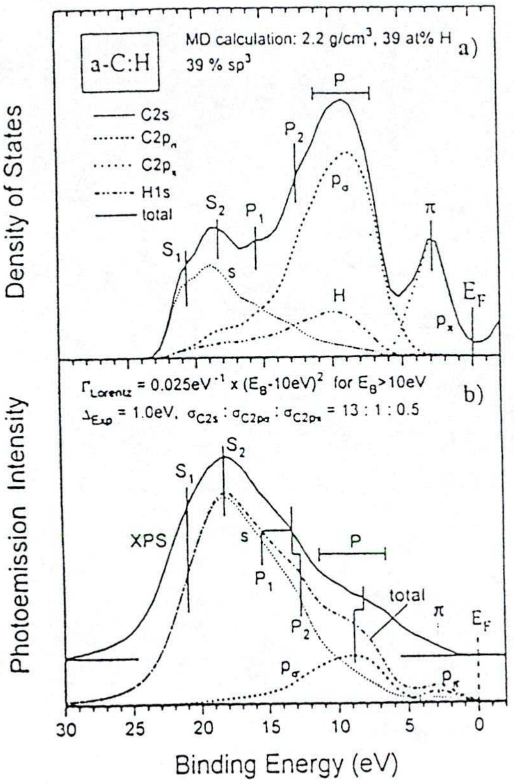

Fig. 3.2.3 (a) Density of states and partial densities of states for a model structure of a-C:H.(b) experimental valence band spectrum (solid line) of a-C:H and its simulation [90].

Electron energy loss spectroscopy (EELS)

EELS was discussed before in section (3.1.2) in determining the sp^2 and sp^3 proportions. The advantages of this method can be used to probe the transitions from the valence band to the conduction band, which benefits in mapping the electronic structure of the material. Fig. 3.2.4 show the EELS in the region of the C_{1S} core level to conduction band transitions for a two samples prepared by two different techniques [91]. Two peaks appears on the spectra, first at 285.5 eV which corresponds to the transitions between C_{1S} core level and π^* conduction band level and the second one at 290 eV corresponds to the transition between C_{1S} core level and the σ^* conduction band level. The EELS spectra of different samples proves that a-C:H has appreciable amount of sp^2 hybridized carbon atoms and they give a further evidence for that the lower energy part of the conduction band states are formed by π^* states of sp^2 hybridized carbon atoms.

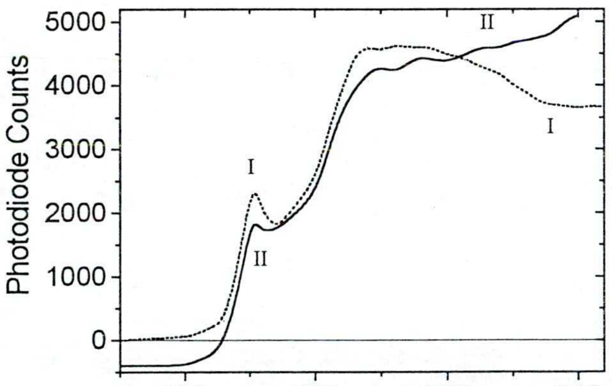

Fig. 3.2.4 EELS in the region of the C_{1S} core level to conduction band transitions [91]

3.2.2. Tail states and mobility edges

The mobility edge is defined as the energy separating states that are localized from those that are extended. By considering a single band, if the disorder is strong, the whole band can be localized, and for weaker disorder, the centre of band consists of extended states and only the band edge states are localized. The mobility edges occur at energies at which the density of states N(E) is roughly one third of its free electron value [86], this estimation confirmed by Jackson et al [92] experiments on a-Si:H. The difference between the energies of the mobility edges in the valence and conduction bands is called the mobility gap.

The mobility gap in many amorphous semiconductors corresponds to a photon energy at which the optical absorption coefficient has a value of $\sim 10^4$ cm^{-1}. It is, in intrinsic materials, equal to twice the activation energy for electrical conduction, that is twice the slope of $\ln\sigma$ against $1/kT$. That means it can be determined from the electrical measurements particularly conductivity (σ), thermoelectric power, Hall effect, and drift mobility. In most of amorphous semiconductors, the mobility gap equal to the optical gap. It depends on the short range order as in a-Si:H rather than the random fields due to point defects.

In amorphous carbon, both valence and conduction band edges are due to π states of hybridized carbon atoms as we mentioned before in section 2.1. The high enough π density of sates (DOS) in a-C support the extended states while the DOS in a-C:H falls and the π and π^* bands will become localized especially at high hydrogen content where the hydrogen atoms saturate the sp^2 sites converting them to sp^3 sites. Another unique aspect of amorphous carbon is its medium range order. In usual amorphous semiconductors the disorder is short ranged [86] and the mobility edges are determined by quantum-mechanical tunneling rather than such classical concepts as percolation. In a-C and particularly in a-C:H, the medium range order is of greater importance than the short range order in determining the band gap.

In amorphous carbon a series of π bonded clusters of different sizes can be formed and the $\pi-\pi^*$ energy splitting depends on cluster size being larger for a smaller cluster and vice versa. Thus optical gap width is determined by the largest clusters. In that case, when the scale of medium range order is large, the smallest sized, largest gap clusters will dominate the mobility edges and there will be a long tail of localized states due to states from the larger clusters. Optical gap and mobility gap are different when π states of sp^2 sites is tailing deeply into the gap. Next we discuss potential fluctuations near band edges for two amorphous carbon forms – a-C and a-C:H – which demonstrate different relation between optical and mobility gap.

In Fig. 2.2.1 we show the effect of π bonded clusters on local band gaps, mobility edges and optical band gaps for a-C and a-C:H [93]. The presence of sp^2 bonded clusters produces large fluctuations in the local band edges. In a-C:H both sp^3 and sp^2 hybridized carbon atoms are present and the wide gap regions in the figure corresponds to sp^3-bonded region, whose σ states lie at least ~ 3 eV from the midgap. The narrower gap regions arise from the π-bonded clusters. The presence of sp^3 sites and the variation in cluster gaps are seen to produce extremely large fluctuations in the band-edge energies. These fluctuations are much larger and tend to be much longer range than those in any other elemental amorphous semiconductors.

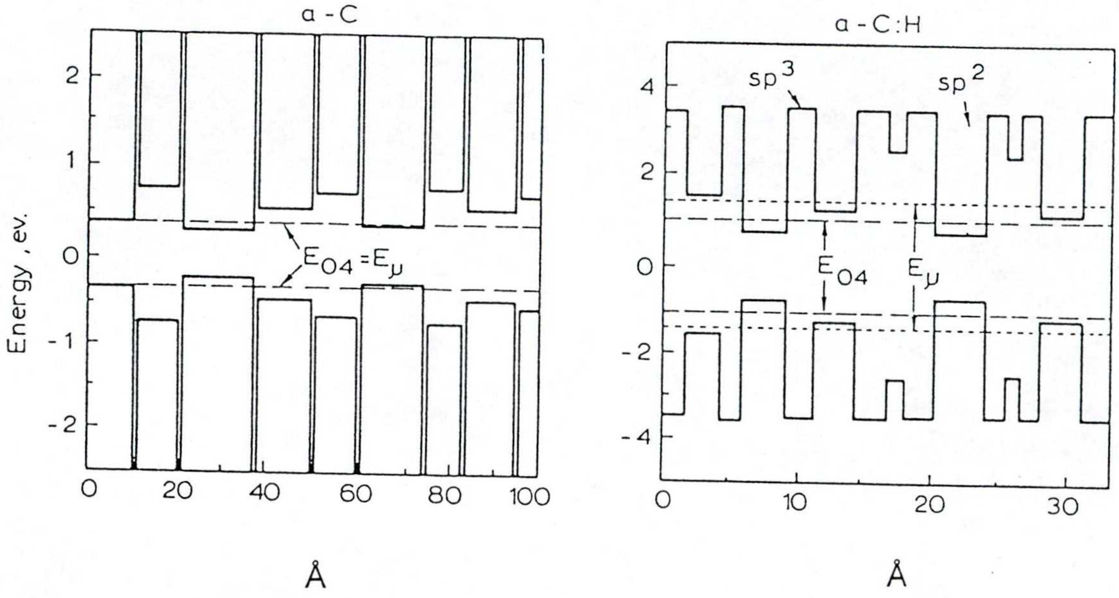

(a) (b)

Fig. 2.2.1. Schematic band model for (a) a-C and (b) a-C:H [93]

The gap of the σ phase, which is over 6 eV, acts as tunnel barrier between each π cluster and tends to localize π states within each cluster. The "optical" band edges, which depend just on the density N(E) of states, will vary principally with the cluster size distribution. In contrast, the mobility edges depend strongly on the width of sp^3 barriers. Widening the barriers will tend to force the mobility edges further into the bands, well beyond the optical band edges. Thus E_{μ} will exceed E_{04} for π states of a-C:H. Experimental evidence for this reasoning comes from luminescence measurements that is from the observation of large polarization memory of a-C:H photoluminescence [94] and from excitation energy dependence of luminescence spectra and intensity [95,96]. DC electrical properties and their temperature dependence, which will be discussed in chapter 6 give further support of different energetic position of mobility edges and optical edges in a-C:H.

In sputtered a-C more than 90 % of carbon atoms are threefold coordinated [97] and they form also cluster of different sizes which introduces fluctuations of band edges as it is seen Fig. 2.2.1.a. Because small concentration sp^3 hybridized carbon atoms,, large potential barriers which would localize π electrons within π bonded clusters are not dominant feature in a-C. Thus π electrons excited beyond E_{04} gap are mobile, therefore the mobility gap corresponds to optical gap.

3.2.3. The optical absorption edge

The fundamental absorption edge is related to electronic states near band edges and that depends on these parameters which modify the electronic states distribution in this energy region. The optical absorption edge of amorphous carbon is strongly influenced by the deposition conditions, such as, the ion energy, bias voltage, substrate temperature, gas type and it also depends on the thermal of annealing. In this section we discuss the optical absorption of amorphous carbon and the relationship between the optical gap and the deposition parameters.

The optical absorption at the fundamental edge for amorphous semiconductors can be divided into three regions as it is shown in Fig. 2.3.1 [98]. The region above $\alpha=10^4$ cm^{-1} corresponds to band to band transitions between extended states [99,100]. Below this lies the Urbach tail in which the absorption falls rapidly and offer in an exponential manner, due to transitions between localized tail states and band states. The exponential dependence arises from exponential density of states distribution and the slope represents the slope of the broader of the tails. Finally there is offer an addition step in absorption at the base of the tail due to absorption by midgap defect states.

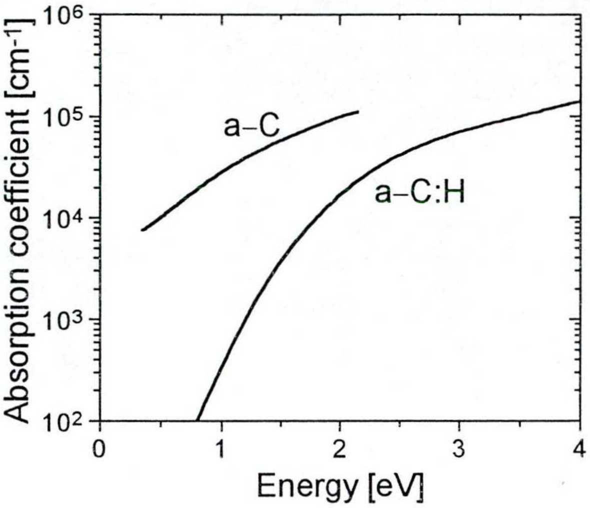

Fig. 2.3.1 Principal absorption scheme for plasma deposited a-C:H [98].

In the absence of sharp band edges in amorphous semiconductors the optical gap is defined empirically. The empirical definition of optical gap in an amorphous semiconductor such as the Tauc or E_{04} gaps correspond to placing optical band edges at a certain density of states near the band edges. The E_{04} gap means that energy at which the optical absorption coefficient (α) is 10^4 cm^{-1} and the Tauc gap is given by fitting the absorption coefficient α to the Tauc formula for $\alpha = 10^4 - 10^5$ cm^{-1}.

$$(\alpha E)^{1/2} = B (E-E_T) \qquad (2.3.1)$$

where E_T is the Tauc optical gap and B is a constant. From equation (2.3.1) we can get the Tauc optical gap value by deducing the intercept, that is extrapolation of linear part on the energy dependence of absorption coefficient plotted according to Eq. 2.3.1 gives E_T as an intercept at $\alpha = 0$.

The optical absorption around the fundamental absorption edge measured by several authors for a-C [97,101-104] and for a-C:H [62,81,82,105-109]. The optical absorption edge shown in Fig. 2.3.2 for a-C [97] and a-C:H [81]. The disorder in these forms causes the absorption edges to be broad. The broad slope of the absorption edges due to the wide range of cluster sizes.

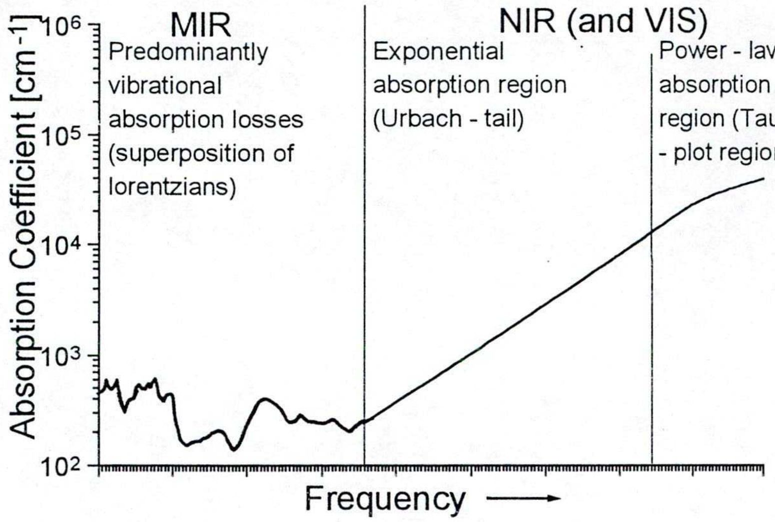

Fig. 2.3.2 Optical absorption edge for a-C and for a-C:H[81,97].

The edges are quite broad indicates no sharp increase of absorption coefficient can be observed in the edge region. This behaviour is in close relation with medium range ordering of sp^2 hybridization carbon atoms because π band and bottom of conduction band states. The energy splitting between bonding and antibonding π states ($\pi-\pi^*$ splitting) depends on cluster sizes [22], therefore the broad absorption edges indicate that a range of cluster sizes are present, each with its local band gap. The largest significant sp^2 clusters rather than the average cluster size determine the optical gap. Robertson [22] has derived the relation between sp^2 cluster sizes and optical gap from his structural model and for the case of aromatic clusters

$$E_g \cong 6/M^{1/2}\ \text{eV} \tag{2.3.2}$$

where M is the number of rings and for acenic clusters the gap falls more rapidly

$$E_g \cong \frac{60}{(M+2.16)^2}\ \text{eV} \tag{2.3.3}$$

The slope of absorption edge corresponds to a range of cluster sizes. The $E_g = 0.5$ eV for sputtered a-C gives by using Eq. 2.2.2 - M=140 for a large clusters and it can be assumed that M=35 for a typical cluster. The optical gap can also be expressed by the cluster diameter or in plane correlation length L_a(Å) as

$$E_g \cong 7.7/L_a\ \text{eV} \tag{2.3.4}$$

From this formula L_a = 9 Å typical correlation length can be deduced for sputtered a-C. The optical gap for the hard a-C:H is nearly 1.2 eV, which gives M=25 for the large clusters and perhaps M=6 for average clusters or L_a = 3.8 Å. In the case of soft a-C:H a gap of 2.5 eV gives M=5 for the large clusters and roughly M=2 for a typical cluster size.

The optical gap depends strongly on the deposition parameters. Fig. 2.3.3 shows the variation optical gap with deposition self bias, with substrate temperature and the influence of thermal annealing performed at different temperatures on the optical gap. The results of Fig. 2.3.3 were measured on a-C:H films deposited from RF plasma of benzene at 30 µbar pressure. The optical gap decrease by increasing the bias voltage. The before discussed structural background of the broad optical absorption edges and of the different gap values suggest increasing both of cluster sizes and ring numbers in sp^2 coordinated carbon clusters

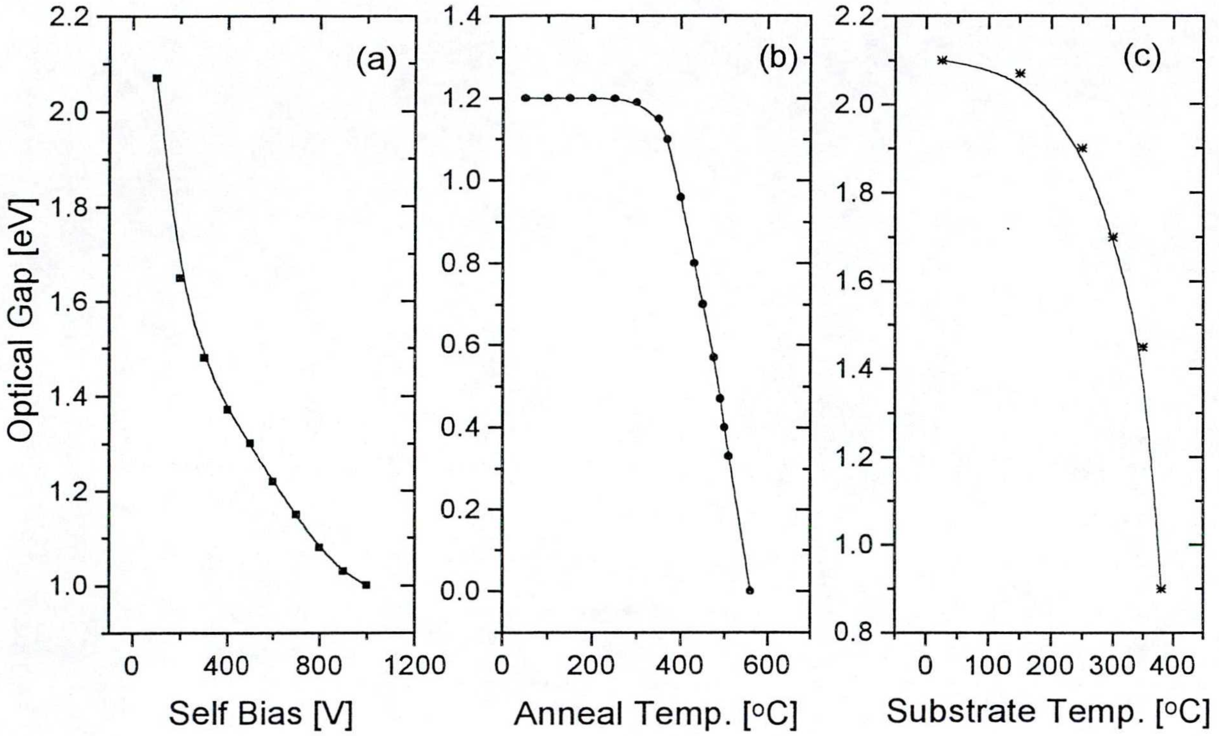

Fig. 2.3.3 Optical gap dependence of (a)Bias Voltage [110], (b)Annealing Temperature [38] and (c)Substrate Temperature [111] for the a-C:H samples.

with self bias to account for decreasing optical gap. This is in good accordance with the increasing ratio of sp^2 coordinated carbon atoms compared to sp^3 coordinated ones when the deposition voltage increases (see 3.1.2. section).

The effect of substrate temperature on the optical gap of a-C:H samples prepared by a dc glow discharge of acetylene at 300-400 V self bias voltage [111]. There is no significant change in the optical gap from room substrate temperature to 520 K but above this temperature the optical gap decreases from 2 eV to 0.9 eV. Moreover, at ~700 K the nature of the films became graphite like [111]. Functional form of this dependence is different from that of deposition voltage dependence however the similar reasoning was used to explain qualitatively of optical gap

The influence of annealing on the optical gap of a-C:H samples is shown in Fig. 2.2.3b [38]. In this plot no appreciable change can be observed up to 520 K annealing temperature above which a sharp dependence of optical gap begins. It was explained by decrease of hydrogen content and increase of proportion of sp^2 coordinated carbon atoms on expense of sp^3 coordinated ones [38]. Moreover they suggest that above ~880 K the sp^2 of 100 % aromatic phase is dominant. Changes of optical properties caused by thermal treatment were observed at lower annealing temperature (~520 K) compared to the previously discussed results [91,112]. Shift of absorption edge to lower energies was general observation and the interesting effect was the restoration of original state by layer illumination of heat treated samples [112]. No hydrogen effusion is expected near 520 K annealing temperature [39,76] therefore structural rearrangement results in increase of mean and larger cluster sizes [112].

3.2.4. Localized states in the gap

The electronic states in amorphous semiconductors can be classified as extended states and localized states. Extended states lie within the bands and it conduct at 0°K (i.e. electrical conductivity has a value at absolute zero). The mobility edges separate the extended states from the localized states as we discussed before in section (3.2.2).

In this section we review briefly localized states, and defect configurations in amorphous carbon and the relationship between the defect creation energy and the σ and π bonds creation energy. Then, we deal with defect density of states measured by different methods and discuss the influence of deposition parameters and thermal annealing on the defect density of states.

Localized states

Localized states can be classified either band tail states or deep states. They lie in the gap between the E_C (conduction band edge) and E_V (Valence band edge) as shown in Fig. 2.4.1. The region of low density of states between the mobility edges defines the mobility gap which like the band gap of crystalline semiconductors [100].

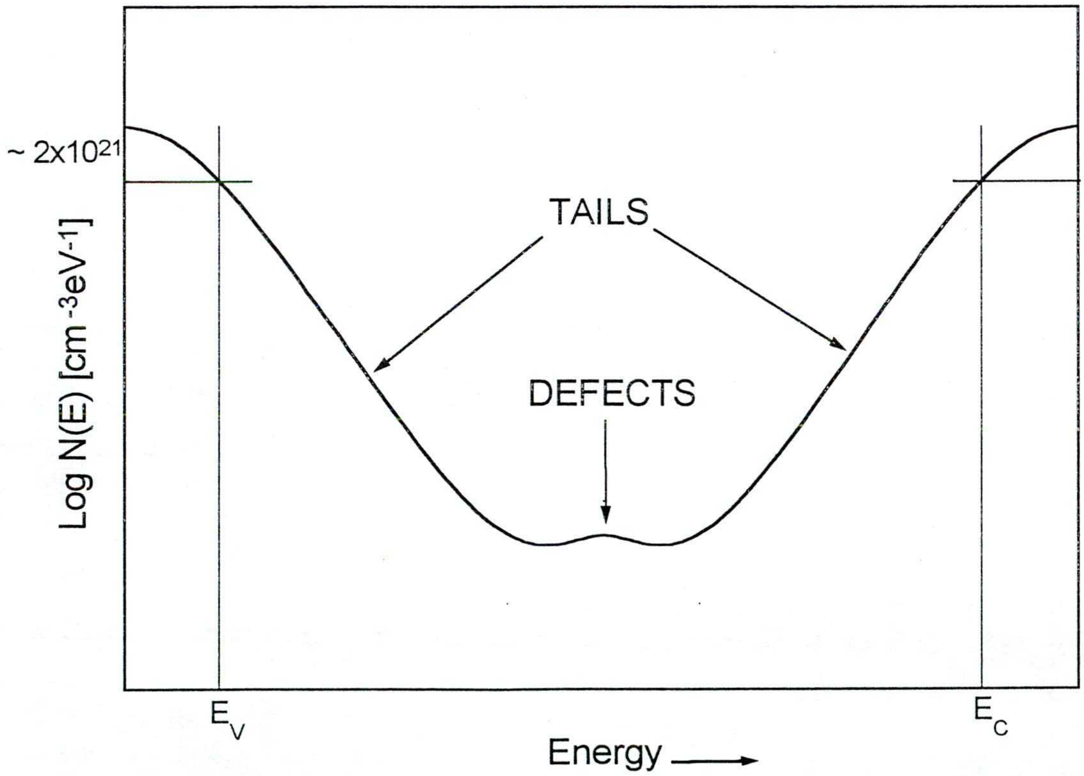

Fig. 2.4.1 Schematic picture of electron states near the band gap region of an amorphous semiconductor, showing extended and localized states, tail and defect states.

The tail states lie adjacent to the mobility edges whereas the deep states, which are more localized than the tail states, lie near the midgap and it is related to the defect configuration. The localization length of the tail states depends also on their distance from the mobility edges.

Defect configuration

The defect configuration in amorphous carbons is more complicated than for a-Si [69]. For a-Si the defect principally is the dangling bond (a dangling bond defined as an isolated trivalent site), where the trivalent Si site formed by breaking σ bond. On the other hand, in amorphous carbons the defect formed by breaking either σ or π bond. Due to the weaker π bonding, π defects are expected to predominate as a result of lower creation energy, which gives a state near midgap[69]

For a more quantitative description of localized states Robertson and O'Reilly [69] have used the Huckel of π states: All states around the gap arise from π states within this model putting the orbital energy E_p=0, the π electron spectrum tends to be symmetric about E=0. The tail states are the states of large clusters. Any clusters with an odd number of π states give a state near E=0 which is half filled i.e. paramagnetic defect level. The defect creation energy for π defect E_d can be written as [113]

$$E_d = N(E_N - \overline{E}_N) \qquad (2.4.1)$$

where N is the number of sites, E_N is the total π energy per site of the defect cluster, and $\overline{E}_N$ is the π energy of the equivalent non-defect cluster with a similar number of states.

Fig. 2.4.2 shows the defect creation energy as a function of number of sites for olifinic chains and for aromatic clusters. In this figure we can see, the rapidly decrease of E_d for the olifinic chain defects and the slowly decease of E_d for aromatic clusters. The maximum defect

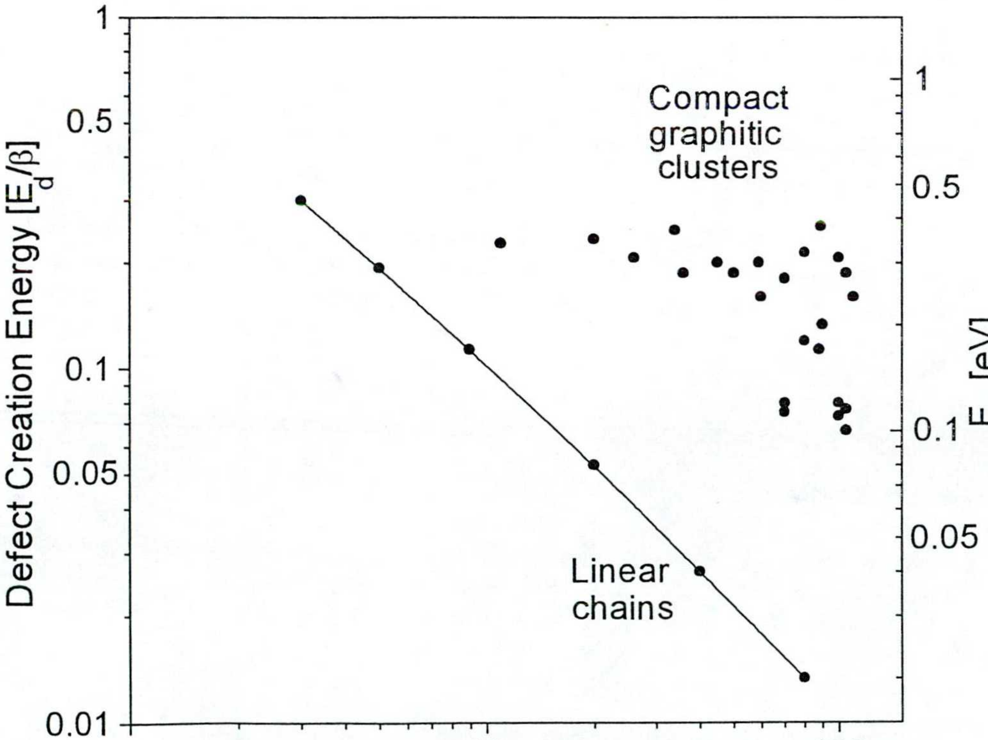

Fig. 2.4.2 Calculated E_d for π bonded clusters as a function of cluster size[113].

creation energy for aromatic defects is 0.4 eV as shown in Fig. 2.4.2 while E_d for σ defects is equal to the half of the C–C bond energy, i.e. 1.8 eV. Thus, E_d for π defects is much smaller than E_d for σ defects and other important point is, that E_d is not a single valued for π defects.

In all amorphous carbons the σ and π bonds are mixed. For example, a-C:H consists of mixed σ and π bonded system as we mentioned in section (3.1.2) and it has high defect densities because the low creation energy of π defects. The unpaired electron in these mixed systems will occupy a π orbital because the dangling bond is an isolated trivalent site [69] and it is expected to adopt planar configuration, by analogy to the methyl radical CH_3 and therefore unpaired electron occupy π orbital. Indeed, we can say that defect states and tail states in a-C:H are basically same character.

Optical absorption and Photoluminescence (PL), low temperature electrical conduction, electron spin resonance (ESR) are experimental methods generally used fro study localized states in the gap. Transitions from electronic states deep within the band gap to extended states eg. to conduction band states results in a subgap optical absorption which is seen an excess absorption above the Urbach tail. The excess absorption is found to be proportional to dangling bond density as measured by ESR. But in amorphous carbon no excess absorption is apparent in a-C:H samples of a higher spin density was explained by a higher excitations from midgap defect levels to be well above 1/2 E_{opt} [113].

Photoluminescence in a-C:H has no direct relation to the deeply localized states. Photons are emitted by radiative recombination of excited π states localized on sp^2 coordinated clusters and Photoluminescence efficiency does not show any correlation with unpaired spin density [114]. Density of localized states near Fermi level can also be determined from low temperature electrical conductivity, however there are several discrepancies with fitting of conductivity data for a-C:H with variable range hopping model and therefore we discuss the transport properties in a more detail in chapter 6.

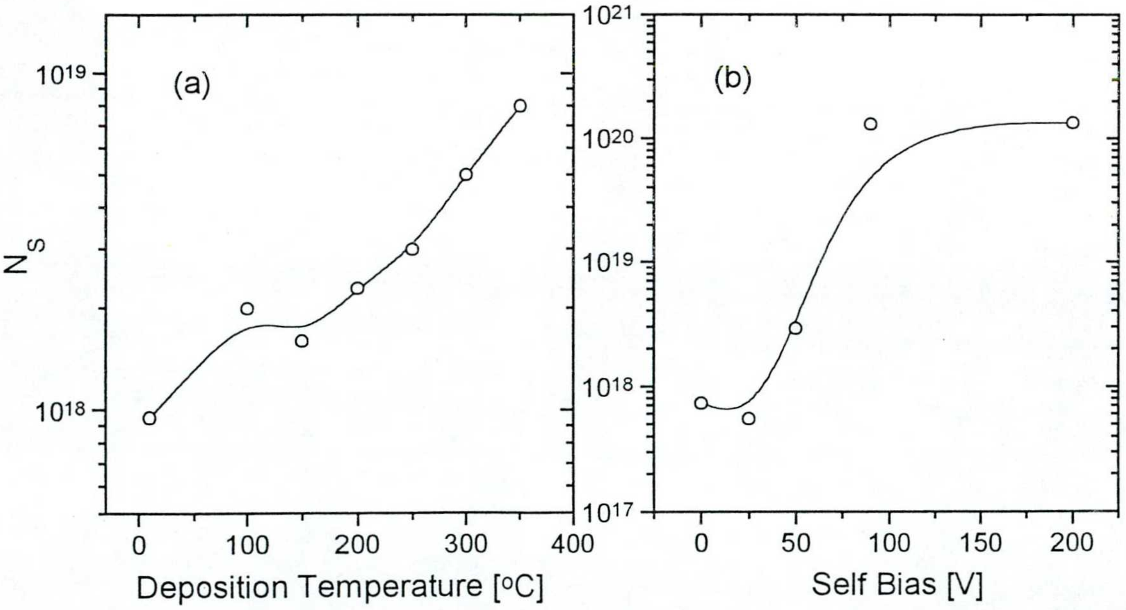

Fig. 2.4.3 Spin density N_s vs. deposition temperature (a) and vs. bias voltage (b) for plasma deposited a-C:H [100,118,121].

The singly occupied, paramagnetic defect states densities can be measured directly by electron spin resonance. In evaporated a-C Oreszko et al. [115] found 18^{18} cm^{-3} spin density which was relatively independent of annealing temperature (Fig. 2.4.3.a). Spin densities ranging from 10^{16} to 10^{21} cm^{-3} have been measured in plasma deposited a-C:H depending on deposition conditions. Fig. 2.4.3.b shows the spin density dependence of bias voltage [121] for a-C:H samples prepared by rf plasma decomposition of methane. The data of Reyes-Mena et al. [116], Tamor et al. [117] and Fabisiab et al. [118] suggest that spin density N_s passes through a maximum as a function of bias voltage for plasma deposited a-C:H.

The low spin density of soft a-C:H deposited at low voltages may be due to hydrogen passivation of defect states while the similar low spin density in high bias voltages is presumably related to electron delocalization effect because of large graphitization [113]. From temperature dependence of ESR spectra for a-C:H deposited at -400 V self bias Arcon and his coworkers [119] concluded that a-C:H contains centers of isolated electron spins which locally order below 50 K.

In Fig. 2.4.4 shows the dependence of spin density and ESR line width as a function of discharge pressure [37]. More than one order of magnitude increase of spin density can be attributed to the loss of hydrogen. The reduction in linewidth indicates an increase in the sp^2 cluster size [120].

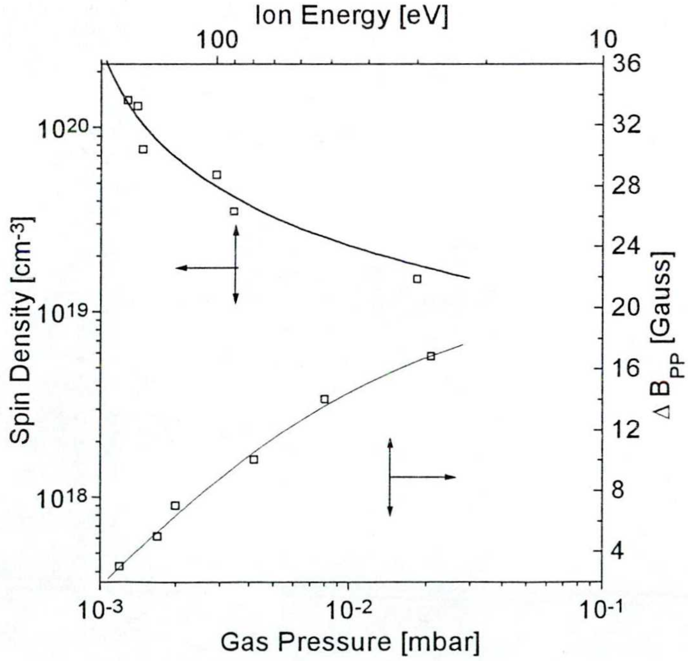

Fig. 2.4.4 The spin density and ESR linewidth as function of discharge pressure [Ref. 37].

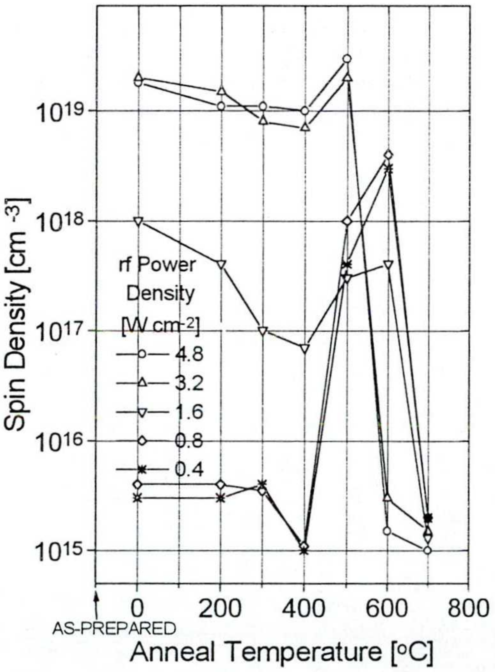

Fig. 2.4.5 The spin density as a function of annealing temperature for a-C:H [Ref. 116].

Influence of thermal annealing on spin density of a-C:H deposited at different RF power is shown in Fig. 2.4.5 [116]. Most of the samples shows no change in spin density up to 580 K. Above that temperature the spin density is seen to increase with thermal annealing and then to decline above ~800 K.

4. PREPARATION OF a-C:H SAMPLES

4.1. Radio frequency (rf) glow discharge technique

However several techniques are used for preparing a-C:H films, here we will discuss radio frequency (rf) glow discharge process only for a simple reason, because that was used for preparation of our samples. The rf technique is a simple powerful one compared with other techniques and a high deposition rates with appropriate gases can easily be achieved. Furthermore, many variables can be controlled in the plasma deposition technique such as rf power, discharge pressure, gas flow rates, pumping speed, sample temperature, discharge frequency, electrode spacing, electrode material and reactor geometry. We will discuss below some important features of rf glow discharge technique.

The rf power can be coupled capacitively or inductively to the discharge system as it is shown in Fig. 4.1.1.a The most popular and widespread technique for deposition of dense a-C:H thin films is the capacitively coupled system. In this technique the two electrodes mounted parallel to each other, like a capacitor, and the substrate placed on the powered electrode, usually the power generator is coupled through a capacitor which allows the accumulation of dc voltage on the powered electrode. The applied surface ratios ofthe electrodes acquires a negative self bias what can be regulated between 0 and few kV. The inductively coupled rf glow discharge shown in Fig. 4.1.1.b has been used less extensively, it is a popular technique for deposition of softer films. In the case of inductive coupling, the floating substrate bias is only a few volts below the plasma potential.

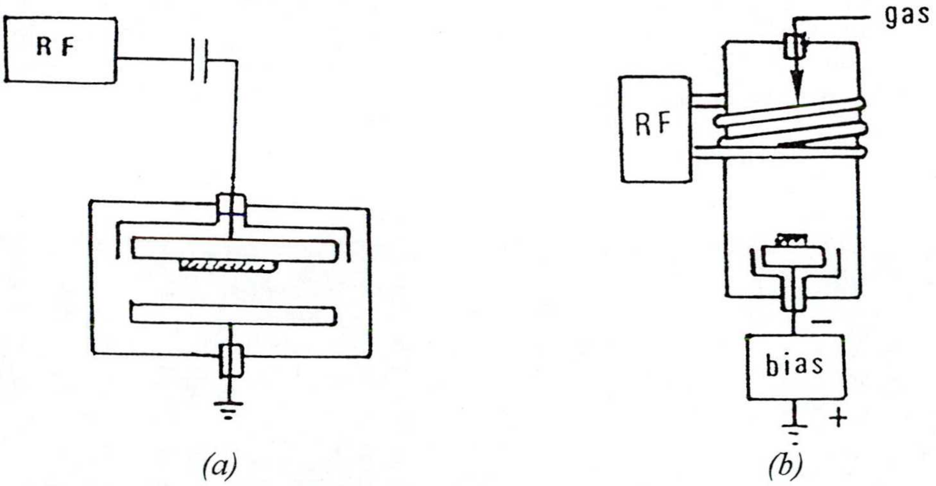

(a) (b)

Fig. 4.1.1. Schematic illustration of capacitvely coupled (a) and inductively coupled (b) rf plasma technique [125].

Regarding the frequency of the input power, there are two distinct regions, i.e. low and high frequency and the boundary between them is given by the ion plasma frequency:

$$f_{pi} = \frac{1}{2\pi}\left(\frac{n_i e^2}{m_i \varepsilon_o}\right)^{1/2} \qquad (1)$$

where n_i and m_i are respectively the ion density and ion mass. Assuming $n_i \approx n_e \approx 10^{10}$ cm^{-3} the calculated values of f_{pi} are found to be 5.4 MHz for CH_4 ions and 2.4 MHz for C_6H_6 ions. In the 13.6 MHz glow discharge, the rf field frequency is sufficiently high, therefore the ions requires many rf cycles to cross the sheath while electrons are able to follow the rf field. Due to capacitive coupling, the steady state dc current must be zero. If the powered electrode area is smaller than the grounded part of the system, it develops a negative self bias voltage U_{SB} relative to ground. Such situation shown in Fig. 4.1.2.

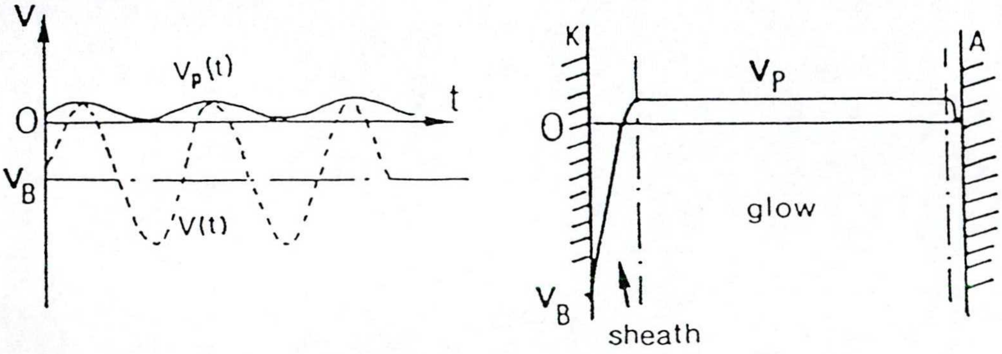

Fig. 4.1.2 RF modulation of plasma and self bias voltage [125].

The net results is ion bombardment of the substrate, which is placed on the powered cathode during the film growth. The ratio of the elctrode potential will be proportioned to their surface ratios [122]:

$$U_{SB}/V_A = (S_A / S_C)^2,$$

where S_C and S_A are the respective area of the cathode and anode.

The bias voltage is related to the rf power (W) and the operating pressure (P) as:

$$U_{SB} = k\,(W/P)^{1/2} \qquad (2)$$

where k depends on factors such as the electrodes area [113]. That means the U_{SB} is a linear function of the square root of the ratio of the rf power over the discharge pressure.

The ion energy E_i depends on U_{SB} and the ion mean free path in the sheath. E_i correlates with the self bias voltage U_{SB} at low pressure in the non-collisional sheath region as:

$$E_i \approx e\,U_{SB}$$

while at typical operating pressures [108] there is a spectrum of ion energies with a mean value of

$$E_i \approx k`\,U_{SB}\,P^{-1/2}$$

where k` is a constant. That means the E_i directly proportional with the self bias voltage, that is why the most of authors used the self bias voltage as indication for the ion energy.

Discharge region

The discharge region consists of glow region, in which the ions are generated by collision with electrons and a space charge region or ion sheath, across which the ions are accelerated to reach the cathode. The time averaged potential is constant in the plasma and decreases in the sheath which are formed in the vicinity of the two electrodes. At the cathode (small electrode) the sheath potential V_{SH}, the time averaged difference between the plasma potential and the cathode potential is given as:

$$V_{SH} = V_P + U_{SB}$$

In strongly asymmetric rf discharge systems the bias voltage much larger than the plasma potential V_P (100-1500 V coupled to 10-30 V). Thus the bias voltage U_{SB} often used as a measure for the sheath potential at the cathode.

In capacitively coupled rf glow discharges the net current equals zero, i.e. the flux of positive ions on the growing a-C:H film is balanced by an equivalent flux of electrons. This is a perquisite for the deposition of insulating films or for the deposition on insulating substrates. The latter requires high rf frequencies (> 1MHz) because at low rf frequencies the charging of the substrates surface during one rf period may lead to significant reduction of the ion energy.

The process parameters such as bias voltage U_{SB} and discharge pressure P effect considerably physical and structure properties of a-C:H films. Especially the bias voltage U_{SB}, which determines the energy of the film forming hydrocarbon ions (at given pressure), was found to have a strong influence on the properties and structure of the growing a-C:H films [123]. Hydrogen content and optical gap decreases, while density and refractive index increases by increasing deposition voltage. Although the detailed behaviour is more complex what we discuss parallel with our results. It is a general trend as the deposition voltage increases the properties of a-C:H layers change from soft polymer-like through diamond-like to graphitic behaviour. Increasing substarte temperature influences similarly the material properties, however, its effect is much weaker compared to deposition voltage. Moreover under discharge process energetic particles bombardment heats the powered electrode, therefore it should be cooled to deposit samples at constant temperature.

Properties of a-C:H film as well as groth rate of the layer depends on hydrocarbon precursor. Properties of the films prepared at the same low self bias voltage by using different gases are considerably different whereas at the same high self bias voltage, the films properties slightly affected [124] i.e. their structures are near to each other.

The deposition rate v varies with the ionization potential and molecular weight of the source gas as shown in Fig. 4.1.3. The highest growth rate is achieved by using benzene precursor, while the deposition rate from methane plasma is smaller by more than one order of magnitude compared to benzene. For a given gas the deposition rate v has been found to vary with bias voltage and gas pressure as :

$v = K'' U_{SB} P$

where K" is a constant. This equation was checked for various source gases (methane, acetylene and benzene) [108,124,33,35,125].

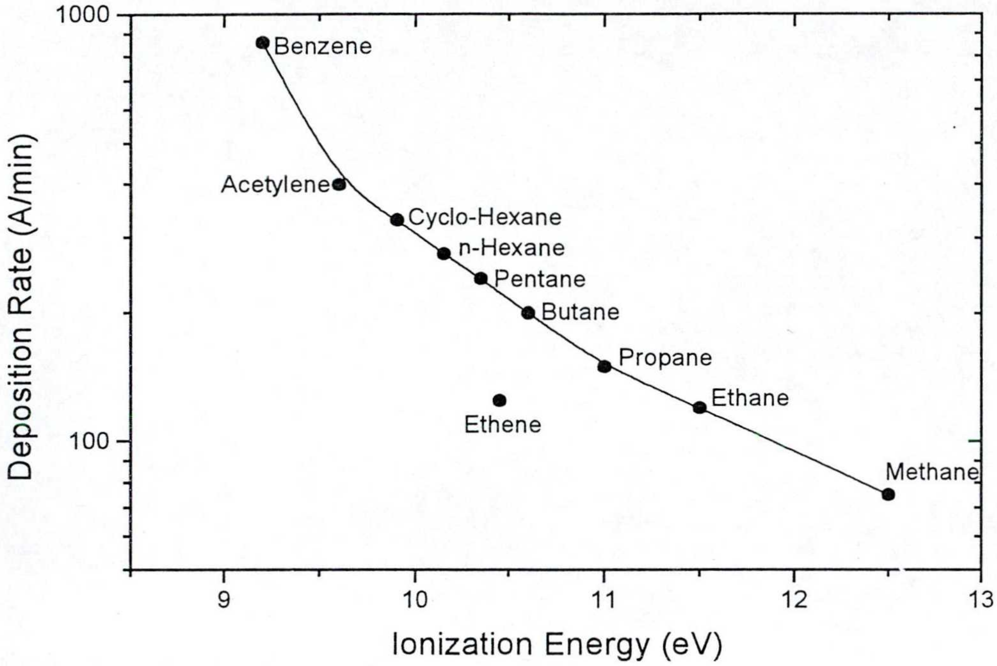

Fig. 4.1.3. Deposition rate of a-C:H vs. ionization energy of hydrocarbon precursor molecule [124,33]

4.2. Deposition of a-C:H thin films

In Fig. 4.2.1 we can see schematic illustration of the rf glow discharge system used in our laboratory for deposition a-C:H samples. It is a capacitively coupled technique, and it consists of :

- A glass chamber where the two electrodes mounted in it taking the ratio between these two electrodes large, provided that, the smaller electrode is the powered one. The larger electrode is connected to the ground. The smaller electrode is attached to a cooling system, which is isolated electrically from the power generator.

- A vacuum system consists of two stages for the low and high vacuum levels to reject the contaminated gases from the system before the deposition process and to control the discharge evacuation level through the deposition process. Appropriate gauges attached to the vacuum system.

- A rf 13.6 MHz generator adjusted by using a matching circuit and connected with the small electrode via a capacitor. The U_{SB} can easily be measured by the oscilloscope connected between the powered electrode and the ground in which a resistances box was connected serially to the oscilloscope as shown in the equipment.

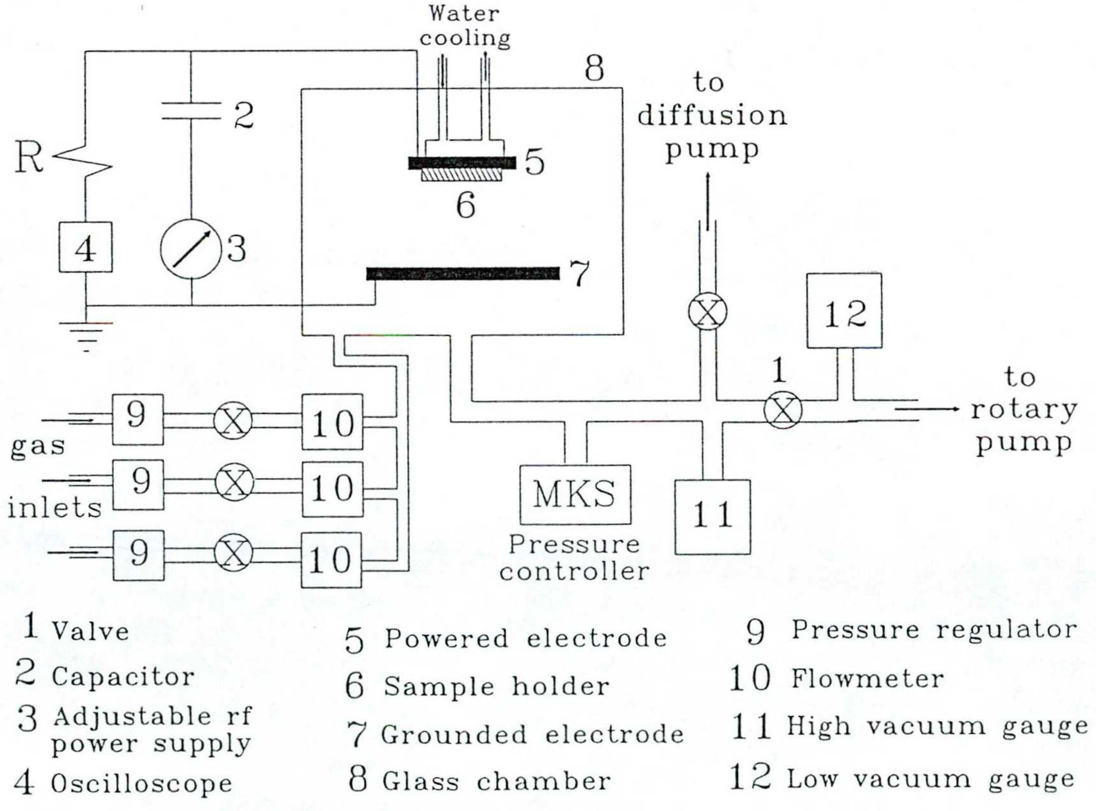

Fig. 4.2.1 Schematic illustration of the RF plasma deposition system used in our laboratory for preparation of a-C:H layers.

- The gas flow controller part contains gas supply and controlling elements (regulators, flowmeters, and valves) where the gas type is choosen and measure the flow rate through the deposition process.

Our deposition system makes it possible to prepare high quality a-C:H samples by changing self bias voltage from zero to -1500 V and by varying process pressure from 20 mtorr to atmospheric pressure. The deposition process itself starts by evacuation to less than 10^{-6} torr. Cleaning of the substrate surface was prepared by argon plasma discharge for a 1-2 minutes. Then, the process gas permitted to flow with a rate regulated in the range of 5-15 sccm and the rf power was adjusted to produce the needed self bias voltage. The benzene vapour and the methane gas were used as a source materials. For optical and electrical measurements the samples was prepared on the substrate materials of quartz or Corning glass (7059). For infrared and elipsometry measurements a-C:H samples were prepared onto silicon wafer substrate material. To avoid disturbing substarte luminescence a-C:H samples for Raman measurements were deposited onto metallic substrates for example onto Al or stainless steel. Water cooling of powered electrode prevented warming up the substarte higher than 350 K. Various deposition times were choosen to prepare samples of 0.1-5 μm thicknesses.

4.3. Qualification of the a-C:H samples

Variety of experimental methods were used for qualification of the deposited a-C:H layers. Due to deposition technique, a considerable amount of hydrogen is incorporated into the samples. The hydrogen content plays an important role in determining the electronic properties of a-C:H, because it controls not only the sp^2 and sp^3 hybridised carbon sites but also the morphology of the deposited films which in turn determines the electron density of states to a large extent. Absolute hydrogen content and other contamination was measured in collaboration by Research Institute of Particle and Nuclear Physics where the elastic recoil detection analysis (ERDA) [126] was worked out for similar analysis of other materials. The absolute concentration depth profile of hydrogen and other atomic components can be easily determined in a single measurement by combined elastic recoil detection (ERD) and Rutherford back scattering spectrometry (RBS) [126]. The measurements performed by ^{4}He nuclei of 2.5 MeV energy.

Fig. 4.3.1 shows the depth distribution of absolute hydrogen content for a-C:H samples deposited at -200 V self bias from benzene and methane source gases. Hydrogen distributes homogeneously through the sample in both cases; the absolute hydrogen content is 42 % for the methane sample which slightly higher than the 37 % measured for the benzene sample deposited by -200 V U_{SB}. Homogen distribution of hydrogen was observed at higher voltages also, that is demonstrated in Fig. 4.3.2 for samples deposited at -200, -500 ,-1000 V self biases from methane. From comparing the results of different samples on Fig. 4.3.2 we can see, that absolute hydrogen content decreases with increasing deposition voltage. This dependence is represented in Fig. 4.3.3 for a-C:H samples prepared from benzene and methane. Some

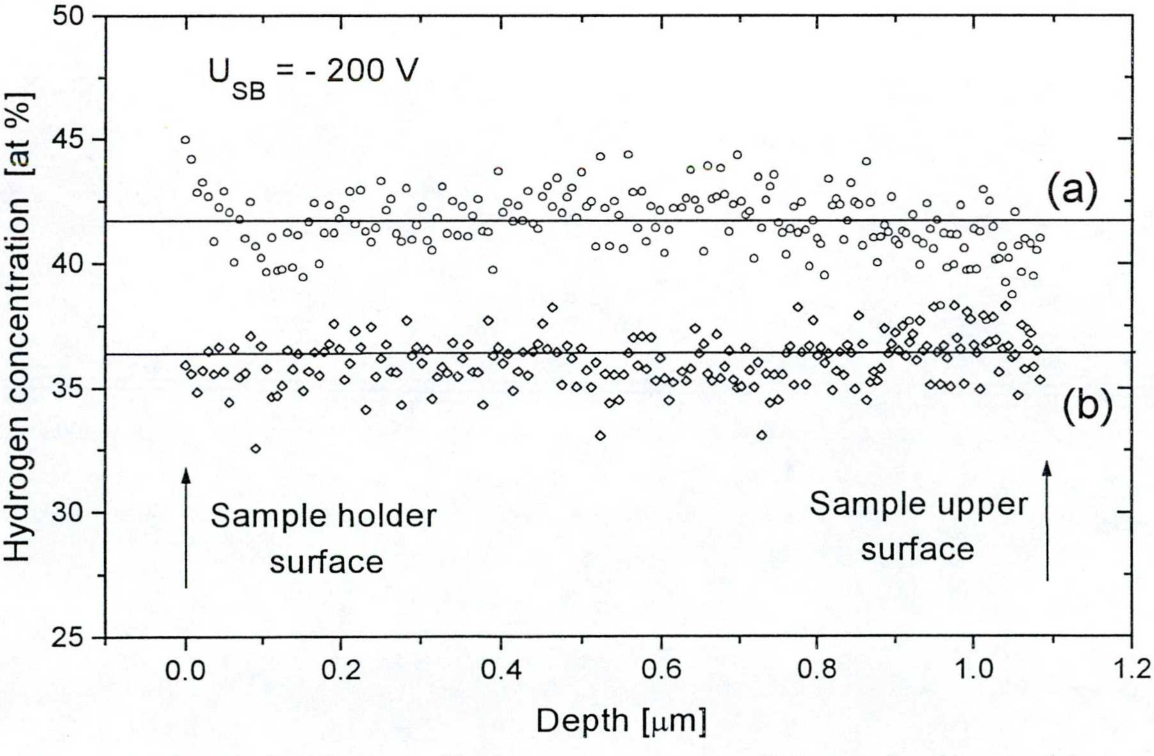

Fig. 4.3.1 Depth distribution of hydrogen content in a-C:H samples deposited at U_{SB} =-200 V from (a) methane and (b) benzene.

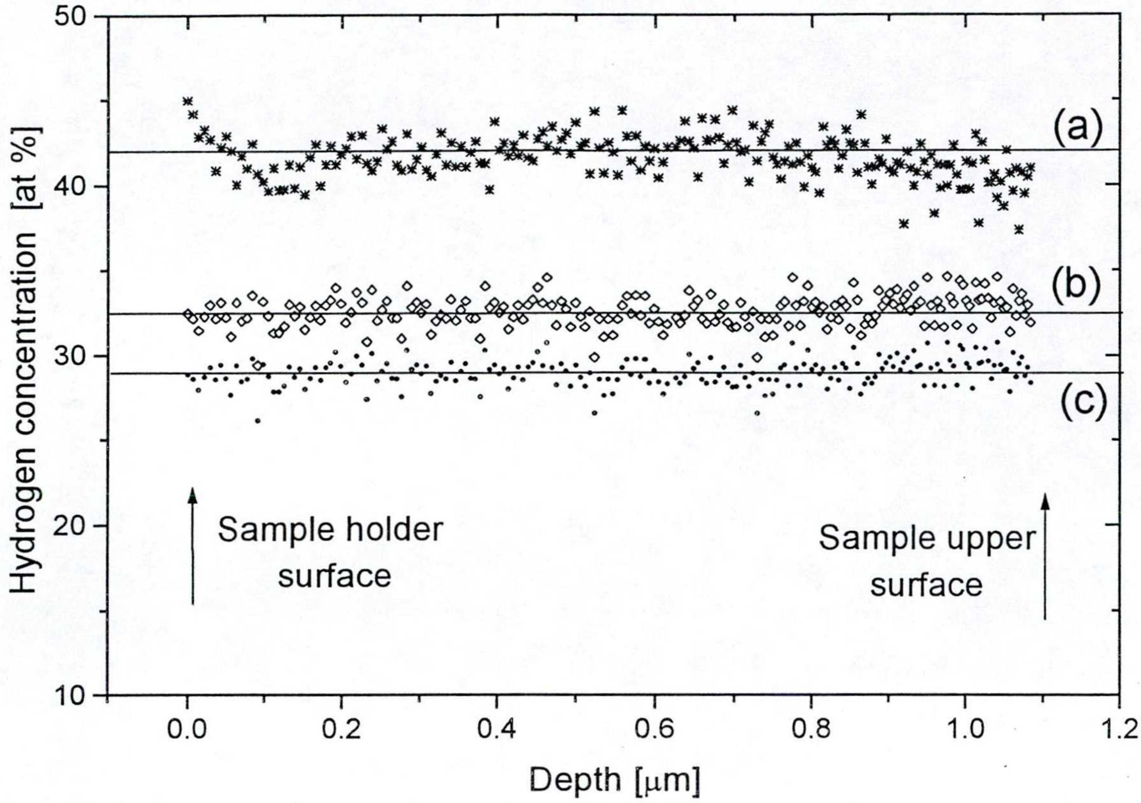

Fig. 4.3.2 Depth profile of hydrogen in a-C:H samples deposited by (a) U_{SB} =-200 V, (b) U_{SB} =-500 V, (c) U_{SB} =-1000 V.

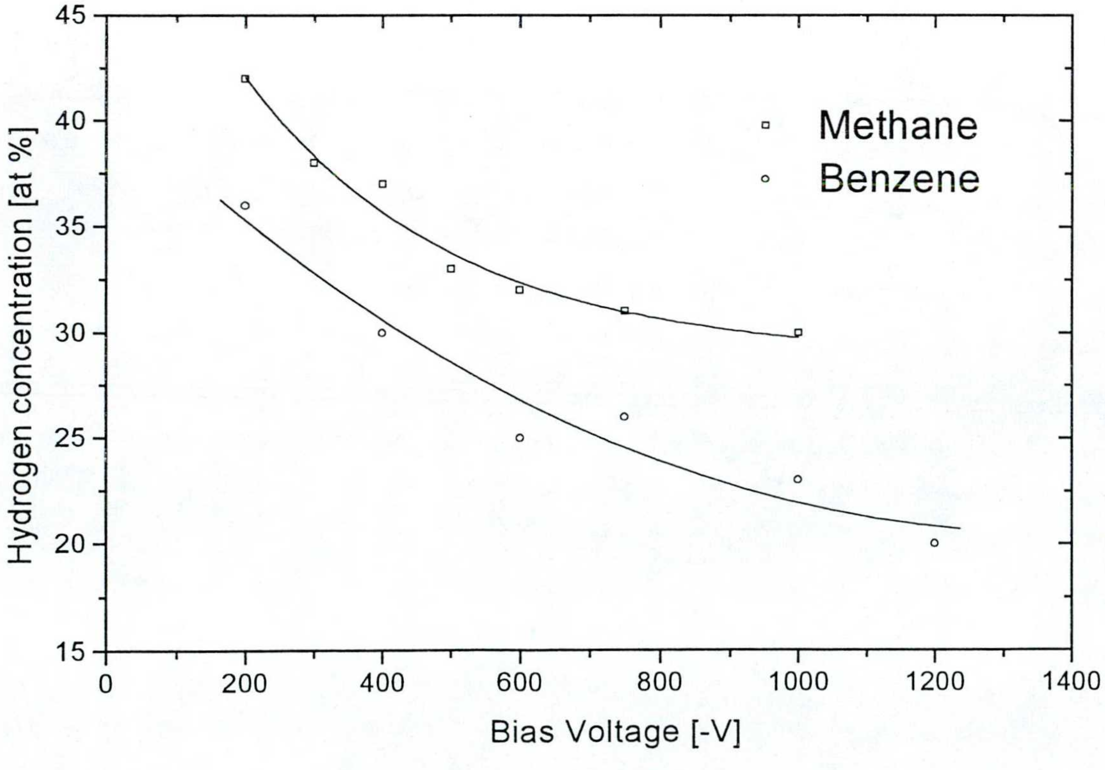

Fig. 4.3.3 Hydrogen concentration as a function of self bias voltage for different source gases (methane and benzene).

Raman spectra measured by visible light excitation was the simplest method to control a morphicity of samples. It is well known, that both crystalline and microcrystalline materials exhibit well defined Raman peaks. In contrast all scattering bands of amorphous materials are broad and in the most cases they have asymmetric shape with a large total width. Here we only show a typical Raman spectra of our a-C:H samples (Fig. 4.3.4), exact discussion of Raman properties is in section 5.2.

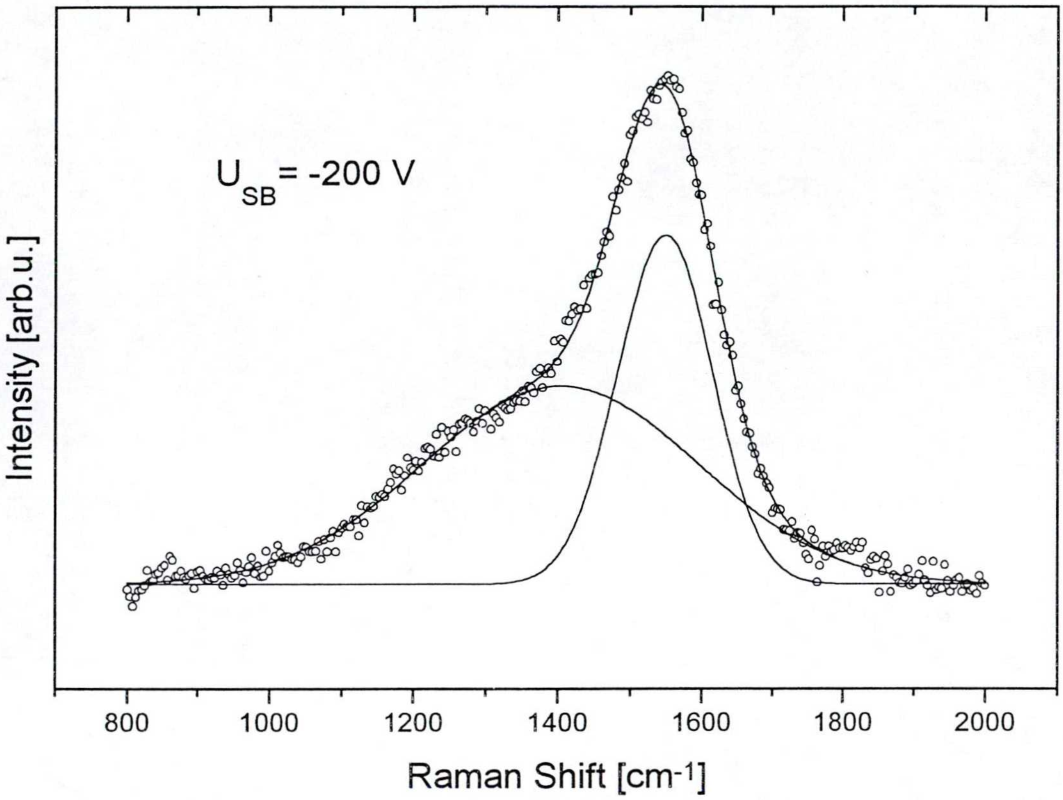

Fig. 4.3.4 Raman spectra excited by 2.09 eV photon energy for a-C:H sample deposited at -200 V self bias.

Direct current (dc) conductivity measured at room temperature turned to be sensitive method to check sample quality with respect to localised and quasi localised electronic density of states. In table 4.3.1 we have summarized deposition parameters (self biases, process

Table 4.3.1 preparation parameters, sample thicknesses and room temperature conductivity measured for several a-C:H samples.

Deposition Voltage (-V)	**Process pressure (mtorr)**	**Source gas**	**Thickness (μm)**	**Conductivity ($\Omega^{-1}cm^{-1}$)**
200	60	Methane	0.62	8.0×10^{-10}
300	60	Methane	0.65	2.21×10^{-8}
400	60	Methane	0.77	6.93×10^{-7}
500	60	Methane	1.219	2.50×10^{-4}
500	80	Methane	1.594	9.42×10^{-6}
500	100	Methane	1.325	1.62×10^{-2}
600	60	Methane	0.797	1.97×10^{-3}
700	60	Methane	0.80	1.93×10^{-2}

pressures and, source gas), sample thicknesses and room temperature conductivity (σ_{RT}) measured in several a-C:H samples. Reproducibility of σ_{RT} is in one order of magnitude, which is similar to and better than that published in literature [128].

Intermediate range ordering of sp^2 coordinated carbon atoms in samples deposited at $U_{SB} < -200$ V was tested by measuring room temperature luminescence intensity. Luminescence is sensitive for ordering due to weaker localization of π electrons in more ordered, larger clusters of sp^2 sites. By this method reproducibility of sample properties was found as good as ~30 %, what is considered a good value for an amorphous material.

5. BONDING PROPERTIES AND INTERMEDIATE RANGE ORDER

5.1. Carbon-carbon and carbon hydrogen bonding properties

Infrared (IR) absorption measurements is a very powerful method to study bonding properties of a-C:H samples. Due to different atomic weight and different bonding strength, the C–C and C–H stretching vibrations appear at different wavenumbers, however saturated olifinic and aromatic C–C bonding shows also characteristic vibration frequencies. The properties of this material are primarily determined by the relative occurrence of carbon-carbon and carbon-hydrogen sp^3 and sp^2 bonding configurations. The sp^2 structures are thought to be predominantly graphite-like, while diamond-like a-C:H contains mostly tetrahedrally coordinated (sp^3) carbon atoms. The hydrogen exists in a-C:H as CH_1, CH_2, and CH_3 bonds. The essence of this section is to study bonding configurations of a-C:H thin films and how the hydrogen content affect the threefold sp^2 and fourfold sp^3 coordinated carbon atoms when the self bias voltage changes from low to high.

IR transmission spectra of a series of a-C:H samples deposited by a plasma decomposition of methane under self bias voltage from -200 V to -700 V onto silicon wafers substrates were measured by using FTIR microscope. A typical spectrum measured in 500-5000 cm^{-1} wavenumber range on sample deposited at -700 V self bias is shown in Fig. 5.1.1. This spectrum is not corrected neither for background nor for interference fringes. Spectra of this form can not be used for determination of IR absorption bands. By polynomial fitting was removed the background and sinusoidal fitting correction was done for removing interference fringes. IR transmission curves obtained by this correction are shown in Fig. 5.1.2 for three different samples as an examples to show characteristic behaviour observed in the case of low, intermediate, and high self bias voltages.

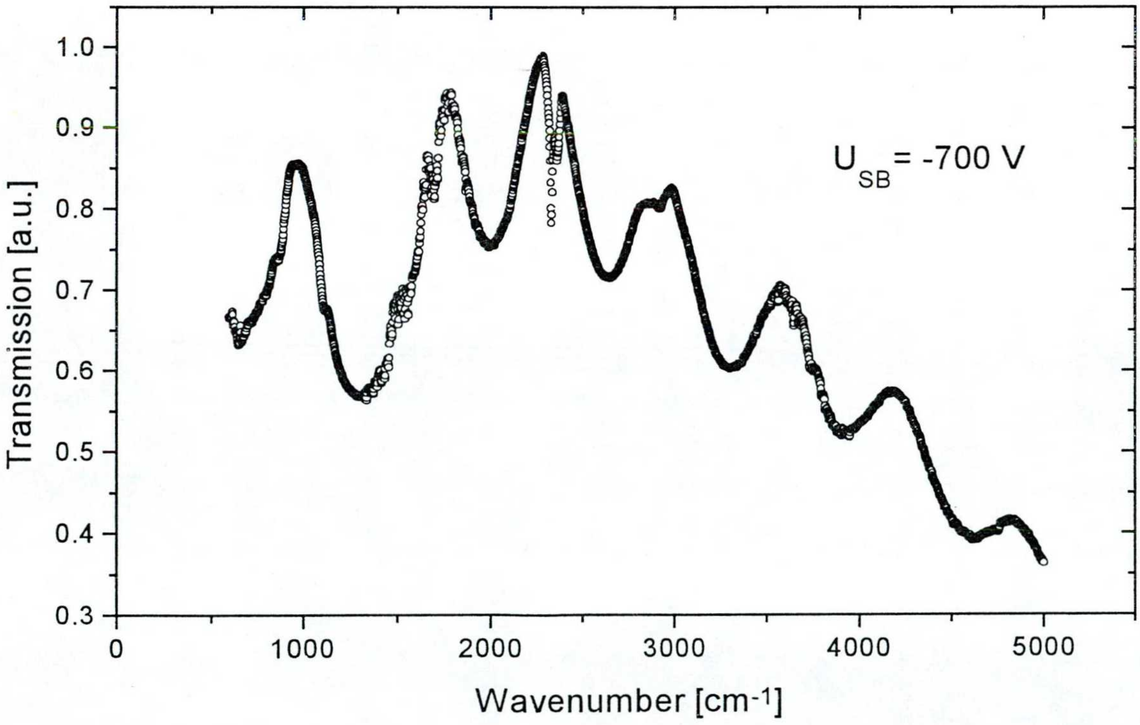

Fig. 5.1.1 Typical IR transmission curve modified by interference fringes for -700 V a-C:H sample. Transmission was not corrected for background.

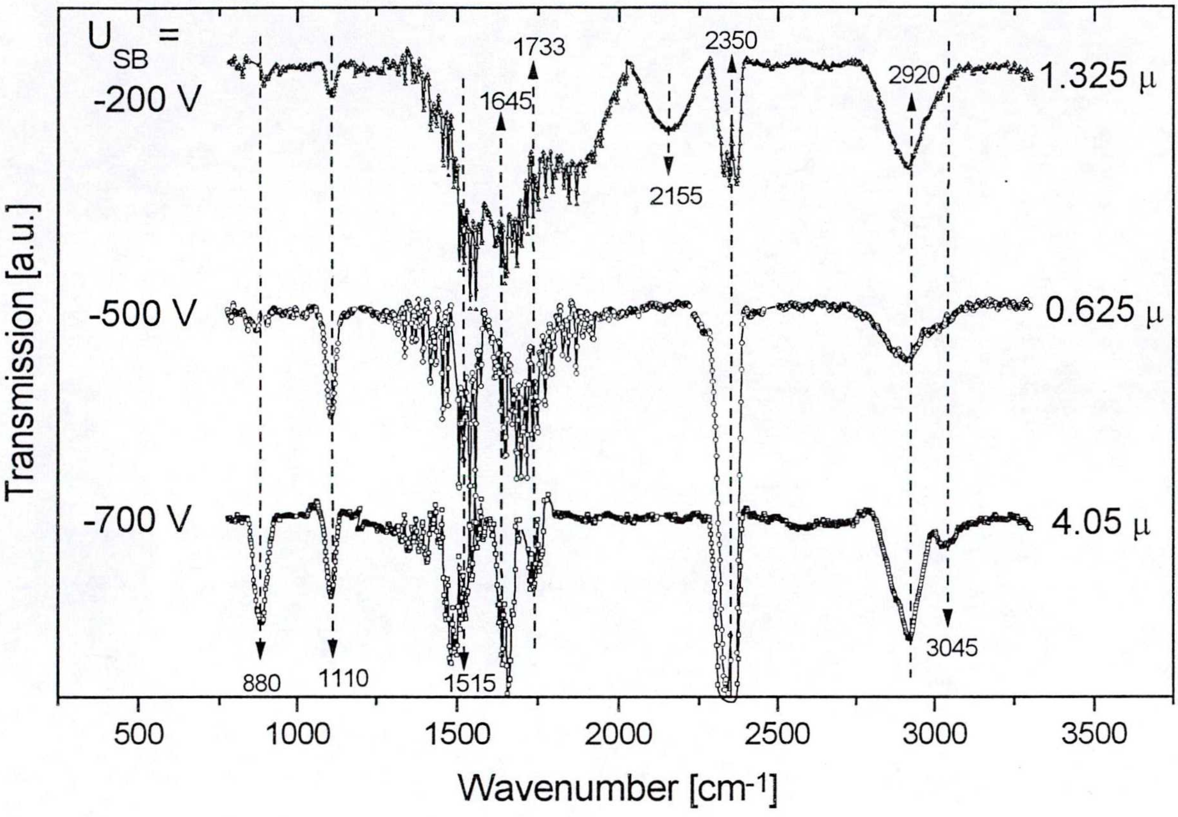

Fig. 5.1.2 IR spectra for different self bias a-C:H samples obtained by removing background and interference fringes.

The main band in the high frequency region, around 2900 cm^{-1} is due to the C–H stretching vibrations. Deconvolution of this band is shown later. There is an additional band observed in low self bias (-200 V) sample at which can be attributed to the existence of sp^1 C≡C (acetylene) stretching vibrations around 2155 cm^{-1}. This band totally absent from the spectra of -500 V and -700 V samples. The very sharp absorption peak around 2350 cm^{-1} was observed in all samples studied is related to vibrations of carbon dioxide (CO_2) which exists in atmosphere, that because measurements were performed in ambient atmosphere by a focused measuring beam. The absorption bands are below 2000 cm^{-1} related to C–H deformation vibrations and C–C IR active vibrational modes. Next we discuss those bands which are assigned unambiguously.

The decomposition of high frequency 2900 cm^{-1} band of samples prepared by U_{SB} = -200 V, -500 V, and -700 V shown in Figs. 5.1.3-5.1.5. Four Gaussian bands fit experimental results very well for every samples studied. Predicted frequencies [130,61] and assignments of the decomposed peaks are listed in Table. 5.1.1. The lowest wavenumber peak around 2850 cm^{-1} is sp^3 CH_2 symmetric stretching vibration, the integrated intensity of this band is much lower in sample of -700 V compared to the other two. The absorption band around 2920 cm^{-1} is assigned to sp^3 CH stretching mode was observed with the highest integrated intensity in sample -700 V. The third band studied around 2970 cm^{-1} is due to sp^3 CH_3 antisymmetric stretching vibrations, and shows similar intensity for -200 and -500 V samples, but for -700 V sample it has a very little value. The fourth peak with respect to -200 V sample lie near to 3000 cm^{-1} assigned to olefinic sp^2 CH mode but the other two samples have peak at around 3038 cm^{-1} which can be attributed to aromatic sp^2 CH stretching mode. This peak is well resolved in sample of -700 V, while it appears as a small shoulder on the broad CH stretching absorption band. The sp^1 C–H stretching vibration around 3300 cm^{-1} was not observed in our samples.

From the above decomposition it can be concluded that the higher self bias voltage samples prefer the aromatic sp^2 CH monohydride, while olefinic sp^2 CH is formed at low self

Table. 5.1.1 C–H stretch absorption bands, predicted [130,61] and observed for a-C:H samples prepared by different self biases..

Band	Configuration	Predicted frequency (cm^{-1})	Observed frequency (cm^{-1}) U$_{SB}$ (V)		
			-200	-500	-700
1	sp^{1}CH	3305			
2	sp^2 CH (arom.)	3050		3038	3037
3	sp^2 CH$_2$ (olef.)	3020			
4	sp^2 CH (olef.)	3000	3004		
5	sp^3 CH$_3$ (asym.)	2970	2953	2980	2963
6	sp^2 CH$_2$ (olef.)	2945			
7	sp^3 CH$_2$ (asym.)	2925			
8	sp^3 CH	2915	2914	2913	2916
9	sp^3 CH$_3$ (sym.)	2870			
10	sp^3 CH$_2$ (sym.)	2855	2858	2850	2855

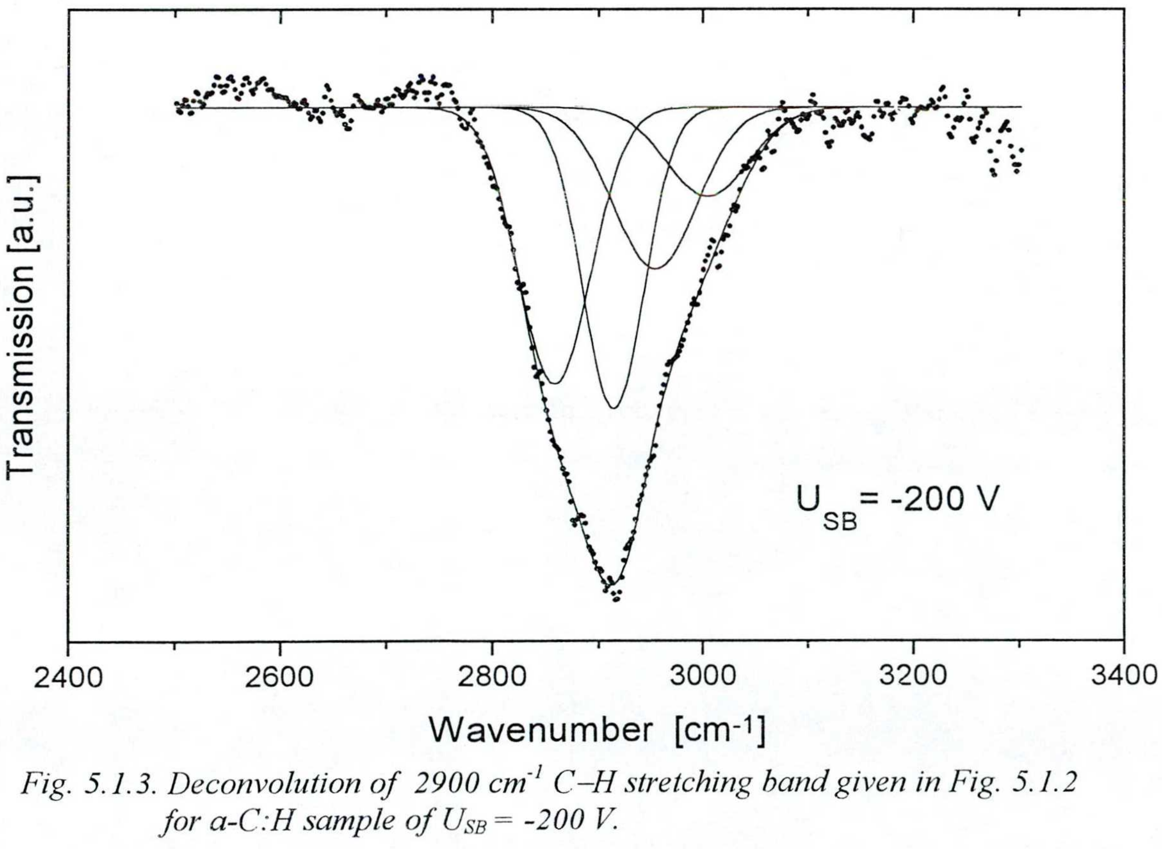

Fig. 5.1.3. Deconvolution of 2900 cm^{-1} C–H stretching band given in Fig. 5.1.2 for a-C:H sample of U$_{SB}$ = -200 V.

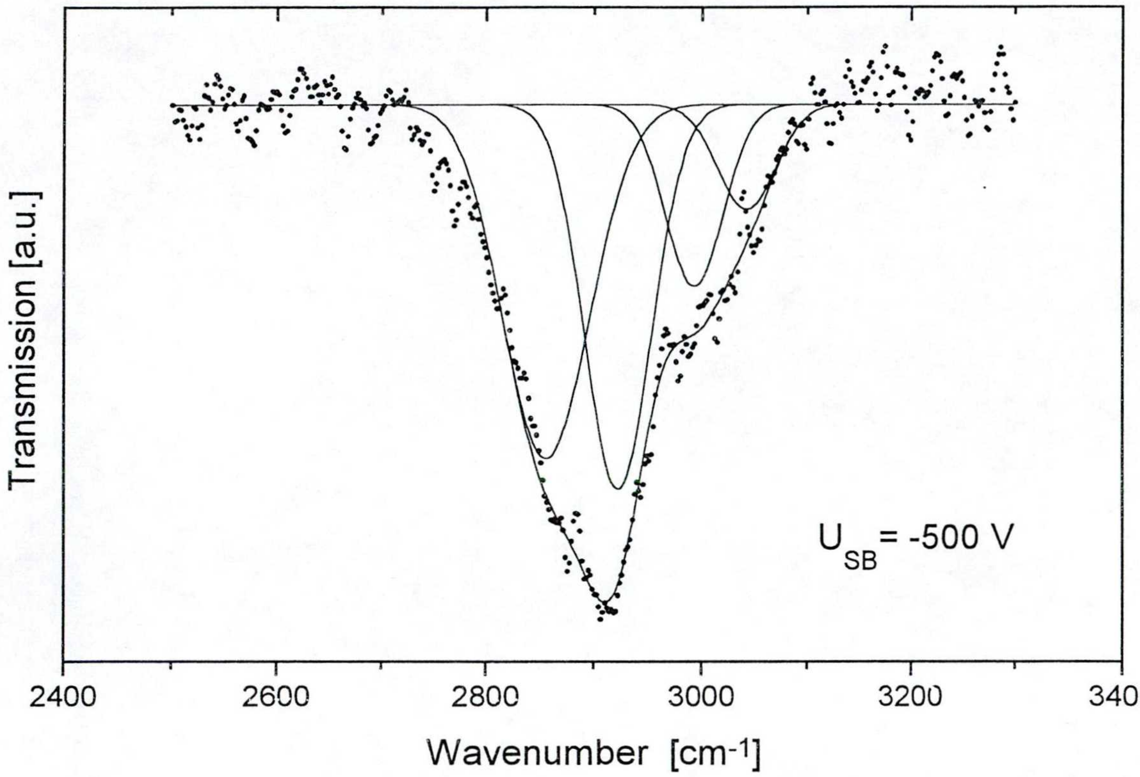

Fig. 5.1.4. Deconvolution of 2900 cm^{-1} C–H stretching band given in Fig. 5.1.2 for a-C:H sample of U_{SB} = -500 V.

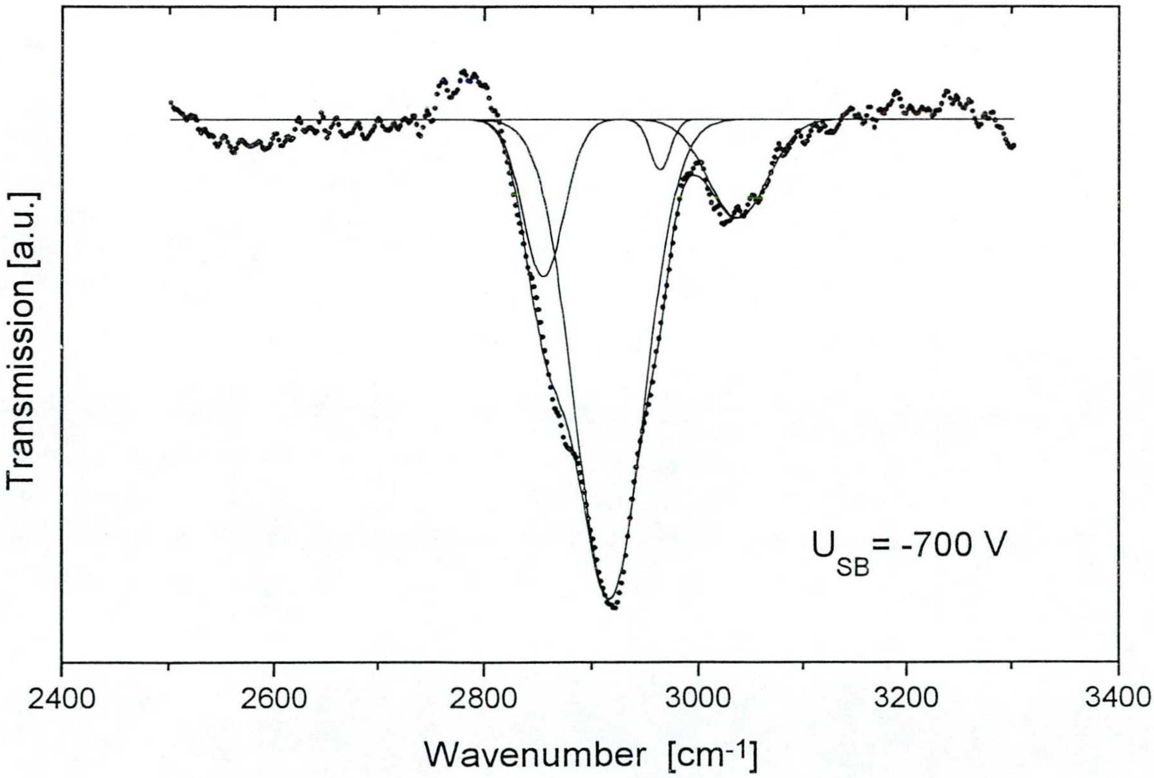

Fig. 5.1.5. Deconvolution of 2900 cm^{-1} C–H stretching band given in Fig. 5.1.2 for a-C:H sample of U_{SB} = -700 V.

bias voltages (-200 V). The sp^3 CH$_3$ antisymmetric mode absorption as well as the dihydride sp^3 CH$_2$ band intensity decreases by increasing self bias voltage, in accordance with decreasinghydrogen content. Integrated intensity of the -2900 cm^{-1} multiple band thicknesses decreases by increasing self bias voltage from -200 V up to -700 V as a result of decreasing hydrogen content. The intensity shown in Fig. 5.1.2 was normalized with respect to layer.

The low frequency region is divided in to three smaller regions that is 800-1000 cm^{-1}, 100-1200 cm^{-1} and 1200-2100 cm^{-1} wavenumber ranges. First we deal with 1200-2100 cm^{-1} region, where C–H deformation and C–C stretching absorption bands can be observed. Fig. 5.1.6 shows experimental results after removing background and interference fringes. In this region transmission curves are very noisy and a reasonable decomposition of bands can not be made. We put lines shown in the figure to point out the positions at which the active modes can be found. The line at 1450 cm^{-1} indicates the out-of phase sp^3 CH$_3$ deformation vibration. This band can be seen on spectra of -200 V sample and its intensity decreases by increasing self bias voltage until -700 V; where it disappears. The 1370 cm^{-1} sp^3 CH$_3$ can not be seen. The 1515 cm^{-1} line indicates the C–C mixed sp^2/sp^3 configurations, this band is clearly observed for all samples investigated.

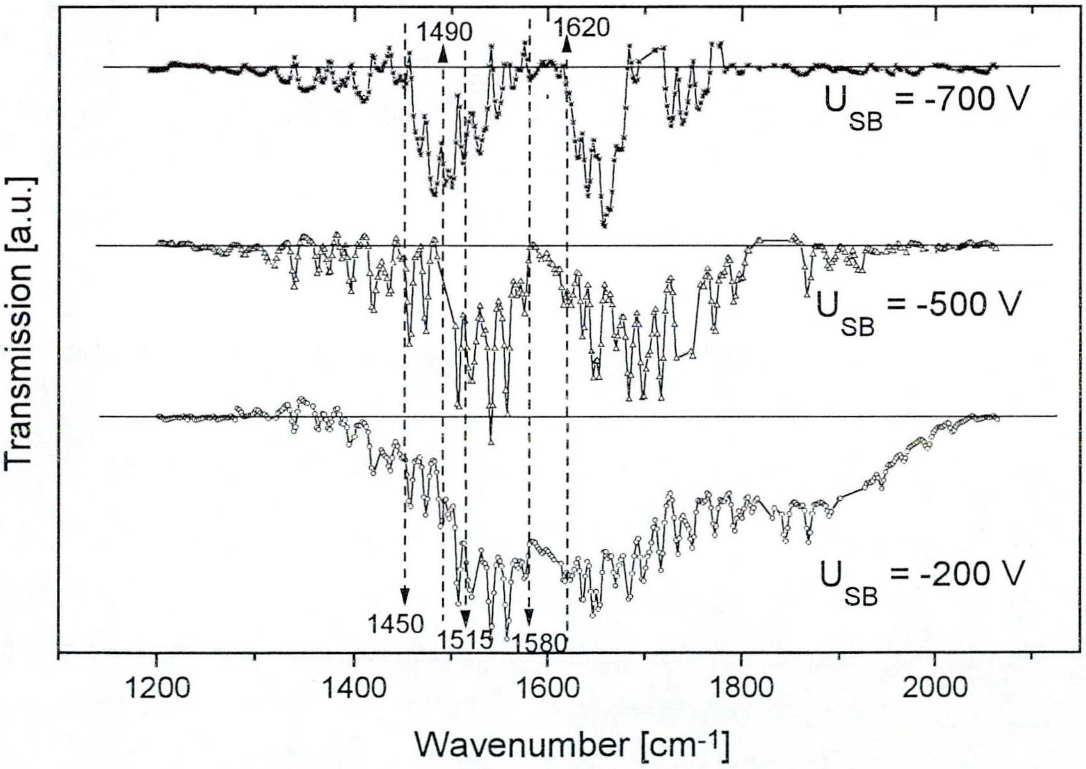

Fig. 5.1.6. Low frequency region of IR transmission spectra of a-C:H samples prepared under different self bias voltages.

Broad absorption region of 1620-1680 cm^{-1} may be due to the C=C sp^2 configurations [131] which can be seen in the three samples shown in Fig. 5.1.6. The line at 1620 cm^{-1} indicates absorption due to the C=C olefinic sp^2 configuration, in this region a considerable absorption can be observed only for the low self bias sample, but for higher self bias sample no absorption was found (see sample of -700 V). The C=C aromatic sp^2 configuration gives absorption around 1580 cm^{-1} however no appreciable absorption band can be observed for all samples studied. Absorption around 1700 cm^{-1} observed only for the low and intermediate self bias samples can be due to C=O vibration, the same configurations can be expected over 1800 cm^{-1} as clearly shown on the shoulder for the -200 V sample [131].

From the above interpretation of absorption region shown in Fig. 5.1.6 we can conclude that the sp^3 CH_3 groups and the olefinic sp^2 configurations are dominant at lower and intermediate self bias voltage samples, but in samples of -700 V bias the sp^3 CH_3 groups can not be detected and aromatic C=C vibration band around 1580 cm^{-1} was not unambiguously observed.

In the wavenumber range of 1000-1200 cm^{-1} shown in Fig. 5.1.7 is the location of the C–H deformation vibrations. There is an intensive band at 1110 cm^{-1} due to sp^2 CH_2 olefinic wagging mode. This mode is dominant for the higher self bias voltage samples (-500 V and -700 V samples) but for the lower self bias voltage (-200 V) sample it seems to be accompanied by other configuration probably due to sp^3 CH_3 degenerate deformation mode. However all of three bands exhibits some fine structure. For a more exact assignment of absorption bands in this region further experiments should be performed.

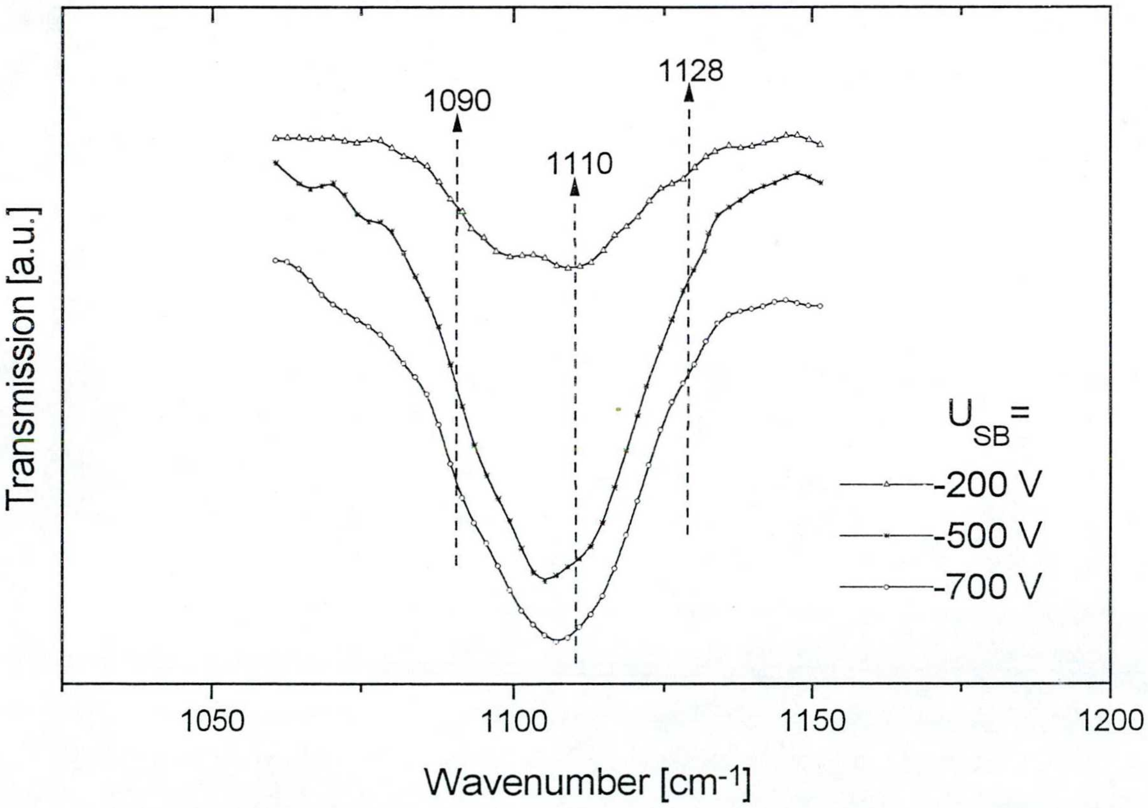

Fig. 5.1.7. Low frequency part of IR transmission spectra of a-C:H samples prepared under different self bias voltages.

Third region in the range of 800-1000 cm^{-1} shown in Fig. 5.1.8. In this region the sp^3 C–C vibrations are clearly observed around 880-895 cm^{-1} for -700 V sample as a wide band and a small shoulder at 910 cm^{-1} due to olefinic sp^2 CH_2 deformation twist mode. For -200 V sample there are two bands at 910 cm^{-1} and 870 cm^{-1} which can be due to the olefinic sp^2 CH_2 deformation twist mode and olefinic C–C sp^2 mode. The intermediate self bias voltage sample

(-500 V) has two bands in this region one of those at 840 cm^{-1} is due to olefinic sp^2 CH bending vibrations and around 910 cm^{-1} due to the olefinic sp^2 CH$_2$ deformation vibrations. An intensive band appearing around 870 cm^{-1} in both -700 V and -500 V self bias samples can be attributed to A$_{2u}$ IR active out-of-plane lattice mode observed in graphite.

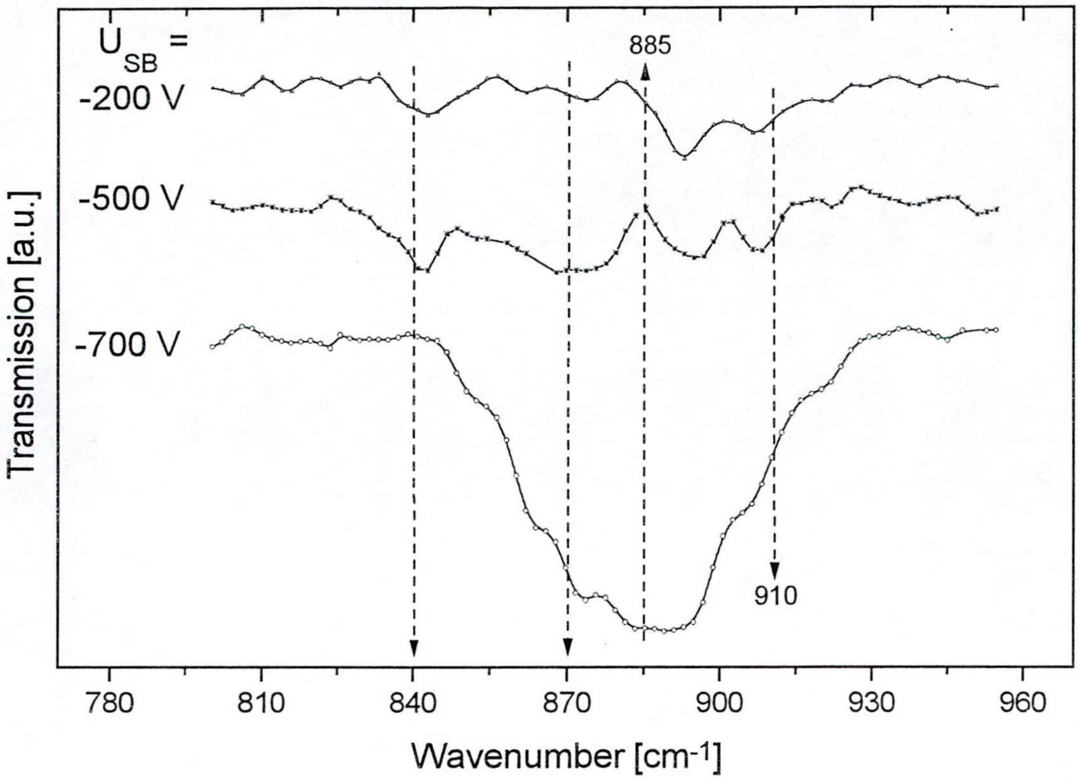

Fig. 5.1.8. Low frequency part of IR transmission spectra of a-C:H samples prepared under different self bias voltages.

From this region we can conclude that the higher self bias voltage sample (-700 V) has appreciable absorption in the region of C–C sp^3 hydrogen free mode, however a weaker band appears at olefinic sp^2 CH$_2$ twist region, but the sp^3 C–C vibration absorption practically absent in the other two samples at the same time appreciable absorption was observed in the olefinic sp^2 CH and CH$_2$ vibration regions.

Infrared spectra of a-C:H presented here are very complex and their main features were only discussed before. However some important consequences follows from the above discussion :

i) There are sp^2 and sp^3 hybridized carbon atoms in every samples being deposited either high or low self bias voltages. sp^1 hybridized carbon atoms were observed in sample of U_{SB} = -200 V.

ii) A considerably percent of sp^3 hybridized carbon atoms is bonded to hydrogen. As the hydrogen content of samples decreases by increasing self bias the sp^3 hybridized carbon atoms prefer bonding to other carbon atoms.

iii) Incorporated hydrogen is distributed between sp^2 and sp^3 coordinated carbon atoms.

iv) Intermediate range ordering of sp^2 coordinated carbon atoms can be realized by forming olefinic chains of different length in both low and high voltages samples.

v) Aromatic ring structure of sp^2 coordinated carbon atoms can be only formed at high voltages. However the E_{1u} in plane IR active mode of graphite at 1580 cm^{-1} was not observed any a-C:H sample except -700 V sample has a little absorption band, as in Fig. 5.1.6 it can be seen.

5.2. Ordering of sp^2 coordinated carbon atoms

Raman spectroscopy is a one of the excellent optical methods to investigate hydrogenated amorphous carbon (a-C:H). It is considered as a rich source of information about bonding configuration of the carbon atoms, and extensively used to study intermediate range ordering of sp^2 coordinated regions. In addition Raman scattering is sensitive to changes in translation symmetry or to structural disorder also. In section 3.1.4 we showed the Raman spectra of diamond, graphite and different amorphous carbon forms as well as annealing dependence of the Raman spectra. In this section we present results of our Raman measurements on a-C:H samples prepared in our laboratory and the analysis of these spectra as well as the comparison of our results to those of other groups, to find a correlation between the main Raman features and film structure, proposed earlier by different groups. The other goal of our study is to compare Raman spectra excited by IR and visible photons.

Raman spectra of a-C:H sample series deposited by plasma decomposition of methane at different self bias voltages between 0 and -1200 V were studied by using visible and infrared wavelength for excitation [132]. To avoid luminescence effect of silicon carbon interface because of the deeply penetrating IR photons, metallic substrates (Al, stainless steel, and Au covered silicon wafers) were used as substrate materials. Visible light excited Raman spectra were measured by frequency doubled Ti-Saphire laser, working at 445.3 nm wavelength and were detected through a SPEX 1404 double monochromator with a photon counting system. These measurements were performed in cooperation with Physical Institute of Technical University of Erlangen. IR Raman scattering was recorded with a Bio-Rad Digilab dedicated FT-Raman spectrometer working with Spectra Physics Topaz Nd:YVO_4 laser at 1060 nm wavelength. These measurements were done in cooperation with the Physical Chemistry Institute of the Joszef Attila University in Szeged. Both of the two experiments used back-scattering geometry and the film thicknesses were from few hundred nanometer up to several micron.

Raman spectra excited by 2.78 eV in the 800-2000 cm^{-1} range for a series of samples prepared under different self-bias voltages are shown in Fig. 5.2.1. The shape of these spectra similar to those published earlier [68] and its variation with self bias voltages is in excellent agreement with the results of Ramsteiner et. al. [68], Xu et al [65], Dillon et. al. [57], Tamor et al. [66,67]. The spectra are usually decomposed into two Gaussian components one of which is called G peak related to zone center LO phonon mode of graphite around 1580 cm^{-1} and the other is the disordered peak around 1350 cm^{-1} usually observed in microcrystalline graphite too. The actual positions and intensities of these peaks depends on the preparation conditions and excitation wavelength.

The intensity ratio of these two Raman bands is widely used for characterisation of nano-, or microstructure of amorphous carbon films taking into account an analogy to microcrystalline graphite [133,57]. There are some difficulties with the interpretation of I(D)/I(G) ratio, because in microcrystalline graphite I(D)/I(G) increases with decreasing crystallite sizes [58] at the same time in a-C:H samples this ratio increases with bias voltages [66,65]. The analogy suggests that graphite clusters are smaller in samples prepared at higher voltages than those ones prepared at low bias voltages, what is in strong contradiction with the structural picture, which is capable to explain optical gap and DC conduction [69]. To solve this problem it was suggested, that microcrystalline analogy is only appropriate for films containing large ordered graphitic clusters [66].

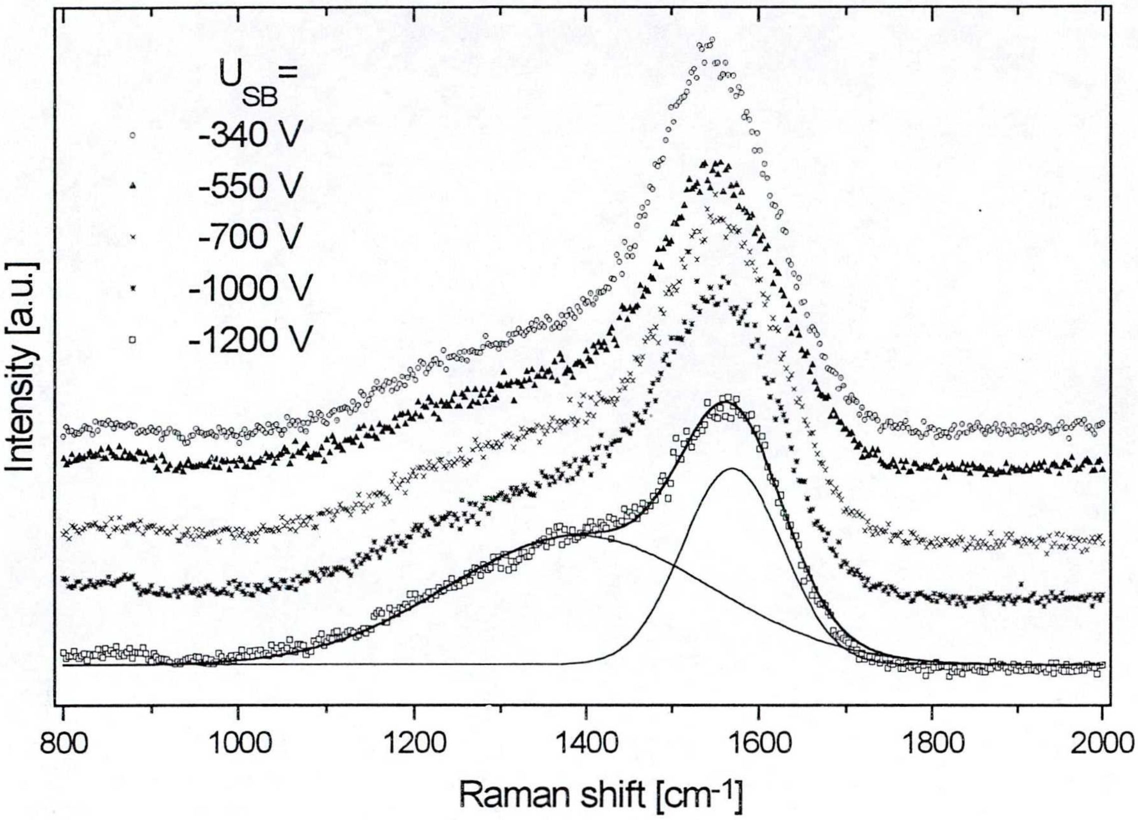

Fig. 5.2.1. Raman spectra excited by visible light of a-C:H sample series deposited by different bias voltages [132].

The main characteristics of Raman spectra excited by visible light were determined by fitting with two Gaussian. Table. 5.2.1 summarizes results of this fitting. The low U_{SB} samples has a G peak position at smaller wave numbers (~1550 cm^{-1}) comparing to that of graphite (1580 cm^{-1}). By increasing U_{SB} the G peak is narrowing and tend to higher wave numbers as it is shown in Fig. 5.2.1. The intensity ratio I_D/I_G increased by increasing U_{SB}, but this ratio not exceed one. The width of G line decreased and the width of D line increased by increasing U_{SB} which can be attributed to that intermediate range ordering more similar to graphite structure is forming by increasing self bias.

Table. 5.2.1 The D and G peak positions and the integrated intensity ratio (I_D/I_G) of two Raman bands of a-C:H samples deposited at different self bias voltages.

$\|U_{SB}\|$ (V)	Weight ($\mu g/mm^2$)	I_D/I_G	D Peak Pos.(cm^{-1})	D Peak Width (cm^{-1})	G peak Pos.(cm^{-1})	G peak Width (cm^{-1})
135	1.2	0.403	1336	222	1550	116
340	1.6	0.541	1344	258	1551	137
550	3.1	0.722	1360	290	1556	138
700	4.4	0.924	1366	295	1560	130
1000	7.4	0.953	1373	294	1559	130
1200	5.7	0.633	1383	296	1568	117

All samples were prepared by rf plasma decomposition of CH_4 at 60 mtorr process pressure and gas flow rate of 16 sccm/min unless -135 V sample which was prepared at 300 mtorr and 8.5 sccm/min.

Raman spectra measured in Fourier transform spectrometer by 1060 nm excitation are shown on Fig. 5.2.2 for a three samples -600 V, -700 V, and -800 V. considerable change in the whole wave number range can be seen comparing to the spectra measured by visible light. Scattered intensities at wave numbers of D peak was increased over that of G peak in every samples studied and new peaks or shoulders can be observed in that range. Raman spectra probed by visible photons (Fig. 5.2.1) are dominated by G peak, of which position and half width changes slightly with deposition voltages [132]. At the same time a good resolved G peak in Raman spectra excited by IR photons appears only for samples deposited at -700 V, but for -200 V sample almost no appreciable scattered intensity at the G peak position can be seen [134] (Fig. 5.2.3).

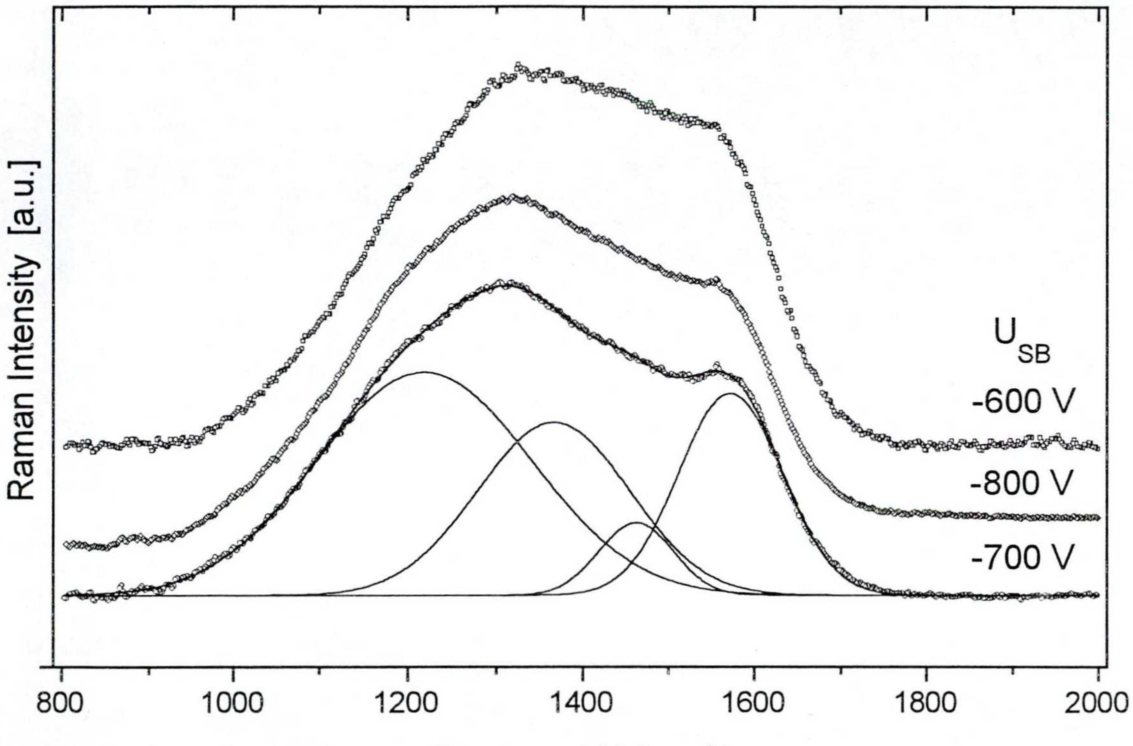

Fig. 5.2.2. Raman spectra excited by IR photons for a-C:H samples [132].

IR excitation much more sensitive for graphitic carbon formation than the visible one due to resonant excitation of the lowest energy $\pi-\pi^*$ electronic transitions. That means the strong difference between IR spectra of low U_{SB} (-200 V) and high U_{SB} (-700 V) samples as shown in Fig. 5.2.3 taken from Ref. [134] proving that, the higher self-bias voltage (-700 V) samples prefers graphite ordering whereas the low self-bias voltage (-200 V) samples has sp^2 coordinated carbon atoms in other (no graphitic) medium range ordering. Raman spectrum of -700 V sample was decomposed by using four Gaussains with locations at 1218, 1366, 1460 and 1571 cm^{-1}. The bands centered at 1366 cm^{-1} and 1571 cm^{-1} shown in Fig. 5.2.2 could easily be assigned to those observed in microcrystalline graphite when visible light excitation were used. The bands at 1218 and 1460 cm^{-1} was not observed earlier for a-C:H layers. By analogy to amorphous and crystalline silicon and from an evaluation of vibrational density of states [59] a wide band can be predicted around 1200 cm^{-1}, which is assigned to tetrahedrally bonded carbon scattering in the absence of long range order. The band at 1460 cm^{-1} does not correlate any peaks of phonon density of states of graphite, instead of this we have to consider some sort

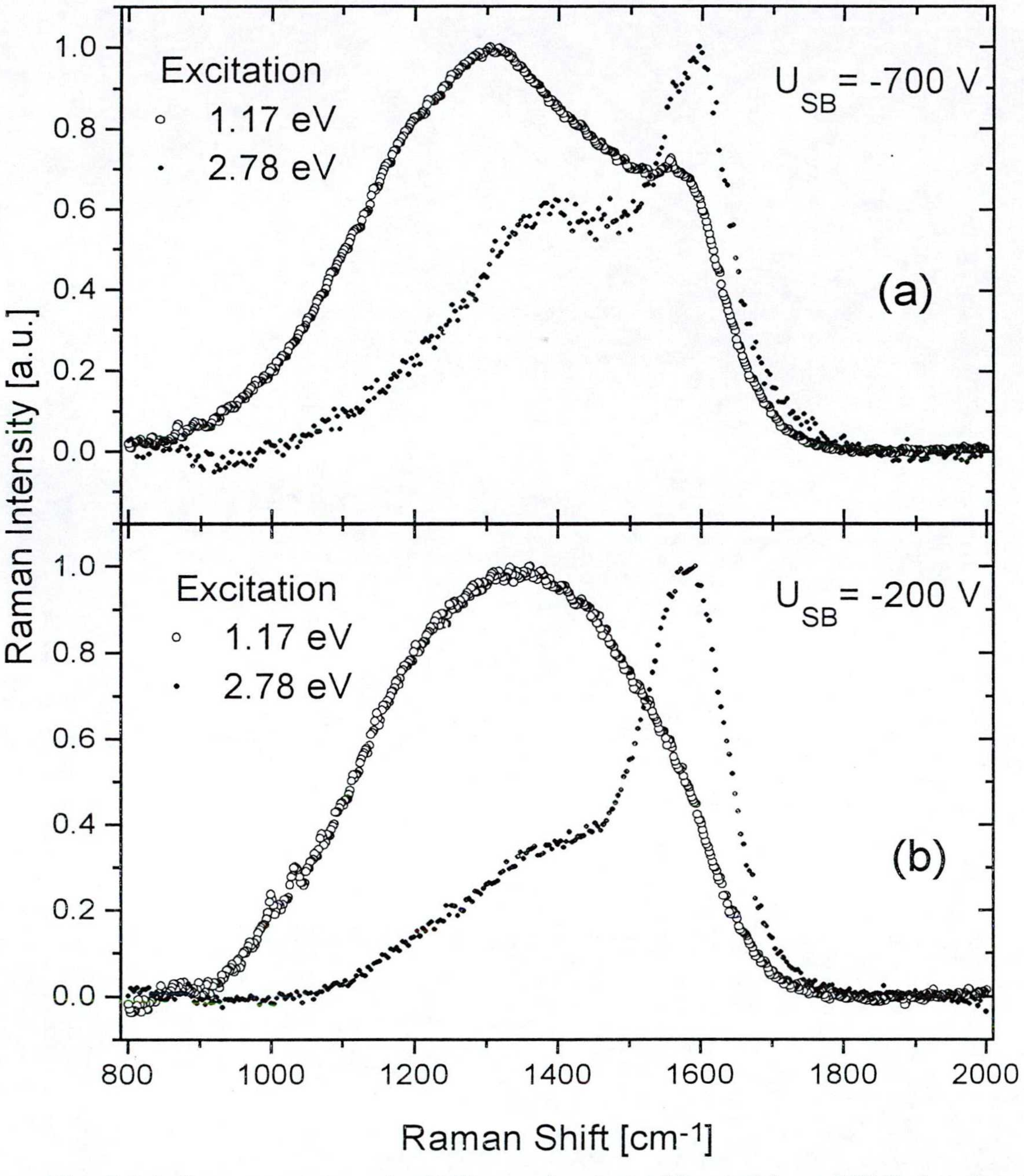

Fig. 5.2.3. Raman spectra of a-C:H samples excited by visible and IR light taken from Ref. [134]. (a) for sample U_{SB} =-700 V and (b) for sample of U_{SB} =-200 V.

of other local structure such as linear or branching chain with double bands (C=C) of carbon atoms. Similar behavior was observed in polyvinyl and polyacetylene, when excitation wavelength was changed. The band around 1460 cm^{-1} in Raman spectra of a-C:H layer can be assigned to conjugate double bond segments of different length. This explanation is in good agreement with the results of Pócsik et al [135] for microcrystalline graphite, where they proved, that the D band in Raman spectra of microcrystalline graphite can not be explained by a peak appearing in the phonon density of states rather that is related to local vibrations coupled to electronic transitions, which are resonantly excited by tuning excitation energy.

Fig. 5.2.4 shows Raman spectra of a-C:H samples prepared by U_{SB} = -200, -500, and -650 V but by using electrode geometry different from the earlier one. The grounded electrode was attached to a hollow copper tube to increase the areas of that electrode. As it is clear from Fig. 5.2.4, the main characteristics of Raman spectra did not change, i.e. the G and D peak are dominant and appear near to the same wavenumbers as before. A more appreciable change can be observed in the intensity ratio of the two peaks (I_D/I_G). Decomposition of Raman spectra by using two Gaussian bands give results listed in Table. 5.2.2.

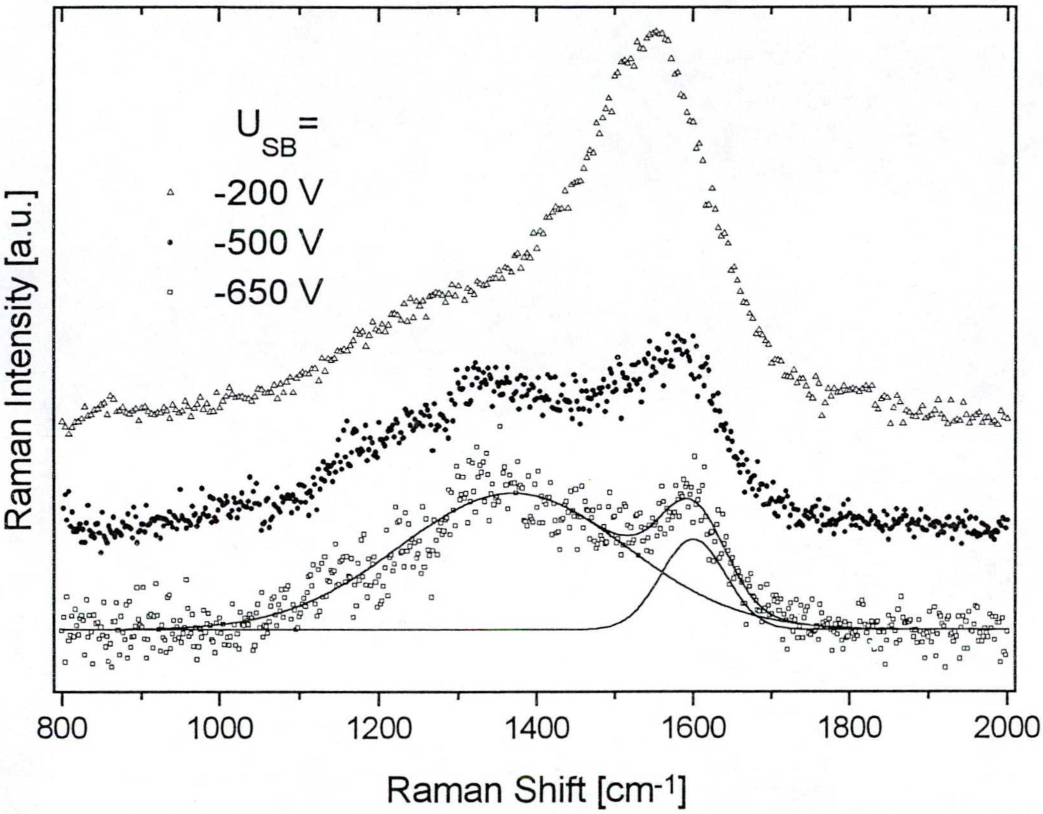

Fig. 5.2.4. Raman spectra for a-C:H samples excited by visible light of different self bias voltages.

Table. 5.2.2. Results of two Gaussian Decomposition of Raman bands in Fig. 5.2.4.

$\lvert U_{SB}\rvert$ (V)	Weight ($\mu g/mm^2$)	I_D/I_G	D Peak Pos.(cm^{-1})	D Peak Width (cm^{-1})	G peak Pos.(cm^{-1})	G peak Width (cm^{-1})
200	1.21	1.64	1403	383	1549	132
500	1.81	3.82	1365	330	1583	105
650	0.75	3.72	1324	245	1593	110

From comparison of data summarised in Figs. 5.2.1 and 5.2.4, we can conclude for the influence of special electrode geometry onto Raman spectra and indirectly onto structure of a-C:H layers. Although there are no samples deposited by same U_{SB} by using different electrode geometry however comparison may by informative between samples of self biases near to each other. D peak position and half width change significantly for samples of high as well as low self bias voltages. G peak is shifted to larger wavenumbers and its half width decreases for samples of high self biases. The latter change indicates, that the intermediate range ordering of

sp^2 coordinated carbon atoms has more graphitic character than in samples prepared by other electrode geometry.

General trend of both G and D peak positions and half width introduces a significant change of I_D/I_G ratio. Increasing D peak intensity indicates formation of larger clusters from sp^2 coordinated carbon atoms [66]. From G peak position and line width it seems to be acceptable, that sheets of fused aromatic ring structure are fovourised as the self bias increases.

Annealing experiments give further arguments for interpretation of Raman spectra or for their structural origin. Thermal treatment was performed by progressive stages (1,3, and 6 hours) at 620 K, which temperature is slightly lower than the hydrogen effusion temperature. Raman spectra excited by visible light are shown in Fig. 5.2.5 and Fig. 5.2.6 for samples of -200 V and -500 V self biases after different stages of annealing. These spectra show typical changes observed for both low and high self bias samples. A general trend is the developing of well defined G and D bands and Raman spectra is more similar to that of microcrystalline graphite after thermal annealing than before. Results of two Gaussian decomposition of Raman spectra measured after every annealing stages are summarised in Table. 5.2.3.

Table. 5.2.3. Decomposition results of annealed samples which listed in Table. 5.2.1

$\lvert U_{SB}\rvert$ (V)	Ann. Time (Hour)	I_D/I_G	D Peak Pos.(cm^{-1})	D Peak Width (cm^{-1})	G peak Pos. (cm^{-1})	G peak Width (cm^{-1})
200	0	1.64	1403	383	1549	132
200	1	2.35	1370	274	1574	86
200	3	2.06	1384	276	1577	88
200	6	1.99	1383	262	1582	82
500	0	3.82	1365	330	1583	105
500	1	3.4	1408	300	1607	83
500	3	3.34	1398	296	1585	83
500	6	2.71	1390	265	1595	76
500	0	3.72	1324	245	1593	110
650	1	2.8	1309	221	1577	141
650	3	4.48	1369	236	1597	81
650	6	6.15	1365	269	1603	74

The G peak position shifts from 1549 cm^{-1} to 1582 cm^{-1} for sample of U_{SB} = -200 V and in addition its half width decreases by ~50 cm^{-1} at the end of annealing process. These changes strongly suggest a transition in intermediate range ordering, formed by sp^2 coordinated carbon atoms, from olefinic chain structure to a more graphitic arrangement. Peak position as well as small half width indicates formation of small sheets of fused six fold rings similar to graphite of small crystallite sizes. Because no hydrogen effusion was observed at ~620 K from diamond like samples (U_{SB} = -200- -700 V) [39] therefore structural rearrangement takes place. A possible modification proved by IR measurements [39] is an increase of aromatic sp^2 CH groups at expense of olefinic sp^2 CH groups. It seems also to corroborate with changes observed in the disordered band properties after annealing. D peak position shifts to nearer to 1350 cm^{-1} detected in microcrystalline graphite and half width decreases continuously. G peak shows rather scattering than shift into either direction after annealing samples of U_{SB} = -500 and -650 V, but more pronounced change of half width can be observed.

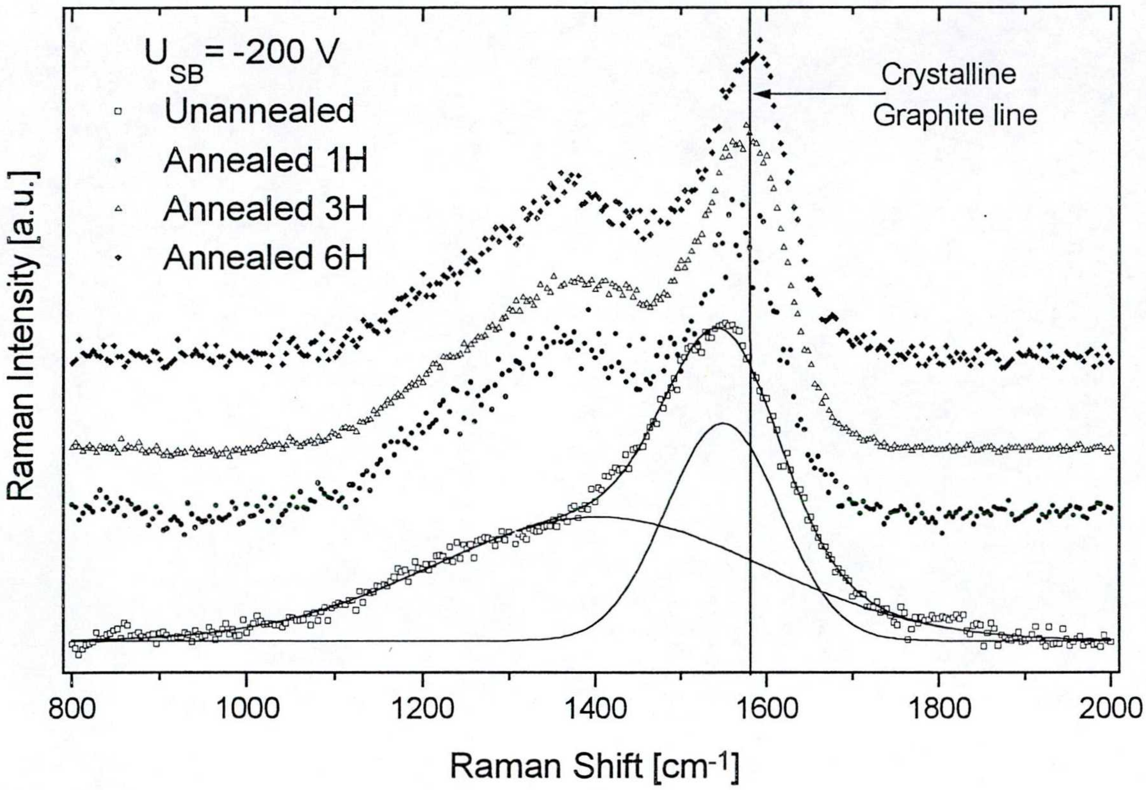

Fig. 5.2.5 The effect of annealing on Raman spectra of -200 V a-C:H sample.

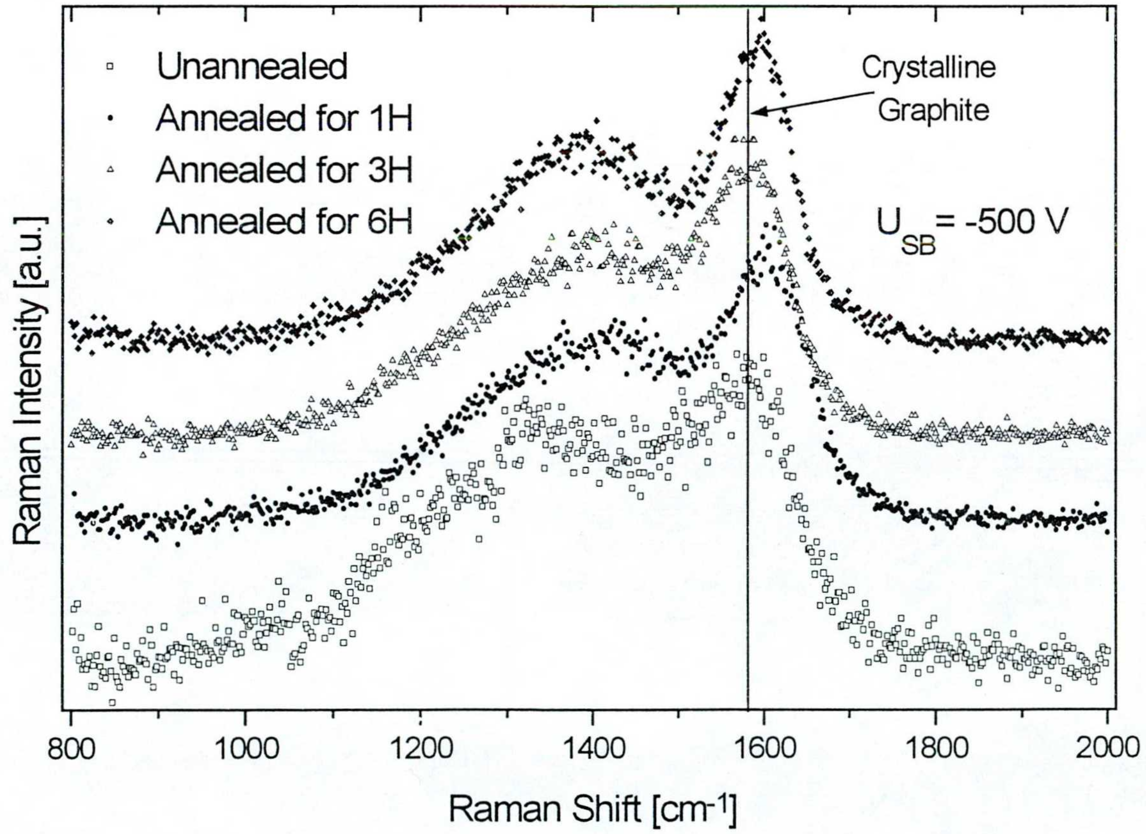

Fig. 5.2.6 The effect of annealing on Raman spectra of -500 V a-C:H sample.

Decrease of G peak half width indicates narrowing cluster size distribution. There is scattering in D peak position for samples of U_{SB} = -500 , -650 V, however half width of this band decreases also after annealing. Smaller hydrogen content and more extensive medium range ordering of high voltages samples compared to low voltages ones may explain a different behavior of the former samples under annealing. However we should emphasize that the whole spectra of high voltages samples more similar to spectrum of microcrystalline graphite after annealing than before. The ratio of D and G peak integrated intensity decreases after annealing what indicates increasing intermediate range ordering, if we suppose that microcrystalline graphite picture [58] is applicable in our case.

Exception of -650 V sample is related to a more noisy Raman spectra measured after annealing what we have extracted from Raman measurements:

i) There are sp^2 and sp^3 coordinated carbon atoms in a-C:H samples.

ii) Intermediate range ordering of sp^2 coordinated carbon atoms depends on deposition voltages.

iii) Graphitic clusters of different sizes can be formed in high voltages ($|U_{SB}| > 600$ V) samples which clusters are the dominant way of intermediate range ordering, but formation of olefinic chains of different lengths can be expected in samples of low self bias ($|U_{SB}| < 500$ V) being main form of intermediate range ordering.

iv) From decomposition of D peak in Raman spectra excited by IR photons we show that small amount of sp^2 carbons may olefinic chains in high voltages samples too, and the sp^3 hybridization carbons with no hydrogen bonds give Raman peak around 1200 cm^{-1} in every samples studied.

v) The properties summarised before are in good agreement with our IR measurements.

vi) Thermal annealing performed at moderate temperature results in more graphitic intermediate range ordering of low voltages samples and in general increases cluster sizes in treated samples.

5.3. Proton relaxation and its temperature dependence

Despite nuclear magnetic resonance (NMR) being a very powerful method for investigating condensed matter, its possibilities have not been fully used in the case of a-C:H investigations, probably because of the relatively large amount of material needed for an NMR sample. This section deals with the first results of proton NMR investigations of systematic sample series prepared from benzene in our own laboratories.

The samples were deposited by rf glow discharge from benzene under a number of different self-bias conditions. In a view the relatively large amount of sample needed for NMR measurements benzene was selected because of its vigorous deposition rate. The preparation conditions were limited to the more productive ones. The samples were prepared under 80 mtorr pressure; the self-bias voltages (U_{SB}) were -200, -400, -500 and -600 V; for the sake of easy removal, a copper plate was used for deposition.

Proton (^{1}H) NMR spin-lattice relaxation times (T_1) were measured by a Bruker SXP spectrometer at 90 MHz frequency by the inversion recovery pulse sequence [136]. The temperature of the samples was regulated in the 77-300 K temperature range.

The T_1 relaxation processes show a two-exponential behaviour, similarly to the results of Jäger et al. [137], who attributed the short lifetime components to the CH groups with sp^2 and sp^3 electron configuration, and the long lifetime component to the CH_2 units, with sp^3 configuration. This sort of complex behaviour is expected from the large compositional and structural variability of these materials. Two-exponential fitting gives acceptable results in all cases throughout the whole temperature range. The temperature dependence of the longer and shorter time constants can be seen in Figs. 5.3.1 and 5.3.2, respectively.

The longer relaxation time has a monotonic increase with decreasing temperature. The temperature dependence shows Arrhenius-type temperature dependence, the best fitting straight lines are displayed in Fig. 5.3.1. The slope of this fitted straight line together with the activation energy (E_a) values are listed in Table. 5.3.1. The self-bias voltage dependence suggests non-monotonic behaviour, having minimal T_1^{long} values in the sample prepared by -500 V. Activation energy values, calculated from the temperature dependence of the T_1 relaxation time components. The shorter relaxation time components show a practically temperature independent relaxation process in the -200V sample, and a slight temperature dependence in the other samples (see Fig. 5.3.2); the activation energies are listed in Table. 5.3.1.

Table. 5.3.1 Activation energy values, calculated from the T_1 relaxation time components.

U_{SB} (V)	E_a (meV) of T_1^{long}	E_a (meV) of T_1^{short}
-200	17.6±1.5	0.34±0.30
-400	10.8±0.7	1.30±0.24
-500	11.4±0.5	1.59±0.51
-600	12.7±1.2	1.39±0.51

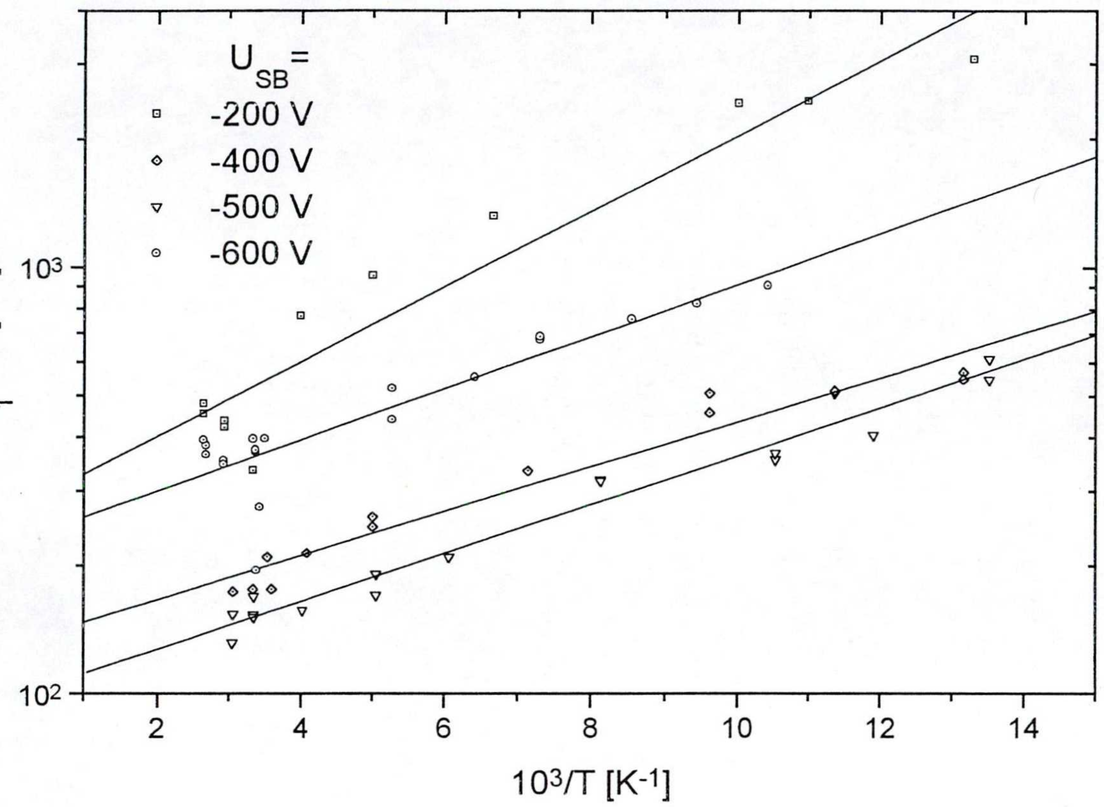

Fig. 5.3.1 Temperature dependence of the longer relaxation time T_1^{long} *component measured in a-C:H samples, deposited at different self-bias voltages.*

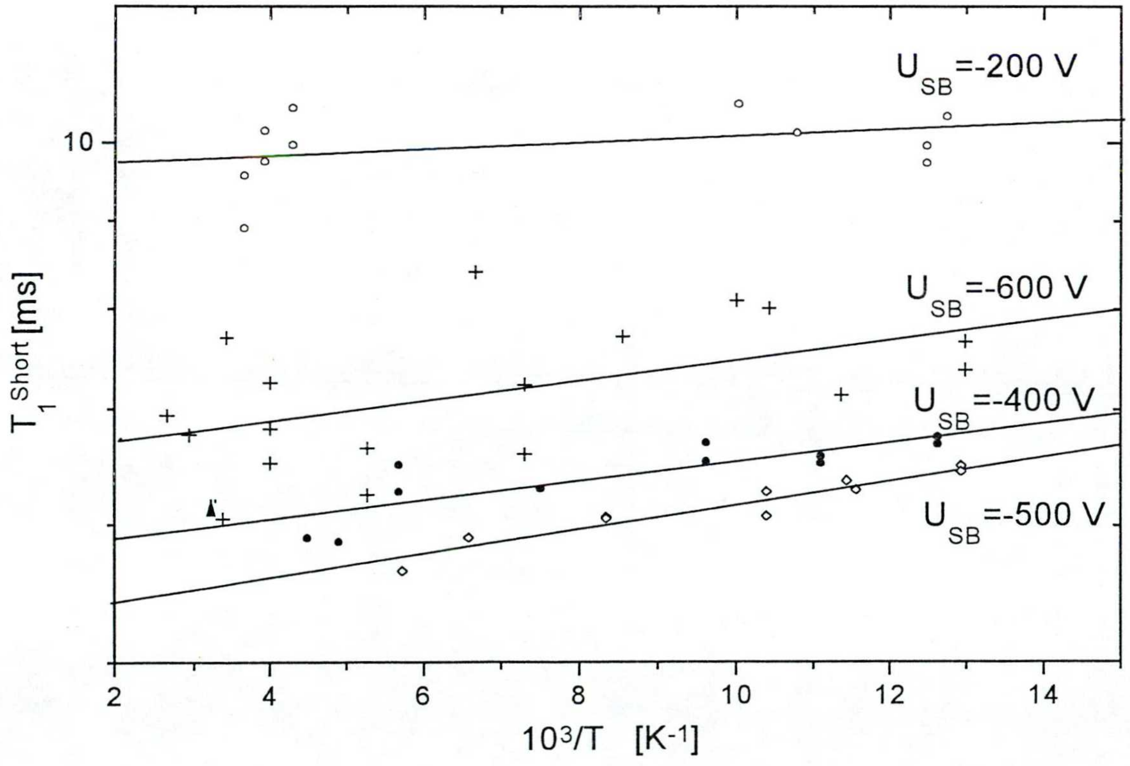

Fig. 5.3.2 Temperature dependence of the shorter relaxation time component, $T_1^{short.}$.

The relative weights of the different relaxing components as a function of temperature can be seen in Fig. 5.3.3. That was found to be practically temperature independent down to 77 K in every sample studied. At the same time the relative weight of the long life-time component varies non-monotonically with the self-bias voltage (U_{SB}).

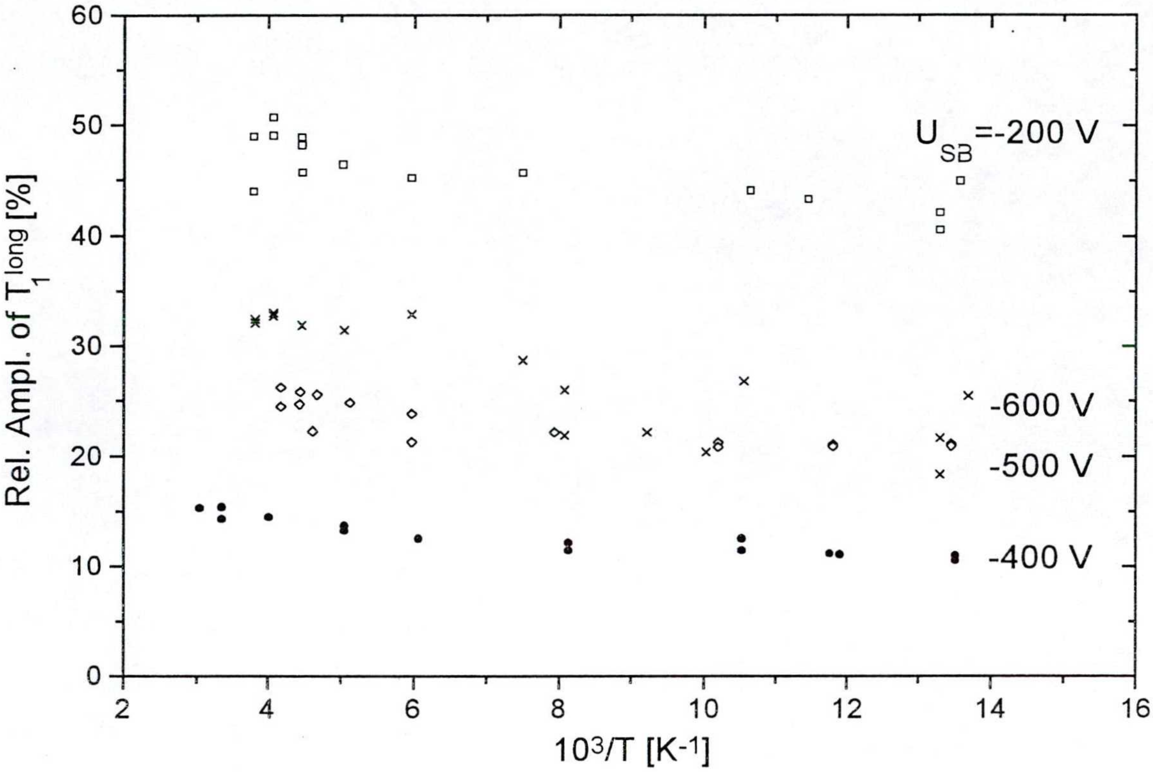

Fig. 5.3.3 Relative weight of the slowly relaxing component in the T_1 relaxation process.

It is known that absolute hydrogen content and the C and H bonding properties vary in a wide range, depending on deposition conditions [22]. Samples studied in these experiments have a hydrogen content decreasing from 44 at.% in the sample prepared by -200 V to 37 at.% in the sample prepared by -600 V U_{SB} [138]. Our experiments show sensitive variation of ^1H NMR relaxation properties with the structure and bonding characteristics of the sample. First we deal with the relative weight of the two distinct relaxing components and its temperature dependence.

The temperature independent relative weight of the two independent sub-systems, (Fig. 5.3.3) having the shorter and the longer relaxation time can be expected when these two relaxation time components are connected with regions of different electron configurations, and the transformation between the two regions cannot be realized at or below room temperature. However, there is an NMR phenomenon, viz. cross-relaxation [136], which could make a coupling between the magnetization of the two sub-systems. Such an effect could be observed when the differences between the relaxation times of the two components differ strongly, like at the low temperature end in our case. Around 80 K the ratio between the two relaxation times is around 300, and there is still no sign of cross relaxation (saturation of the increase of the longer life-time). This gives an upper limit of this cross relaxation, which should have an even longer time constant which, in turn, would relax the slower sub-system by the means of the help of the quicker one.

The relative weight of the short life-time component shows an unexpectedly big change in self-bias voltage dependence. The relaxation time measurement in such a case records the whole magnetization of the two different life-time components. Because this nuclear magnetization is a simple sum of the proton magnetization, this is equivalent with the number of protons in the different components. The sample prepared by -200 V self-bias has a nearly equivalent amount of hydrogen in the short and the long relaxation time components. Roughly 15% of the hydrogen in the sample prepared by -400 V belongs to the slowly relaxing component only and this ratio increases to 50% in the case of U_{SB} = -200 V. This change is greater than the change in the total hydrogen content. The decrease of U_{SB} below -400 V results in the increase of this ratio again, even the hydrogen content of these samples decreases further on.

Apart from the share of the two components, the absolute value and the temperature dependence of the relaxation times cannot be easily explained. In organic crystals the strongest relaxation is usually caused by the end group rotations and configuration changes in aliphatic chains. We know from Jäger et al. [137] that the CH_2 chains are the slowly relaxing components here. The chain motion takes place in a rough amorphous neighborhood, with strong differences from site to site. However the activation energy of this relaxation is unusually small. Our data for each of the samples studied show a roughly one order of magnitude smaller activation energy for these H_2 groups than that usually found in organic crystals.

This longer relaxation time component increases monotonically in cooling from room temperature (Fig. 5.3.1). The well known minimum of the end group rotation dominated relaxation process was not found in our experimental temperature range. It seems that if such a minimum exists in these samples, it should be above room temperature. This sort of minimum was detected in a-C:H prepared from methane [138]. However the strongly different H/C ratio in benzene and methane might cause structural differences between the samples prepared from these two source-materials.

The other interesting result was the very small value (5-10 ms) of the shorter relaxation time. In comparison with the longer relaxation time, it depends much less on U_{SB}, and their temperature dependence is also very weak, when it depends on temperature at all.

These fast relaxing regions cannot be aromatic ones. The local proton density in this region is much smaller than in the aliphatic regions. The relaxation strength is connected with the strength of the interactions between the protons, but because of their much smaller density, this should be much smaller, and longer relaxation time values should be expected, just the opposite of the measured data.

Our results for the relative weight of the slowly relaxing component (Fig. 5.3.3) are in agreement with the idea that the fast relaxation process can be attributed to the sp^2 configured olefinic CH groups, whose amount increases with increasing U_{SB}; although over 400V sp^2 carbons may prefer aromatic bonding configurations.

The other barely explainable result is the temperature dependence of this relaxation. The activation energy in this case is the activation energy of the motion that generates the fluctuations with the frequency needed to relax the high energy state of the spin. This motion, which generates a such an effective relaxation process in a temperature independent manner, is unknown in the present NMR literature.

This relaxation process shows some similarities with the low activation energy motion in glasses, which was discovered in neutron scattering by Frick and Richter [139]. Just recently a new NMR technique was developed to study slow motions, based on the unexpectedly large electric field gradients appearing in disordered systems in the nm range [140,142]. Motion in such a field is able to generate the temperature independent fluctuations, which are able to generate the relaxation processes we have observed. The intensive electron spin resonance (ESR) signal is well known in a-C:H, with increasing unpaired spin density by increasing self-biasing [116], so the presence of unpaired spins should be taken into consideration. The results of these different measuring methods should be studied in detail.

Finally we can conclude that hydrogenated amorphous carbon samples were deposited from rf glow-discharge plasma of benzene, under different self-bias conditions. Two-exponential spin-lattice relaxation processes were recorded on all samples in the whole temperature range. The share of the protons in the two relaxational sub-systems was found to be temperature independent, but varied strongly on deposition conditions. The activation energy of the longer relaxation time component was found to be much smaller than the usual values in organic crystals. The mechanism of the faster relaxation is not yet known. Its unusually small, nearly zero E_a has few parallels in the literature.

6. ELECTRICAL TRANSPORT

Density of electron states both at the band edges and deep within the gap can be probed by different methods among these by optical and electrical measurements. In this section we report on direct current (dc) conduction measurements performed on a-C:H samples deposited at different self biases and the next chapter is devoted to results of optical study. Our electrical investigations was motivated by the question how the electrical conduction takes place in tails of localized π states and near to band edges. For this reason the density and distribution of π states in a-C:H samples have been modified by choosing different deposition parameters and temperature increae rates, above room temperature. The dc electrical properties dependence on thermal treatment of samples have also been investigated for understanding real conduction between localised gap states. Our results concerning electrical conduction have been compared with variable range hopping, multiphonon tunneling and simple thermally activated conduction mechanism.

6.1. Experimental method

The a-C:H samples used in our experiment were prepared by decomposition of methane in a rf glow discharge system. Details of the preparing procedure are given in chapter 4. Table. 6.1.1 summarizes deposition parameters and thicknesses of samples used in electrical measurements. The sample thickness was evaluated by gravimetric method using the different densities [43] corresponding to each U_{SB}. The sample thicknesses in our electrical measurements were comparable to each other because the conductivity exhibits thickness dependence what will be discussed later. The error in microbalance weighting was ± 0.5 μg and in measuring the coated area was ±1% cm^2.

Electrical measurements were performed on gap type electrode arrangement, with other words planar geometry was used. This type of electrodes arrangement is commonly used in study of amorphous semiconductors and insulators. However, we have checked electrical conductivity and its temperature dependence in sandwich type electrode arrangement as well, i.e. in transverse geometry. Samples of gap type arrangement were deposited onto Corning 7059 glass substrate, electrical conductivity of which at room temperature was smaller by more than 3 orders of magnitude than a-C:H sample of the smallest conductivity. Electrodes were evaporated Au strips of 10 mm length and 2 mm wide with spacing of 0.1-1 mm from which other. Electrical currents scaled

Table. 6.1.1 Deposition parameters and thicknesses of a-C:H samples studied in electrical measurements; p-plasma pressure, v-gas flowing rate, U_{SB}-substrate self bias, and d-thickness.

$\lvert U_{SB}\rvert$ (V)	P (Pa)	ν (sccm/min.)	d (μm)
200	8	16	0.516
300	8	16	0.650
400	8	16	1.000
500	8	16	1.219
600	8	16	0.797
700	8	16	0.800

with gap widths very well, as it is clear from Fig. 6.1.1, so any corrections due to leakage current need not taken into account. Therefore measurements were performed mostly with 400 μm gap width. Sandwich type samples were deposited either onto silicon wafer covered by evaporated Au or onto indium tin oxide (ITO) covered glass substarte as lower electrode and evaporated Au of 1-3 mm diameter was used as top electrode. Contact wires were fixed by silver paste and thermal treatment of samples at ~420 K for 30 minutes in vacuum. Contact properties will be discussed in the next section.

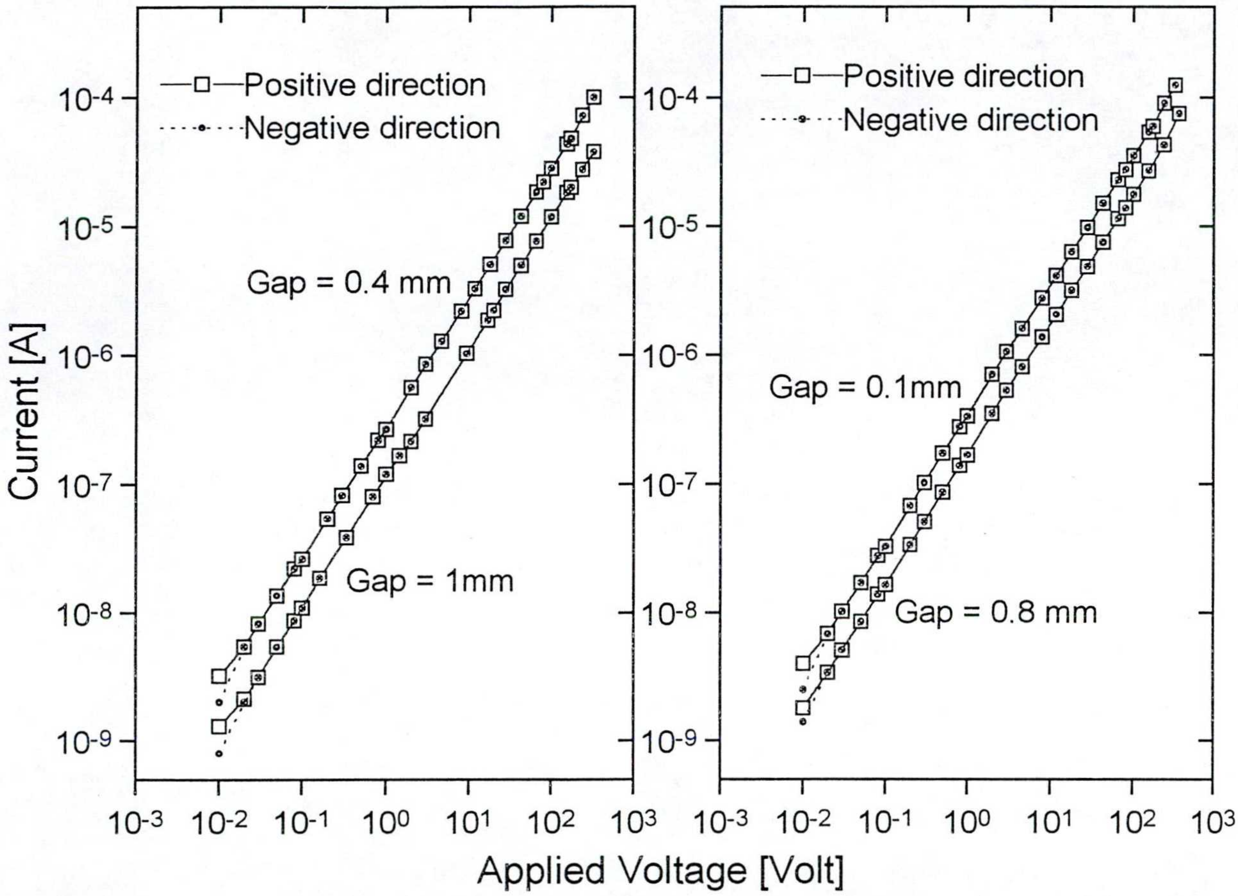

Fig. 6.1.1 Current Voltage characteristics measured in a-C:H sample of U_{SB} = -500 V in gap type geometry with different electrode spacing given on curves.

Electrical measurements were carried out in evacuated (10^{-3} torr) Faraday cell inside of which an electrically isolated copper block heated by resistances surved as oven to study temperature dependence of conductivity and influence of thermal treatment. A heat conducting Silicon grease was used to make a good thermal contact between oven and glass substrate. Calibration of sample and oven temperature was made by using two copper-constantan thermocouples. A block schema of measuring setup is illustrated in Fig. 6.1.2. This setup consists of two power supplies, one of them is direct current (dc) accumulator (0-300 V) to feed the sample and the other, 200 Watt programmable power amplifier is an alternative current (ac) to heat the sample. Two current amplifiers served to amplify the thermocouple and the sample current respectively. Current amplifier makes it possible to measure sample currents as small as 10^{-12} A. Signals are digitalized by a A/D converter and stored and handled by an IBM computer. The whole measuring system is computer controlled and programmable; the heating rate as well as current sampling time can be chosen. For example in most cases the heating current was checked and controlled by computer in every 10 seconds. Current, voltage and temperature values in most cases were recorded in the temperature range of 300-620 K by steps of 2 K. All thermal treatments and conductivity measurements were performed in the dark vacuum (10^{-3} torr). The used electric field strength in conductivity measurements were between 10^2 V/cm and 10^4 V/cm for samples of different U_{SB}.

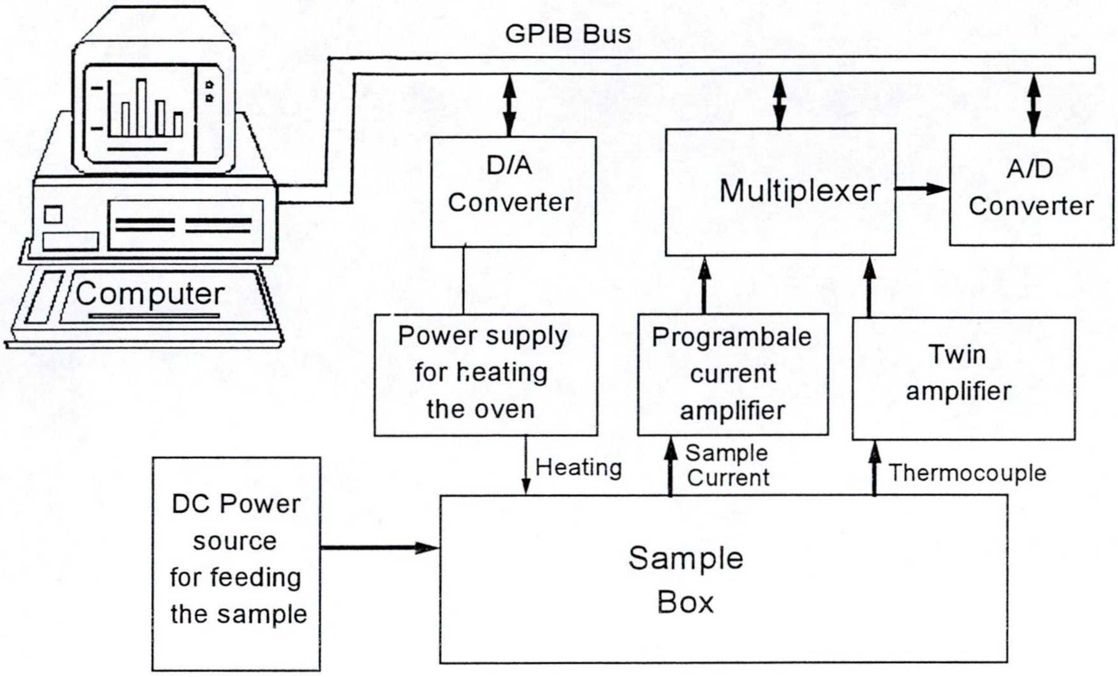

Fig. 6.1.2 Schematic illustration of measuring system used for study of dc electrical properties

Temperature dependence of dc electrical conduction was measured under heating by heating rate of 0.03 K/sec. however it was also measured under cooling process in several cases to control whether some structural rearrangements were attained or not under heating the sample. Data were also obtained by a very slow heating process with a 15 minutes waiting time at every 2 K. Thermal treatment was performed at 620 K for 6 hours long time in the measuring system after heating up slowly the sample up to this temperature. Fluctuation of sample temperature under annealing was ~ (±0.5) K. To make a good statistics, several samples but at least two ones deposited by the same parameters were measured.

6.2. Current-voltage characteristics and noise measurements

Both electrical contacts deposited onto insulating or semiconducting a-C:H layers and applied electric field can influence considerably conducting processes. Therefore it is important to study contact behaviour and to determine high-field and low-field range. An ohmic contact is defined as one that is capable of supplying and removing charge carriers from the bulk material at exactly the required rate, without either producing an accumulation of excess carriers or blocking their passage. In this case there exists equilibrium between levels in the metal and the corresponding levels in the conduction band of insulator or semiconductor, ensuring a free supply and removal of whatever carriers may be need in the presence of current flow. In the case of blocking contact, there are far fewer free carriers at the metal interface than in the bulk semiconductor material and the supply of carriers from the metal is therefore restricted. Finally for an injecting contact (for majority carriers, to be distinguished from minority carrier injection) there is an accumulation region at the metal interface and that serves as a ready source of excess electrons in the presence of a negative bias at the metal contact. Here we are interested in ohmic contacts; a more detailed description of contact properties can be found in Ref. [144].

The mechanism of low-field conduction applies to quasi-equilibrium conditions where the distribution of localized carriers in energy does not depart significantly from the thermal equilibrium distribution. Quantitatively this may be expressed by the condition

$$eE \ll R_{ij}\ kT \qquad (6.2.1)$$

where e is the electronic charge, E means the electronic field strength, R_{ij} is the pair spacing (fill and empty), k and T are the Boltzman constant and temperature respectively. This inequality implies numerically that, with R_{ij} = 1nm and T=300 K, the field should not be higher than come 10^4 V/cm. Once this order of magnitude of field is significantly exceeded, three types of phenomena may arise which were not present at low fields:

i) The probability of emission from localized centers may be affected;
ii) The average energy of the carriers in localized levels may be increased implying an enhanced effective temperature in the localized levels;
iii) Excess carriers may be introduced into levels in which they were not present in equilibrium, either by injection from end contacts or by a valence like processes from lower-lying levels.

In studying electrical transport mechanism of a-C:H layers. Ohmic contacts and low-field conduction are strongly favorized. Since the measurements are carried out on thin films, it is essential to know the properties of the surface and interfacial regions in order to deduce from thin-film measurements the properties of the bulk material. For crystalline semiconductor contacts, a number of techniques have been employed [145] to obtain information about the barrier height, surface states, screening length; for instance I-V characteristic, frequency and bias dependence of the capacitance C(ω) and C(V), internal photoemission, and the contact and surface photovoltage. We have used I-V characteristic measurement to obtain results for contact and to determine the highest electric field strength above which departure from ohmic behaviour takes place.

I-V characteristics for every a-C:H samples studied were measured at room temperature in the measuring setup introduced in the previous section. Calibrated dc voltage varied in the range of 10^{-3}–$3x10^{2}$ V was applied and the dc current was detected by using appropriate amplification. Both planar and transverse geometry have been used in I-V measurements. Fig. 6.2.1 shows I-V characteristics for five a-C:H samples deposited by U_{SB} = -200 V, -300 V, -400 V, -500 V, and -700 V. The sample thicknesses are listed on each U_{SB} curve in Fig. 6.2.1. Positive and negative direction corresponds to a voltage applied to top metallic electrode. Apart from the initial stage, the same current value can be measured in the two voltage direction. departure from this behaviour for small electric fields might be connected to gap type geometry or to some surface conductance, since no similar behaviour can be observed for sandwich type samples. I-V characteristics plotted in Fig. 6.2.1 exhibits ohmic behaviour or in other words resistance of those samples does not depend on the electric field strength.

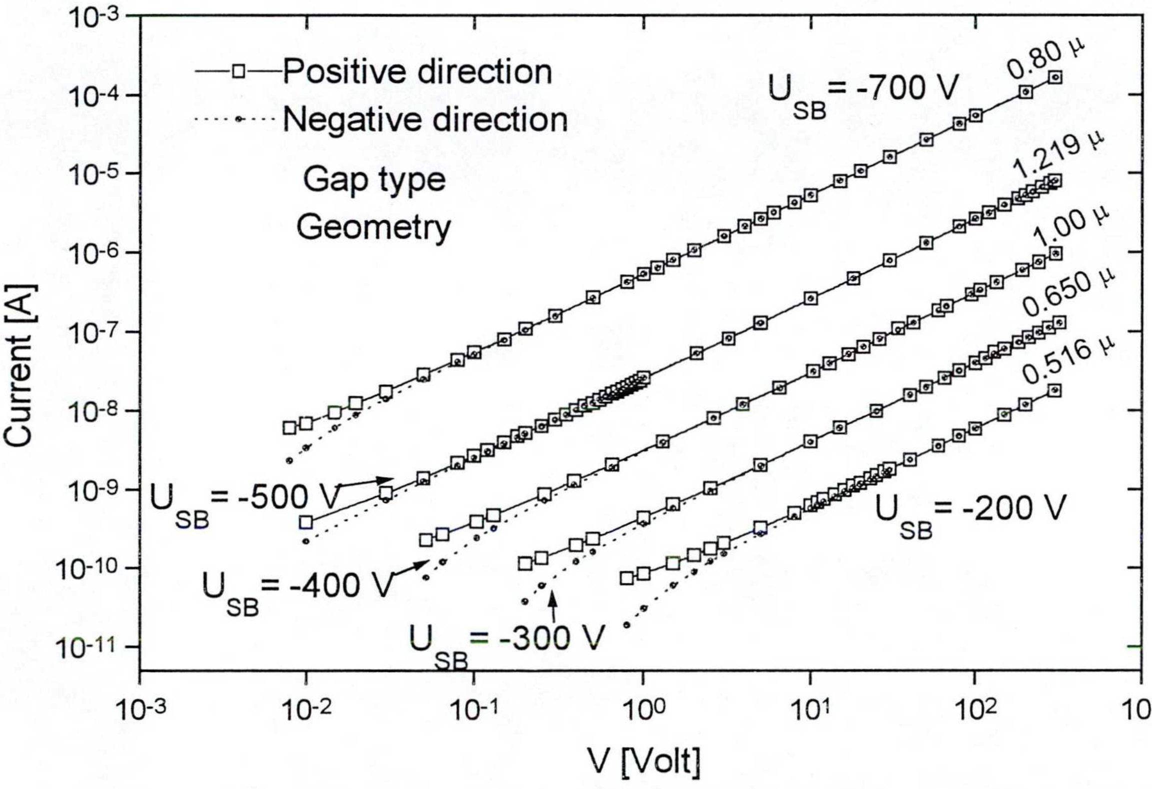

Fig. 6.2.1 Voltage-Current characteristics measured at room temperature for a-C:H under different U_{SB}. at room temperature. Sample thicknesses listed on curves. Metallic contacts are evaporated gold.

The I-V characteristics measured in sandwich geometry are shown in Fig. 6.2.2 for a-C:H samples of U_{SB} = -200 V and -500 V. Electrical currents measured in different applied voltage directions corresponds to each other even at small voltages too however the ohmic character is not as good as it was in gap type configuration in the case of -200 V sample. Due to some difficulties to prepare ohmic contact on sandwich type amorphous samples, a gap type electrode geometry is mostly used to study electrical transport in amorphous insulators and semiconductors. Departure from ohmic behaviour of I-V characteristics for a-C:H samples appears at electric field higher than ~10^{4} V/cm (Fig. 6.2.2.) in a good accordance with observation for gap type electrode geometry.

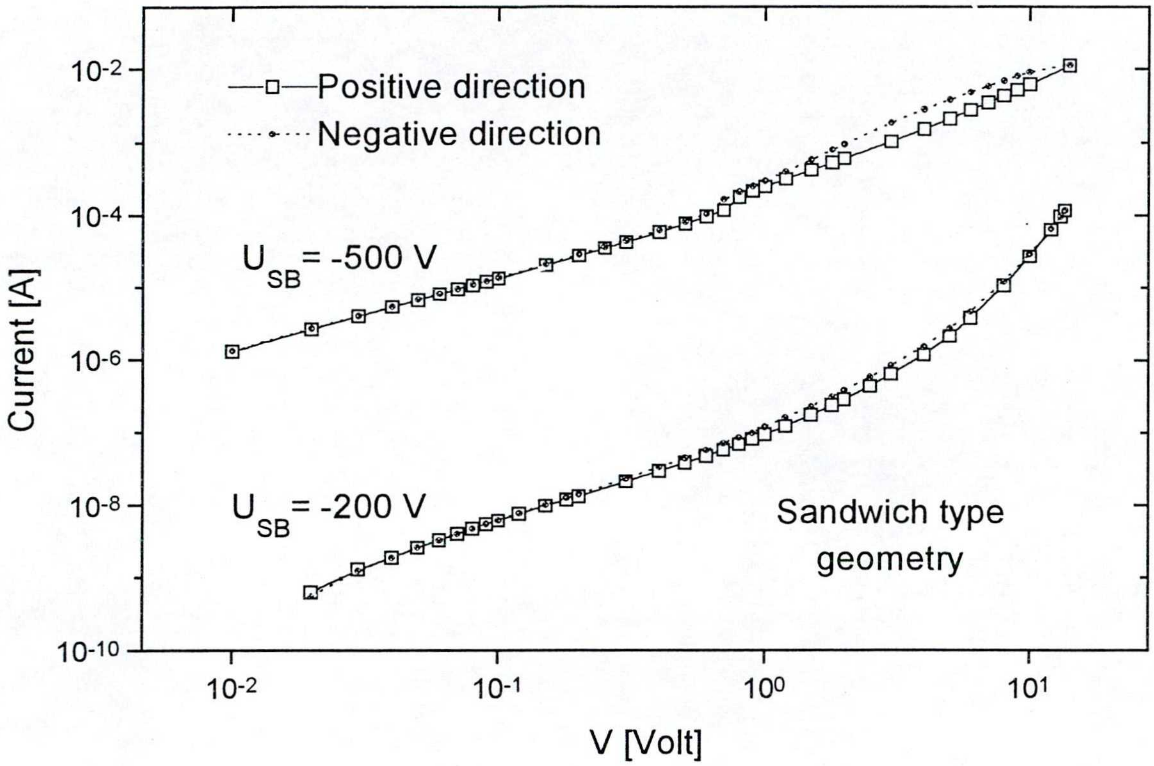

Fig. 6.2.2 Voltage-Current characteristics measured at room temperature for a-C:H under different U_{SB}.. Sample thicknesses as in the text. Metallic contacts are evaporated gold.

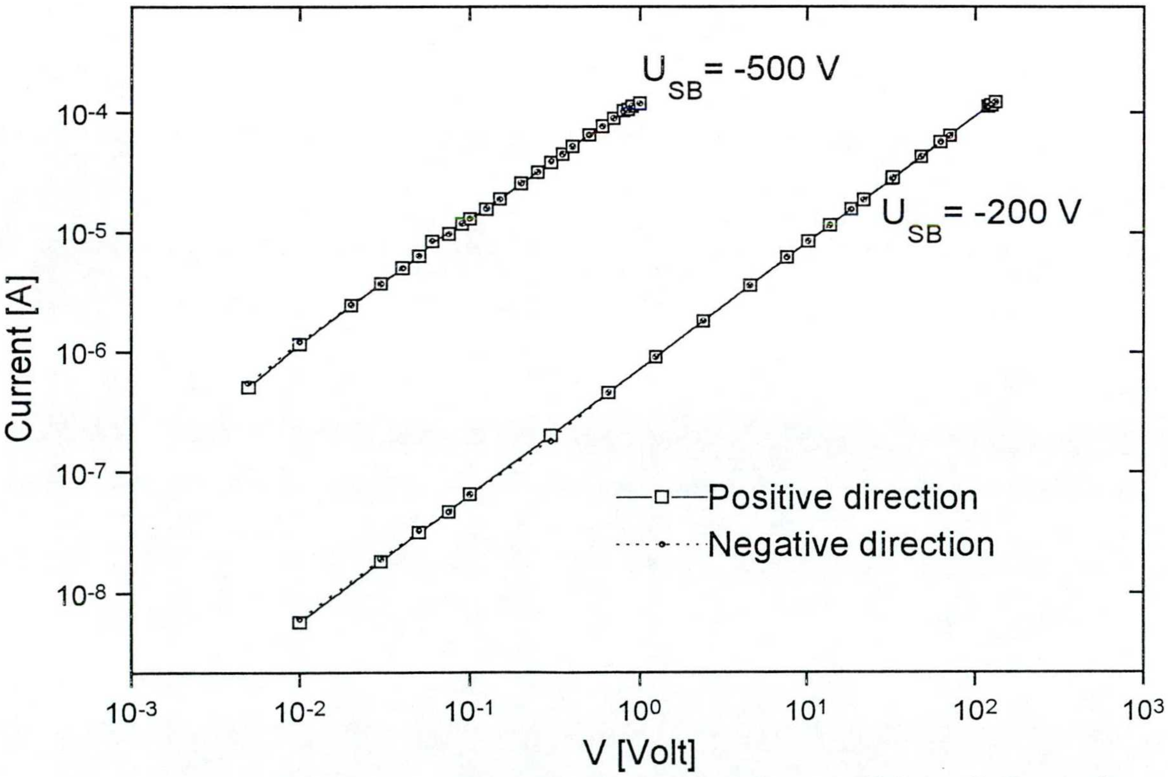

Fig. 6.2.3 Voltage-Current characteristics measured at 620 K for a-C:H samples prepared under different U_{SB} .

When we study temperature dependence of electrical transport it is important to know whether the contacts are ohmic or not at the given temperature. Another important point is the influence of annealing on the contact behaviour. Therefore we have measured I-V characteristics at 620 K for every a-C:H samples studied and the room temperature I-V curves were also measured following six hours thermal annealing performed at 620 K. Fig. 6.2.3 shows the high temperature I-V characteristics for two different samples while Fig. 6.2.4 represented the effect of annealing onto current-voltage curves. Evaporated Au electrodes give ohmic contact on a-C:H layers even at 620 K too, and departure from this behaviour for low electric fields, observed at room temperature, does not appear. This prove surface effect, as we have proposed earlier, for interpretation of poor Ohmic behaviour of contacts at low fields. thermal annealing decreases resistance of all samples however no significant change in Ohmic dependence of current on applied voltage was observed except of low-field behaviour of low self bias samples. Therefore it can be concluded, that the observed changes in conducting process at high temperature and after annealing can not be due to modification of contact properties.

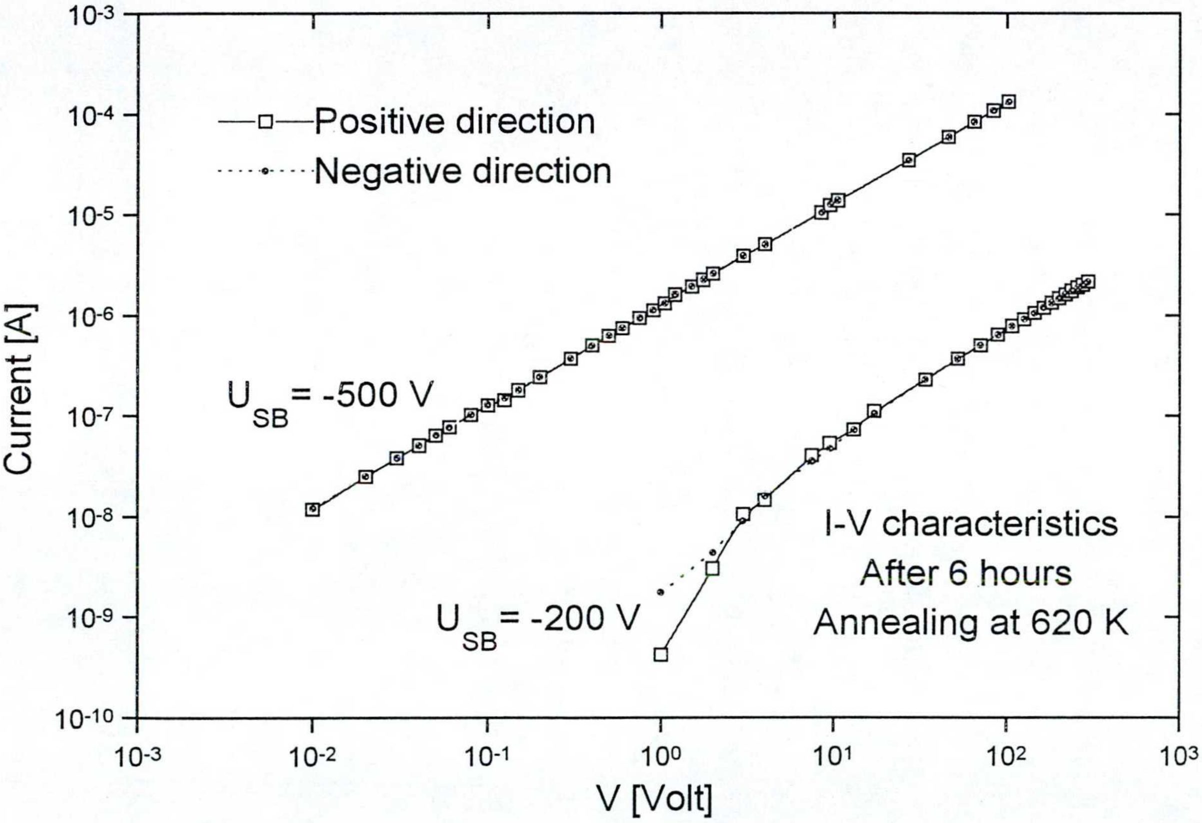

Fig. 6.2.4 Voltage-Current characteristics measured after annealing process for a-C:H samples prepared under different U_{SB}. .

Noise measurements

Study of electrical noise properties in a-C:H samples helps us to clear real conduction mechanism in thin material. Here we examine two samples only (sample I deposited by U_{SB} = -250 V and sample II prepared by U_{SB} = -550 V), which have different intermediate range ordering namely the sp^2 coordinated carbon content and the average cluster sizes are smaller for samples of U_{SB} = -250 V than for those of U_{SB} = -550 V. These supply different localized states distribution in the gap for hopping processes of charge particles.

Sandwich-type specimens of 1–2 μm thickness, with evaporated Au upper and lower electrodes were used for measurements of current fluctuations at 300 K in vacuum and in the voltage range in which the contact behaviour was ohmic. A detailed description of measuring system can be found in [146].

Current noise power spectra measured in two frequency ranges of 10^{-3} – 5 Hz and 1–10^{3} Hz are shown in Fig. 6.2.5 for samples I and II [147]. In the low frequency range colored current noise was observed in both sets of samples; the noise power shows $1/f^{\beta}$ frequency dependence with β =1.14 and 1.23 fitted slopes for sample I and sample II, respectively. A small variance in β was found from sample to sample although it was not larger than that can be measured on different spots of the same sample. Background noise was measured by replacing the sample with a low noise resistor of 90 MΩ, and it was proven that no correction of spectra is needed.

1/f dependence of noise power continues at larger frequencies, as it is shown on the right part of Fig. 6.2.5; however, the colored noise crosses the white noise level at ~800 Hz and ~40 Hz for sample I and sample II, respectively. It was found that the measured white noise intensity is 2-3 orders of magnitude larger, than the corresponding noise, calculated from the dc resistance of the sample at the measuring temperature [148]. In order to check our measuring system, we measured the thermal noise of a resistor of 90 MΩ, and the Jonhson noise level was reproduced by an error of 5%. Further investigations are needed to resolve this discrepancy.

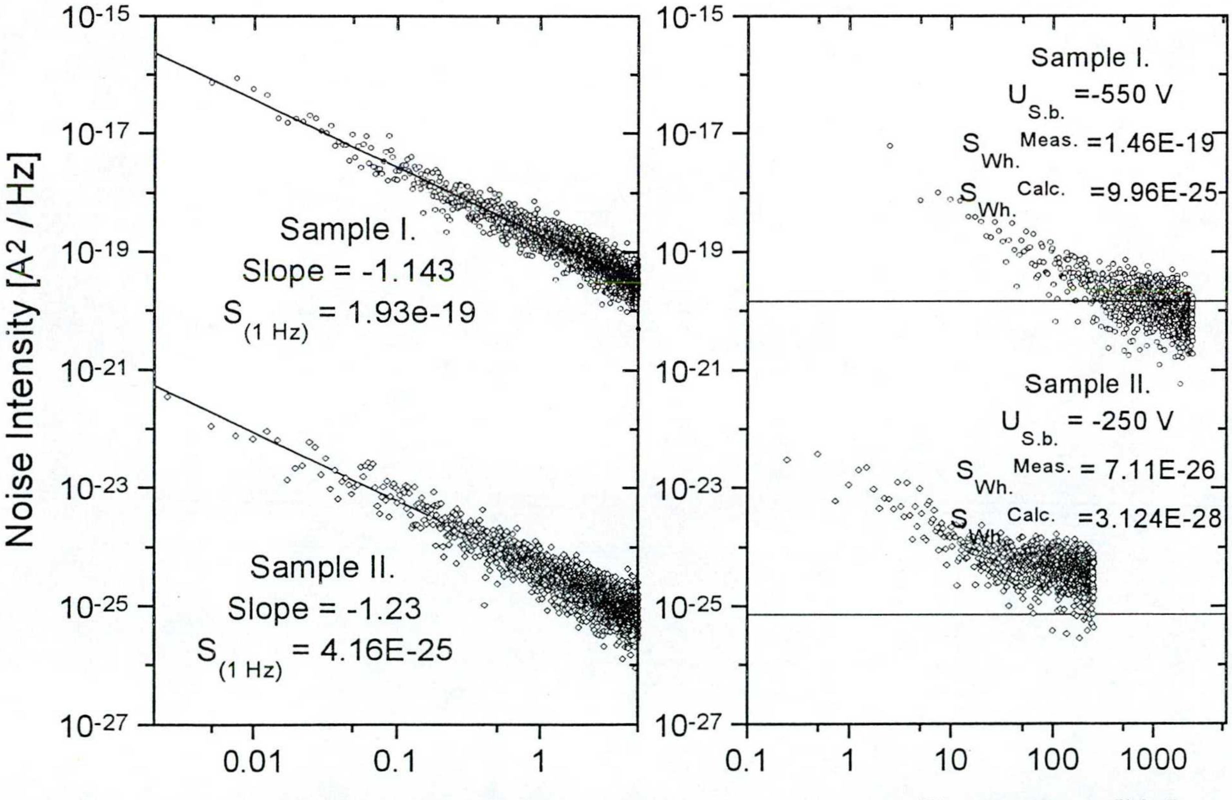

Fig. 6.2.5 Current noise power spectra measured by U_{dc} (operating voltage) = 200 mV at room temperature for the different a-C:H samples..

The absolute noise power was found to vary with film properties being larger in samples deposited at higher self biasing. It can be seen from Fig. 6.2.5 that there is a difference of roughly five orders of magnitude between the colored noise power of the two sample sets. Taking into account a so called relative noise – dividing the measured noise intensity by the dc current going through the sample – the same relation was found a roughly ten times larger relative noise power at the sample deposited at higher U_{SB}.

Preliminary results of moderate heat treatments of a-C:H layers at 500 K showed that the absolute noise power decreased, and the crossing point of the colored noise and white noise moved towards lower frequencies.

To explain current noise properties of a-C:H films we should refer first to the equivalent occurrence of the 1/f frequency dependence of noise in samples having different sp^2 coordinated carbon content but are characterised by clustering these carbon atoms on different levels. This suggests that current noise is related to structural peculiarities which results in hopping conduction process of charged particle. The film structure is built up from sp^2 bonded clusters, which are embedded in sp^3 bonded matrix. The total number of sp^2 atoms, and size distribution of sp^2 bonded clusters can be varied by U_{SB}, which means, that both of these quantities are larger in the films prepared at higher self biases [22].

Deep localized states and band tails states, generated by the sp^2 bonded clusters, take part in electronic conduction at room temperature because states corresponding to sp^3 bonded sites lie at much higher energies. Electrons should move from one cluster to the next one in real space, when a dc current goes through the sample. The electronic conduction of such cluster system shows a percolation feature: one dimensional conducting lines are formed by a continuous series of conducting inter-cluster junctions, which may be branching. Inter-cluster conductivity rises or falls, as a consequence of the atomic re-arrangements, and this process creates the fluctuation. A hierarchical structure of these conducting lines can be supposed for these junctions and 1/f frequency dependence is the consequence [149].

Different relative noise power in two sample sets may be a consequence of electron localization. In smaller clusters stronger electron localization, or confinement of electrons results in longer electron life times, which shift the noise power spectra to lower frequencies. This concept is in good agreement with the fact that colored noise crosses white noise level at frequencies of ~40 Hz and ~800 Hz for samples prepared at –250 V and -550 V respectively. Further experiments are in progress in attempt to understand the noise properties of a-C:H films in detail.

6.3. Structural and temperature dependence of direct current conductivity

Localized states in the gap, their concentration and energetic distribution influence considerably those macroscopic properties which are important in whatever application of an amorphous semiconductor. Direct current (dc) electrical measurement is a powerful method to determine gap states properties. Our aim was, that to determine energetic distribution of localized states in a-C:H layers near band edges and relate that to structural properties of samples. Therefore we investigated temperature dependence of dc electrical conductivity σ_{dc} near and above room temperature and its variation with sample structure as well. Structural properties of a-C:H samples were controlled by variation of deposition self bias voltage from -200 V to -700 V and the other parameters of deposition process were not changed.

Bonding properties, that is hydrogen content, percent of sp^2 coordinated carbon atoms compared to sp^3 ones, clustering of sp^2 sites vary considerably with deposition self bias of a-C:H samples as it was proven by our Raman and IR measurements discussed in section V. Therefore strong modification of π states of sp^2 sites together with localized states concentration and distribution can be expected with U_{SB}. Results of our dc conductivity ($\sigma_{dc}(RT)$) measurements give further evidence of this picture. In Fig. 6.3.1 we can see the dependence of room temperature dc conductivity (a) and semilogarithmic (b) plotting. The σ_{dc} increases by ~10 orders of magnitude when self bias changes from 200 V to 700 V. This extremely large change of σ_{dc} indicates a significant modification of localized states through

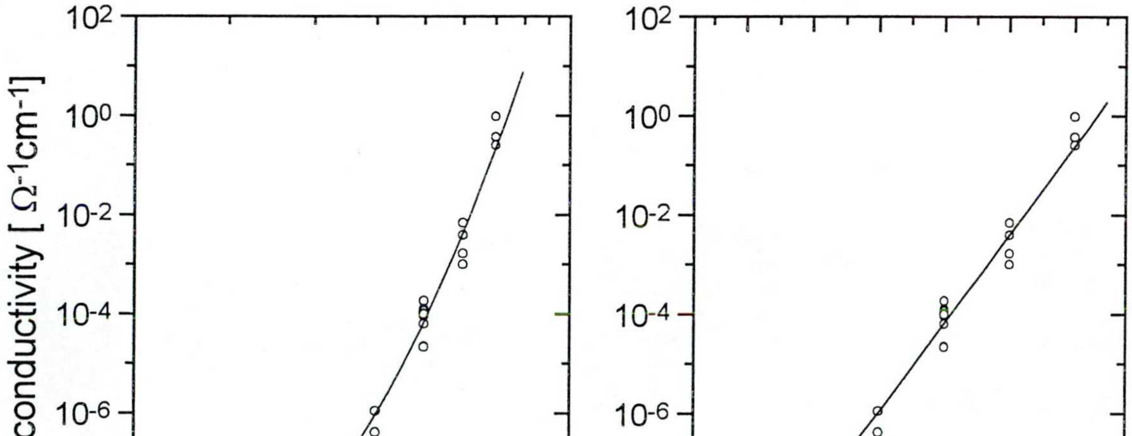

Fig. 6.3.1 Quadratic and linear fits of room temperature dc conductivity $\sigma_{dc}(RT)$ as a function of self bias voltage for a set of a-C:H samples prepared under different self bias voltages. σ_{dc} was measured in planar geometry with electrodes spacing of 400μ.

which electrical conduction takes place. Increase of the density of π states of sp^2 sites alone is not able to explain 10 order increase of σ_{dc}. A plausible explanation might give percolation pecularities of sp^2 coordinated carbon clusters, but the first difficulty appears when we would like to explain deposition voltage dependence of σ_{dc}. Above percolation threshold σ_{dc} should show power law dependence with an exponent of two on percolating sites what is not the case shown in Fig. 6.3.1(a). It is true, that in Fig. 6.3.1(a) the dependence of σ_{dc} on deposition self bias is plotted, but the concentration of sp^2 coordinated carbon atoms vary roughly linearly with self bias [150]. It seems to be more probable that σ_{dc} depends on sizes of sp^2 coordinated clusters rather than numbers of sp^2 sites. How the exponential dependence of σ_{dc} on U_{SB} follows from this condition is subject of further investigation.

In Table. 6.3.1 we summarized σ_{dc}(RT) and thickness for several samples at each deposition voltages. These results represent reproducibility of conductivity; nearly one order of magnitude difference between conductivity of a-C:H samples obtained by same U_{SB} is the worst case. This gives an error of 10% compared to 10 order magnitude increase of σ_{dc} when U_{SB} changes from -200 V to -700 V. The factor of 2-4 between σ_{dc} of samples prepared by same U_{SB} acceptable if we taken into account, that the measured area was 10 mm x 0.4 mm. However it should be mentioned that σ_{dc} depends on sample thickness–what we discuss later; conductivity decreases as the sample will be thinner.

Table. 6.3.1 a-C:H sample sets at different self bias voltages

U_{SB} (-V)	**Conductivity σ_{RT} ($\Omega^{-1}cm^{-1}$)**	**Thickness (μ)**	**U_{SB} (-V)**	**Conductivity σ_{RT} ($\Omega^{-1}cm^{-1}$)**	**Thickness (μ)**
200	2.51189×10^{-10}	0.297	400	2.13796×10^{-7}	1.00
200	4.46684×10^{-10}	0.188	400	1.61436×10^{-8}	0.91
200	8.51189×10^{-10}	0.297	400	4.16869×10^{-8}	0.77
200	4.81948×10^{-10}	0.578	400	2.08449×10^{-8}	0.60
200	4.85289×10^{-10}	0.095			
200	8.53174×10^{-10}	0.205	500	1.86209×10^{-4}	0.859
200	4.16869×10^{-10}	0.546	500	6.55893×10^{-5}	0.75
200	2.98538×10^{-10}	0.469	500	9.18776×10^{-5}	0.625
200	9.0272×10^{-10}	0.62	500	1.25893×10^{-4}	0.719
200	3.38844×10^{-10}	0.344	500	1.14815×10^{-4}	1.219
200	4.0738×10^{-10}	0.564	500	1.02329×10^{-4}	0.764
300	4.90908×10^{-8}	0.36	600	0.00391	0.688
300	1.65959×10^{-8}	0.48	600	0.00166	0.85
300	1.63305×10^{-8}	0.65	600	9.977×10^{-4}	0.797
300	1.62181×10^{-8}	0.13	600	0.00698	1.141
300	8.91251×10^{-8}	0.22			
300	2.69153×10^{-8}	0.56	700	0.25119	0.406
			700	0.36559	0.75
			700	0.96225	0.80

Temperature dependence of σ_{dc} in the range of 300-620 K was measured on an as prepared samples. Fig. 6.3.2 displays temperature dependence of σ_{dc} in Arrhenius plot for a-C:H samples obtained by six different self bias voltages. Several orders of magnitude increase in room temperature conductivity when deposition voltage changes from -200 V to -700 V indicates the significant role of structural ordering in electrical conduction. Higher temperature starts to "compensate" the influence of the as prepared structural differences because the change of conductivity with self bias at higher temperatures reduces to four orders magnitude only. The temperature dependence of conductivity does not follow the

$$\sigma_{dc}(T) = \sigma_0 \exp(-E_\sigma/kT) \qquad (6.3.1)$$

simple Arrhenius law, since $\ln\sigma$ versus $1/T$ curves, shown in Fig. 6.3.2, are not linear. The gradient of these curves

$$E_{act.} = -k\frac{d[\ln \sigma_{dc}(T)]}{d(1/T)} \qquad (6.3.2)$$

i.e. the actual activation energy (E_{act}) is used to characterize temperature dependence of conductivity. Fig. 6.3.3 shows E_{act} as a function of reciprocal temperature calculated by derivation of curves in Fig. 6.3.2. It is a general behaviour that E_{act} increases with temperature, however the slope of increase depends greatly on deposition voltage. Three times larger increase of E_{act} for sample of -200 V than for that of -700V in the same temperature range may indicate a more wider distribution of tail states in the former sample. The strong fluctuation of E_{act} appears at 500K above which a transition to another conduction mechanism is indicated by the significant increase of derivatives. Measurements up to higher temperatures can not be

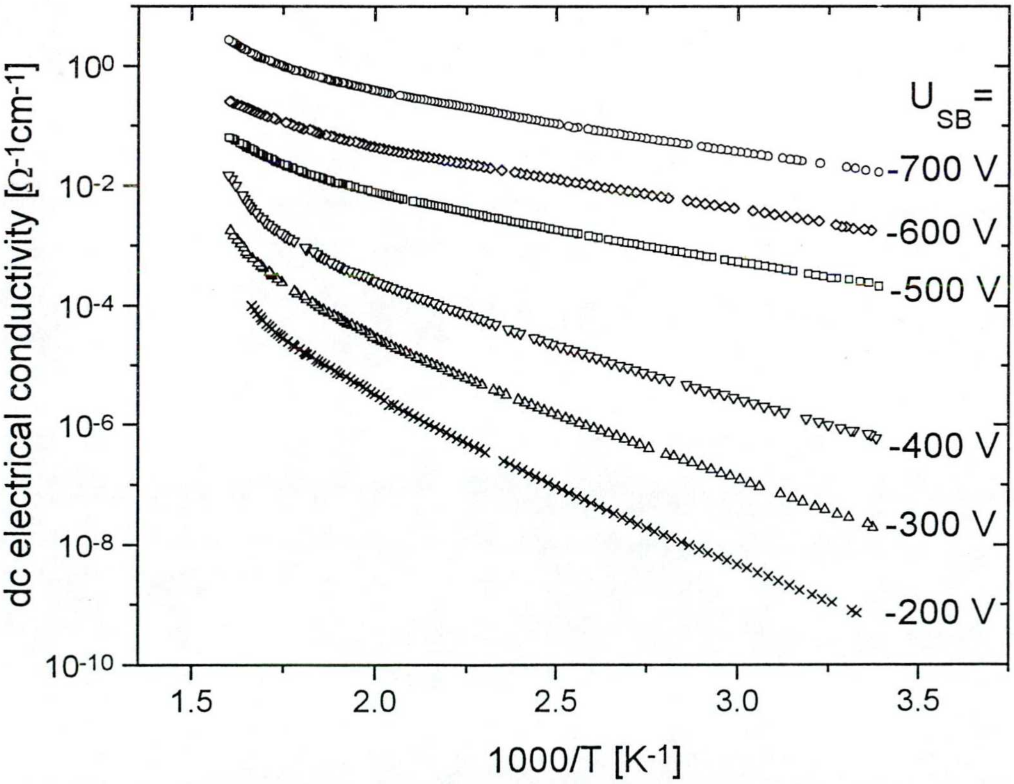

Fig. 6.3.2 Temperature dependence of dc conductivity for a-C:H samples deposited at different self bias voltages. σ_{dc} was measured in planar geometry with electrodes spacing of 400 μ.

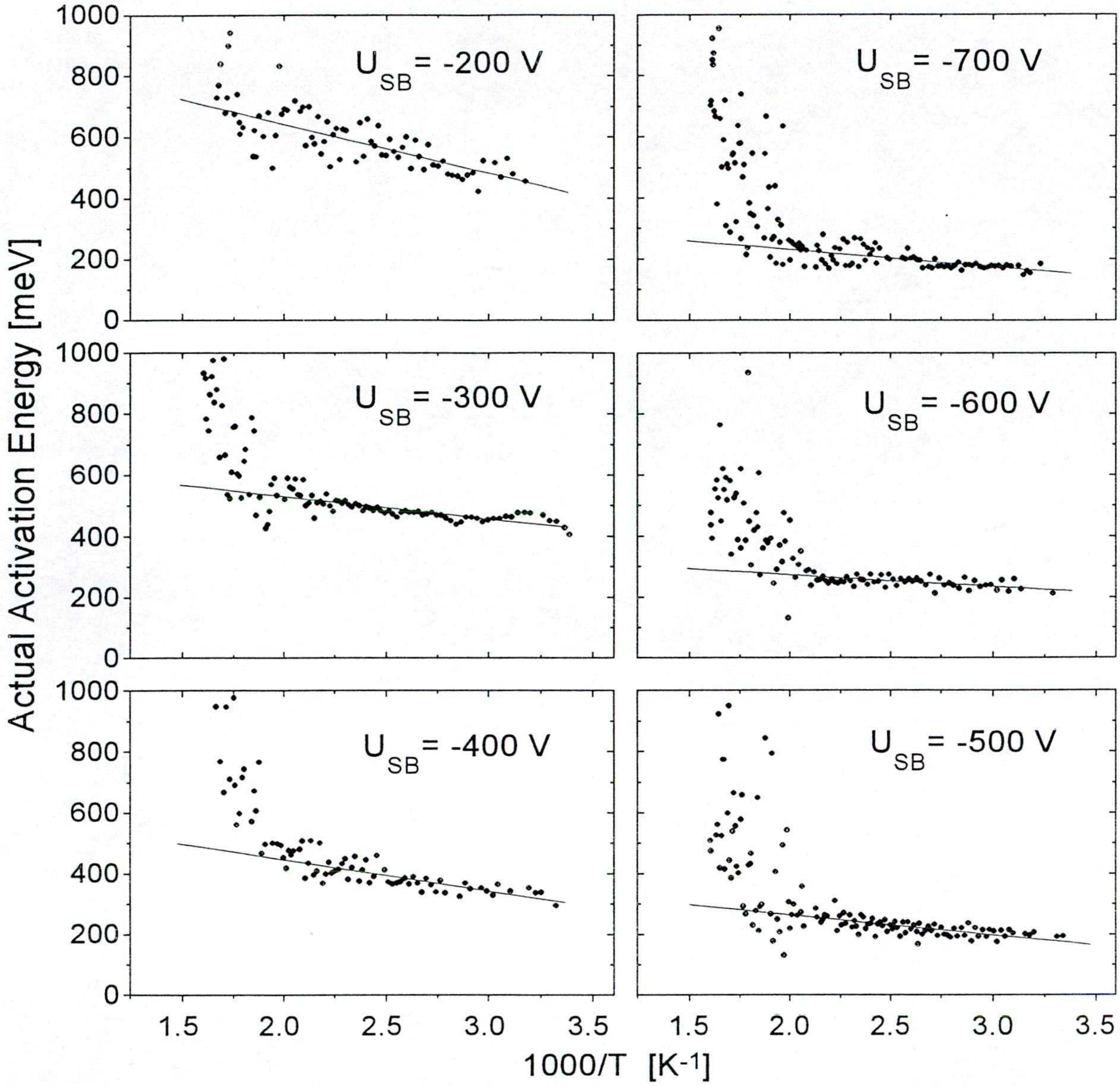

Fig. 6.3.3 Temperature dependence of actual activation energy for a-C:H samples prepared by different self bias voltages. The straight lines are guide for the eye.

continued because about 620 K effusion of hydrogen and different hydrocarbons begins from the sample. This results in significant structure changes and measured σ_{dc} does not characterize the original sample.

One of the difficulties in interpreting dc electrical conduction at and above room temperature in a-C:H is the continuous curving of $\ln\sigma_{dc}$ versus 1/T dependence, what indicates that the process does not have a single activation energy as shown in Fig. 6.3.3. However at these temperatures it is expected that electrical transport takes place by carriers excited into band tails or up to mobility edges and the process is characterized by thermal activation of charge particles from the Fermi level. Departure from this behaviour, we think, is connected with special properties of tail states originated from π bonds of sp^2 sites. The energetic position of these tail states is influenced considerably by the distribution and ordering of sp^2 carbon atoms, it is therefore important to compare electrical properties of a-C:H samples of different material structure and also to study effect of annealing.

6.4. Effect of annealing

If there is a true relation between the temperature dependence of E_{act} and the barrier height distribution – as it appears from the effect of deposition voltage – then thermal annealing should influence curving of $\ln\sigma_{dc}$ versus T^{-1} dependence. Thermal annealing performed at 620 K does not exceed the effusion temperature of different hydrocarbons [39,76] , however, unbonded hydrogen begins to effuse at this temperature. Usually 6 hours annealing time was chosen because weight loss of sample can be observed for longer times. Fig. 6.4.1 shows the time dependence of conductivity increase under annealing at 620 K for two different samples.

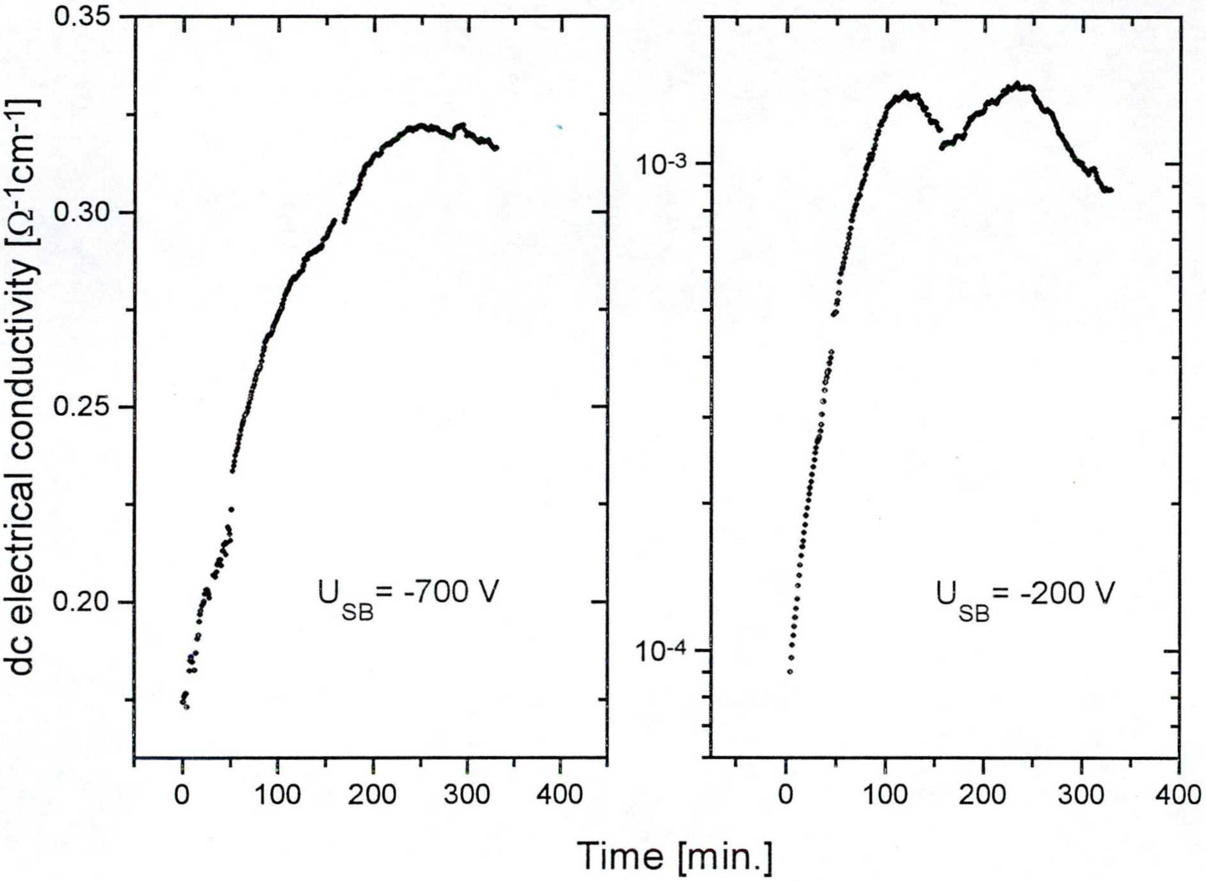

Fig. 6.4.1 Time dependence of dc conductivity increasing under thermal annealing at 620 K for samples of U_{SB} =-200 V and -700 V.

The first stage is more steep while after ~2 hours a slow change observed for both two samples. 2-3 hours seems to be needed to reach some saturation under which a five times larger increase of conductivity occurs for sample of U_{SB} = -200 V than of U_{SB} = -700 V, however, the overall form of conductivity increase is very similar for both of these two samples.

Temperature dependence of dc conductivity after annealing is shown in Fig. 6.4.2. Heat treatment increases conductivity in every samples, but the strongest effect is in the lowest self bias sample; the other interesting point is the much larger increase of the room temperature conductivity than the high temperature one. The $\ln\sigma_{dc}$ versus 1/T curves can not be fitted by straight line even after annealing, however, the curving becomes much smaller. It is seen on Fig. 6.4.3, where the temperature dependence of E_{act} calculated using Eq. (6.3.2), is shown for annealed states of samples deposited by different self bias. Heat treatment decreases the slope of E_{act} versus 1/T curve in every cases and the most significant decrease of slope is for samples of -200 V. Reduction of the absolute value of E_{act} over the whole temperature range (Figs. 6.3.3 and 6.4.3) is another effect of annealing, what was observed with an only exception of the sample of -700 V. The overall effect, what we would like to emphasize, is that the temperature dependence of dc conductivity becomes more Arrhenius-type after annealing than it was before.

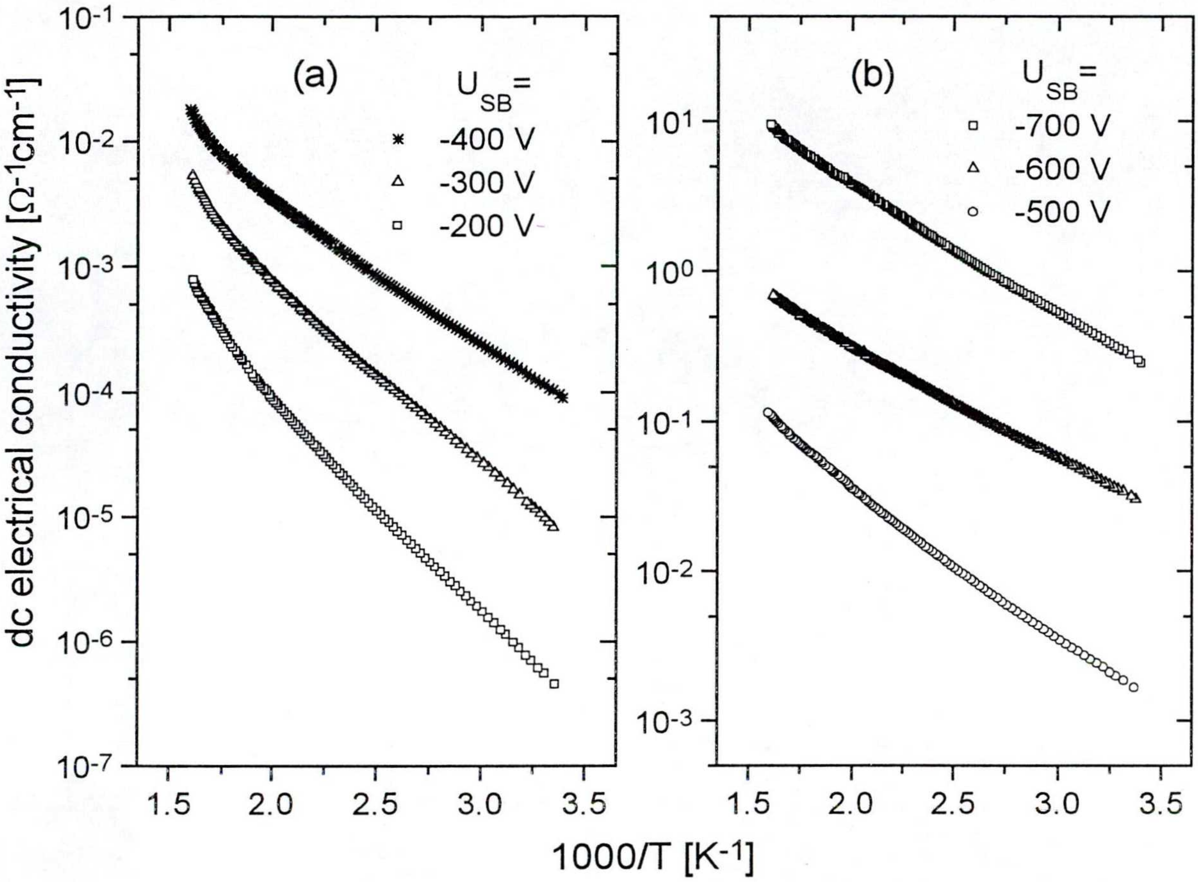

Fig. 6.4.2 Temperature dependence of dc conductivity after annealing at 620 K for 6 hours of a-C:H samples deposited at different self bias voltages.

Under annealing further formation of sp^2 coordinated carbon atoms and their aggregation into larger clusters can be expected. This structural transformation decreases barriers for π electrons and increases their delocalization which results in more pronounced increase of conductivity near room temperature than higher one in samples deposited at $U_{SB} < 500$ V as seen from comparison of Figs. 6.3.2 and 6.4.2. In other samples ($U_{SB} > 500$ V) similar behaviour with smaller extent of changes caused by annealing is a consequence of the already higher degree of clustering in unannealed states in these samples [67,132]. These differences are well seen on kinetic curves of conductivity increase under annealing too as shown in Fig. 6.4.1, being the overall form of time dependence similar to those two samples, but it is saturated at much lower level of increase for sample of -700 V than - 200 V.

Structural transformation under annealing makes the intermediate ordering of samples deposited at low self biases similar to that of high voltages ones [112] (and see Raman measurements in section 5.2). This clearly appears in the curving of $\ln\sigma_{dc}$ in reciprocal temperature dependence of Figs. 6.3.2 and 6.4.2 as well as in temperature dependence of E_{act} as shown in Figs. 6.3.3 and 6.4.3. In addition, temperature dependence of dc conductivity in samples of -600 V and - 700 V approaches the nearly Arrhenius type behaviour after annealing. These changes strongly suggest that curving of ln σ_{dc} vs. reciproc temperature is in close relation with broad distribution of tail states or in other words with wide distribution of barriers for hopping of π electrons. Either high deposition voltage or thermal treatment favors more extended clustering of sp^2 sites which delocalizes π electrons inside the clusters (similar e.g. to graphite sheets) and decreases barriers for hopping to other clusters; as a result conductivity increases and E_{act} shows sight dependence on temperature.

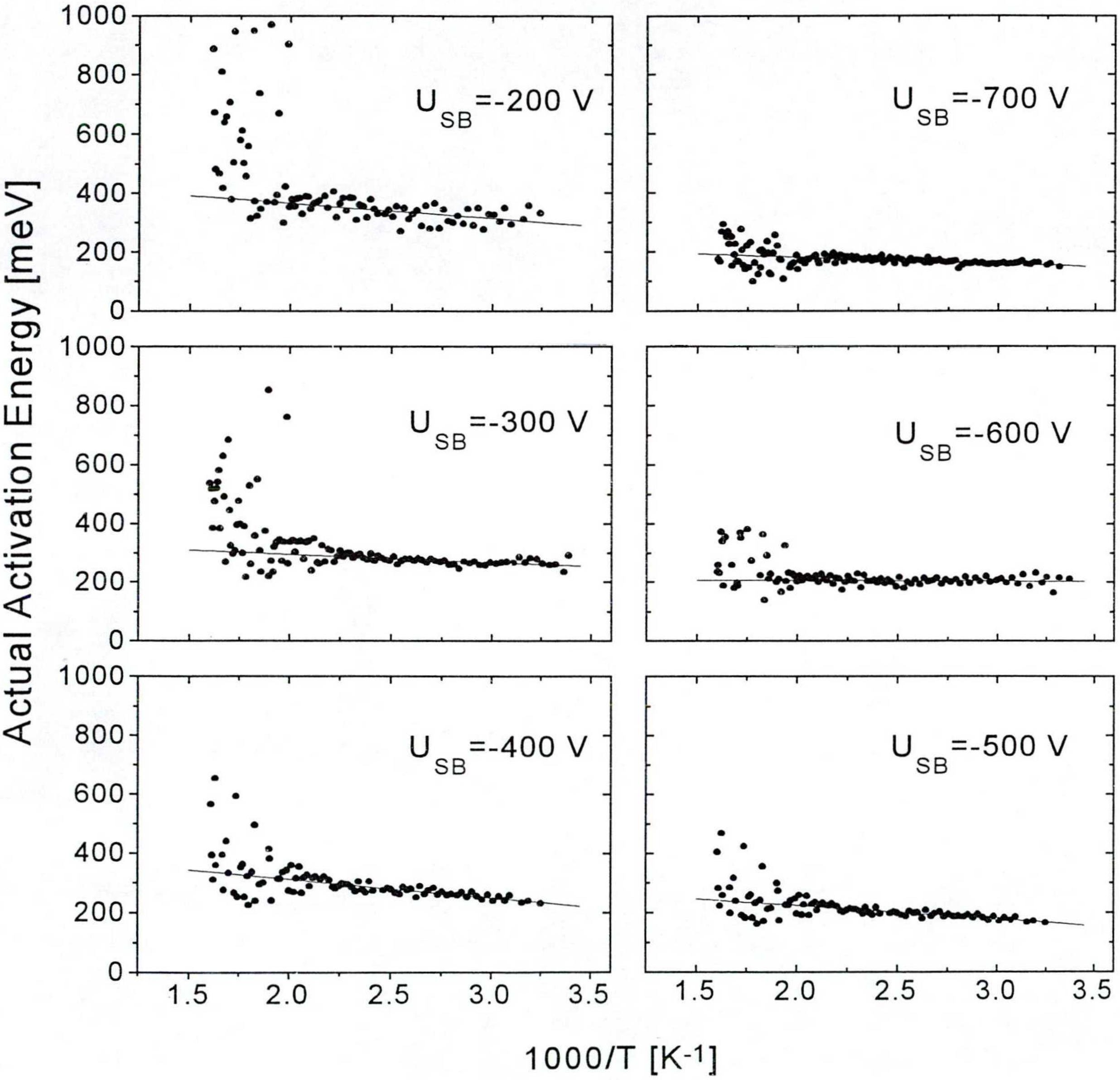

Fig. 6.4.3 Temperature dependence of actual activation energy after annealing for a-C:H samples prepared by different self bias voltages. The straight lines are guide for the eye.

6.5. Compassion with different transport models

Temperature dependence of dc conductivity have already been investigated in evaporated [151] and sputtered [152-154] amorphous carbon (a-C) and its hydrogenated form (a-C:H) [105,106,111,128] with the aim to relate electrical transport with localized states distribution across the gap. Variable range hopping (VRH) [155] was suggested by numerous authors at low temperature [151,152,156]. A better fit of experimental points by multiphonon tunneling was also demonstrated in a-C [153]. Thermally activated hopping of carriers in the region characterized by high density of localized states [111,106] as well as simple thermal activation of carriers into extended states [105] was taken into account to explain temperature dependence of conductivity in a-C:H above room temperature. It seems, that there is more consistency concerning conduction mechanism derived for a-C than a-C:H owing partly to the large variation of material structure in the last case.

For an amorphous semiconductor the possible conduction mechanisms are hopping of carriers between localized states in the gap and transport by carriers excited beyond the mobility edges. At low temperatures the variable range hopping of carriers in the narrow band of localized states near Fermi level is fovorized giving the well known $T^{-1/4}$ temperature dependence of dc conductivity [155]. Near and above room temperature the dominant conduction mechanism is hopping of carriers excited into tail states and transport by carriers at conduction or valence band edges (E_c or E_v respectively).

We compare our experimental results with different transport processes namely with variable range hopping (VRH) in the band of localized states near Fermi level, multiphonon tunneling and thermally activated hopping in tail states. At first we start with VRH transport mechanism. Reliability of this conduction is because temperature dependence of σ_{dc} follows excellently the $T^{-1/4}$ law–characteristic temperature dependence of VRH–up to ~500 K. It is shown on Fig. 6.5.1 for a-C:H samples deposited by different self biases. Fig. 6.5.1 shows that the experimental points up to 500 K can be fitted reasonably well according to [155]

$$\sigma(T) = \sigma_{0VRH} \ \exp\left[-\left(\frac{T_{0VRH}}{T}\right)^{1/4}\right] \tag{6.5.1}$$

where σ_{0VRH} is the pre–exponential factor and T_{0VRH} parameter is given by Mott [155] as:

$$T_{0VRH} = \frac{16\alpha^3}{k \ N(E_F)} \tag{6.5.2}$$

where $N(E_F)$ is the density of localized states near Fermi level, α is the coefficient of exponential decay of the localized states and k is the Boltzmann constant. Parameters of fitting to $T^{-1/4}$ law are summarized in Table. 6.5.1 for samples shown in Fig. 6.5.1 and for several other samples. Table contains also exponent values related to multiphonon tunneling process what will be discussed later. We estimated from T_{0VRH} fitting parameter, by using Eq. 6.5.2, the density of localized states near Fermi level. In this calculation α^{-1} =10 Å was supposed which is used generally for amorphous semiconductors. $N(E_F)$ decreases with deposition self bias in a good agreement with expectation. Because sp^2 coordinated carbon content decreases and hydrogen content increases with decreasing deposition self bias, a decreasing number of localized states in the gap seems to be probable. Comparison with the ESR results [116,121], the low rf power samples show dominant diamond–like structure whereas the high rf ones show a predominant graphite structure, and the spin density increased by increasing the rf power. The trend of $N(E_F)$ with self bias is in agreement with change of $\sigma_{dc}(RT)$, however about two orders of magnitude increase of $N(E_F)$ is not able to explain 9 orders of magnitude increase of $\sigma_{dc}(RT)$ when U_{SB} changes from -200 V to -700 V

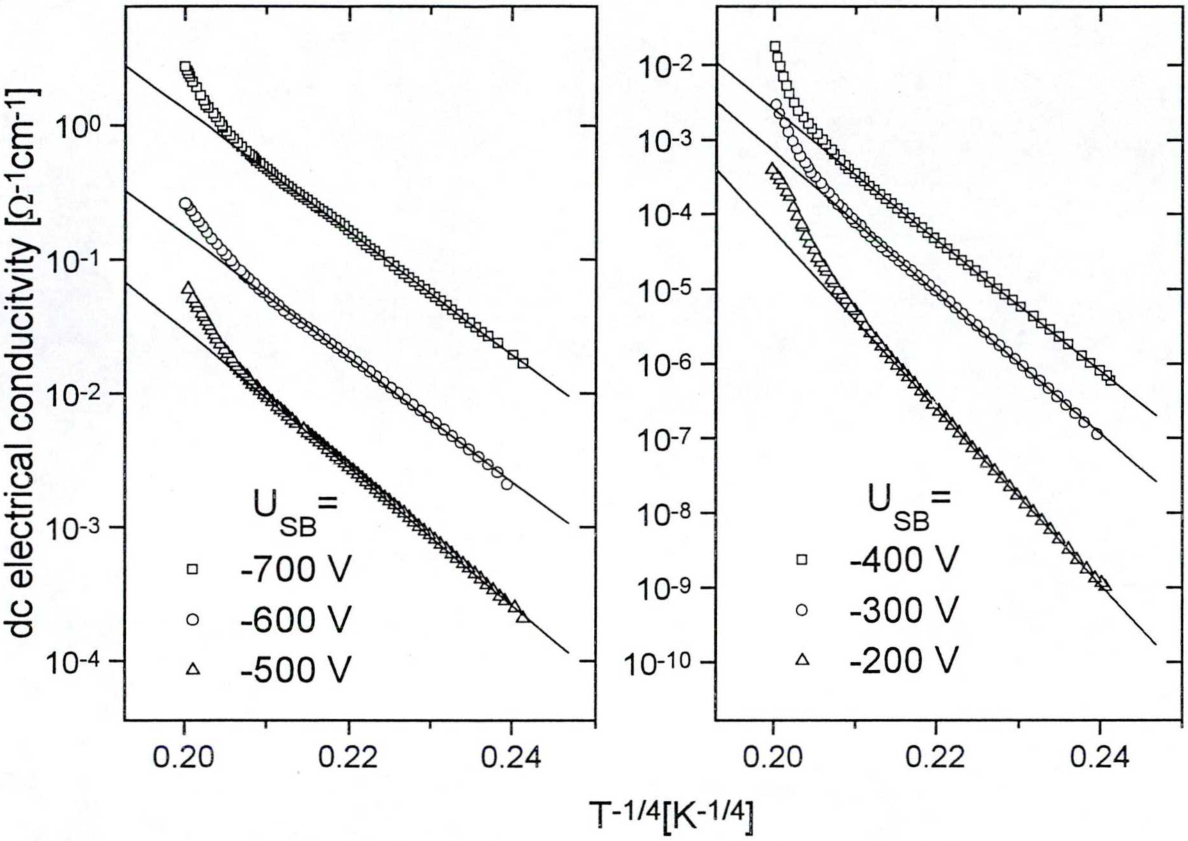

Fig. 6.5.1 Temperature dependence $T^{1/4}$ of dc conductivities for different self bias voltage samples. The straight lines are the fitting with the VRH theory.

The pre-exponential factor σ_{0VRH} in Eq. 6.5.1 can be determined from the intercept of the straight lines at T= ∞ Fig. 6.5.1 with vertical axes. These σ_{0VRH} values, listed in Table. 6.5.1 are much higher than those determined from temperature dependence of σ_{dc} measured at low temperature [157,98], however results in Ref. [112] are related to unhydrogenated samples. The σ_{0VRH} can be calculated from experimentally determined $N(E_F)$ by using next equation [86]:

$$\sigma_{0VRH} = \left(\frac{N(E_F)}{\alpha kT}\right)^{1/2} \left(\frac{3e^2 \nu_{ph} \phi_0}{2}\right) (2\pi)^{-1/2} \qquad (6.5.3)$$

where ν_{ph} is the phonon frequency and ϕ_0 is a constant of the order close to unity. Taking α^{-1} = 10 Å, T= 500 K and $\nu_{ph} \sim 10^{13}$ Hz, values of σ_{0VRH} calculated by using Eq. 6.5.3 are several decades lower, than the experimental values reported in Table. 6.5.1. It is noteworthy that similar discrepancy between experimental and calculated values of σ_{0VRH} occurred in many

Table. 6.5.1 Characteristic parameters of dc electrical conductivity determined from experimental results and from fitting to variable range hopping transport or multiphonon tunneling process as well.

where, $T_0 = \dfrac{16\alpha^3}{kN(E_F)}$, by taking the decay in localization length $\alpha^{-1} = 10$ angstroms $N(E_F)$ was calculated,

Pre-exponential value: $\sigma_0 = \left(\dfrac{N(E)}{\alpha kT}\right)^{1/2} \left(\dfrac{3e^2\nu\phi_0}{2}\right)(2\pi)^{-1/2}$, calculated by using $\nu = 10^{12}$ Hz, T=300 K, $\phi_0 \approx 1$

Average hopping distance: $\overline{R} = 0.75\left(\dfrac{3}{2\pi\alpha N(E_F)kT}\right)^{1/4}$, Average energy of hopping: $\overline{\Delta w} = \dfrac{3}{4\pi\overline{R}^3 N(E_F)}$, and

Energy range from E_F where conduction occur: $E_m = kT^{3/4}T_0^{1/4}$, taking into account k is the Boltzman constant.

Experimental data		VRH fitting parameters and calculations							Multiphonon tunneling	
U_{SB} (V)	**σ_{RT} $\Omega^{-1}cm^{-1}$**	**T_o (K)**	**$N(E_F)$ ($eV^{-1}cm^{-3}$)**	**σ_o(Exp.) ($\Omega^{-1}cm^{-1}$)**	**σ_o(Calc.) ($\Omega^{-1}cm^{-1}$)**	**$\overline{R}$ (Å)**	**$\overline{\Delta w}$ (eV)**	**E_m (eV)**	**a** ($\Omega^{-1}cm^{-1}K^{-p}$)**	**p exponent**
-200*	$8.0x10^{-10}$	$5.52x10^{9}$	$3.36x10^{16}$	$3.46x10^{19}$	$5.52x10^{-21}$	204	0.835	1.69	$6.998x10^{-48}$	15.418
-300*	$2.21x10^{-8}$	$2.25x10^{9}$	$8.24x10^{16}$	$5.65x10^{15}$	$8.65x10^{-21}$	163	0.667	1.35	$6.653x10^{-38}$	12.213
-400*	$6.93x10^{-7}$	$1.67x10^{9}$	$1.11x10^{17}$	$9.5x10^{14}$	$1.0x10^{-20}$	151	0.619	1.26	$4.842x10^{-35}$	11.391
-500*	$2.5x10^{-4}$	$1.99x10^{8}$	$9.32x10^{17}$	$6.1x10^{8}$	$2.91x10^{-20}$	89	0.364	0.738	$7.745x10^{-21}$	6.673
-600*	$1.97x10^{-3}$	$1.28x10^{8}$	$1.45x10^{18}$	$2.69x10^{8}$	$3.63x10^{-20}$	79.7	0.326	0.662	$3.656x10^{-18}$	5.969
-700*	$1.93x10^{-2}$	$1.23x10^{8}$	$1.51x10^{18}$	$1.90x10^{9}$	$3.7x10^{-20}$	78.9	0.322	0.655	$4.122x10^{-17}$	5.927
-300	$4.82x10^{-8}$	3.37x109	$5.51x10^{16}$	$2.85x10^{20}$	$1.77x10^{-21}$	180.4	0.738	1.498	$5.750x10^{-39}$	12.56
-500	$2.49x10^{-4}$	$1.97x10^{8}$	$9.42x10^{17}$	$5.93x10^{18}$	$7.33x10^{-21}$	88.7	0.363	0.736	$7.586x10^{-21}$	6.677
-200	$4.29x10^{-10}$	$9.94x10^{9}$	$1.86x10^{16}$	$3.82x10^{23}$	$1.03x10^{-21}$	236.5	0.967	1.963	$3.980x10^{-54}$	17.78
-400	$1.31x10^{-7}$	$1.76x10^{9}$	$1.05x10^{17}$	$3.91x10^{14}$	$2.45x10^{-21}$	153.5	0.628	1.274	$5.012x10^{-36}$	11.50
-600	$5.55x10^{-3}$	$6.83x10^{7}$	$2.72x10^{18}$	$1.98x10^{7}$	$1.24x10^{-20}$	68.1	0.278	0.565	$8.500x10^{-16}$	5.206
-700	$2.8x10^{-2}$	$7.93x10^{6}$	$2.34x10^{19}$	$9.83x10^{3}$	$3.65x10^{-20}$	39.75	0.163	0.329	$1.288x10^{-9}$	2.972

* Means those samples listed in Fig. 6.3.2.

** Means a is the intercept of fitting curves when using the power law fittting.

amorphous materials [86]. In explaining our results with variable range hopping process a further difficulty arise. The σ_{0VRH} increases linearly with T_{0VRH} when the deposition voltage changes from -200 V to -700 V as it is shown in Fig. 6.5.2. This is just opposite of that, what is expected, because of N(E_F), which increases by self bias voltage, is in reciproc relation with T_{0VRH} (Eq. 6.5.2) and is in linear relation with σ_{0VRH} (Eq. 6.5.3). These discrepancies accounted before make it strongly questionable, that above room temperature the variable range hopping process in the localized states near Fermi level where the real conduction mechanism.

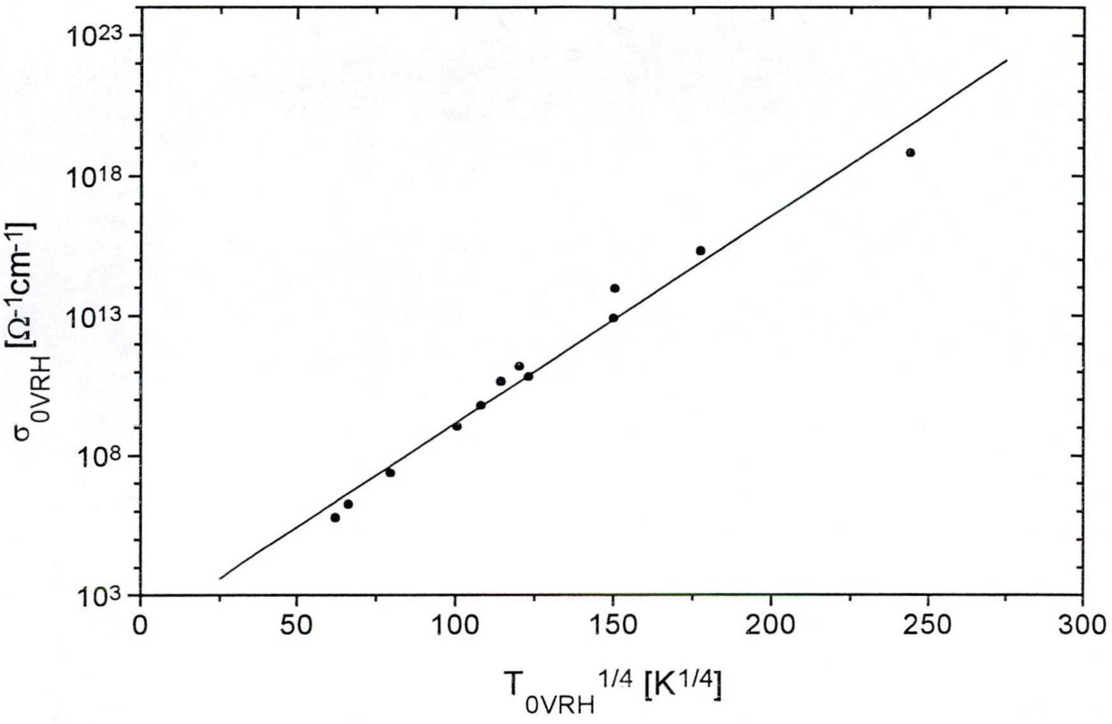

Fig. 6.5.2 Relation between σ_{0VRH} and T_{0VRH} for samples deposited by different self biases.

N(E_F) and σ_{0VRH} were estimated by supposing α^{-1} = 10 Å, however it influences significantly the calculated values. The localization length of electron wavefunction can be determined from the study thickness dependence of σ_{dc}. Experimental results are plotted in Fig. 6.5.3 for sample of -500 V, however similar behaviour was observed for other samples. Conductivity decreases with decreasing layer thickness down to 0.22 μ below which conductivity starts to increase. For other amorphous semiconductors the thickness dependence of σ_{dc} does not show minimum, but it decreases further with sample thickness [162]. Distinct behaviour in temperature dependence of σ_{dc} for samples of different thicknesses also occurs. For several amorphous semiconductors the $T^{-1/4}$ temperature dependence of σ_{dc} turns to $T^{-1/3}$ dependence when conduction changes from 3D into 2D. It takes place when sample thickness becomes smaller than the average hopping distance. From the slopes of $T^{-1/4}$ and $T^{-1/3}$ dependence the localization length α^{-1} and density of states N(E_F) can be calculated. From Fig. 6.5.3 one can see no transition to $T^{-1/3}$ dependence occurs in the studied temperature range. This gives further evidence, that electrical conduction near and above room temperature does not take place by variable range hopping of carriers through localized states near Fermi level.

Continuos curving of σ_{dc} vs. 1/T indicates, that transport process of a-C:H does not exhibit single activation energy in the measured temperature range. Non-activated dc transport measured in a-C:H is similar to that for the small polarons which if formed in the strong electron-lattice coupling [161]. But in the case of a-C:H small polaron formation is not expected because π electron share weakly localized or delocalized inside the sp^2 bonded sizes. Hence with increasing localization length (α^{-1}) decreases the probability of single phonon hopping [86] and multiphonon hopping process can be expected.

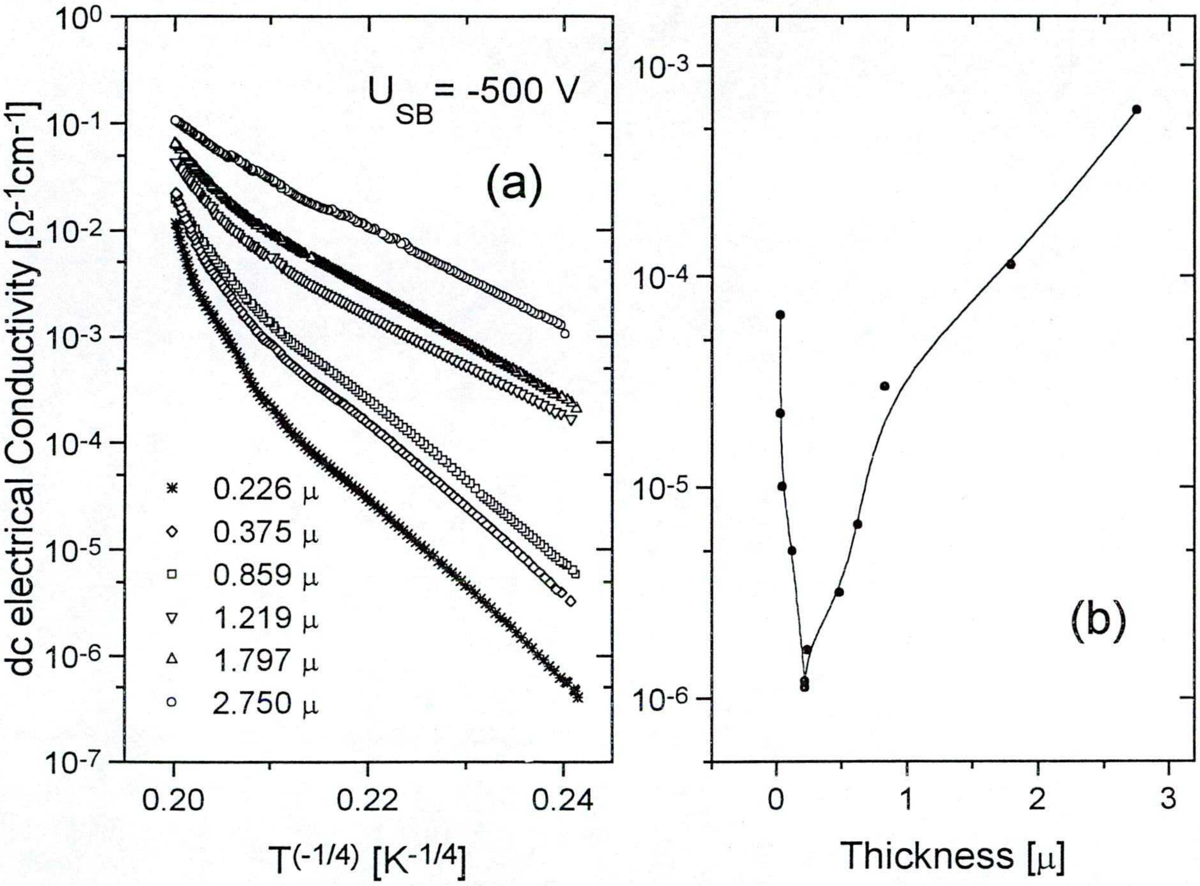

Fig. 6.5.3 (a) Temperature dependence of σ_{dc} for a-C:H samples of different thicknesses prepared by U_{SB} = -500 V and (b) Thickness dependence dc conductivity for a-C:H sample of U_{SB} = -500 V.

The dc hopping conductivity can be given by the equation [86] (for electrons)

$$\sigma_{dc} = \frac{N(eR)^2\nu}{6kT} \tag{6.5.4}$$

where N is the number of localized carriers, R is the hopping distance and ν is the hopping rate. Single phonon hopping is expected to occur when the site energy difference Δ and the polarization energy (lattice deformation) are less than the maximum phonon energy $\hbar\omega_m$. However when $\hbar\omega_m$ and Δ are comparable and the localization length (α^{-1}) much higher than the lattice constant (a_0), the probability of single phonon tunneling becomes very small [86]. In this case the multiphonon tunneling process gives the major calculation to electronic conduction [161].

Supposing weak electron–lattice interaction, the hopping rate due to multiphonon tunneling of localized electron is given by [86,161]

$$\nu = C \exp(-\gamma p) \exp(-2\alpha R) (T/T_0)^p \qquad (6.5.5)$$

where $C \cong \omega_0 / 2\pi$, $p = \Delta/\hbar\omega_0$, and $T_0 = \hbar\omega_0/k$. ω_0 is the frequency of the acoustic phonon which is coupled most effectively to localized electrons and p means the number of phonons involved in hopping process. The localization length (α^{-1}) is expected to be much higher than the average lattice separation (a_0) according to weak localization of π electrons. Since localized electrons with large localization length couple only to long wavelength phonons [161], therefore ω_0 in our case is smaller than the maximum phonon (Debye) frequency ω_m and is given by $(a_0/\alpha^{-1})\omega_m$ [161]. For the weak coupling, γ parameter lies between 2 and 3. Since density of localized states must be $N(E_F)kT$, from Equations 6.5.4 and 6.5.5 σ_{dc} is proportional T^p. The value of p should be an integral number; if Δ or ω_0 distributes around a certain mean value, p will be nonintegral.

In Fig. 6.5.4 the temperature dependence of dc electrical conductivity is plotted on double-logarithmic scale to demonstrate power law dependence. Straight line fitting was used

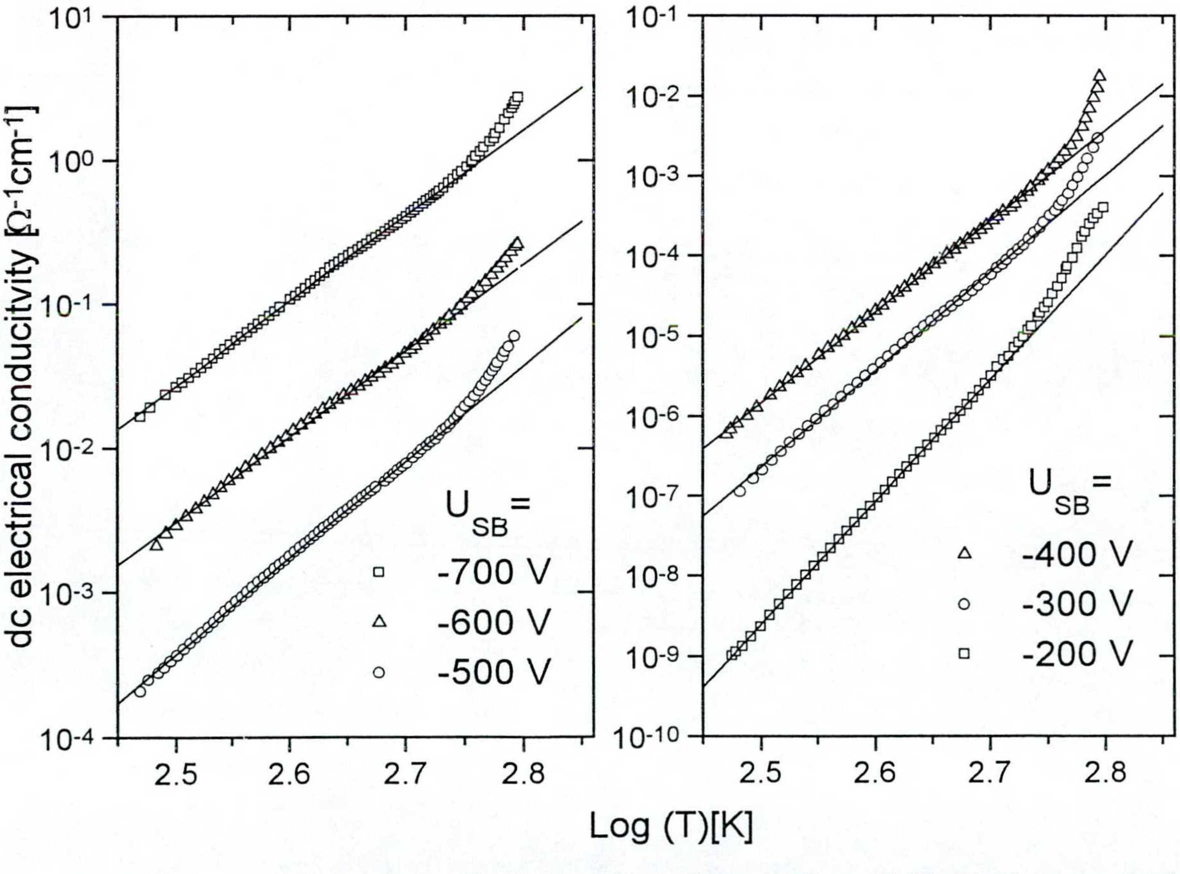

Fig. 6.5.4 Temperature dependence dc electrical conductivity for a-C:H samples prepared by different self bias voltages in double logarithmic plot. Straight lines were fitted to determine exponent of power law dependence.

to determine exponent of power law dependence. These exponent are listed in Table. 6.5.1; the number of phonons taking part in hopping process decreases appreciable by increasing deposition voltage. We have calculated σ_{dc} from Equations 6.5.4 and 6.5.5 taking $N(E_F)$ and p from Table. 6.5.1 and using the following parameters : $\gamma=4.5$, $\omega_0 = 2\times10^{11}\ s^{-1}$, T=300 K, $N=N(E_F)kT$, $R=N^{-1/3}$, and $\alpha^{-1} = 10$ Å. The theoretical curve and experimental results shown in Fig. 6.5.5 for a-C:H sample of U_{SB} = -200 V (a) and -700 V (b). Fitting of experimental data, especially at high temperatures is poor for -200 V sample and it becomes even worse for samples of higher self biases (-700 V as in Fig. 6.5.5.b). It should be mentioned, that some of these parameters were chosen arbitrary, however they are reasonable values. If we try to use other parameter set similar difficulties arise as before with fitting σ_{dc} in the whole temperature range. Our conclusion is that the multiphonon tunneling process fail to describe temperature dependence of dc conductivity of a-C:H above room temperature.

The more likely form of conduction mechanism is the conduction in tails or in extended states. At first we start with the strong change of slope on $\ln\sigma_{dc}$ versus 1/T curves which appears roughly at 500K for samples of different self biases (Fig. 6.3.2). Above this temperature a much larger slope indicates a transition to another conduction mechanism, when charge carriers are excited further from the Fermi level, into the bands of extended states. This transition is also indicated by the large scattering of derivatives at ~ 500K in Fig. 6.3.3. It is,

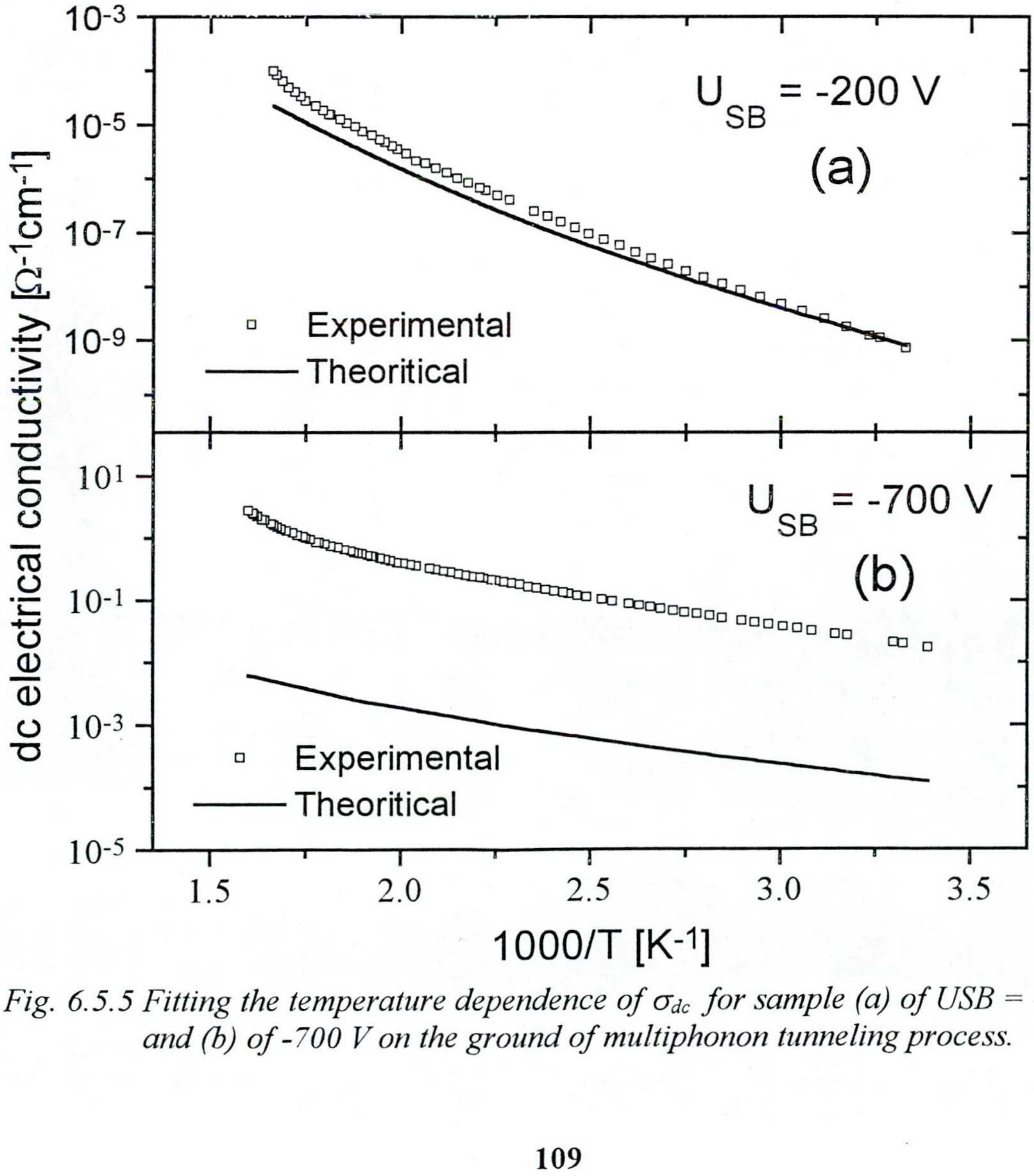

Fig. 6.5.5 Fitting the temperature dependence of σ_{dc} for sample (a) of USB = -200 V and (b) of -700 V on the ground of multiphonon tunneling process.

however, difficult to determine the activation energy of extended states conduction due to the narrow temperature range, in which sample structure is stable (hydrogen effusion). Taking E_{act} at 550K as an approximation, then the ~ 0.9 eV for sample of -200 V and ~ 0.4 eV for sample of -700 V are acceptable values if we compare these with the respective gap energies of 1.25 eV and 0.52 eV calculated from optical measurements for the two samples. Annealing shifts this transition temperature to a slightly higher one (Fig. 6.4.2) but it does not disappeared entirely what means that this change of slope observed at 500K, is not a consequence of structural changes occurring under conduction measurements at high temperature, rather a real transition to the other conduction mechanism.

Below ~500 K conduction is expected predominantly by hopping of carriers in localized tail-states connected to band edges and the temperature dependence of dc conductivity is characterised by the next equation (for electrons) :

$$\sigma_{dc} = \sigma_1 \exp\left[-\frac{E_A - E_F + w_1}{kT}\right], \tag{6.5.7}$$

where E_A is the extremity of conduction band tail states, E_F means the Fermi energy and w_1 is the activation energy for hopping [86]. Since the principal temperature dependence originates from the term of carrier activation (E_A -E_F), approximately linear dependence of ln σ_{dc} versus 1/T follows from Eq. 6.5.7. However, we should take into account three further factors in analysis of linearity: i) 'statistical' shift of Fermi level, ii) temperature dependence of band edges and iii) temperature dependence of hopping energy (w_1).

Let us examine the influence of the first two factors; if E_A - E_F has the following temperature dependence:

$$(E_A - E_F)_T = (E_A - E_F)_0 - \gamma T \tag{6.5.8}$$

where γ is the temperature coefficient, then ln σ_{dc} versus 1/T plot remains straight line with slope of E_0/k and with $\sigma_1\exp(\gamma/k)$ intercept on the σ_{dc} axis [86]. To evaluate statistical shift of Fermi level, we need its position in the gap. Undoped a-C:H was found n-type semiconductor with nearly fixed position of the Fermi level relative to the valence band, when deposition temperature was changed between 150 and 300°C [106]. Therefore we think that the temperature coefficient of the band edge (E_c) with respect to E_F would be about half of the temperature coefficient of the gap. From optical measurements as a function of temperature for amorphous materials the temperature coefficient of the gap is ~ 4 - 8 x 10^{-4} eV/K [158], then change of ~ 0.06 - 0.12 eV in the position of band edge comparing to E_F would be expected when temperature increases from 300 K to 600 K. If all states are assumed to shift rigidly with the bands, than shift of E_A respect to E_F is the same, however, since optical gap has negative temperature coefficient, the (E_A - E_F) decreases as the temperature increases. Therefore neither the statistical shift of E_F nor the temperature dependence of E_g does explain the increase of E_{act} with temperature in a-C:H.

Temperature dependence of w_1 is characterized by the next equation :

$$w_1 = \frac{3}{4}\left(\frac{8}{9}\right)^{3/4}\left[\frac{(kT)^{3-n}(\Delta E)^n \alpha^3}{\pi n^n N(E_c)}\right]^{1/4} \tag{6.5.9}$$

when variable range hopping of carriers is considered in tail states around energy E_m, at which the number of carriers is maximal [86]. ΔE means the width of the distribution of localized states, $N(E_c)$ is the density of localized states at the mobility edge, α^{-1} is decay length of the localized states and n is an exponent related to density of states distribution at the edge of conduction band. Supposing n=1, a linear density of states distribution, then w_l would have a $T^{1/2}$ temperature dependence (Eq. 6.5.7) what should be taken into account when we examine temperature dependence of dc conductivity. For evaluation of the temperature dependence of w_l. , we should choose values of parameters in Eq. 6.5.7 and calculate w_l at T = 300 K and T = 500 K , in the interesting temperature range. By supposing linear density of tail states (n=1), ~ 2×10^{21} cm^{-3} eV^{-1} for $N(E_c)$, ~0.3 eV for the range of tail states and α^{-1} = 10 Å, we will get w_l=0.05 eV at 300 K and w_l= 0.0645 eV at 500 K. In the same temperature range the increase of E_{act} is ~0.4 eV and ~0.1 eV for samples of U_{SB} = -200 V and -700V respectively what could not be explained by the increase of w_l. However, because significant structural differences exist between these two samples, we should use different parameters for the two cases. Due to stronger localization, $\alpha^{-1} < 10$ Å is more acceptable for sample of -200V and the wider energy range of localized states is also expected in this case. With parameters of α^{-1} = 5 Å and ΔE=0.5 eV, the hopping energies are 0.095 eV and 0.123 eV at 300 K and 500 K respectively. This increase is still small comparing to 0.4 eV increase of E_{act} in sample of -200 V, so the conclusion is that the temperature dependence of hopping energy does not explain the increase of E_{act} with temperature.

It seems more probable that this departure from simple Arrhenius behaviour of dc conductivity is linked closely to properties of localized tail states. In a-C:H the π states of sp^2 coordinated carbon atoms form tail states at energies depending considerably on numbers and clustering of sp^2 sites [22]. Effect of cluster size distribution on the energetic positions of π states is especially important in samples of low sp^2 content and results in quite broad energy distribution of tail states, but this effect can be weak in samples of much higher sp^2 content. The bonding heterogeneity (σ and π bonds) in a-C:H results in special properties of tail states giving a wide range of barrier heights for π electrons. Bulk conductivity of a similar heterogeneous lattice as a function of conductive nodes was simulated by Adler, Flora and Senturia [159] and the evaluation of temperature dependence of dc conductivity gave a continuously curving $\ln\sigma$ versus 1/T dependence. No activation energy can be determined unless in the case of small width of tail states.

Our results for a-C:H are in a good qualitative agreement with those gained by simulation of site percolation [159], however, the temperature gives a new dimension to the classical percolation problem. The conduction is not a that sort of simple conducting-or-not alternative in amorphous matter, like it is used in classical percolation description. The situation in amorphous matter (and so in a-C:H as well) is similar to the quantum percolation phenomena [163]. In such a case the percolation is investigated in the system of barriers, which can easily be passed for electrons over certain energies, but not for lower energy electrons, and there is a distribution of these barriers in the sample.

This way we have a generalized percolation problem, where is a static configuration of these barriers at a given temperature and time, as a static basis, and a dynamical process of electrons with different energies, which try to pass these barriers by some way, some sequence. Practically each static configuration will have a threshold energy, when an electron with that energy is able to pass the system, i.e. the system percolates for these electrons. Of course, different deposition condition prepares, and annealing changes further this static configuration of the barriers in the sample, so the threshold energy for percolation will be different, depending on these parameters. The actual activation energy, E_{act} is closely connected to the distribution of the energy barriers.

The a-C:H samples has an archipelago structure, sp^2 coordinated 'semimetallic' islands are embedded in the sea of insulating sp^3 coordinated matrix. The electrons are more-or-less delocalized inside these π-bonded sp^2 islands, and the sp^3 matrix act as barrier, localizing, confining the sp^2 islands. This localization has another parameter, the size-distribution of the sp^2 islands, clusters, whether the same amount of sp^2 carbon is distributed in a few larger, or many smaller islands, what causes a change in the distribution of barrier heights and widths of the sp^3 matrix between the islands. This sort of changes in barrier distribution causes large changes in the conductivity, because of the strongly non-linear contribution of the barrier height to the conduction.

That is, what we have observed in the case of amorphous carbon. Sample of U_{SB} = -200 V, of which the sp^2 coordinated carbon content is the smallest among the studied ones, shows 5 order of magnitude increase of conductivity and ~ 0.4 eV enhancement of E_{act} in the temperature range of 300-600 K. In contrast, samples of U_{SB} = -700 V, with sp^2 content of the largest among the investigated specimens, showing the largest room temperature conductivity, exhibits only 1.5 order of magnitude increase of conductivity and ~ 0.1 eV enhancement of E_{act} over the same temperature range. It is also hard to understand the 7 order of magnitude differences in the room temperature conductivity between these two samples exclusively from the increase of sp^2 coordinated carbon content (~30 at%) [160], however it seems quite reliable if we take into account the cluster size distribution, and as a consequence of this, the percolation behaviour of conducting paths.

7. OPTICAL PROPERTIES

One of the most important applications of a-C:H films is the coating of optical elements, where this film act as both mechanical protection and as an anti-reflection coating. With regard to this application the optical properties of a-C:H layers are of peculiar interest. Layers of a-C:H exhibited an optical gap E_{opt} [113,61,62], a refractive index n [164], and a characteristic hardness [171] all of which are strongly influences by the impact energy of the film forming particles. This energy determined by the deposition parameters, e.g. the negative self bias voltage and pressure [125]. Using benzene in the plasma deposition process, a soft "polymer-like" layer can be deposited, with E_{opt} ~3 eV and n ~ 1.7, at low self bias (~100 V) and high pressure (>5 Pa). However high deposition voltage (~1000 V) and low pressure (< 3 Pa) are favorable for hard diamond-like film with E_{opt} ~1.3 eV and n ~1.9-2.2 [172]. Although, at much lower than ~1000 V self bias, a-C:H extends from about e.g. 100 V to 1kV in methane discharge depending on process pressure [173].

Our study was concentrated onto influence of deposition voltage on the optical properties, such as dielectric function, refractive index, optical gap as well in order to find relation between optical characteristics and structural properties of these thin layers. Spectral ellipsometry and transmission measurements were employed to determine, in the UV, visible and near infrared region, optical properties of samples obtained from methane plasma by self biases of 200-700 V. In this chapter at first we review shortly optical properties and relation between them. In the subsection of 7.1 principal of ellipsometry is introduced and it is followed by experimental results obtained with this method and by discussion of relation between optical and structure properties. In the next subsection we are dealing with how the transmittance measurements can be used for determination absorption edge and layer thickness. the results of transmittance measurements are also presented there. Optical absorption gap and their relation to bonding properties of samples are discussed in the subsection of 7.3.

The optical properties of an isotropic absorbing medium are mostly conveniently expressed in terms of the complex index of refraction N=n+ik and the complex dielectric function $\varepsilon = \varepsilon_1 + i\varepsilon_2$, where the refractive indices n and k and the dielectric constants ε_1 and ε_2 are all real functions of photon frequency ω [165–167]. The two representations are related at any given frequency according to

$$\varepsilon_1 = n^2 - k^2 ,\qquad \varepsilon_2 = 2nk \tag{7.1}$$

The optical constants are connected together with the general Kramers-Kronig dispersion relations. Thus if $\varepsilon_2(\omega)$ is known over the whole range of photon frequencies, $\varepsilon_1(\omega)$ can be calculated at any frequency:

$$\varepsilon_1(\omega) = 1 + \frac{2}{\pi}\int_0^\infty \frac{\xi}{\xi^2 - \omega^2}\varepsilon_2(\xi)\, d\xi \tag{7.2}$$

where ξ takes values other than ω. A similar expression connects $n(\omega)$ and $k(\omega)$. Because energy is conserved in optical transitions, such transitions are absorptive and contribute to $\varepsilon_2(\omega)$, the imaginary part of the dielectric function. Their contribution to the dispersive part $\varepsilon_1(\omega)$ is computed from Eq. 7.2.

A common way to discuss theoretical properties of metals and semiconductors is to describe the dielectric function in terms of the electronic band structure of a crystal and distinguish between bound and free electrons (or free carriers). One can assume that both additively contribute to the $\varepsilon = \varepsilon_1 + i\varepsilon_2$. Unlike metals, the optical properties of semiconductors are governed by the bound electrons, because the number of free carriers is several orders of magnitude less. We may therefore consider interband transitions; optical properties of amorphous semiconductors can be understood from one-electron excitations. Because values of ε_1 and ε_2 can be related by means of Karmers-Kornig relations, therefore it is sufficient to determine $\varepsilon_2(\omega)$, for theoretical approach. However, in this case, one must know $\varepsilon_2(\omega)$ for all the values of ω in order to calculate $\varepsilon_1(\omega)$.

The real part of the complex dielectric function $\varepsilon_1(\omega)$, describes the polarization aspect of an electron system. In solids such ass insulators or semiconductors the interband polarizability and its associated dielectric function $\varepsilon_1(\omega)$ are responsible for the characteristic optical properties in the visible and UV ranges as only polarizability is effective at high photon frequencies [167].

For amorphous semiconductors the imaginary part of the complex dielectric function $\varepsilon_2(\omega)$ times ω^2 is proportional to the convolution of the optical density of states in the valence and conduction bands for which energy is conserved, and is given by

$$\omega^2\,\varepsilon_2(\omega) = \text{const}\ \Sigma|\langle f|P|i\rangle|^2\,\delta\,(E_f-E_i-\hbar\omega) \qquad (7.3)$$

P is the momentum operator and the sum is over all initial (i) valence and final (f) conduction-band states separated by an energy $\hbar\omega$. The δ function describes the conservation of energy. For a constant matrix element this equation reduces to

$$\omega^2\,\varepsilon_2(\omega) = \text{const} \int_0^{\hbar\omega} g_c(E)\ \ g_v(E - \hbar\omega)\ \ d\omega \qquad (7.4)$$

where $g_c(E)$ and $g_v(E- \hbar\omega)$ are the one-electron density of states of the conduction and valence bands, respectively. The loss of long-range order in amorphous materials leads to the relaxation of the k-conservation selection rule for optical transition. Consequently the $\varepsilon_2(\omega)$ spectra of amorphous materials are smooth in contrast to the spectra of their single-crystal counterparts which show structure of singularities.

The usual assumption is that the density of states of the conduction band $g_c(E)$ is featureless and can be considered to be a step function [174] then the product $\omega^2\ \varepsilon_2(\omega)$ is proportional to the integral of the density of valence-band states. In amorphous semiconductors it is also assumed that the density of states just beyond the mobility edges has a square-root dependence on energy. If band edges are parabolic the Eq. 7.4 reduces to

$$\omega^2\,\varepsilon_2(\omega) = B\,(\hbar\omega - E_0)^2 \qquad (7.5)$$

which defines the optical gap E_0. Eq. 7.5 gives $\varepsilon_2(\omega)$ spectra for excitations at the absorption edge. The constant B proportional to joint density of states. Below mobility edge the band tails are exponential and Eq. 7.5 yields the Urbach tail.

7.1. Optical properties determined by spectral ellipsometry

Ellipsometry measures the change in polarization state of a linearly polarized beam of light after non-normal reflection from the sample to be studied. The term ellipsometry originates from the fact that the light becomes elliptically polarized after the oblique reflection (Fig. 7.1.1) due to the different reflection coefficients for p- and s- polarized light (p stands for parallel and s for perpendicular). The polarization state can be defined by two parameters, for example, the relative phase and relative amplitude of the orthogonal electric-field components of the polarized light wave. On reflection, both electric-field components are modified in a linear way, and therefore a single ellipsometric measurements provides two independent parameters. By measuring the polarization ellipse, one can determine the complex dielectric function of the sample.

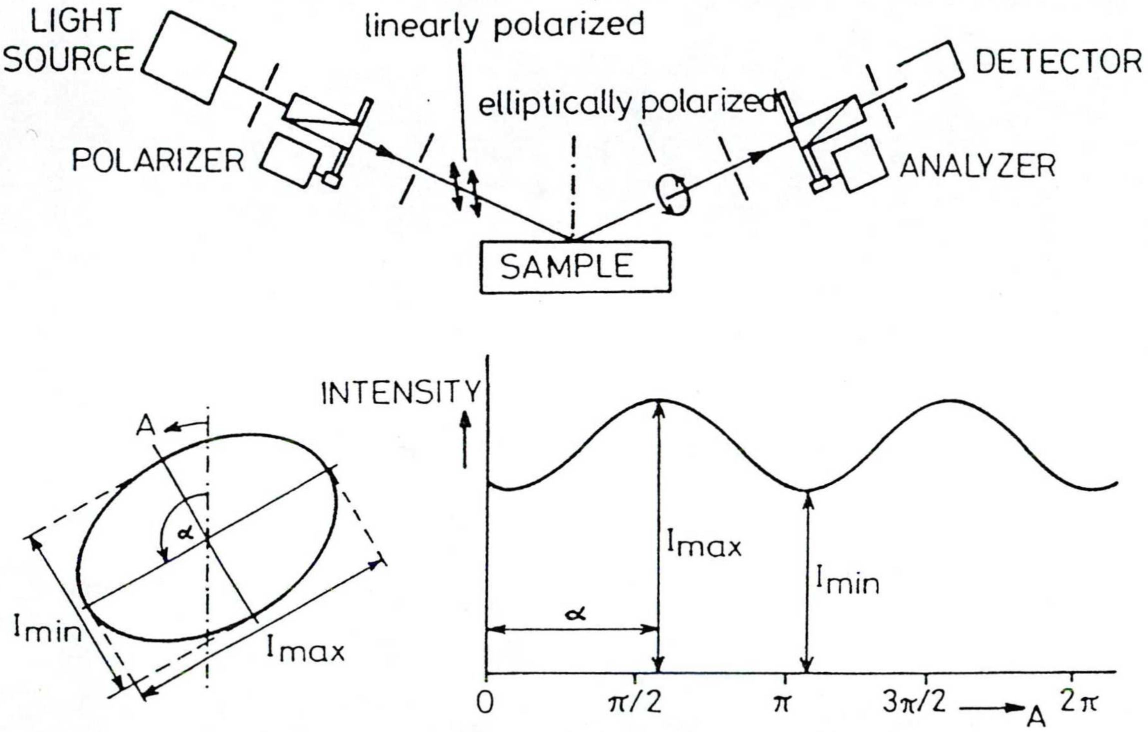

Fig. 7.1.1 Principle of a rotating analyzer ellipsometer. Riedling (1988). Ellipsometry for Industrial Application. Springer-Verlag, Wien, New York.

Here we outline some results of electromagnetic theory as background to help in understanding of different techniques used to determine the optical properties of a materials. An incident plane wave propagating in the z-direction of a local orthogonal coordinate system can be represented as

$$E_i(\psi,t) = \mathrm{Re}\left[(\hat{x}E_x + \hat{y}E_y)\exp\left(i(\omega t + d - \frac{N\omega}{c}z)\right)\right] \qquad (7.1.1)$$

where E_x and E_y are the complex field coefficients describing the amplitude and phase dependencies of the projections $E_i(\psi,t)$ along the x and y axes. The complex dielectric constant ε is connected to complex refractive index N through $\varepsilon = N^2$. If the electromagnetic wave is reflected by a smooth surface; the outgoing wave can be represented in the absence of anistropic effects in another local coordinate system as

$$E_i(\psi, t) = \mathrm{Re}\left[(\hat{x}E_x + \hat{y}E_y)\ \exp\left(i(\omega t + \delta - \frac{N\omega}{c}z')\right)\right] \tag{7.1.2}$$

where in both local coordinate system the x axes are in plane of incidence, the y axes is perpendicular to the plane of incidence, and the z and z' axes define the plane of incidence.

In this approximation, the effect of the surface is described by two coefficients r_p and r_s. These complex reflection coefficients describe the influence of the sample on the field components parallel (p) and perpendicular (s) to the plane of incidence. Thus four quantities – two amplitudes and two phases – are necessary to characterize the incoming wave completely, and four more are necessary to describe the sample. Consequently, the properties of the sample are obtained if the properties both incident and reflected waves are known. Reflectometry and ellipsometry are two techniques for obtaining this information.

It is useful to rewrite four parameters describing the plane waves Eqs. 7.1.1 and 7.1.2 into four new parameters by means of the concept of the polarization ellipse. The polarization ellipse is the focus traced out in time by the endpoint of the electric field vector E(ψ,t) at any fixed plane $z = z_i$. The polarization ellipse has two attributes that can be termed amplitude and shape. The amplitude $E = (|E_x|^2 + |E_y|^2)^{1/2}$ is a scalar whose square is proportional to the energy density of the wave or intensity I. The intensity is the only quantity of interest in reflectance or transmittance measurement and one of the quantities of interest in a polarimetric measurements. The shape is an intensity independent, complex quantity, and a possible representation is the polarization state, $\chi = E_x/E_y$. In ellipsometry, the ratio of polarization states yields a somewhat different perspective of the sample compared to reflectance. By Eqs 7.1.1 and 7.1.2,

$$\frac{\chi_r}{\chi_i} = \frac{r_p E_r / r_s E_y}{E_x / E_y} = \frac{r_p}{r_s} \tag{7.1.3.a}$$

$$= \rho = (\tan\psi)\, e^{i\Delta} \tag{7.1.3.b}$$

The complex reflectance ratio ρ is conveniently expressed as an amplitude ratio tan ψ and a phase difference Δ. Ellipsometry is very powerful [176]; in any single-measurement operation, two independent parameters are determined simultaneously. For example, both real and imaginary parts of the complex dielectric function ε of a homogenous material can be obtained together at every wavelength without Kramers-Kronig analysis. Further advantages and some disadvantages are reviewed in Ref. [176].

ρ or ψ and Δ (the ellipsometric angles) only describe the reflection properties of the surface in question. Above they give no information about the structure or even the composition of the sample. To obtain this information some optical model of the surface must be assumed. Most optical models use flat semi-infinite substrates with one or more nominal adherent layers of uniform thickness on the surface. All interfaces are assumed to be sharp, and all layers are assumed to be composed of optically isotropic materials. Vertical inhomogenities or interface layers can easily be accounted for if ψ and Δ are calculated from known sample parameters, that is, we can approximate by a stack of sufficiently thin homogenous layers with suitable graded refractive indices. After a layer model is selected, the ellipsometric equation (Eq. 7.1.3.b) describing the ellipsometric properties of the model may be derived from the Fresnel equation [175]. The ellipsometric equation has dependencies in the complex refractive indices and film thickness in the model.

To obtain ellipsometric spectra, we employed a SOPRA ESG4 rotating polarizer spectroscopic ellipsometer at an angle of incidence of 75.25°. A substrate model was then used to calculate the optical constants from the measured ellipsometric angles. Optical constants were determined in the photon energy range of 1.47-4.59 eV (270 - 840 nm). Series of a-C:H samples prepared in radio frequency (rf) plasma discharge of methane (60 mtorr) by varying the negative self bias (U_{SB}) in the range of 200 V < $|U_{SB}|$ < 600 V were studied. The substrate material was <111> oriented P doped Si wafer (Wacker, 5.6-10.4 Ωcm).

Ellipsometric measurements on our samples were performed in collaboration with Institute for Technical Physics and Material Sciences, Fraunhofer Institute and Universität Erlangen.

For characterization of a-C:H sample series studied in optical measurements we summarized deposition self biases and some physical properties of the layer in Table. 7.1.1. Refractive indices at 500 nm. and optical gaps determined by spectral ellipsometry are given in this Table. The properties of a-C:H show strong correlation with deposition voltages.

Table. 7.1.1 Summary of preparation conditions and some properties of investigated a-C:H samples as well as properties of diamond [10] and graphite [11].

Deposition voltage U_{SB}(V)	**Hydrogen content at%**	**Refractive index at $\lambda = 0.5$ μm**	**Optical gap (eV)**	**dc conductivity ($\Omega^{-1}cm^{-1}$)**
-200	42	2.19	1.25	$4.1x10^{-10}$
-300	38	2.18	1.27	$4.9x10^{-8}$
-400	37	2.17	1.24	$4.2x10^{-6}$
-500	34	2.14	1.08	$4.5x10^{-3}$
-600	32	1.91	0.52	$2.3x10^{-2}$
Diamond	-	2.42	5.4	10^{-18}
Graphite	-	2.52	-0.04	$2.5x10^{4}$ (⊥c)

Increasing ratio of triple coordinated (sp^2 hybridized) carbon atoms relative to fourfold coordinated (sp^3 hybridized) ones with deposition self bias results in considerable change in electronic band structure of a-C:H samples. It can be expected an increasing number of localized states in mobility gap as well as a higher concentration of tail states as the deposition self bias increases. The direct current (dc) electrical conductivity of $4x10^{-10}$ $\Omega^{-1}cm^{-1}$ and $2.3x10^{-2}$ $\Omega^{-1}cm^{-1}$ measured at room temperature for a-C:H samples with U_{SB} = -200 V and -600 V respectively supply strong evidence for a large number of localized states in high voltage samples [169]. Relation between bonding structure and optical properties are discussed later.

Fig. 7.1.2 shows the photon energy dependence of the real part of the complex refractive index n for samples deposited at different self biases determined by spectral ellipsometry. Interference effects appearing in the IR region results from the insufficiently large sample thickness. The curves show unambiguous dependence on deposition voltage with the largest change observed for the -600 V sample. As the deposition voltage decreases the spectral dependence of the refractive index becomes less pronounced; this is in good agreement with a trend of more diamond-like behaviour. At 2.5 eV the diamond's refractive index is n = 2.42; a-C:H samples deposited by self biases of -200 V to -400 V take values of n similar to diamond. A strong decrease of refractive index can be observed as the photon energy increases from the IR region through the visible toward the UV region. Near 2 eV the curves, except for the -600 V samples, approach the same value and weak dispersion occurs in the IR region. The spectral dependence of n of a-C:H layers is considerably different from that of diamond, or of graphite.

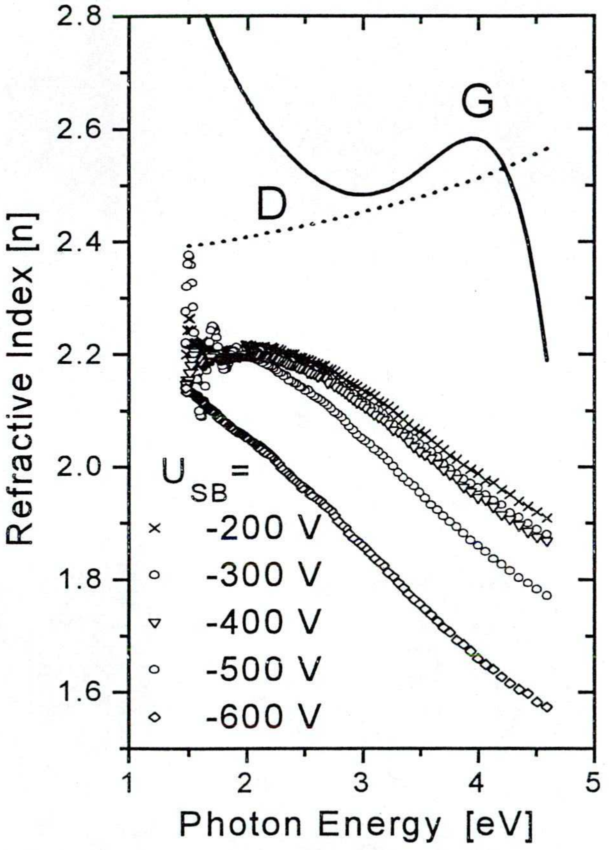

Fig. 7.1.2 Photon energy dependence of the real part of the complex refractive index for different a-C:H samples. For comparison curve D shows n for the diamond [10] and curve G shows n for crystalline graphite, when E ⊥ c [11].

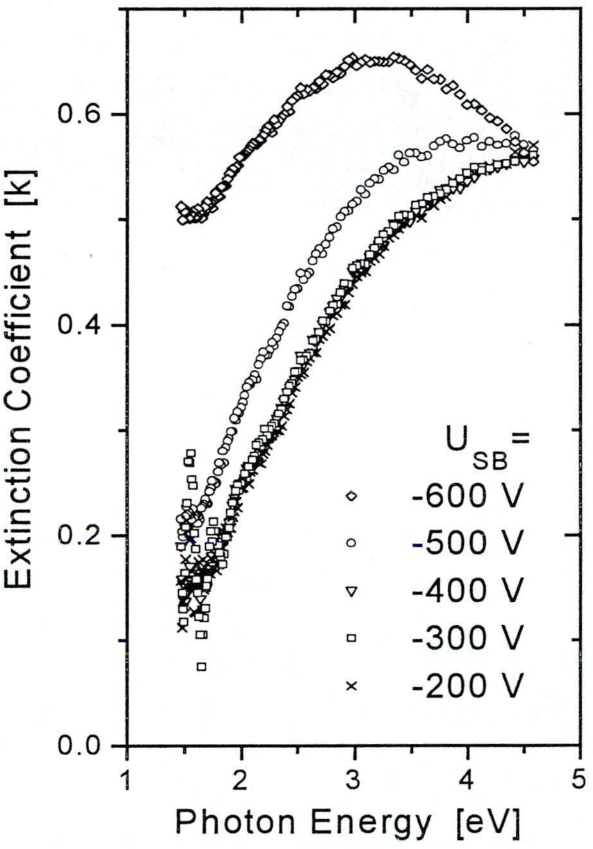

Fig. 7.1.3 Imaginary part k of the complex refractive index vs. photon energy for different a-C:H samples.

Fig. 7.1.3 shows the spectral dependence of the extinction coefficient (the imaginary part of the complex refractive index). With decreasing photon energy, the k approaches zero in good agreement with the fact that at these frequencies the a-C:H layers become transparent. The -600V sample is an exceptional case in this respect since, due to its large density of localized states in the gap, it displays considerable absorption in this IR region too. With increasing photon energy k increases sharply to a maximum which is in the 3 - 3.5 eV region for the -600 V sample, and it shifts to larger energies with decreasing deposition voltage. The absorption edge lies below this maximum, where k increases rapidly. The absorption edge is shifted to higher photon energy as the deposition voltage decreases thereby indicating a larger optical gap in these samples.

By using the relation between complex refractive index and complex dielectric functions (Eq. 7.1) we determined the dielectric functions ε_1 and ε_2. Fig. 7.1.4 displays the photon energy dependence of ε_1 for different a-C:H layers. With increasing U_{SB}, ε_1 tends to be smaller in the whole photon energy range studied; however, the most pronounced decrease occurs at U_{SB} = -500 V. The $\varepsilon_1(\omega)$ shows a weak spectral dependence in the IR region and a stronger dependence on photon energy appears in the visible and UV region for all samples. Our $\varepsilon_1(\omega)$ spectra of a-C:H samples prepared by 200–400 V self biases exhibits similar properties to that measured for diamond-like samples which were prepared from benzene plasma at U_{SB} = -1000 V [172]. The diamond-like sample annealed at 480 °C displays nearly the same $\varepsilon_1(\omega)$ spectrum [172] as that of our 600 V sample.

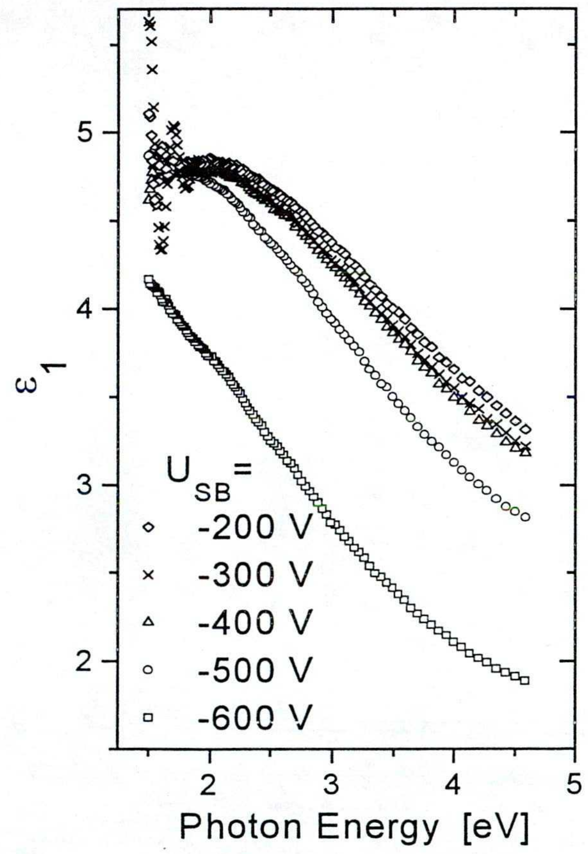

Fig. 7.1.4 Real Part of dielectric function ε_1 vs. photon energy for a-C:H layers of different self biases.

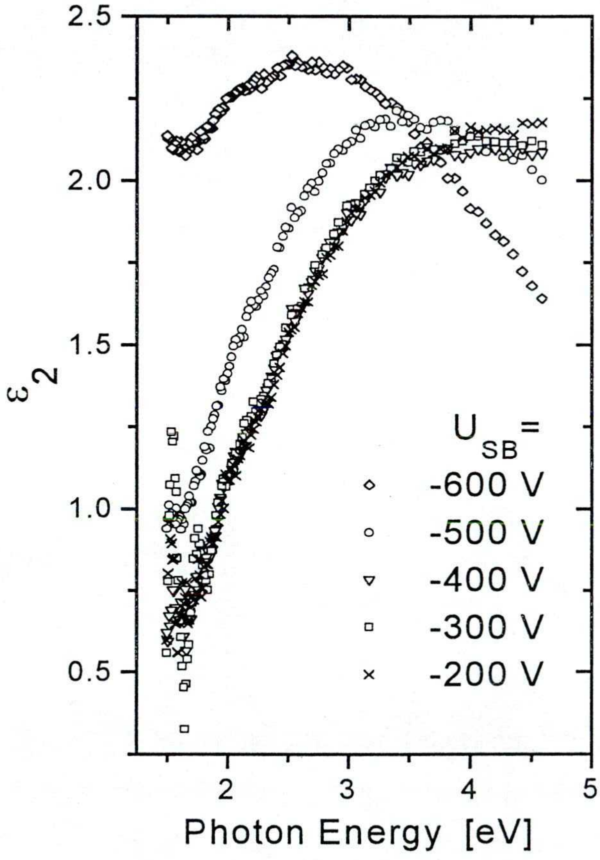

Fig. 7.1.5 Imaginary part of dielectric function ε_2 vs. photon energy for different a-C:H layers of different self biases.

The $\varepsilon_2(\omega)$ spectra, (Fig. 7.1.5) display a broad maximum which shifts to higher energies as the deposition self bias decreases. The position of the maximum was determined by derivation of $\varepsilon_2(\omega)$ curves. Fig. 7.1.6 shows deposition voltage dependence of maximum position; it decreases from 4.667 eV to 2.695 eV as the deposition voltage increases in the range of 200-600 V. The inset of Fig. 7.1.6 shows $\delta\varepsilon_2/\delta\varepsilon$ as a function of photon energy for different samples except for -300 V sample, because the derivatives in the range of -200 V to -400 V is close to each other. However, it is clear from Fig. 7.1.5 that the $\varepsilon_2(\omega)$ dispersion curves for samples of -200 to -400 V are very similar to each other and the more stronger change occurs in the case of -500 V sample. The spectral dependence of ε_2 shows the usual behaviour: it sharply increases with energy below ~3 eV thereby indicating an absorption edge in that region. Then spectrum rises to a peak, ε_{2max} whose position varies with sample structure.

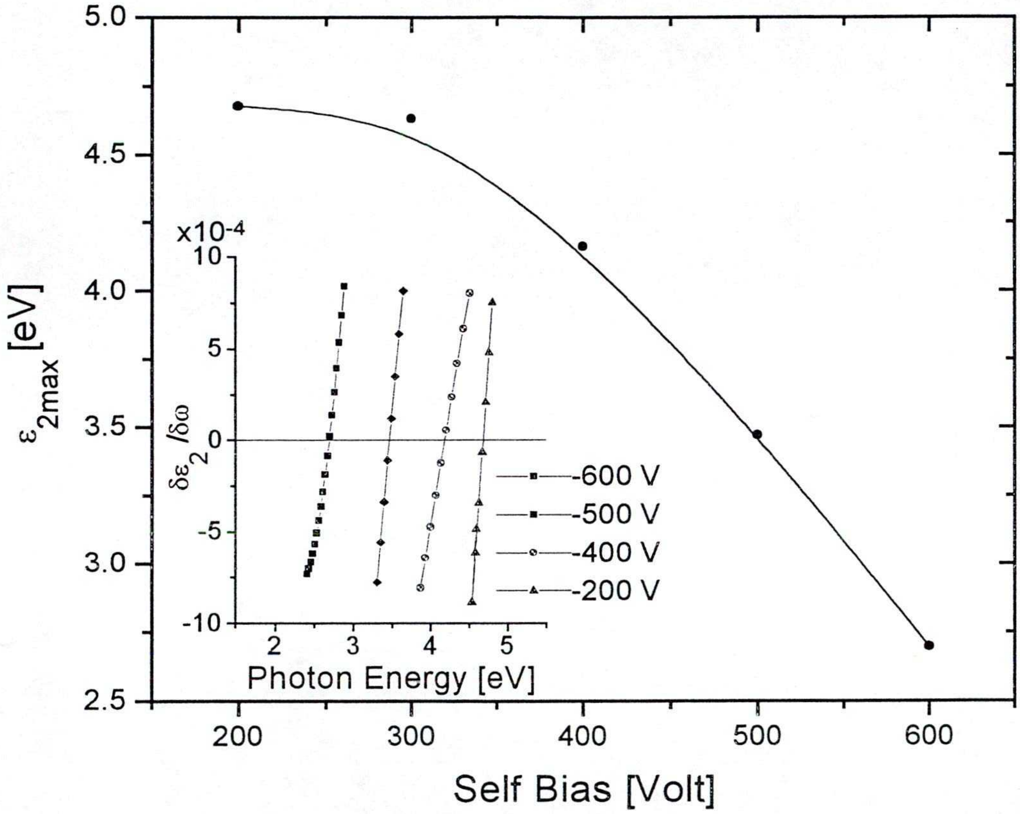

Fig. 7.1.6 Energy of the maximum in $\varepsilon_2(\omega)$ plotted versus deposition voltage. The inset shows the first derivative $\delta\varepsilon_2/\delta\omega$ vs. photon energy for a-C:H samples at different self biases.

Our aim is to relate the measured optical properties to the bonding structure of a-C:H layers. At sp^3 bonding sites each of the four valence electrons of a carbon form tetrahedrally directed σ bonds with four adjacent carbon atoms; these bonds give diamond its rigidity and wide band gap. At sp^2 sites, as in graphite, three of the valence electrons form triagonally directed σ bonds such as the strong intralayer σ bonds of graphite. The fourth electron is placed $p\pi$ orbital lying normal to the layer and this forms weaker π bonds which give rise to the anisotropic metallic character of graphite.

The electronic band structure of an amorphous carbon layer which contains sp^3 and sp^2 hybridized carbon atoms can be described as follows. The σ bonds give rise to valence band of filled bonding (σ) states and a conduction band of empty antibonding (σ^*) states, separated by a wide band gap of at least 5 eV. The filled π band and the empty π* band lie largely within the σ–σ* gap. Therefore the electronic structure of an a-C:H layer depends primarily on the π states because these states lie closest to the Fermi level. The π bonding strongly favors clustering into aromatic rings rather than olefinic chains and also favors the clustering of separate rings into graphitic sheets [113], which considerably influences the π–π* splitting and the band gap of a-C:H.

As is proven by both IR absorption and dc electrical measurements the ratio of sp^2 coordinated carbon atoms increases by changing deposition voltage from -200 V to -600 V (Chapter 5 and 6). If these carbon atoms were to form graphite clusters then an increasing refractive index could be expected with increasing deposition voltage – which just the opposite to the experimental results (Fig. 7.1.7). The sample of U_{SB} = -600 V shows the smallest refractive index among the a-C:H layers studied and in addition the spectral dependence of the refractive index does not resemble that of graphite (Fig. 7.1.1). Although the IR absorption band observed at 1580 cm^{-1} indicates formation of graphite clusters in samples of U_{SB} = -500 V and -600 V, the refractive index is not dominated by these structural units. The refractive index seems to change parallely with the average density, which starts to decrease at about U_{SB} = -500 V for a-C:H samples prepared from methane [113].

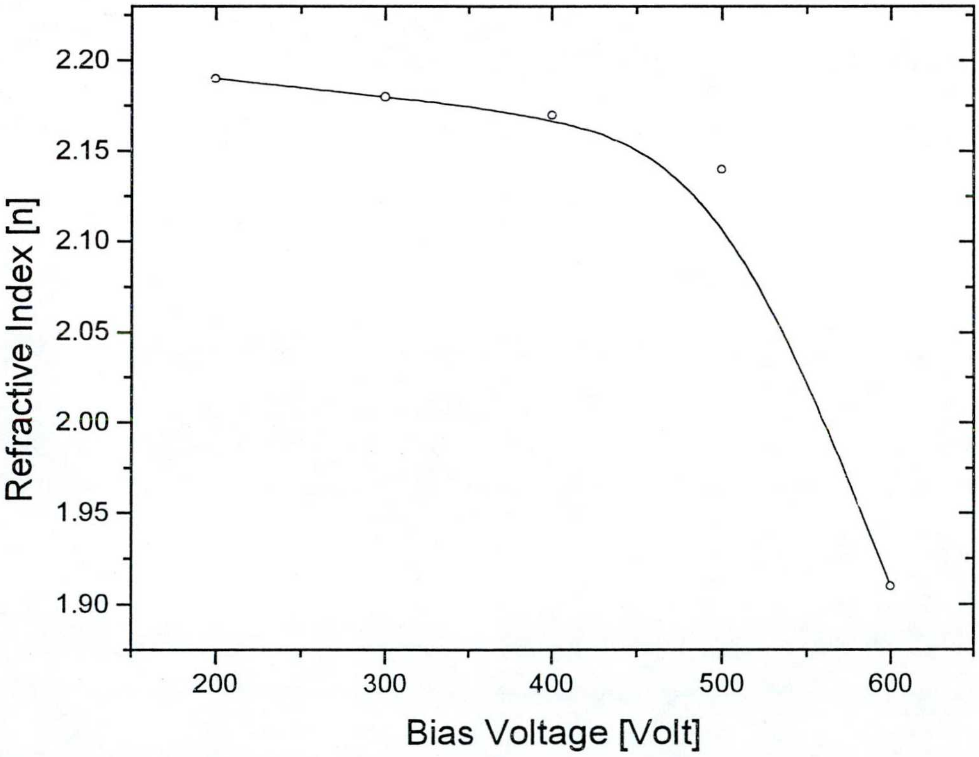

Fig. 7.1.7 Refractive index (n) at λ = 500 nm. of a-C:H samples plotted vs. deposition voltage.

The a-C:H samples prepared in the self bias range of -200 to -400 V display diamond-like behaviour. Their refractive index approaches that of diamond and they show insulating properties (Table. 7.1.1). However, it should be mentioned that the overall spectral dependence of n for these low self bias samples is in contrast to that of diamond. Differences in the bonding properties of diamond-like samples compared to the properties of the layers prepared at high voltages offer an explanation for the structural background of different behaviour. Important features of IR spectra of diamond-like samples are as follows: i) there is no absorption at 1580 cm^{-1} due to aromatic sp^2 carbon atoms, ii) there is an absorption band at about 2180 cm^{-1} assigned to sp^1 hybridized carbon atoms, iii) the sp^2 hybridized carbons are in olefinic configuration, iv) the most intensive absorption occurs near 3000 cm^{-1} assigned to C–H stretching bands. Intermediate range ordering of sp^2 coordinated carbon atoms and it might be the formation of sp^1 hybridized carbons are main structural features in determination of optical properties similar to diamond, because hydrogenated sp^3 carbons yields soft, polymeric properties with low refraction index (~1.7).

The $\varepsilon_1(\omega)$ (Fig. 7.1.4) does not show any structure over 3 eV photon energy in contrast to graphite [11]; this strongly suggests, that no extended graphite structure is present in the samples. The ε_1 values and their slow change with photon energy make their behavior more similar to that of diamond at least in the case of low voltages samples. $\varepsilon_1(\omega)$ follows the trend what is expected from $\varepsilon_2(\omega)$ taking into account the Kramers-Kornig relation. According to that the dispersion maximum of 600 V sample is located at much smaller energy than our measuring range.

The broad maximum in $\varepsilon_2(\omega)$ and its energetic position can be understood if we suppose increasing clustering of sp^2 coordinated carbon atoms with increase U_{SB}. Increasing cluster sizes result in decreasing $\pi-\pi^*$ splitting and red shift of the maximum in the $\varepsilon_2(\omega)$ spectrum. As a consequence the optical gap decreases from ~1.3 eV to ~ 0.5 eV as the U_{SB} changes in the range of -200 to -600 V. Experimental evidence for more extended clustering in high voltages samples comes from IR and Raman measurements (Chapter 5).

Supposing Transition matrix element in Eq. 7.3 to be energy independent, then the $\varepsilon_2(\omega)$ is proportional with the joint valence and conduction band density of states. Therefore, as it can be inferred from $\varepsilon_2(\omega)$ spectra, the joint density of states displays maximum at different energies in samples prepared in self bias range of 200-600 V. It is quit reliable, because in this photon energy range the $\pi-\pi^*$ transitions are dominant. The $\pi-\pi^*$ energy splitting correlates with cluster size, that is larger cluster size corresponds to smaller $\pi-\pi^*$ energy splitting. The peak position of $\varepsilon_2(\omega)$ occurring at smaller energy by ~ 2 eV for 600 V sample compared to 200 V sample indicates that the dominant cluster sizes considerable larger in this sample than in the lower voltages ones. This peak position in density of states might be corresponds to energy of mobility edge in a-C:H, because both temperature dependence of dc conduction and photoluminescence measurements [177,178] confirm that carriers excited by optical gap energy do not become delocalized following excitation.

7.2. Transmission in visible and near infrared region; interference fringes

The complex dielectric function as well as the complex refractive index of different a-C:H samples determined by spectral ellipsometry were discussed in previous section. Here we have outlined advantages of ellipsometry and its dependence on optical model. For comparison optical absorption coefficient in the absorption edge region and the optical gap were determined by optical transmission measurements for different a-C:H samples. The agreement between results obtained by the two methods is quite well as it is demonstrated later.

The absorption coefficient (α), when $n^2 >> k^2$, can be determined from the transmission (t) of thin layer of the material by using equation [179]:

$$t = \frac{(1-R^2)\left[1+(\lambda\alpha/4\pi n)^2\right]}{(e^{\beta}-Re^{-\beta})^2+4R\ \sin^2(\xi+\zeta)}, \tag{7.2.1}$$

where R means reflection coefficient at normal incidence, $\beta = \alpha d/2$, d is the layer thickness and $\xi = 2\pi nd/\lambda$ is the phase shift; angle of ζ is calculated by $\mathrm{tg}\ \zeta = \alpha\lambda\left\{2\pi\left[n^2+\frac{\lambda^2\alpha^2}{16\pi^2}-1\right]\right\}^{-1}$. In the case, when interference fringes do not occur (because surface roughness or due to other reasons), relation between t,R and α is the following [179]:

$$t = \frac{(1-R)^2\left[1+(\lambda\alpha/4\pi n)^2\right]}{e^{\alpha d}-R^2e^{-\alpha d}} \tag{7.2.2}$$

If $n^2 >> k^2$ or $(\alpha\lambda/4\pi) < 1$, the absorption coefficient in the transmission range from $(1-R)/(1+R)$ to 10% is calculated by equation

$$t = \frac{(1-R)^2\ e^{-\alpha d}}{1-R^2\ e^{-2\alpha d}} \tag{7.2.3}$$

Even this simple formula requires enormous computation. For transmission t < 10 % (henceforward $n^2 >> k^2$) the calculation of absorption coefficient can be done by equation

$$\alpha = \frac{1}{d}\ \ln\frac{(1-R)^2}{t} \tag{7.2.4}$$

Now we proceed discussion with thin layer deposited on substarte material of which refractive index differs from the layer material and from vacuum (or ambient) too. Reflection from layer substrate boundary and substarte ambient boundary need to take into account. In the most simple case, when absorption of the layer material is very strong and absorption of substrate is negligible then Eq. 7.2.4 related to free standing sample should be modified:

$$\alpha = \frac{1}{d}\ \ln\frac{(1-R_1)(1-R_2)(1-R_{12})}{t} \tag{7.2.5}$$

where R_{12}, R_2, and R_1 are the reflection coefficient of thin layer-substrate boundary, of substrate-ambient boundary and thin layer-ambient boundary respectively. Samples of different thicknesses we need; thin layers of $\alpha d >> 1$ can be used to determine reflection coefficient because thick layer excludes reflection from back surface. Thin layers, for which $\alpha d \leq 1$ or $(1-R)/(1+R) > t > 10$ % in the most transparent region, are used for determination of transmission. The absorption coefficient is calculated from Eq. 7.2.2 when t > 10 % and from Eq. 7.2.3 in the case of t < 10 %.

It is possible to determine absorption coefficient by measuring transmission only through samples of different thicknesses. If $\alpha d_1 > 1$ and $\alpha d_2 > 1$ where d_1 and d_2 are the layer thicknesses or transmission t_1 and $t_2 < 10$ %, then absorption coefficient of the layer material is determined from the equation

$$\alpha = \frac{1}{d_2 - d_1} \ln\frac{t_1}{t_2} = \frac{1}{d_2 - d_1} \frac{I_1}{I_2} \qquad (7.2.6)$$

where I_1 and I_2 are light beam intensity having transmitted through the sample of d_1 and d_2 thickness.

We employ Eq. 7.2.6 to calculate absorption coefficient from transmission. The a-C:H samples used in this optical measurements were deposited onto corning 7059 glass which is transparent in the studied wavelength range. A set of samples with different thicknesses were prepared by each deposition voltages. Transmission measurements were performed on Carry 17 double beam spectrometer; substrate material was placed into the comparable beam. Accuracy of transmission measurements was ~ 0.01 %. Several transmission curves are shown in Figs. 7.2.1-7.2.3 for samples of U_{SB} = -200 V, -300 V, and -500 V. Data handling and determination of absorption coefficient were performed by computer. For calculation of α a pair of samples was chosen, which displays appropriate transmittance in the given wavelength range.

Absorption Coefficients from transmission curves similar to those shown in Figs. 7.2.1-7.2.3 was determined only 350-700 nm (3.54-1.77 eV) range because thick layers which satisfy conditions for Eq. 7.2.6 in the infrared region practically can not be prepared.

For any calculation from transmission curves we need larger thickness d. Commonly we measured d of all samples used in different measurements by gravimetric method. Accuracy of weight measurements was ~ 10^{-6} gr, and determination of surface area 10^{-1} mm^2. However there is an important conditions which influence considerably layer thickness measured by this method. Plasma is etching substrate material at the beginning deposition process under which substarte weight is decreasing; the etching becomes stronger at higher deposition voltages. Therefore we have determined layer thicknesses from interference fringes occurring in the infrared region.

In general all investigated a-C:H films are transparent in the IR region however transparency decreases by increasing self biases. Outside the region of fundamental absorption ($h\nu > E_{opt}$) or of the free-carrier absorption (for longer wavelengths), the dispersion of n and k is not very large. In transmission curve there is a maximum at,

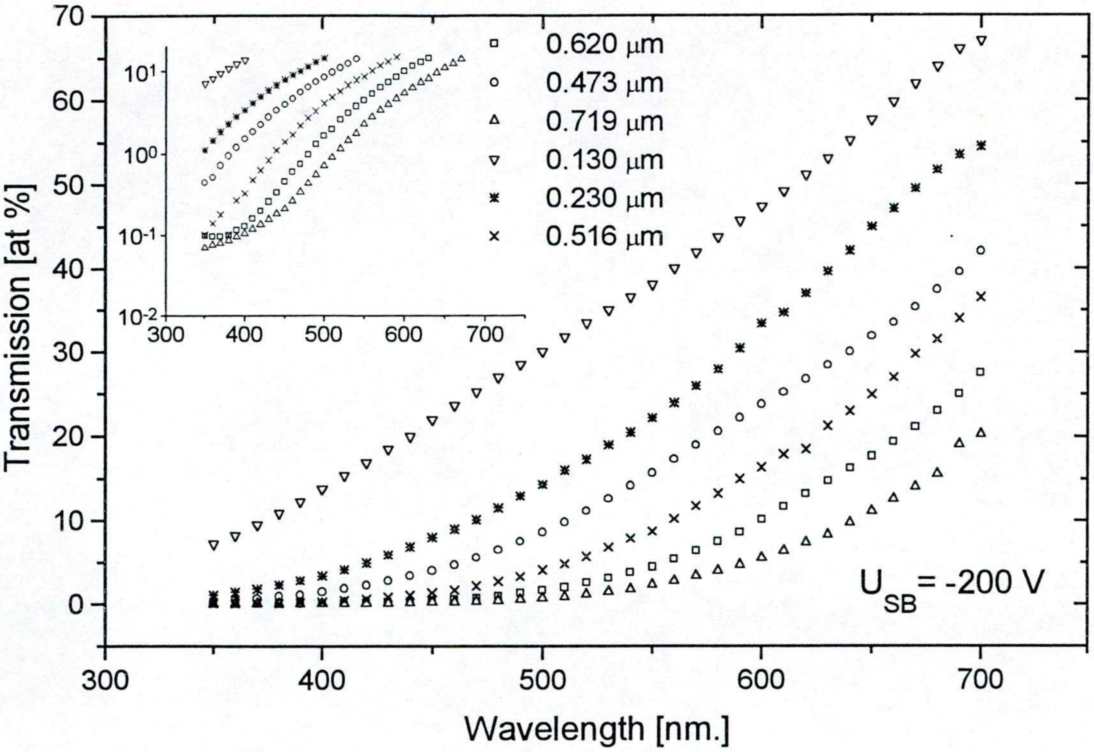

Fig. 7.2.1 Wavelength dependence of transmission in a-C:H samples of U_{SB} = -200 V. Sample thicknesses are listed. The inset shows small transmission region.

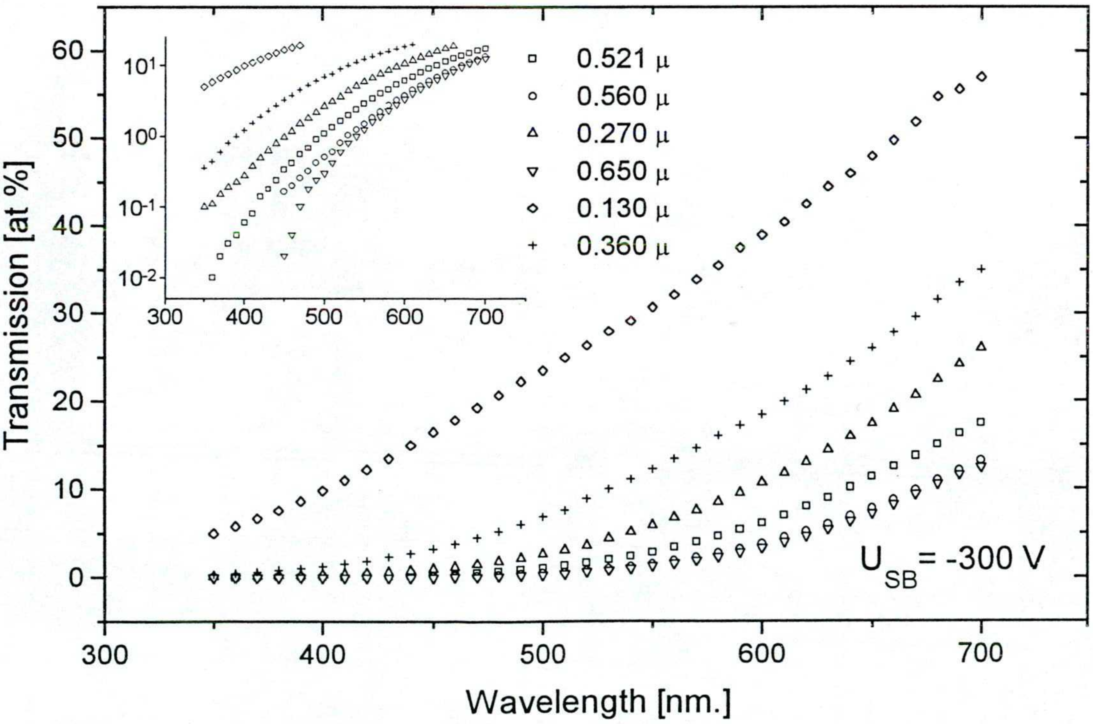

Fig. 7.2.2 Wavelength dependence of transmission in a-C:H samples of U_{SB} = -300 V. Sample thicknesses are listed. The inset shows small transmission region.

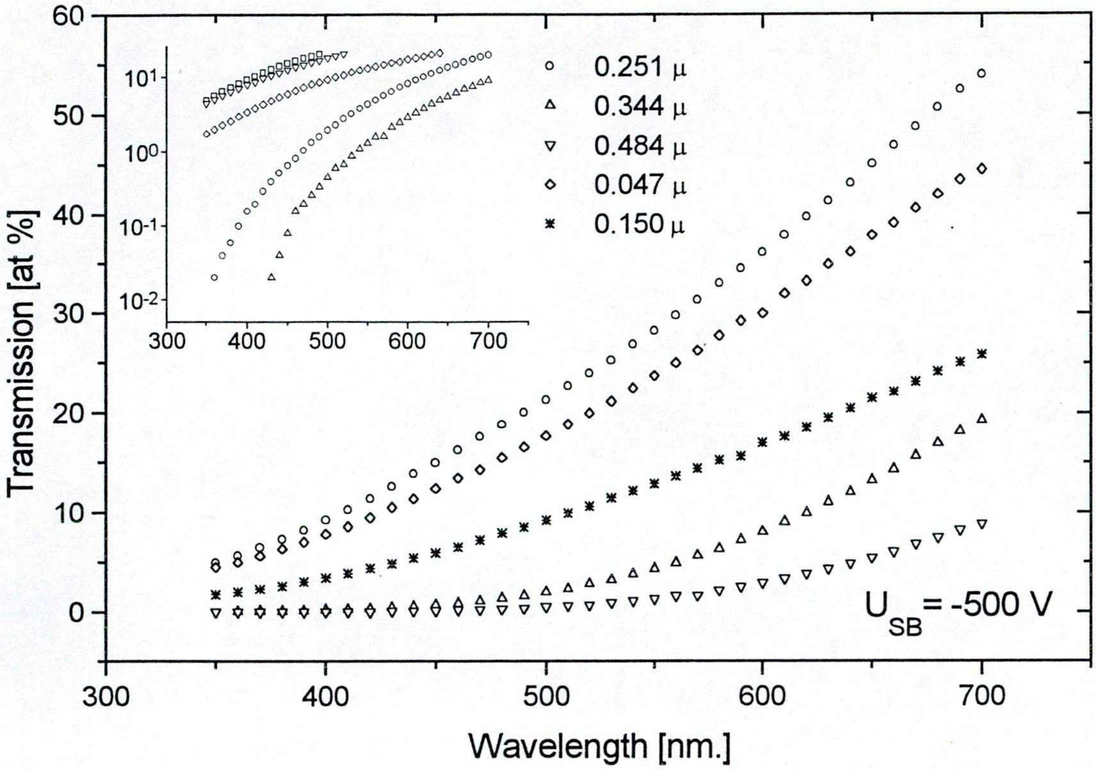

Fig. 7.2.3 Wavelength dependence of transmission in a-C:H samples of U_{SB} = -500 V. Sample thicknesses are listed. The inset shows small transmission region.

$$\lambda_{max} = \frac{4nd}{m}, \ m = 2, 4, 6, ... \qquad (7.2.7.a)$$

and a minimum at,

$$\lambda_{min} = \frac{4nd}{m}, \ m = 1, 3, 5, ... \qquad (7.2.7.b)$$

where m is the order number, n is the refractive index of the semiconducting layer, d is the thickness and λ is the wavelength. In the case of a semiconductor films on a transparent non-absorbing substrate, the thickness (d) can be calculated from two maxima or minima using Eq. 7.2.8

$$d = \frac{M\lambda_1\lambda_2}{2(\lambda_2 n_1 - \lambda_1 n_2)} \qquad (7.2.8)$$

where M is the number of oscillations between two extrema (M=1 between two consecutive maxima or minima). In the case of weak dispersion of n and k of our samples as shown before from ellipsometric measurements, the two refractive indices n_1 and n_2 can be replaced by a constant refractive index n and Eq. 7.2.8 is replaced by

$$d = \frac{\lambda_1\lambda_2}{2n(\lambda_2 - \lambda_1)} \qquad (7.2.9)$$

Then, by taking the refractive index values for each self bias voltage from ellipsometric measurements at 800 nm and the wavelengths from transmission data corresponding to two consecutive maxima or minima, the thicknesses of a-C:H samples can be determined.

The transmission curves in the visible and near IR region with the interference fringes pattern are shown in Figs. 7.2.4-7.2.6. For calculation of layer thickness from Eq. 7.2.9, first we determined wavelength of maximums or minimums by fitting interference curves. Results are summarized in Table. 7.2.1 together with refractive index used for calculation and with layer thickness determined by gravimetric method. Difference of layer thickness determined by the two methods increases with deposition self bias in a good agreement with the increasing etching process at higher self biases.

Table. 7.2.1 Summary of thicknesses calculated by using gravimetric and optical methods for a-C:H samples prepared by different self biases. We have also indicated deviation in % between thicknesses determined by different methods.

No.	**Deposition voltage U_{SB} (V)**	**Refractive index at $\lambda = 0.8$ μm**	**Thickness (μm) Gravimetric**	**Thickness (μm) Optical**	**Thick. No.***	**Difference %**
417	-200	2.2	0.516	0.548	2	6.2
425	-200	2.2	0.719	0.801	5	11.4
525	-200	2.2	0.62	0.727	4	17.3
467	-300	2.17	0.56	0.75	4	34
468	-300	2.17	0.65	0.82	4	26.2
469	-300	2.17	0.94	1.127	5	19.9
247	-400	2.18	1.00	1.29	6	29
484	-400	2.18	0.77	0.972	4	26.2
391	-500	2.22	0.484	0.626	1	29.3
392	-500	2.22	0.344	0.519	1	50.8
411	-500	2.22	1.190	1.467	4	23.3
405	-600	2.13	0.688	0.959	3	39.4
413	-600	2.13	0.797	1.118	2	40.3

* Means the number of thicknesses which calculated by using wither two maximums or two minimums, since the mean of those thicknesses listed in the optical thicknesses column.

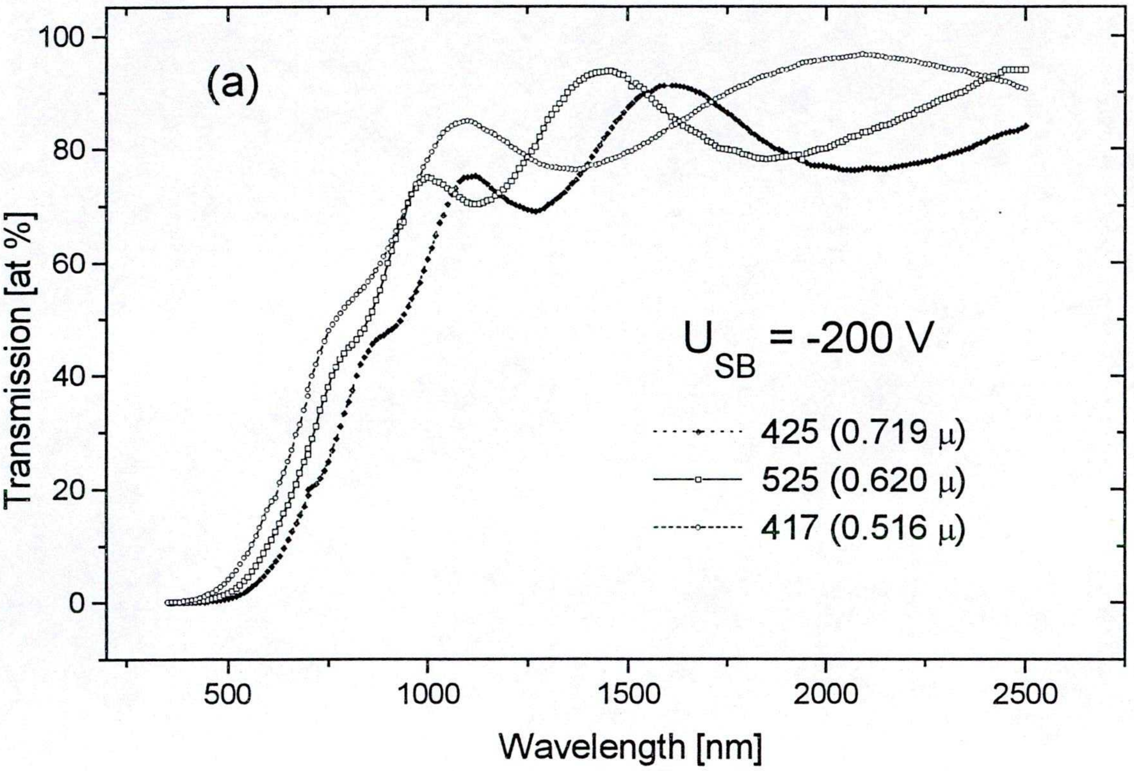

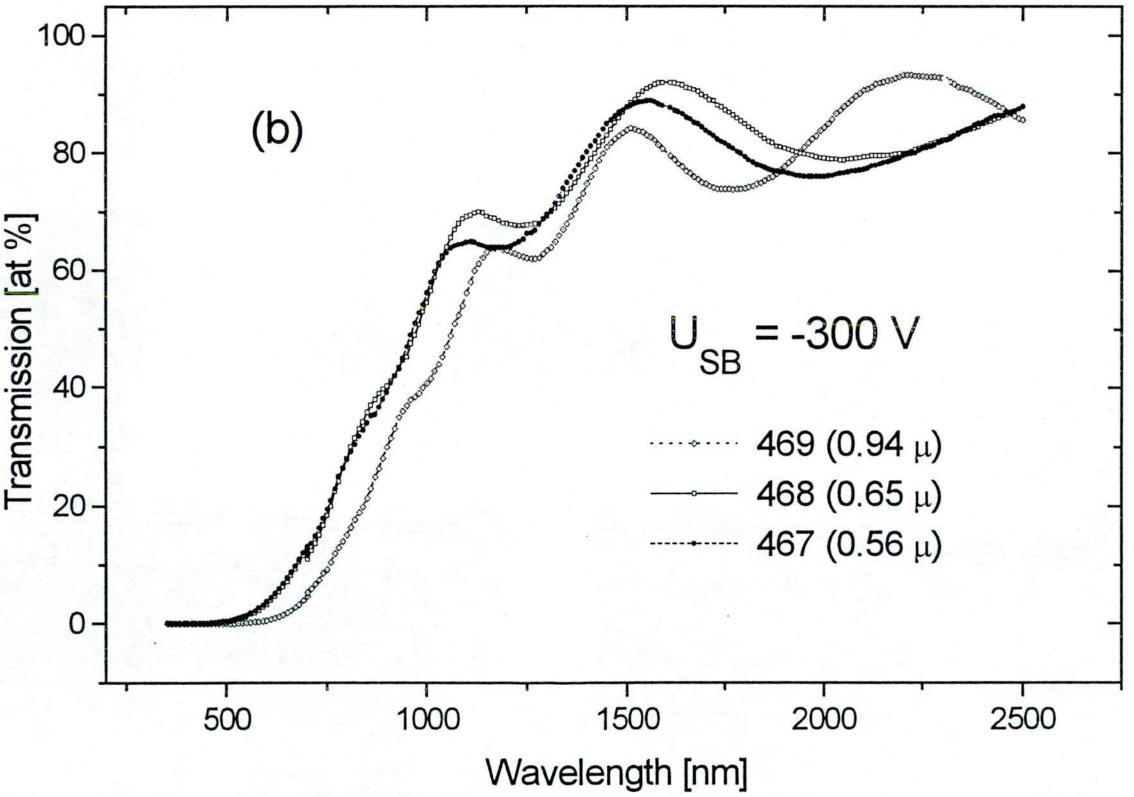

Fig. 7.2.4 Wavelength dependence of transmission in the visible and near IR region: (a) for a-C:H sample of -200 V and (b) for a-C:H sample of - 300 V. Listed thicknesses are taken from gravimetric measurements

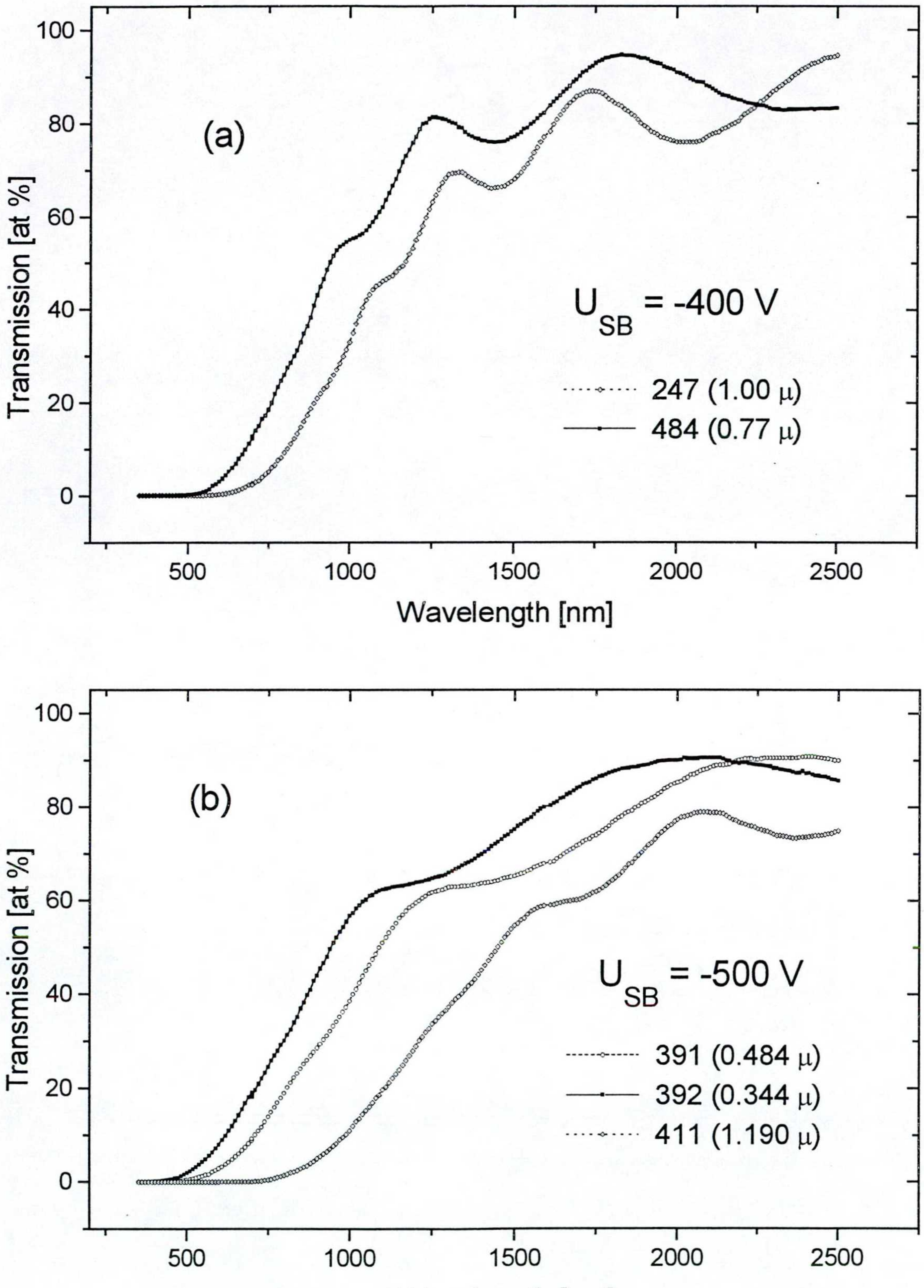

Fig. 7.2.5 Wavelength dependence of transmission in the visible and near IR region: (a) for a-C:H sample of -400 V and (b) for a-C:H sample of -500 V. Listed thicknesses are taken from gravimetric measurements.

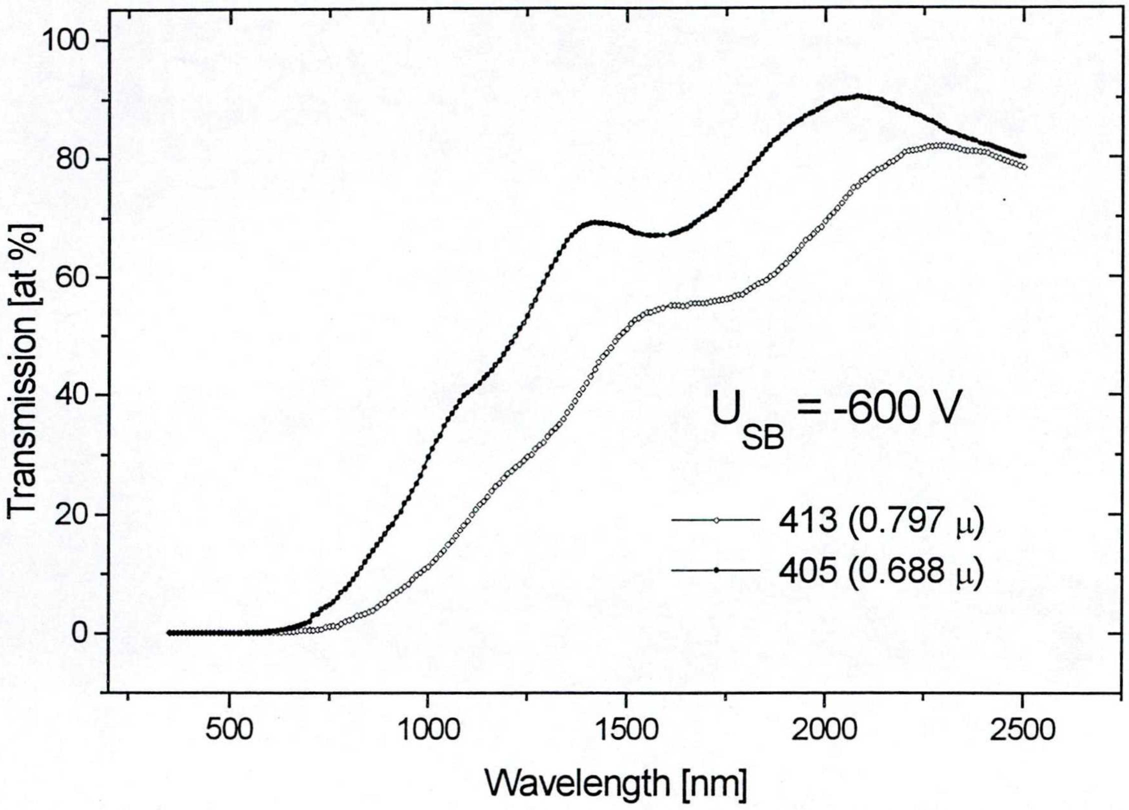

Fig. 7.2.6 Wavelength dependence of transmission in the visible and near IR region for a-C:H sample of -600 V. Listed thicknesses are taken from gravimetric measurements.

7.3. Absorption edge, optical gap and their dependence on bonding structure

In this section we present our experimental results for optical absorption spectra measured by spectral ellipsometry and optical transmission. Then spectral dependence of absorption coefficient is fitted to Tauc equation and optical gap are determined. From these values, by employing some results of theoretical calculation concerning two phase model, the characteristic cluster sizes and ring number can be determined.

Fig. 7.3.1 displays spectral dependence of absorption coefficient calculated from extinction coefficient (Fig. 7.1.3) according to $\alpha = 4\pi k/\lambda$. The absorption spectra calculated from transmission measurements according to $\alpha = [1/(d_2-d_1)] \ln (t_1/t_2)$ are shown in Fig. 7.3.2. comparing these Figures, it is appearent that no considerable difference between absorption coefficient at given photon energy determined by the two experimental methods; however transmission measurement supply more pronounced difference between spectra of low voltages samples compared to ellipsometry. Here we should remark that absorption spectra were constructed from several parts related to sample pairs of different thicknesses in the case of

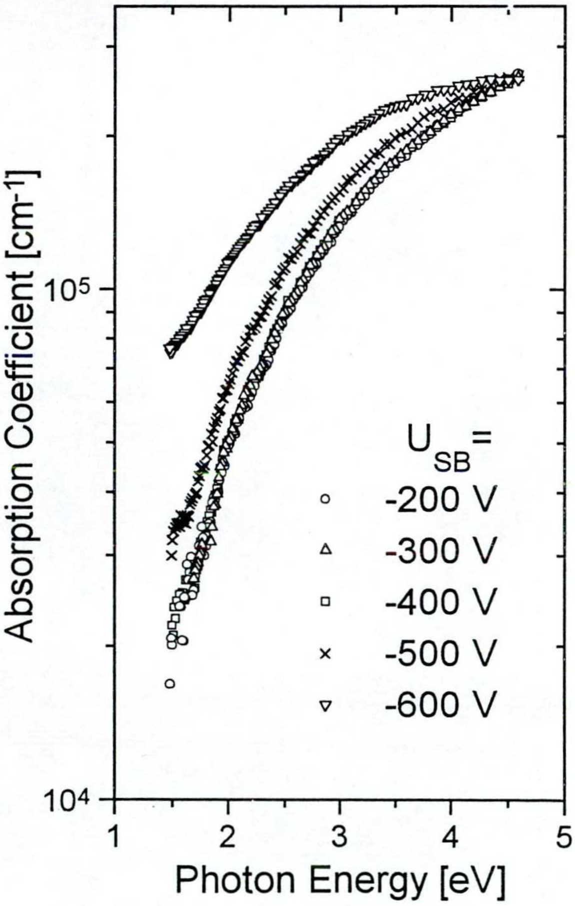

Fig. 7.3.1 Optical absorption spectra of a-C:H layers deposited by different self biases as they are listed. Spectra were calculated from extinction coefficient measured by spectral ellipsometry.

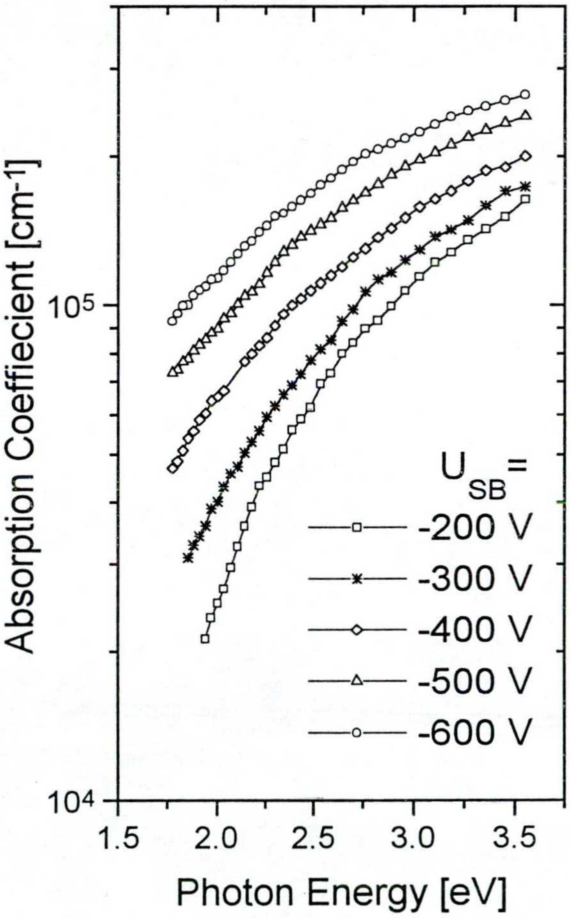

Fig. 7.3.2 Optical absorption spectra of a-C:H samples deposited by different self biases as they are listed. Spectra were determined from results of transmission measurements.

transmission measurements and jumping occurred often between joining parts. It might cause uncertainties as large as 10%.

The absorption spectra near edge region quite broad compared e.g. to that of amorphous silicon which would indicate a wide distribution of cluster sizes, each of clusters is characterized with its local band gap. With decreasing deposition voltage, absorption in the whole photon energy range decreases in good agreement with decreasing number sp^2 coordinated carbon atoms in low voltages samples. Relation between absorption curves indicates the different cluster size distribution too in the studied samples; these appears roughly one order difference in absorption coefficient for samples of -200 V and -600 V in the IR region, where photons excite transition corresponding to large cluster sizes at the same time near 5 eV the absorption approach the same value for these samples.

In the absence of a sharp band edges in an amorphous semiconductor the optical gap is defined empirically as either as the E_{04} gap, the energy at which the optical absorption coefficient $\alpha = 10^4$ cm^{-1}, or the Tauc gap given by fitting α to the Tauc formula :

$$(\alpha\hbar\omega) = B\ (\hbar\omega - E_T)^2 \tag{7.3.1}$$

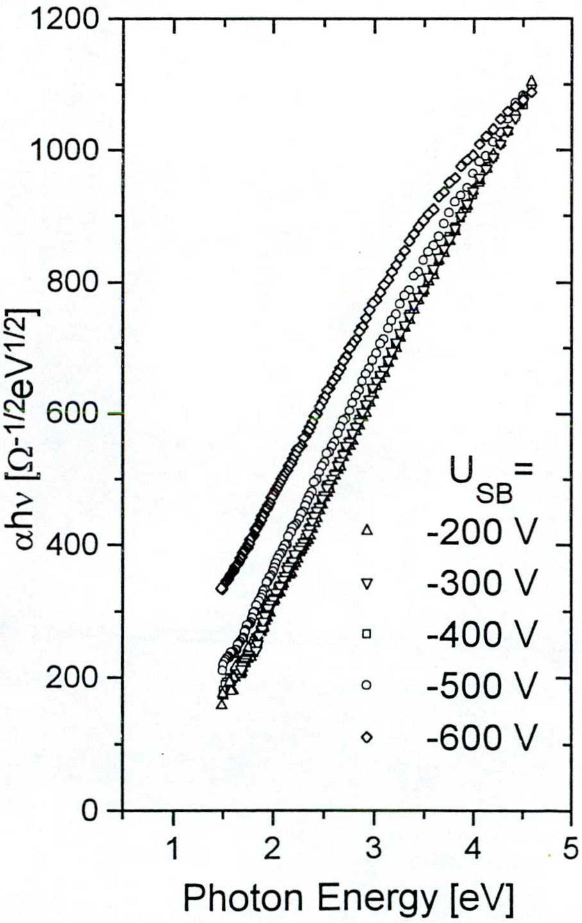

Fig. 7.3.3 Optical absorption data of Fig. 7.3.1 are replotted to show fitting α to the Tauc empirical equation.

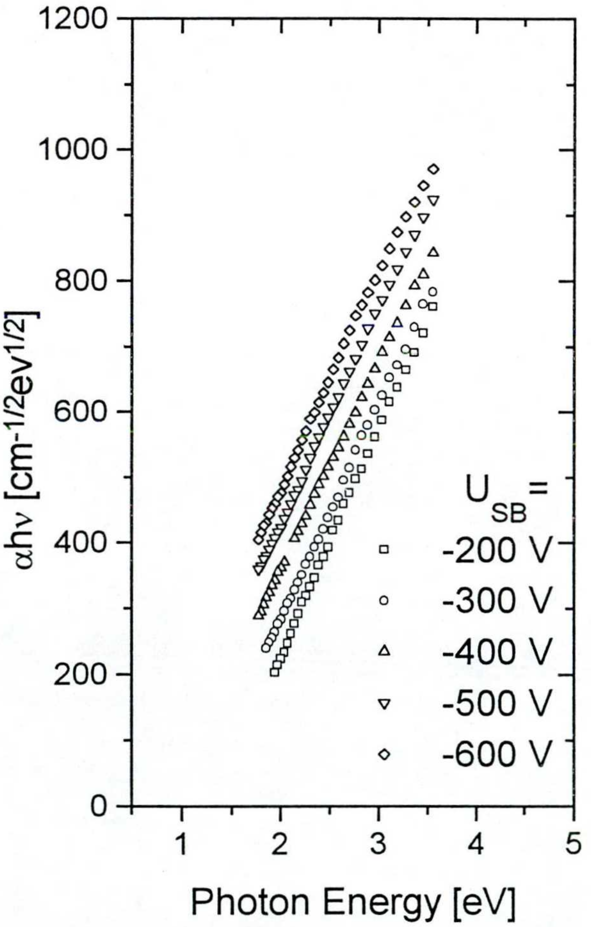

Fig. 7.3.4 Optical absorption data of Fig. 7.3.2 are replotted to show fitting α to the Tauc empirical equation.

for $\alpha = 10^4$ -10^5 cm^{-1}. In Figs. 7.3.3 and 7.3.4 the absorption coefficient are plotted to show fitting to the Tauc formula. Extrapolation of linear part to the $\alpha = 0$ absorption gives the E_T optical gap. In Table. 7.3.1 the optical gap values and B constant are summarized.

A considerable decrease of optical gap occurs at -500 V deposition self bias, however optical gap values determined from transmission measurements decreases more gradually with increasing self bias.

The optical gap E_g depends on the degree of clustering of π states. From Huckel calculations it was found [113] that the gap of compact clusters declines slowly with M according to the approximate relation

$$E_g \cong 2\frac{\beta}{M^{1/2}} \tag{7.3.2}$$

where M is the number of rings in the cluster and $\beta \cong -2.9$ eV. It can also be expressed as

$$E_g \cong 7.7/L_a \text{ eV} \tag{7.3.3}$$

where L_a (Å) is the cluster diameter or correlation length. The gap of acenic clusters falls off more rapidly, as roughly

$$E_g \cong \frac{60}{(M+2.16)^2} \text{ eV} \tag{7.3.4}$$

the observed optical gap corresponds to the largest significant clusters which is characterized with smallest gaps. By employing Eqs. 7.3.2 and 7.3.3 the ring numbers and cluster diameter were calculated. In Table. 7.3.1 the results of calculation are summarized for samples of different self biases. From E_g = 1.25 eV gap, M=21 and L_a = 6 Å are derived for the largest clusters in a-C:H sample of -200 V. For sample of -600 V the E_g = 0.52 eV corresponds to M=124 ring numbers and to L_a = 15 Å in plane correlation length.

Table. 7.3.1 Optical gaps, number of rings M in the significant largest clusters and cluster diameter calculated by employing Eqs. 7.3.2 and 7.3.3.

U_{SB}	**Ellipsometry**				**Transmission**			
(V)	**E_T (eV)**	**M**	**L_a (Å)**	**B**	**E_T (eV)**	**M**	**L_a (Å)**	**B**
-200	1.25	21	6.16	334.4	1.32	19	5.8	346.5
-300	1.27	20	6.06	336.7	1.13	26	6.8	329.3
-400	1.24	21	6.21	335.3	0.88	43	8.75	314.9
-500	1.08	28	7.13	329.5	0.70	68	11	327.9
-600	0.52	124	14.81	294.2	0.52	124	14.8	327.5

The optical gap of a-C:H is determined by medium range ordering of sp^2 coordinated carbon atoms in contrast to other σ bonded amorphous semiconductors such as a-Si:H in which band gap depends only on the short range order.

8. SUMMARY

Bonding structure, electrical, and optical properties of amorphous hydrogenated carbon (a-C:H) layers prepared by radio frequency (rf) plasma decomposition of methane and in some cases benzene under different self biases were studied. The large variability of bonding properties of this material which represented by the sp^2 and sp^3 coordinated carbon ratios give its interesting properties. By changing the deposition parameters we can prepare, diamond-like, graphite-like and polymeric layers. The question how the electrical, and optical properties are related with bonding properties and nanostructure of a-C:H) motivated our research work on this material. Here we summarize those results, obtained by us which contribute considerably to further understanding structure properties of a-C:H and its relation to important macroscopic macroscopic properties.

Considerably different Raman spectra were observed in a-C:H samples when excitation energy decreased from 2.54 eV to 1.17 eV (Fourier Raman spectroscopy). The scattered intensity in the D (disordered) peak region (~1350 cm^{-1}) increased over that of the G (graphite) peak region (~1580 cm^{-1}). Interpretation of Raman data based on the D and G peak intensity ratio (I_D/I_G) can not consider to be established partly because this ratio depends on photon energy used for excitation. Disappearance of G peak in Fourier Raman spectra of low self bias samples indicates that G peak does not relate to small graphite clusters but it should have another origin. In contrast G peak assigned to graphite clusters in the Raman spectra of high self bias samples gained further evidence from our experiments.

Decomposition of D peak in the Fourier Raman spectra exhibits two new bands at 1218 cm^{-1} and 1460 cm^{-1} which were not observed before in a-C:H layers. The band around 1200 cm^{-1}, by analogy to amorphous silicon, is attributed to presence of non-hydrogenated sp^3 hybridized carbon atoms. The band about 1460 cm^{-1} is assigned to conjugate double bond segments of different lengths. These assignments are in good agreement with results of infrared absorption measurements.

Formation of graphite clusters is not solely way of intermediate range ordering of sp^2 coordinated carbons. There may be present olefinic chain segments of sp^2 sites in each a-C:H samples prepared either by high, or by low deposition voltages as it is evidenced by IR and Raman results. However olefinic chains is the dominant medium range ordering in low voltages samples. Aromatic ring structure of sp^2 coordinated carbon atoms can be only formed at high voltages. However the E_{1u} in plane IR active mode of graphite at 1580 cm^{-1} was not observed in any infrared spectra of a-C:H sample except -700 V sample, which has a little absorption band at this wavenumber.

A considerably percent of sp^3 hybridized carbon atoms is bonded to hydrogen. As the hydrogen content of samples decreases by increasing self bias the sp^3 hybridized carbon atoms prefer bonding to other carbon atoms.

The spin–lattice (T_1) relaxation process of hydrogen nuclear magnetization shows two time constant in sample series having considerable different hydrogen content. The relative weights of the two relaxation process depends slightly on temperature but it varies non-monotonically with the hydrogen content. Temperature dependence measured in the range of 70-500 K does not give evidence of that the slowly relaxing component would be the CH_2 chains. The activation energy of the longer relaxation time component was found to be much smaller than the usual values in organic crystals. The short life time can be attributed to CH groups with non aromatic sp^2 carbon atoms.

Temperature dependence of dc conductivity σ_{dc} can not be characterized by single activation energy near and above room temperature neither in low self bias samples nor in high self bias samples. The continuously curving $\ln(\sigma_{dc})$ versus 1/T can be characterized by the derivatives $\partial \ln \sigma_{dc} / \partial (1/T)$, the so called actual activation energy (E_{act}). The E_{act} is 0.4 eV near room temperature but it takes 0.75 eV about 500 K for sample of U_{SB} = -200 V while it increases from 0.2 eV to 0.25 eV in the same temperature range for -700 V sample.

From the fitting to variable range hopping transport we have calculated density of states near Fermi level $N(E_F)$ by using T_0 fitting parameter and $\alpha^{-1} = 10$ Å localization length. $N(E_F) \sim 3.36 \times 10^{16}$ $eV^{-1}cm^{-3}$ for -200 V sample and $N(E_F) \sim 1.51 \times 10^{18}$ eV^{-1} cm^{-3} for -700 V sample would be acceptable, but the pre-exponential factor (σ_0) calculated by using $N(E_F)$ is quite unreasonable and differs considerably from experimental value. Fitting to multiphonon tunneling transport can be made by reasonable parameters only for -200 V samples and in limited temperature range. We suggest that, the real conduction mechanism in the studied temperature range is thermal activated hopping of carriers excited into tail states. Departure from the linearity of the Arrhenius plot, what would not be expected in the case of suggested transport process, is a consequence of the broad energy distribution of barriers due to different bonding configurations of carbon atoms.

Thermal annealing of samples reduces temperature dependence of E_{act} similarly to the influence of increasing deposition voltage. This experimental findings support the relation between barrier distribution and temperature dependence of E_{act}.

The thickness dependence of σ_{dc} vs. temperature does not show transition from three dimensional ($T^{-1/4}$) to two dimensional ($T^{-1/3}$) conduction process. The room temperature conductivity decreases with layer thickness to a minimum following by an increase with decreasing of layer thickness.

Current noise properties were measured first by us in a-C:H samples. $1/f^{\beta}$ frequency dependence with $\beta = 1.14–1.23$ was found. The noise spectral density increases with decreasing sample resistance. The colored noise crosses the white noise at ~40 Hz and ~800 Hz for sample of U_{SB} = -250 V and -500 V respectively.

Dispersion of the real part of the complex refractive index for a-C:H samples prepared by U_{SB} varied in the range of 200–600 V is quite different from that of graphite in 1.5–4.7 eV photon energy range. Samples of -200 V, -300V, -400 V self biases exhibit "diamond -like" behaviour concerning refractive index. This strongly suggest, that no extended graphite structure is present in the samples.

The broad maximum in imaginary part of dielectric function $\varepsilon_2(\omega)$ and its energetic position is in good agreement with increasing clustering of sp^2 coordinated carbon atoms with increase of U_{SB}. As a consequence the optical gap decreases from 1.3 eV to 0.5 eV as the U_{SB} changes in the range of 200-600 V. Experimental evidence for more extended clustering of sp^2 sites in high voltages samples comes from IR and Raman measurements.

If we suppose an energy independent transition matrix element, then $\varepsilon_2(\omega)$ is proportional with the joint valence and conduction band density of states. The different energetic position of the maximum in joint density of states indicates different dominant cluster sizes in the samples. The position of peak in density of states might be corresponds to energy of mobility edge in a-C:H samples, because carriers excited by optical gap energy do not become delocalized following excitation confirmed by dc conduction measurements.

Optical gap corresponds to the largest significant clusters characterized with smallest gaps. The ring numbers and cluster diameter were calculated for samples of different self biases. From $E_g = 1.25$ eV gap, M=21 and $L_a = 6$ Å are derived for the largest clusters in a-C:H sample of -200 V. For sample of -600 V the $E_g = 0.52$ eV corresponds to M=124 ring numbers and to a $L_a = 15$ Å in plane correlation length. This proves that, optical gap of a-C:H is determined by medium range ordering of sp^2 coordinated carbon atoms in contrast to other σ bonded amorphous semiconductors such as a-Si:H in which band gap depends only on the short range order.

ACKNOWLEDGEMENTS

I am deeply indebted to Dr. *Margit Koós*, senior research fellow for her excellent guidance and supervision. She is gratefully thanked as she offered me all the possibilities that facilitated my research work. This work benefited markedly from the suggestions and criticisms of her.

I am very grateful to Dr. *István Pócsik*, who offered me great help during the past four years and also for his valuable comments and for providing constructive valuable remarks, during reviewing my Thesis manuscript.

I am gratefully acknowledge the Hungarian Government, the Hungarian Academy of Sciences for offering me the scholarship and for the Hungarian Science Foundation (OTKA) for its helpful contribution*. Also I would like to express my sincere thanks to the director of the Research Institute for Solid State Physics and Optics, Prof. *Norbert Kroó* and all of the institute staff members.

Grateful thanks to the Ministry of education, Cairo, Egypt for financial support which was provided in the form of scholarship, and also for financial support that facilitated my work. Also, I would like to present my deep gratitude to the Egyptian embassy and the cultural office in Budapest for providing the financial support and for their continuos assistance.

Finally, I present my high appreciation to my parents for their continuous encouragement. Particular thanks and my deep gratitude to my wife *Hoda* for her continuos help, patience during the preparation of this thesis. Also my special thanks to my son *Mohammed*.

---

* Contract numbers were: T-4223, T-017371, T-019165, T-025540, and T-026073.

9. REFERENCES

[1] Korto HW, Heath JR, O'Brien SC, Curl RF, Smalley RE., *Nature,* **318** (1985)162.

[2] S.Iijima, *Nature,* **354** (1991)56

[3] Tanuma SI, Palnichenko A, *J. Mater. Res.,* **10** (1995) 1120

[4] R.F.Davis, *Diamond Films and Coatings,* (Noyes Publishers, New Jerdy) 1993.

[5] J.I. Pankove, *Proc. of the first int. Symp. on Diamond and Diamond Like Films,* (1990) 269.

[6] A.T.Callins and E.C.Lightowlers, in "*Pproperties of Diamond*"ed. J.E.Field, Academic Press, London (1979).

[7] F.Nava, C.Canali, C.Jacoboni, L.Reggiani, and S.F.Korlov, *Solid State Commun.*, **33** (1980) 475.

[8] G.S.Painter, D.E.Ellis, and A.R.Lubinsky, *Phys. Rev B,* **4** (1971) 3610.

[9] N.A.W.Holzwarth, S.G.Louie, and S.Rabii, *Phys. Rev. B,* **26** (1982) 5382.

[10] H.R.Philip and E.A.Taft, *Phys. Rev.* **127** (1962) 159.

[11] E.A.Taft and H.R.Philipp, *Phys. Rev.,* **138** (1965) A197.

[12] C.B.Collins, F.Davanloo, E.M.Juengerman, W.R.Osborn, and D.R.Jander, *Appl. Phys. Lett.,* **54** (1989) 216.

[13] S.A.Solin and A.K.Rawdas, *Phys. Rev.B,* **1** (1970) 1687.

[14] Pham V. Huong, *Diamond and Related Materials,* **1** (1991) 33-41.

[15] Joel W. Ager III, D.Kirk Veirs, and Gerd M.Rosenblatt, *Phys. Rev. B,* **43** (1991) 6491.

[16] R.W.G.Wyckoff, *Crystal Structure,* **1** (interscience, New York 1964).

[17] S.A.Solin, *Physica B,* **99** (1980) 443.

[18] R.J.Nemanich, G.Lucovsky, S.A.Solin, *Solid State Commun.,* **23** (1977) 117.

[19] J.Wagner, M.Ramsteiner, Ch.Wild, and P.Koidl, *Phys. Rev. B,* **40** (1989) 1817.

[20] Fishburn, D.B., *Physics and Chemistry of Carbon,* edited by P.L.Walker (New York:Dekkker) **7** (1971).

[21] Jenkins,G. M., and Kawamura,K., 1976, *Polymeric Crbons* (Cambridge University Press).

[22] J.Robertson, *Advances in Physics,* **35** (1986) 317.

[23] Moore,A.W., *Physics and Chemistry of carbon,* **11**, edited by P.L.Walker (1973) (New York:Dekkker).

[24] M.S.Dresselhaus and G.Dresselhaus, in *Light Scattering in Solids III,* edited by M.Cardona and G.Guntherödt (Springer, Berlin, 1982), P.12.

[25] M.S.Dresselhaus and G.Dresselhaus, *Adv. Phys.,* **30** (1981)139.

[26] Bundy FP, Basset WA, Weathers MS, Hemley RJ, Mao HK, Goncharov AF, *Carbon,* **34** (1996) 141.

[27] R.J.Caveney, in J. Field (ed.), *The Properties od Diamond,* Academic Press. New York, 1979, P.610.

[28] P.J.Heath. *VDI-Berichte,* **762** (1989) 37.

[29] B.V.Spitsyn, L.L.Bouilov, and B.V.Deryagin, *J. Cryst. Growth.,* **52** (1901) 219.

[30] M.Endo, K.Takeuchi, K.Kobori, K.Takahashi, H.Kroto, and A.Sharker, *Carbon,* **33** (1995) 875.

[31] K.Soto, M.Noguchi, A.Demachi, N.Olei, and M.Endo, *Science,* **264** (1994) 556.

[32] S.J.Bull and A.Matthews, *Diamond and Related Materials,* (1992) 1049-1064, Elsevier Science Publishers B.V., Amsterdam.

[33] J.W.Zou, K.Schmidt, K.Reichelt and B.Dischler, *J. Appl. Phys.,* **67** (1990) 487.

[34] B.Dischler, A.Bubenzer, and P.Koidl, *Solid State Commun.,* **48** (1983) 105.

[35] J.W.Zou, K.Schmidt, K.Reichelt and B.Dischler, *.J.Appl. Phys.,* **65** (10) (1989) 3914.

[36] M.A.Tamor, W.C.Vassell and K.R.Carduner, *Appl. Phys. Lett.,* **58** (1991) 592.

[37] R.Kleber, K.Jung, H.Ehrhardt, I.Mühling, K.Breuer, H.Metz and F.Engelke, *Thin Solid Films,* **205** (1991) 274.

[38] B.Dischler, in "*Amorphous Hydrogenated Carbon Films*"ed. P.Koidl and P.Oelhafen, Proc. Euro. Mat. Res. Soc. **17**, 189 (Les Editions de Physique, Paris, 1987).

[39] Y.Bounouh, M.L.Thèye, A.Dehbi-Alsoui, A.Matthews, and J.P.Stoquert, *Phys. Rev. B* **51** (1995) 9597.

[40] J.Fink, T.Müller-Heinzerling, J.Peluger, A.Bubenzer, P.Koidl, and G.Crecelius, *Solid St. Commun.,* **47** (1983) 687.

[41] J.Fink, T.Müller-Heinzerling, J.Pflüger, B.Sceerer, B.Dischler, P.Koidl, A.Bubenzer, and R.E.Sah, *Phys. Rev. B* **30** (1984) 4713.

[42] A.Grill, B.S.Mererson, V.V.Patel, J.A.Reimer and M.A.Pertrich, *J. Appl. Phys.,* **61** (1987) 2874.

[43] C.Jäger, J.Gottwald, H.W.Spiess and R.J.Newport, *Phys. Rev. B.,* **50** (1994) 846.

[44] R.Kleber, K.Jung, H.Ehrhardt, I.Mühling, K.Breuer, H.Metz and F.Engelke, *Thin Solid Films,* **205** (1991) 174-278.

[45] U.Schwerk, F.Engelke, R.Kleber and D.Michel, *Thin Solid Films,* **230** (1993) 102.

[46] S.Kaplan, F.Hansen, and M.Machonk, *Appl. Phys. Lett.,* **47** (1985) 750.

[47] J.Robertson, *Proc. Solid St. Chem.,* **21** (1991) 199.

[48] T.M.Burke, D.W.Huxley, R.J.Newport, G.Bushnell-wye and J.Franks, *Mat. Res. Soc. Symp. Proc.,* **270** (1992) 395.

[49] D.W.Huxely, P.J.R.Honeybone, R.J.Newport, W.S.Howells and J.Franks, *Mat. Res. Soc. Symp. Proc.,* **270** (1992) 493.

[50] J.K.Walters, P.J.R.Honeybone, D.W.Huxley, R.J.Newport, and W.S.Howells, *Phys. Rev. B,* **50** (1994) 831.

[51] J.K.Walters and R.J.Newport, *J. Phys.: Condens. Matter,* **7** (1995) 1755.

[52] B.Dischler "Amorphous Hydrogenated Carbon Films " ed P.Koidl and P.Oelhafen (Les Ulis: Editions de Physiques) p 189.

[53] F.R.Dollish, W.G.Fately and F.F.Bentley "Charaecteristic Raman Frequencies" (New York: Wiely) 1974b.

[54] R.E.Shroder, R.J.Nemanich, and J.T.Glass, *Phys. Rev. B,* **41** (1990) 3738.

[55] R.J.Nemanich and S.A.Solin, *Phys. Rev. B,* **20** (1979) 392.

[56] J.Wagner, N.Ramsteiner, C.Wild, and P.Koidl, *Phys. Rev. B,* **40** (1989) 1817.

[57] R.O.Dillon, J.A.Woollman, and T.Katkanant, *Phys. Rev. B,* **29** (1984) 3482.

[58] F.Tunistra and J.L.Koenig, *J. Chem. Phys.,* **53** (1970) 1126.

[59] D.Beeman, J.Silverman, R.Lyden and M.R.Anderson, *Phys. Rev. B,* **30** (1984) 870.

[60] D.Beeman and R.Alben, *Adv. Phys.,* **26** (1977) 339.

[61] B.Dischler, A.Bubenzer, and P.Koidl, *Appl. Phys. Lett.,* **42** (1983a) 636.

[62] B.Dischler, A.Bubenzer, and P.Koidl, *Solid St. Commun.,* **48** (1983b) 105.

[63] J.Fink, T. Muller-Heinzerlang, J.Pfluger, A.Bubenzer, P.Koidl, and G.Crecelius, *Solid St. Commun.,* **47** (1983) 887.

[64] A.Grill and V.Patel, *Appl. Phys. Lett.,* **60** (1992) 17.

[65] S.Xu, M.Hundhausen, J.Ristein, B.Yan, and L.Ley, *J. Non-Cryst. Solids,* **164-166** (1993) 1127.

[66] M.A.Tamor, J.A.Haire, C.H.Wu, and K.C.Hass, *Appl. Phys. Lett.,* **54** (1989) 123.

[67] M.A.Tamor and W.C.Vassell, *J. Appl. Phys.,* **76** (1994) 3823.

[68] M.Ramsteniner and J.Wagner, *Appl. Phys. Lett.,* **51** (1987) 1355.

[69] J.Robertson and E.P.O'Reilly, *Phys. Rev. B* **35** (1987) 2946.

[70] N.Wada, P.J.Gaczi, and S.A.Solin, *J. Non-Cryst. Solids,* **35-36** (1980) 543.

[71] a.Grill, V.Patel, and B.S.Meyerson, *Proc. of Diamond and Diamond-Like Films and Coatings,* Ed. by R.E.Clausing et al., Plenum Press, New York, 1991.

[72] J.C.Angus, F.Jansen, *J. Vac. Sci. Technol. A,* **6** (1988) 1778.

[73] J.Seth, R.Padiyath, and S.V. Babu, *J. Vac. Sci. Technol. A,* **10** (1992) 284.

[74] A.Dehbi-Alaoui, A.S.James, and A.Matthews, *Surface and Caotings Technology,* **43-44** (1990) 88.

[75] S.Aisenberg, *J. Vac. Sci. Technol. A,* **2** (1984) 369.

[76] R.Stief, J.Schäfer, J.Ristein, L.Ley, and W.Beyer, *J. Non-Cryst. Solids,* **198-200** (1996) 636.

[77] Tersoff , *Phys. Rev. Lett.,* **61** (1988) 2879.

[78] G.Galli and R.M.Martin, *Phys. Rev. Lett.,* **62** (1989) 555.

[79] G.Jungnickel, T.Frauenheim, P.Blaudeck, U.Stephan, and R.J.Newport, *Phys. Rev. B,* **50** (1994) 6709.

[80] S.Iarlori, G.Galli, and O.Martini, *Phys. Rev. B,* **49** (1994) 7060.

[81] F.W.Smith, *J. Appl. Phys.,* **55** (1984) 764.

[82] D.R.Meckenzie, R.C.Mcphedran, N.Savvides, and L.C.Batton, *Phil. Mag. B,* **48** (1983) 341.

[83] D.R.Meckenzie, L.C.Batton, and R.C.Mcphedran, *Phys. Rev. Lett.,* **51** (1983) 280.

[84] J.L.Bredas and G.B.Street, *J. Phys. C,* **18** (1985) L 651.

[85] Li.Fang and J.L.Lannin, *Phys. Rev. Lett.,* **65** (1990) 1905.

[86] N.F.Mott and E.A.Davis, "Electronic Processes in Non-Crystalline Solids" (Oxford, 1979).

[87] N.F.Mott and E.A.Davis, "Electronic Processes in Non-Crystalline Solids" (Oxford, 1971).

[88] D.Wesner, S.Krummacher, R.Car, T.K.Sham, M.Strongin, W.E.Berhardt, S.L.Weng, G.Williams, *Phys. Rev. B,* **28** (1983) 2152.

[89] P.Olhafen and D.Ugatini in *proc. EMRS,* **17** (1987) 267

[90] J.Schäfer, J.Ristein, L.Ley, U.Stephan, Th.Frauenheim, *J. Non-Cryst. Solids,* **198-200** (1996) 641.

[91] Y.Bounouh, M.L.Théye, A.Dehbi-Alaoui, A.Matthews, J.Cernogora, J.L.Fave, C.Colliex, A.Gheorghiu, and C.Sénémaud, *Diamond and related materials,* **2** (1993) 259.

[92] W.B.Jackson, S.M.Kelso, C.C.Tsai, J.W.Allen, and S.J.Oh, *Phys. Rev. B,* **31** (1985) 5187.

[93] J.Robertson, *Phil. Mag. Lett.,* **57** (1988) 143.

[94] M.Koós, I.Pócsik, and L.Tóth, *J. Non-Cryst. Solids,* **164-166** (1993) 1151.

[95] M.Koós, I.Pócsik, J.Erostyák, and A.Buzády, *J. Non-Cryst. Solids,* **226-229** (1998).

[96] M.Koós, I.Pócsik, M.Hundhausen, and L.Ley, in :*Amorphous Carbon:* State of Art, Ed. by S.R.S.Silva, J.Robertson, G.A.J.Amaratunga and W.I.Milne, Word Scientific, Singapore 1988.

[97] J.J.Hauser, *J. Non-Cryst. Solids,* **23** (1977) 21.

[98] M.Vogel, O.Stenzel, R.Petrich, G.Schaarschmidt, and W.Scharaff, *Thin Solid Films,* **227** (1993) 74-89.

[99] J.Tauc, " *Amorphous Semiconductors* " edited by M.H.Brodsky (New York: Plenum), (1973).

[100] N.F.Mott and E.A.Davis "*Electronic processes in Non-Crystalline Solids*", (Oxford 1980).

[101] C.J.Adkins, S.M.Franke, and E.M.Hamilton, *Phil. Mag.,* **22** (1970) 183.

[102] G.Jungk and C.H.Lange, *Phys. Stat. Sol., (b),* **50** (1972) k71.

[103] R.Grigorovichi, A.Devenyi, A.Gheorghiu, and A.Belu, *J. Non-Cryst. Solids,* **8** (1972) 793.

[104] E.T.Arakawa, M.W.Williams, and T.Inagaki, *J. Appl. Phys.,* **48** (1977) 3136.

[105] D.A.Anderson, *Phil. Mag.,* **35** (1977) 17.

[106] D.I.Jones, and A.D.Stewart, *Phil. Mag. B,* **46** (1982) 423.

[107] D.R.McKenzie, R.C.McPhedran, N.Savvides, and D.J.H.Cockayne, *Thin Solid Films,* **108** (1983) 247.

[108] A.Bubenzer, B.Dischler, G.Brandt, and P.Koidl, *J. Appl. Phys.,* **54** 4590.

[109] C.Weissmantel, *Thin Solid Films,* **58** (1979) 101; *Ibid.,* **92** (1982) 55.

[110] P.Koidl, C.Wild, D.Dischler, J.Wagner, M.Ramsteiner, *Materials Science Forum,* **52&53**, (Trans Tech Public, Switzerland, 1989) 41-70.

[111] B.Meryerson and F.Smith, *J.Non-Cryst. Solids,* **35&36** (1980) 435-440.

[112] M.Koós, I.Pócsik, and L.Tóth, *Appl. Phys. Lett.,* **65** (1994) 2245.

[113] J.Robertson, *Proc. Solid St. Chem.,* **21** (1991) 199.

[114] M.Koós and I Pócsik, *Application of Non Crystalline Semiconductors in Optoelectronics,* ed. by A.Audriesh and M.Bertolotti, Kewuer Academic Publishers, Dordrecht (1997) 361.

[115] S.Oreszko, W.Bala, F.Fabisial, F.Roploch, *Phys. Stat. Solidi,* **81** (1984) 579.

[116] A.Reyes-Mena, R.Asomora, J.Gouzaler-Hernamder, and S.S.Chao, *J. Non-Cryst. Solids,* **114** (1989) 310.

[117] M.A.Tamor, J.A.Maire, C.H.Win, and K.C.Mass, *Appl. Phys. Lett.,* **54** (1989) 123.

[118] K.Fabisiab, F.Roploch, Wiecsorek, *J. Phys. D,* **21** (1988) 995.

[119] D.Arcon, P.Cevc, B.Blinc, I.Pócsik, M.Koós, Z.Trontelj, and Z.Jaglievc, *Molecular Nanostructures,* ed. by H.Kuzmany, J.Fink, M.Mehring, and S.Roth, World Scientific (1997) 533.

[120] D.J.Miller and D.R.McKenzie, *Thin Solid Films,* **108** (1983) 257.

[121] J.Ristein ,J.Schäfer, and L.Ley, *Diamond and Related Mater.,* **4** (1995) 508.

[122] K.Köhler, D.E.Horne, and J.W.Coburn, *J. Appl. Phys.,* **58** (1985) 3950.

[123] P.Koidl, C.Wild, B.Dischler, J.Wagner and M.Ramsteiner, *Mat. Sci. Forum,* **52&53** (1989) 41.

[124] P.Koidl, C.Wild, B.Dischler, J.Wagner and M.Ramsteiner, *Mat. Sci. Forum,* **52** (1990) 41.

[125] Y.Catherine, P.Couderc, *Thin Solid Films,* **144** (1986) 265.

[126] F.Pászti, E.Szilágyi, and E.Kótai, *Nucl. Instr. and Meth. B,* **54** (1991) 507.

[127] P.Koidl, C.Wild, R.Lacher, and R.E.Sah, *Diamond and Diamond-like Coatings* ed. by R.E.Clausing et. al., Plenum Press, New York (1991) P.243.

[128] A. Helmbold, P. Hammer, J.U. Thiele, K.Rohwer and D. Meissner, *Phil. Mag. B,* **72** (1995) 335.

[129] J.Tauc, " *Amorphous Semiconductors* " edited by M.H.Brodsky (New York: Plenum), (1974).

[130] A.Grill and V.Patel, *Appl. Phys. Lett.,* **60** (17) (1992) 2089

[131] L.J.Bellamy, *"The Infra-red Spectra of Complex Molecules",* John Wiley & Sons ,Inc., New York (1955).

[132] I. Pócsik, M.Koós, S.H.Moustafa, J.A.Andor, O.Berkesi, and M.Hundhausen, *Microchim. Acta [Suppl.],* **14** (1997) 755.

[133] M.Yoshikawa, N.Nagai, M.Matsuki, H.Fukuda, G.Katagiri, H.Ishida, A.Ishitani, and I.Nagai, *Phys. Rev. B,* **46** (1992) 7169.

[134] I.Pócsik, M.Koós, M.Hundhausen, and L.Ley, *J. Non-Cryst. Solids,* **227-230** (1998) 1083.

[135] I.Pócsik, M.Hundhausen, M.Koós, and L.Ley, *J. Non-Cryst. Solids,* **226-229** (1998) (in press).

[136] Ch. P. Slichter, *Principles of Magnetic Resonance,* Harper and Row, New York, 1963.

[137] C. Jäger, J. Gottwald, H.W. Spiess and R.J. Newport, *Phys. Rev. B,* **50** (1994) 846.

[138] I. Pócsik, M.Koós, S.H.Moustafa, G.Lasanda, P.Bánki, and K.Tompa, *J. Non-Cryst. Soids,* **198-200** (1996) 632.

[139] B. Frick and D. Richter, *Science,* 267 (1995) 1939.

[140] D.C. Alion and J.A. Norcross, *Phys. Rev. Lett.*, 74 (1995) 2383.

[141] G. Papavassiliou, A. Leventis, F. Milia and J. Dolinsek, *Phys. Rev. Lett.*, **74** (1995) 2387.

[142] R. Blinc, *Physics World,* **8** (7) (1995) 25.

[143] J.Robertson, *J. Non-Cryst. Solids,* **164-166** (1993) 1115.

[144] A.K.Jouscher, "Principles of Semiconductor Device Operation." Bell, London, 1960.

[145] S.M.Sze, "Physics of Semiconductor Devices" (Wiley, New-York, 1969)

[146] I. Pócsik, M. Koós and L. Tóth, *Solid State Commun.*, 76 (1990) 103.

[147] M. Koós, S. H. Moustafa and I. Pócsik, Proc. of 13th Int. Conf. on *"Noise in Physical Systems and 1/f fluctuations"* ed. by V. Bareikis and R. Katilius, World Scientific, Singapore (1995) p. 311.

[148] Nyquist, *Phys. Rev.*, **32** (1928) 110, and J. B. Johnson *ibid,* **32** (1928) 97.

[149] I.Pócsik, M. Koós and L. Tóth, in: *Noise in Physical Systems and 1/f Fluctuations;* Ed. by T. Musha, S. Sato and M. Yamamoto, Ohmsha Ltd. Tokyo 1991. pp. 99-102.

[150]V.Ambegaokar, B.I.Halperin, and J.S.Langer, J. Non-Cryst. Solids, **8-10** (1972) 492.

[151] C. J. Adkins , S.M. Freake and E.M. Hamilton, *Phil. Mag.*, **22** (1970) 183.

[152] J.J. Hauser, *Solid State Comm.*, 17 (1975) 1577.

[153] K. Shimakawa, and K. Miyake, *Phys. Rev. Lett.,* **61** (1988) 994.

[154] D. Dasgupta, F. Demichelis, and A.tagliaferro, *Phil. Mag. B,* **63** (1991) 1255.

[155] N.F. Mott, *Phil. Mag.,* **19** (1969) 835.

[156] M.Morgan, *Thin Solid Films,* 7 (1971) 313.

[157] V.Paillard, M.Meaudre, P.Melinon, V.Dupuis, J.P.Perez, S.Vignoli, A.Perez, and R.Meaudre, *J. Non-Cryst. Solids,* **191** (1995) 174.

[158] S.R Elliot, *Physics of Amorphous Materials,* Longman Scientific and Technical, London,1990.

[159] D.Adler, L.P.Flora, and S.D.Senturia, *Solid State Commun.,* **12** (1973) 9.

[160] J. Robertson , J. *Non-Cryst. Solids,* **198-200** (1996) 615.

[161] D.Emin, *Adv. Phys.,* **24** (1975) 305.

[162] M.L.Kuotek in *"Tetrahedrally Bonded Amorphous Semiconductors"* ed. by M.H.Broásky, S.Kirkpartrik, and D.Weaire, AIP Proc. No. 20 (1974) 297.

[163] A.Bunde and S.Havlin: *Fractals and Disordered systems* 2nd Edition, Springer, Heidelberg (1996).

[164] G.A.J.Amaratunga and S.Ravi P.Silva, *J. Appl. Phys.,* **70** (1991) 5374.

[165] J.C.Phillips, *"Bonds and bands in semiconductors"* (Academic, New York, 1973).

[166] J.Tauc, *Prog. Semiconductors,* 9 (1965) 87.

[167] F.Bassani, *Interaction of Radiation with Condensed Matter,* **11** Intl. Atomic Energy Agency, Vienna (1977).

[168] H.R.Philipp and H.Ehrenreich, *Phys. Rev.,* **129** (1963) 1550.

[169] S.H. Moustafa, M. Koós and I.Pócsik, *J. Non-Crystalline Solids,* **227-230** (1998).

[170] J.Tauc, *"Amorphous and Liquid Semiconductors"*ed. by J.Tauc, Plenum, London (1974).

[171] F.B.Pethica, P.Koidl, J.Gobrecht., and C.Schüler, *J. Vac. Technol. A,* **3** (1985) 2391.

[172] J.Wagner and P.Lanteuschlager, *J. Appl. Phys.,* **59** (1986) 2044.

[173] J.Robertson, *Surface and coating technology,* **50** (1992) 185.

[174] G.A.N. Conuell, *Amorphous Semiconductors,* ed. M.H.Bradsky, topics in Applied Physics, **63** (springer, Berlin, 1979) 73.

[175] R.M.A.Azzam and N.M.Bashara, *Ellipsometry and polarized light*, North-Holland, Amsterdam (1977).

[176] M.Fried, T.Lohner, J.Gyulai *in semiconductors and semimetals,* **46** ed. by C.Chnuistofides and g.ghibaudo, Academic Press (1997).

[177] M.Koós, S.H.Moustafa, I.Pócsik, and E.Szilágyi. To be published in *Diamond and Related Materials.*

[178] M.Koós and I.Pócsik, *Physics and Applications of Non-Crystalline Semiconductors in Optoelectronics*, ed. by A.Audriesh and M.Bertolotti, NATO ASI Series, **36** (1996) 361.

[179] Ju.J.Uhanov, *Optical Properties of Semiconductors,* Nauka, Moskva (1977).